



**HAL**  
open science

# Dynamic systems for the translocation of water, ions or electrons

Erol-Dan Licsandru

► **To cite this version:**

Erol-Dan Licsandru. Dynamic systems for the translocation of water, ions or electrons. Other. Université Montpellier, 2015. English. NNT : 2015MONTTS213 . tel-02052090

**HAL Id: tel-02052090**

**<https://theses.hal.science/tel-02052090v1>**

Submitted on 28 Feb 2019

**HAL** is a multi-disciplinary open access archive for the deposit and dissemination of scientific research documents, whether they are published or not. The documents may come from teaching and research institutions in France or abroad, or from public or private research centers.

L'archive ouverte pluridisciplinaire **HAL**, est destinée au dépôt et à la diffusion de documents scientifiques de niveau recherche, publiés ou non, émanant des établissements d'enseignement et de recherche français ou étrangers, des laboratoires publics ou privés.

UNIVERSITÉ de MONTPELLIER

THÈSE

pour obtenir le grade de  
DOCTEUR de l'UNIVERSITÉ de MONTPELLIER

Préparée au sein de l'école doctorale  
ED459 Sciences chimiques Balard  
Et de l'unité de recherche IEM UMR5635

Spécialité : Chimie des Matériaux

Présentée par Erol-Dan LICSandRU

---

# Dynamic Systems for the Translocation of Water, Ions or Electrons

---

Soutenue le 26-05-2015 devant le jury composé de :

|   |                    |
|---|--------------------|
| M. Teodor Silviu BALABAN, Professeur, Université Aix-Marseille III              | Rapporteur         |
| Mme. Andreea PASC, Maître de conférences, Université de Lorraine                | Rapporteur         |
| M. Nicolas GIUSEPPONE, Professeur, Institut Charles Sadron                      | Examineur          |
| M. Pascal DUMY, Professeur, Ecole Nationale Supérieure de Chimie de Montpellier | Examineur          |
| Mme. Sophie TINGRY, Chargée de recherche, Institute Européen des Membranes      | Examineur          |
| M. Mihail BARBOIU, Directeur de recherche, Institute Européen des Membranes     | Directeur de thèse |



## Acknowledgments

Firstly, I would like to thank the Director of my thesis DR. Mihail Barboiu. For the three years I spent in his team, Nanosystèmes Supramoléculaires Adaptatifs, he has been the support and the guiding line of my work. His true passion for science, and particularly, for chemistry are a true inspiration. This native curiosity was translated into an enriched experience for me, allowing me to work on very different subjects from an interdisciplinary perspective. On both a professional, as well as on a personal level I can truly say that I learned a lot from him. I am very grateful for the chance he gave me both as his PhD student and for including me in the DYNANO Marie Curie ITN. I thank Marie Curie actions and the DYNANO project (ITN 298033) for financing my work.

I would like to thank the members of my jury, Pr. Teodor Silviu Balaban and MCF. Andreea Pasc who accepted to be rapporteurs, as well as, Pr. Pascal Dumy, the president of the jury, Pr. Nicolas Giuseppone and CR. Sophie Tingry who accepted to be examiners. I appreciate their presence at my defense and the very constructive questions and comments on my work.

Many thanks are also due to the many people that helped me during this project.

From Institut Européen des Membranes:

Dr. Sophie Tingry, who has been like a second coordinator for my thesis. She gracefully welcomed me in her group, while teaching me electrochemistry. It was a true pleasure to work with her.

Dr. Yves-Marie Legrand, a person to who I owe a lot to. For any problem, professional or personal he is the person to talk to. He is the balance of the team, as well as a great scientist.

Dr. Arie van der Lee, our brilliant crystallographer, who solved many of the crystals in this work. Eddy Petit, who taught me everything I know about NMR and Mass Spectrometry. Arnaud Gilles, who showed me vesicular methods and fluorescence and introduced me in the transport field. Florina Dumitru, who worked on my crystals and was a great conversation partner.

Our many collaborators:

Pr. Nicolas Giuseppone and the SAMS team, Emilie Moulin, Mounir Maaloum, Susanne Schneider, and Thomas Ellis, together with who we had a very fruitful collaboration in the project concerning the triaryl amine nanocontacts.

Dr. Manish Kumar and Yuexiao Shen from Penn State University, who worked with us on the water transport subject.

Marc Baaden and Samuel Murail from Universite Paris 7, who made the molecular simulations for us.

All the members of the DYNANO network - current and future scientists. The experience of meeting so many interesting people, all from different backgrounds, has definitely made me a better scientist and person.

I would also like to thank my other colleagues from the team and from IEM, for the moments and memories we shared: Istvan and Benjamin two great friends, Zhanhu, the happiest person I've met, Yan a very smart young person, Romina and Alina for speaking romanian in the office, Nicolas and Florin for the laughs we had.

Last but not least, I would also like to thank my family and friends, who have been close to me and supported me all these years and to Ileana and Glad who made the trip to see my presentation. Particularly, I would like to thank my grandmother, chemical engineer, who introduced me to chemistry. She always wanted to do a PhD but did not get the chance to make one, for this reason I dedicate this work to her.



## Contents

|   |           |
|---|-----------|
| General Introduction and Objectives .....   | 8         |
| <b>Chapter 1: Cation and Proton Translocation across Vesicular Lipid Bilayers .....</b> | <b>17</b> |
| <b>1.1. Introduction .....</b>  | <b>17</b> |
| 1.1.1. Natural Ion Channels .....   | 18        |
| 1.1.2. Synthetic Approaches .....   | 21        |
| 1.1.3. Objectives and Methods Employed .....  | 32        |
| <b>1.2. Experimental Results .....</b>  | <b>34</b> |
| 1.2.1. Description of Compounds .....   | 34        |
| 1.2.2. Fluorescence Assays .....  | 40        |
| 1.2.2.1. Sodium Transport Experiments .....   | 48        |
| 1.2.2.2. Potassium Transport Experiments .....  | 51        |
| 1.2.2.3. Ion Selectivity Transport Experiments .....                                    | 55        |
| 1.2.2.4. Proton Transport Experiments .....   | 62        |
| <b>1.3. Conclusions and Perspectives .....</b>  | <b>67</b> |
| <b>Chapter 2: Water and Proton Translocation across Vesicular Lipid Bilayers .....</b>  | <b>69</b> |
| <b>2.1. Introduction .....</b>  | <b>69</b> |
| 2.1.1. Natural Water Channels: Aquaporins .....   | 70        |
| 2.1.2. Synthetic Approaches .....   | 74        |
| 2.1.2.1. Dendritic Peptides .....   | 75        |
| 2.1.2.2. Imidazole Quartet .....  | 76        |
| 2.1.2.3. Hydrazide Functionalized-[5] Pillar Arene Derivatives .....                    | 77        |
| 2.1.3. Objectives and Methods Employed .....  | 79        |
| <b>2.2. Molecular Simulations on the HC6 Channel .....</b>                              | <b>80</b> |
| <b>2.3. Experimental Results .....</b>  | <b>84</b> |

|   |            |
|---|------------|
| 2.3.1. Description of Compounds.....  | 84         |
| 2.3.2. Water Transport Experiments.....   | 92         |
| 2.3.3. Proton Transport Experiments.....  | 103        |
| 2.3.4. Effect of Chirality on Transport.....  | 113        |
| 2.3.5. Cation Transport.....  | 116        |
| <b>2.4. Conclusions and Perspectives.....</b>   | <b>117</b> |
| Chapter 3: Molecular Electrodes Systems.....  | 119        |
| <b>3.1. Introduction.....</b>   | <b>119</b> |
| 3.1.1. Electrodeposited Templated Mesoporous Silica and Functionalized Silica             | 121        |
| 3.1.2. Triaryl Amines and Their Properties.....   | 125        |
| 3.1.3. Laccase Biocathodes.....   | 131        |
| 3.1.4. Project Objectives.....  | 135        |
| <b>3.2. Experimental Results.....</b>   | <b>137</b> |
| 3.2.1. Electrode Manufacturing.....   | 137        |
| 3.2.2. Characterization of the Electrode Manufacturing Process by Cyclic Voltammetry..... | 142        |
| 3.2.2.1. Electrochemical Detection of TAAs in the Pores.....                              | 147        |
| 3.2.2.2. Influence of Chain Length in Pore Modification.....                              | 150        |
| 3.2.2.3. Influence of irradiation.....  | 151        |
| 3.2.2.4. Influence of the Self-Assembly of the Compound.....                              | 152        |
| 3.2.3. Impedance Spectroscopy.....  | 153        |
| 3.2.4. Surface Characterization.....  | 156        |
| 3.2.5. Design of Biocathodes.....   | 160        |
| <b>3.3. Conclusions and Perspectives.....</b>   | <b>165</b> |
| General Conclusion.....   | 167        |



|                              |     |
|------------------------------|-----|
| Annexes .....                | 171 |
| Chapter 1 and Chapter 2..... | 171 |
| Chapter 3 .....              | 193 |
| Bibliography .....           | 201 |

## General Introduction and Objectives

Cells are the building blocks of any superior living organism. From a functional point of view they are complex self-regulating systems. Eukaryotic cells, the ones found in evolved organisms, contain, by the roughest description, a nucleus (where the genetic information is found), a cytosol (the internal medium where the organelles, “specialized organs” of the cell are found) and the cellular membrane. This membrane has multiple functions. Firstly, it delimits the intracellular medium from the external medium, providing mechanical support. This gives the cell its shape. It also constitutes an anchoring platform: internally, for the organelles and, externally, for the binding between cells to form tissues. Secondly, and its most important function, is the regulation of metabolites’ transport for the cell. Being a self-regulating transport system, it does cover all functions, from feeding the cell with glucose, to regulating the membrane potential via ion-exchangers and regulating the uptake in water[1]. A model of the cellular membrane is presented in Figure 1.

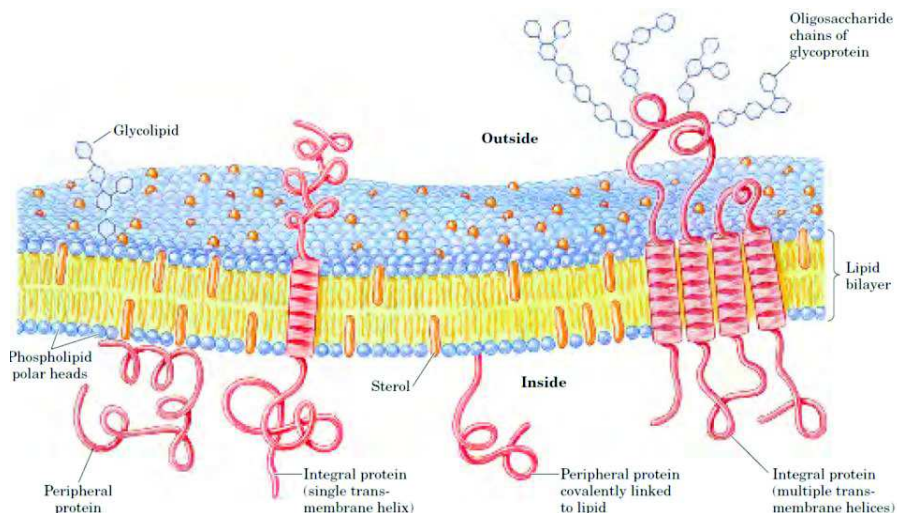


**Figure 1: Fluid mosaic model for membrane structure.** The fatty acyl chains in the interior of the membrane form a fluid, hydrophobic region. Integral proteins float in this sea of lipid, held by hydrophobic interactions with their nonpolar amino acid side chains. Both proteins and lipids are free to move laterally in the plane of the bilayer, but movement of either from one face of the bilayer

of the other is restricted. The carbohydrate moieties attached to some proteins and lipids of the plasma membrane are exposed on the extracellular surface of the membrane. [1]

Regarding energy consumption, there are two types of transport: passive, where no spending of energy is required, and active, where the cell “spends” energy to move species across the membrane. There are four main types of mechanisms for transport through the lipid bilayer of a cell:

- Diffusion and passive osmosis, which are used for small molecules like O<sub>2</sub> and CO<sub>2</sub>, as passive forms of transport, where the driving force of the process is the concentration gradient.
- Using transporters, such as transmembrane proteins, in the form of channels or carriers. These are passive or active forms of transport, which account for the passage of water, nutrients (like sugars for energy), or amino acids (for protein synthesis) and ions. These proteins have been extensively studied because of their efficiency and selectivity.
- Endocytosis, the complex process through which the cell membrane surrounds solid particles or foreign elements (such as bacteria) and internalizes them for consumption - an active form of transport.
- Exocytosis, another complex process in which, the cell, using its membrane, generates a vesicle made up of a lipid bilayer with the purpose of expelling different species out of the cell. These can be metabolites, hormones, enzymes, or waste in general. This too is a form of active transport.[1]

In order to give a general idea of the particular types of transport for small molecules across lipid bilayers, a schematic is presented in Figure 2. All of these with the exception of simple diffusion are mediated by proteins. In a biomimetic or bioinspired approach, one tries to replicate the simplest of these transport mechanisms.

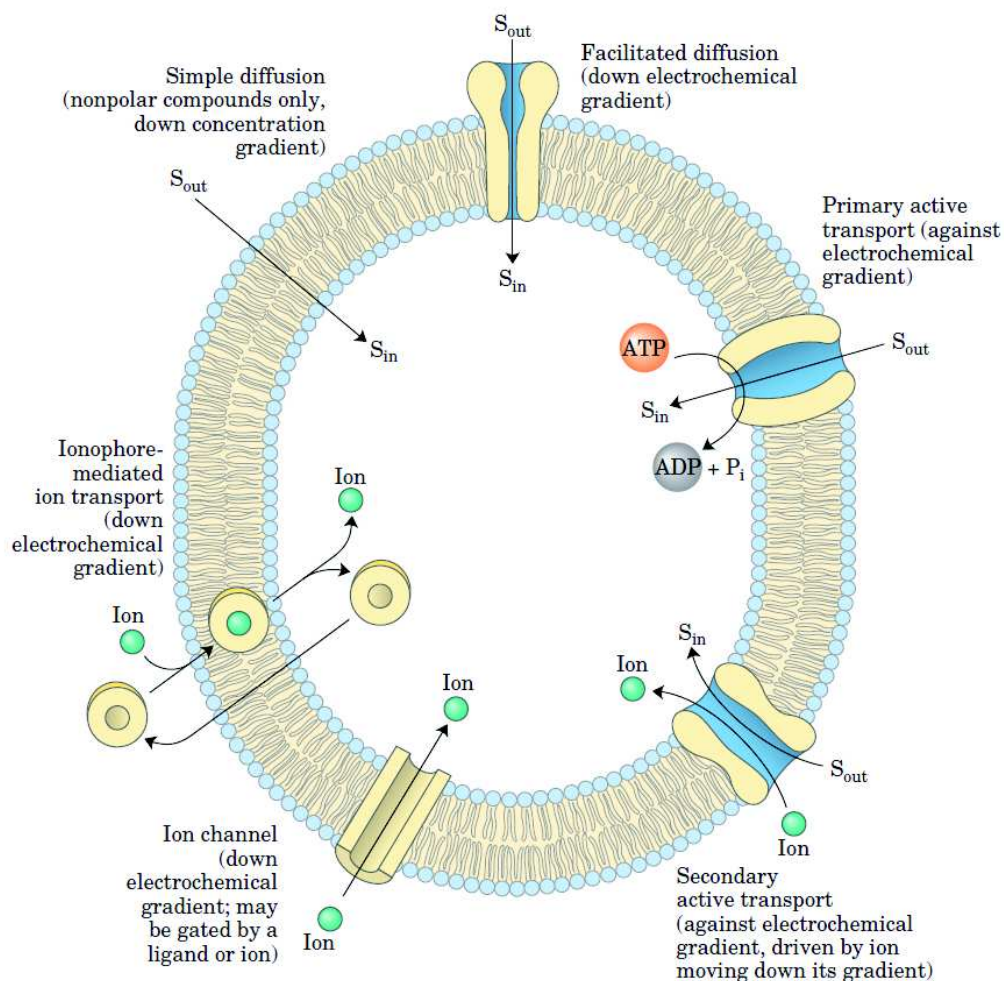
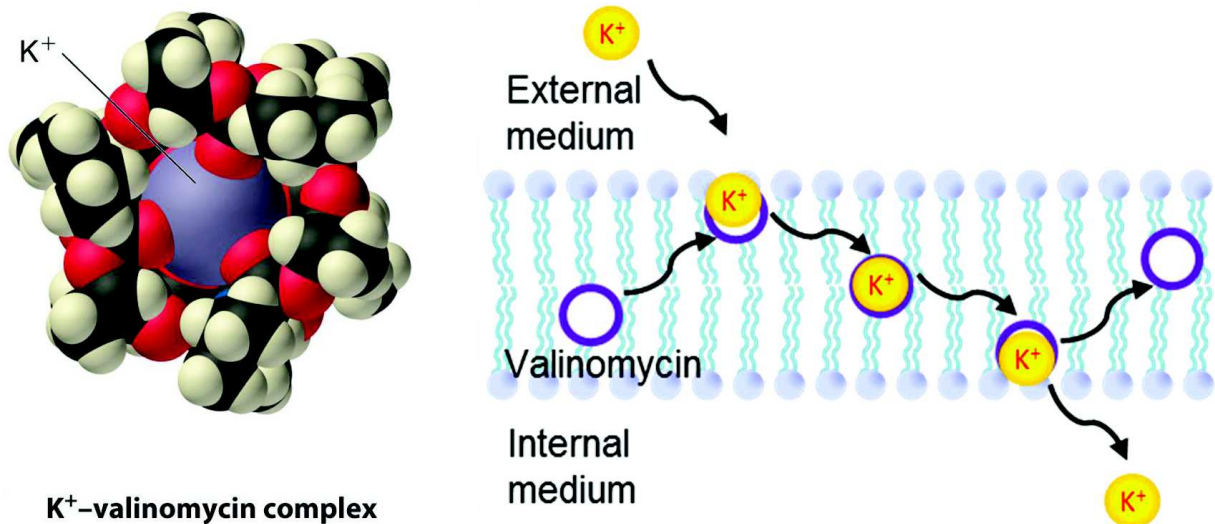


Figure 2: Types of transport of small molecules through lipid bilayers [1]

In the case of this work, two particular mechanisms are of interest. The carrier system is well described in the case of the selective potassium transporter valinomycin [2]–[6]. The transporter resides in the bilayer and complexes an incoming potassium ion when it reaches the interface of the membrane. This complex then moves through the bilayer. The ion is set free through the internal interface of the membrane. The freed protein travels along the membrane and complexes another ion. The schematic of this process for valinomycin transporter is presented in Figure 3. This transport phenomenon is characterized by saturation kinetics based on the availability of the transporter to complex the potassium ion. Although this type of transport is susceptible to inhibition, a

good selectivity overcomes this aspect. In the case of valinomycin the selectivity between potassium and sodium is 20000 to 1.



**Figure 3: Schematic of the carrier mechanism in the case valinomycin system. (Left) valinomycin-potassium complex. (Right) schematic of the transport through the lipid bilayer.**

The second mechanism of interest is facilitated diffusion. Facilitated diffusion is significantly faster than simple diffusion, this difference in speed varies from one system to another. The functioning of facilitated diffusion revolves around energy consumption. In order for an ion to pass through a lipid membrane, it must give up its hydration shell. The activation energy  $\Delta G^\ddagger$  for this process is so high that, under normal conditions, the lipid bilayers are completely impermeable towards charged species such as ions. In the case of facilitated diffusion, the protein effectuates a passive form of transport. It intervenes in the dehydration process of the ion and thus lowers the activation energy  $\Delta G^\ddagger$ . These proteins are different from enzymes, since they do not change their conformation in order to perform the transport function. They stretch from one side to the other of the membrane. Usually, they present polar groups on the inside of the so-formed channel [1]. Figure 4 depicts the facilitated diffusion process.

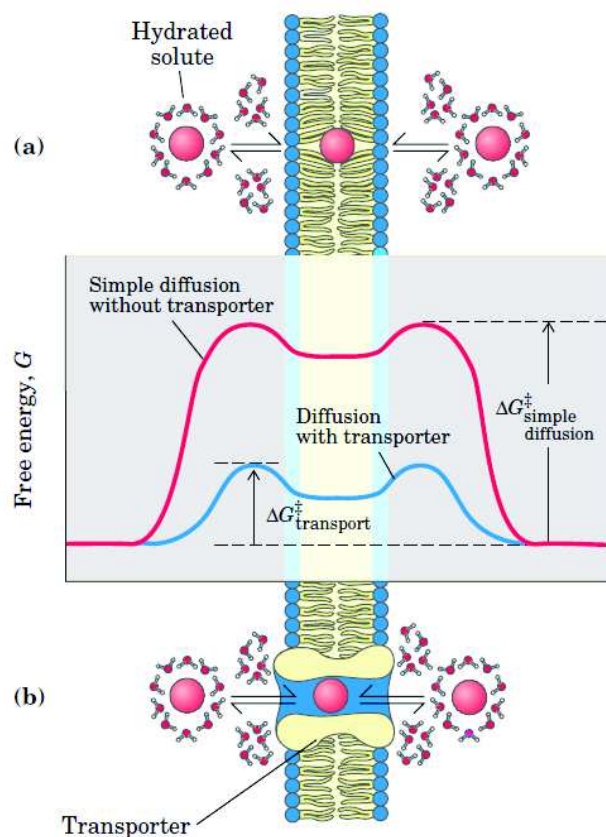


Figure 4: Energy changes accompanying passage of a hydrophilic solute through the lipid bilayer of a biological membrane. (a) In simple diffusion, removal of the hydration shell is highly endergonic, and the energy of activation ( $\Delta G^\ddagger$ ) for diffusion through the bilayer is very high. (b) A transporter protein reduces the  $\Delta G^\ddagger$  for transmembrane diffusion of the solute. It does this by forming noncovalent interactions with the dehydrated solute to replace the hydrogen bonding with water and by providing a hydrophilic transmembrane passageway. [1]

The term biomimetic is defined as to aim in replicating the function and not the form of certain natural functional units by using synthetically generated compounds. These would exhibit, as least in part, the efficiency and selectivity of their natural counterparts, while creating a simpler, easier to apply system. Although the biomimetic term is often used (sometimes wrongly), in this case, we are rather following a **bioinspired** approach, as we are not trying precisely to imitate nature, but only to take a few key elements from known biological processes and to implement them in our artificial systems. In order to create our transporters, we relied on the concepts of self-assembly, dynamic and supramolecular chemistry.

**Supramolecular chemistry** is a field pioneered by C.J. Pedersen, J. M. Lehn and D. Cram [7]. Jean Marie Lehn in his Nobel prize lecture defined it like this: “Supramolecular chemistry may be defined as “chemistry beyond the molecule”, bearing on the organized entities of higher complexity that result from the association of two or more chemical species held together by intermolecular forces” [8]. In a simplistic perspective, supramolecular chemistry stated that the whole is larger than the sum of its parts, namely that the fashion in which molecules group and interact with each other fundamentally changes their properties. Two important concepts are considered in supramolecular chemistry: molecular recognition and self-assembly.

**Molecular recognition** has been defined as a process involving both binding and selection of substrate(s), by a given receptor molecule, as well as performing a specific function [8]. This is a property of biological and chemical systems to distinguish between molecules and regulate behavior accordingly.

**Self-assembly** and multiple binding with positive cooperativity, are processes of spontaneous molecular organization. These also allow to envisage amplification molecular devices [8]. It is a process in which components, either separate or linked, spontaneously form ordered aggregates. Self-assembly can occur with components having sizes from molecular to macroscopic, provided that appropriate conditions are met. The interactions found are physical, and can be: hydrogen bonding, dipole-dipole interactions, guest-host interactions,  $\pi$  stacking and other more specific and punctual cases of interactions.

**Dynamic constitutional chemistry** targets the generation of chemical systems which are dynamic and adaptive, responding to internal and external stimuli. For this the presence of multiple species that reversibly interact at the molecular and supramolecular levels (in an agonistic or antagonistic fashion) is required. “Dynamic interactive systems are defined by networks of exchanging and reversibly connected objects (supermolecules, polymers, biomolecules, biopolymers, pores, nanoplateforms, surfaces, liposomes, cells). They operate under natural selection to allow spatial/temporal and structural/functional adaptability in response to internal constitutional or to external stimulant factors” [9]. The parameters can be physical, such as temperature, pressure,

concentration, or chemical such as the absence or presence of a chemical species, a change in pH generated by addition of acid or base, etc. Depending on the nature of the system, the dynamic aspect can be induced by one or more of the factors mentioned before. A system is dynamic if to an appropriate stimulus the system presents a response.[9]–[24].

The general objective of the first part of this work, spanning over the first two chapters, focuses on the transport across lipid bilayers, the generation and characterization of translocation-effector structures for different species (cations, protons and water). As mentioned previously, in natural systems transport is done via proteins. Proteins are complex structures, with specialized functions, thus they exhibit great selectivity. This also implies that there are many limitations in their use, to name the two most important: difficulty in obtaining them through a synthetic pathway, difficulty in isolating them from organisms. This, in turn also makes them unfeasible from an economic stand point. Another aspect to consider is their sensitivity towards the modification of physical parameters such as temperature, pH, etc., as these variations can lead to a loss of activity. Given these shortcomings the approach chosen is a bioinspired one.

The possibilities in a field of science as wide as the one of supramolecular chemistry are endless. One system that was particularly studied in our group is that of urea [9]–[24]. The urea moiety has the property of self-assembly by generating hydrogen bonds. The –NH-CO-NH– interacts through the oxygen atom with other species containing a slightly positivized proton. In the case of homomeric associations, the urea binds to another urea moiety resulting in a urea ribbon (Figure 5, a). However, by creating more complex structures, that containing this type of hydrogen atom, a heteromeric hydrogen bond can be obtained (Figure 5, b).



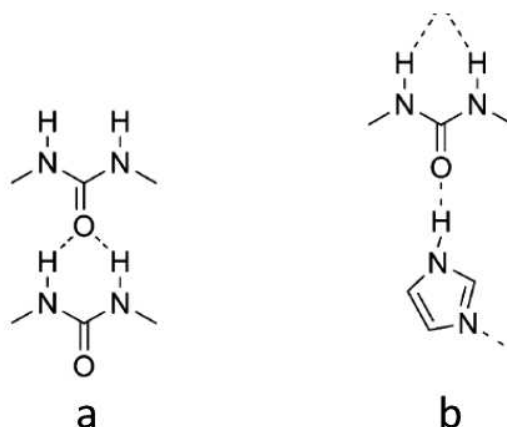


**Figure 5: Urea hydrogen bonding (a) homomeric and (b) heteromeric**

The directionality of the urea type self-assembly has many practical uses. In our group the subject of hybrid materials was exploited using the assemblies of urea based molecules. Moving forward, to the subject of translocation of chemical species urea based compounds, have also been applied to this challenge. The types of species that were successfully transported are cations and anions [19] or water [22]. The types of systems created can be split into mono [16], [17] and polymolecular [15]. These findings will be further presented in chapters 1 and 2.

In order to point out the versatility of urea derivatives, totally different applications are recorded. Sabadini et al report a solvent triggered giant micelles formation, based on a diurea derivative[25]. Fremaux et al apply the directionality of urea moieties in order to obtain aliphatic oligourea foldamers [26]. The spatial orientation of this type of bond is also used by van Gorp et al[27]. They report fibers and gels composed of tris-urea derivatives based on the natural helical structures generated by this type of species.

Professor Lehn applies the tris-urea motif in polydimethylsiloxane based materials to confer these self-healing properties [28]. The generation of three consecutive ureas provides a total of six possible hydrogen bonds. These are extended over the three dimensions, with four being in a single plane and the remaining two in an orthogonal plane to the first one. By incorporating this system in an elastomer, the resulting hybrid material

gains the self-healing properties (being able repair mechanical damage suffered), as a consequence of these very strong directional bonds. The possibility of giving special properties to a material, by inserting a designed supramolecular system, is very likely to be one of the paths towards “intelligent” materials.

Although the third chapter of this work doesn't concern the transport of species through lipid bilayers, it does use the principles defined beforehand. Triarylamines are species that interact and generate supramolecular assemblies. Particular ones self-assemble under irradiation to form cylindrical nanoscale structures. The structures, presenting a cation radical charge, have very good electrical conductivity. These systems were inserted in a mesoporous silica structure in order to preserve the electrical properties. The silica structure was manufactured through a templated electro-deposition technique on gold electrodes. The resulting array presents the property to translocate electrons between the external medium and the gold interface of the electrode. An application was designed for the resulting devices in the form of biocathodes. The details of this project will be treated in detail in Chapter 3.

# Chapter 1: Cation and Proton Translocation across Vesicular Lipid Bilayers

## 1.1. Introduction

Synthetic ion channels are a much more explored subject compared to synthetic water channels. The general approach is bioinspired, starting from the natural ion channels. Frequently used are modified peptides and proteins as well as compounds character of the molecules containing calixarenes or heterocycles. One other common feature is the amphiphilic character of such molecules [29]–[31], containing both a hydrophobic and a hydrophilic part. The hydrophobic part is required in order to have both a good affinity with the lipid bilayer and a significant repulsion of the aqueous environment. The hydrophilic one confers the possibility to interact with the ion, either in its hydrated or in its dehydrated form.

When discussing synthetic ion channels there are a few considerations to keep in mind. One criterion is the structure. Simple structures are preferred to more complex ones for several reasons. One reason would be the limitations of the characterization methods. The more complex a system is, the harder it is to characterize by the standard methods used in ion channels standard experiments. Another reason could be easiness in synthesis, which, of course, makes a species more (or less) available as a potential candidate for further applications. The cost is also an issue, it increasing from simple small self-assembling channels towards isolated proteins.

One other criterion is the compatibility between the membrane and the functional structure. This comes as a consequence of the characterization methods, which work around the insertion of the channels directly in the lipid membrane. There are a few strategies regarding this aspect, namely in generating the hydrophobic part of the

molecule. Long hydrocarbon chains, saturated or unsaturated are usually employed as being the simplest solution to this requirement. When assessing self-assemblies, the properties of the resulting suprastructure should also be taken into consideration, not only the structure of one monomer. For this reason, phenyl rings and other derivatives that are able to generate a more stable and sturdy structure are also included.

### 1.1.1. Natural Ion Channels

The best described ion channels found in the literature are amphotericin and gramicidin. Extensive research was dedicated to them because of their relatively simple structure compared to the much larger protein channels[32]–[38] . They represent the simplest natural ionic channels that are appropriate for comparison to the synthetic solutions.

Amphotericin is the smallest known ionic channel. It has a polyene structure with a polar segment. Multiple monomers assemble in order to form the channel, the polar head aligns towards the aqueous phase while the lipophilic part stays tucked in the bilayer. The length of the hydrophobic part is approximately half the length of the membrane, so self-assembly is required in order to transport ions from one side to the other of the membrane [37], [38] (Figure 6)

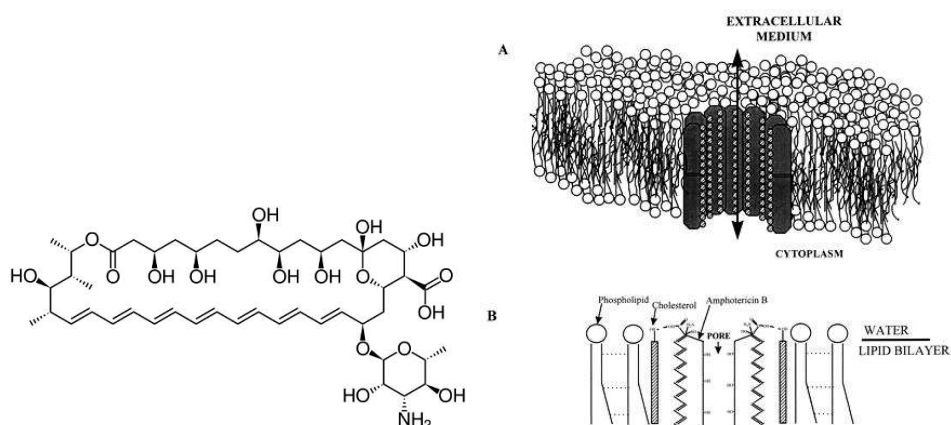


**Figure 6: Linear structure of Amphotericin and schematic of the amphotericin channel [39]**

The gramicidin oligopeptide channel is better known for its properties of being an ionic channel. However, the size of the generated channel also allows the passage of water and as well as protons [40]–[44]. Structurally speaking, gramicidin is a small protein having just 16 amino acid residues. It was one of the first channel proteins to be discovered, by Rene Dubos in 1939, who isolated thyrotricin. The compound in fact contained 20% gramicidin along with 80% tyrocidine. The key to the activity of gramicidin is 4 tryptophan residues, which are in the positions 9, 11, 13, and 15. The way in which these 4 functions are positioned forms the cavity of the channel. It is worth mentioning that gramicidin channels have very little selectivity towards monovalent ions, water or protons. Gramicidin transports the hydronium ion very well because of its similarity in size with  $\text{Na}^+$  [44]. Its channel is generated by a  $\beta$ -helix conformation, made by alternating L and D amino acids. The hydrophilic side is on the inside and the hydrophobic one on the outside. Gramicidin assembles in a dimeric form in order to form a transmembrane channel. The dimeric self-assembly of the gramicidin channels was evaluated from a free energy perspective[45]. These are presented in Figure 7, displaying the favorable energetic profile towards the dimeric form.

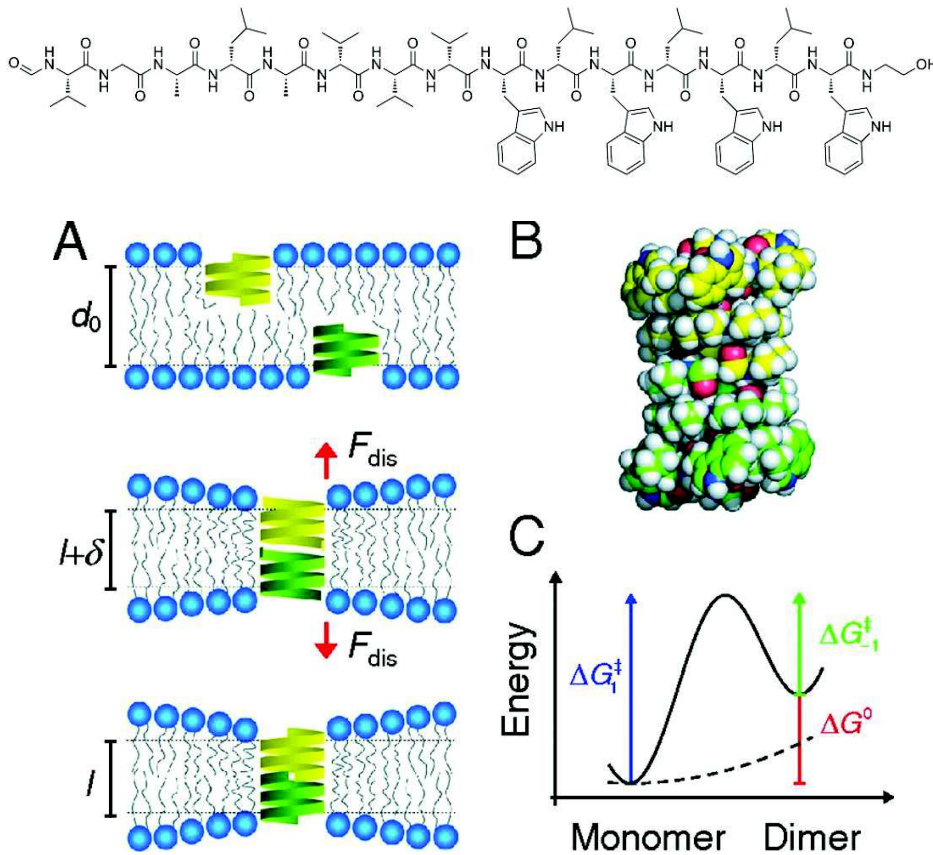


**Figure 7: Linear structure of Gramicidin (up) (A) Formation of a gA channel from two nonconducting subunits. (Top) Nonconducting monomeric subunits. (Middle) Monomers separated by  $\delta$  relative to the conducting state. (Bottom) Conducting channel dimer. (B) Side view of a bilayer-spanning gramicidin channel. The carbon atoms of the two subunits are in yellow and green, respectively. Figure based on energy minimized structure representing a composite of structures determined using solid-state or solution NMR. (C) Energy landscape for the monomer-dimer reaction. The stippled line illustrates the contribution from the bilayer elastic energy. [45]**

The transport mechanisms of the two afford mentioned ion channels are also different. In the case of amphotericin, the ions go through the channels in their hydrated form (with the hydration sphere). In the case of gramicidin, the ions are dehydrated in the interior of the channel, where the hydrophilic residues lie. Both of these channels have applications as antibiotics, against fungi, bacteria and many types of microbes. Their active principle is linked directly to the property of being able to transport ions and to have a good insertion in lipid bilayers. Once in place, they act by changing the electrolyte balance of the microorganism which leads to its death.

### 1.1.2. Synthetic Approaches

There are two types of approaches in the case of synthetic ion channels, based on the employment of unimolecular channels or of polymolecular channels.

The unimolecular channels are large molecules containing a lipophilic body and polar, hydrophilic heads. Their spatial disposition modifies based on how constrictive the environment is. The active structure must be long enough to spread all across the lipid bilayer. One very interesting example is the molecule called “hydraphile”, one of the first unimolecular channel investigated [46]–[50] (Figure 8). This molecule consists of three diaza, 16, 6 crown ethers bound one to another by long dodecyl tails. The ions interact with the macrocycles, while the hydrocarbon tails increase the affinity of the channel towards the lipid membrane. It is interesting to note that the spatial disposition of this compound is not linear, and thus is not forming a perfect sequence of hydrophilic/hydrophobic segments. The mechanism this channel is based on the passage of ions from hydrophilic (aqueous solution) to hydrophobic (lipid bilayer) environments, facilitated by each macrocycle in a different way. The ones on the extremities only have roles as an entrance and respectively as an exit. The middle one, whose size and conformation suffer modifications, provides to the transported ion an equilibration step, necessary as the ion travels through a very hydrophobic environment such as the membrane. By using fluorescence techniques, the species that are able to pass through this system were quantified, in this case water and partially dehydrated ions.

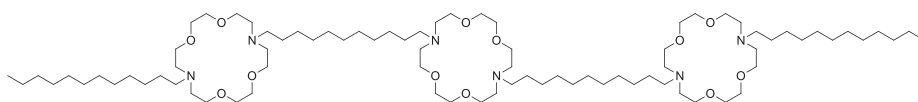


**Figure 8: Hydraphile molecule**

The second class, polymolecular channels are structures resulting from the self-assembly of a number of building blocks. In their case, the characterization is more difficult. Since the systems are usually dynamic and the exact number of molecules is unknown, they can only be characterized on a molecular (or supramolecular) scale. However, direct characterization as an inserted structure is unavailable, as opposed to proteins which have been characterized directly in lipid environments. In case of polymolecular channels, the effect of the transport function is measured. Nevertheless, they do present the advantage of having better solubility, allowing a larger amount of active compound to act on the substrate, by comparison to the unimolecular channels. As presented in the introduction, the types of moieties that are generally used are the ones that present good interactions with the target ions, such as calixarenes/crown ethers or heterocycles. These segments are combined with a support that is compatible with the lipid bilayer.

Thomas Fyles is one of the scientists that has contributed most to this field of research [2], [51]–[54]. Recently, he published together with Jonathan K. W. Chui a very detailed review in which they account and classify all types of engineered synthetic ion channels [53]. These structures were ordered on a bidimensional scale as a function of conductance versus duration based on their Voltage Clamp activity. These are presented in the following figures (Figures 9-11) in order to give a general idea of the vastness of the field.



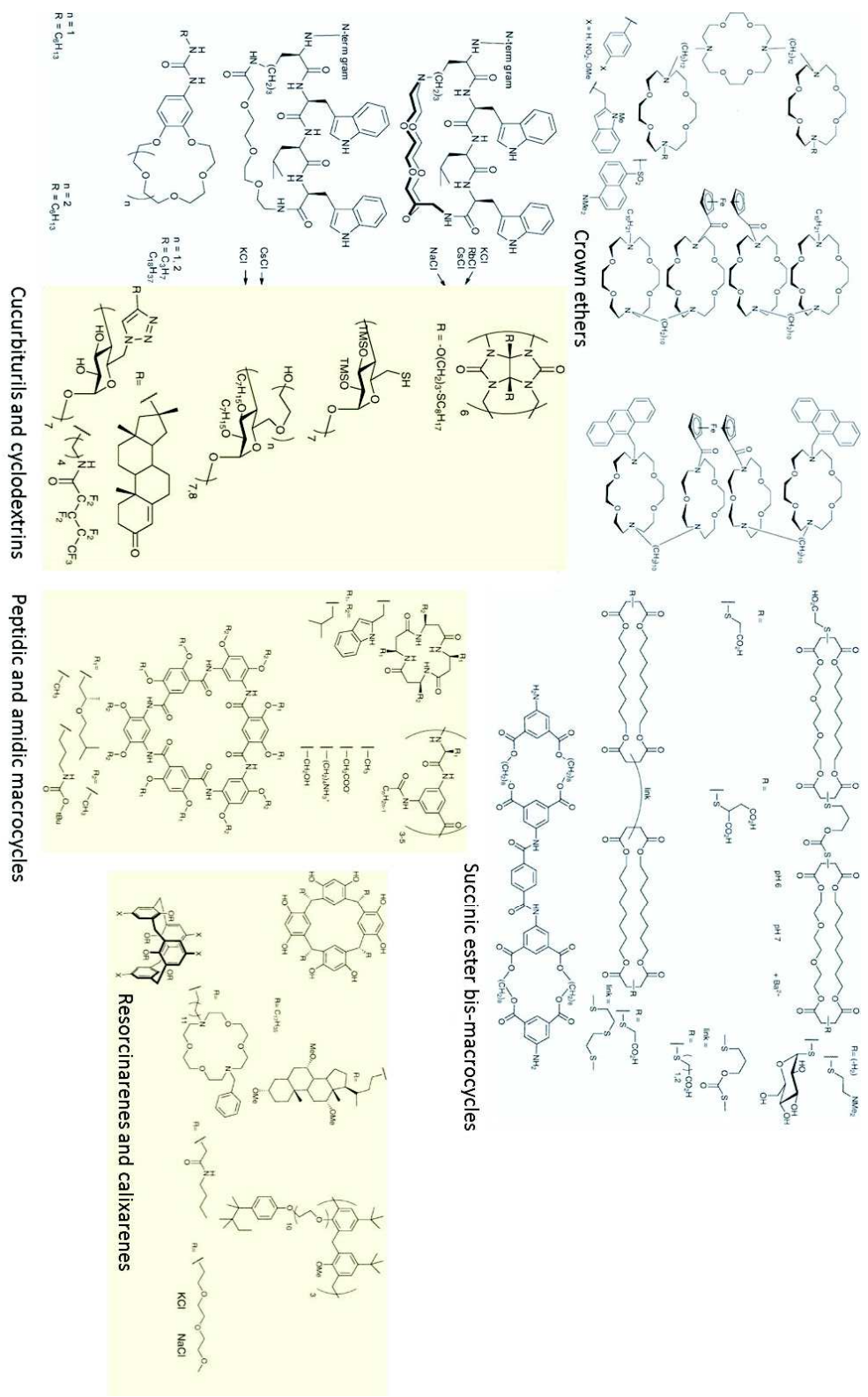


Figure 9: First class of ion channels, peptidic and amidic macrocycles (red underlay) and second class beaded strings topology (blue underlay) [53]

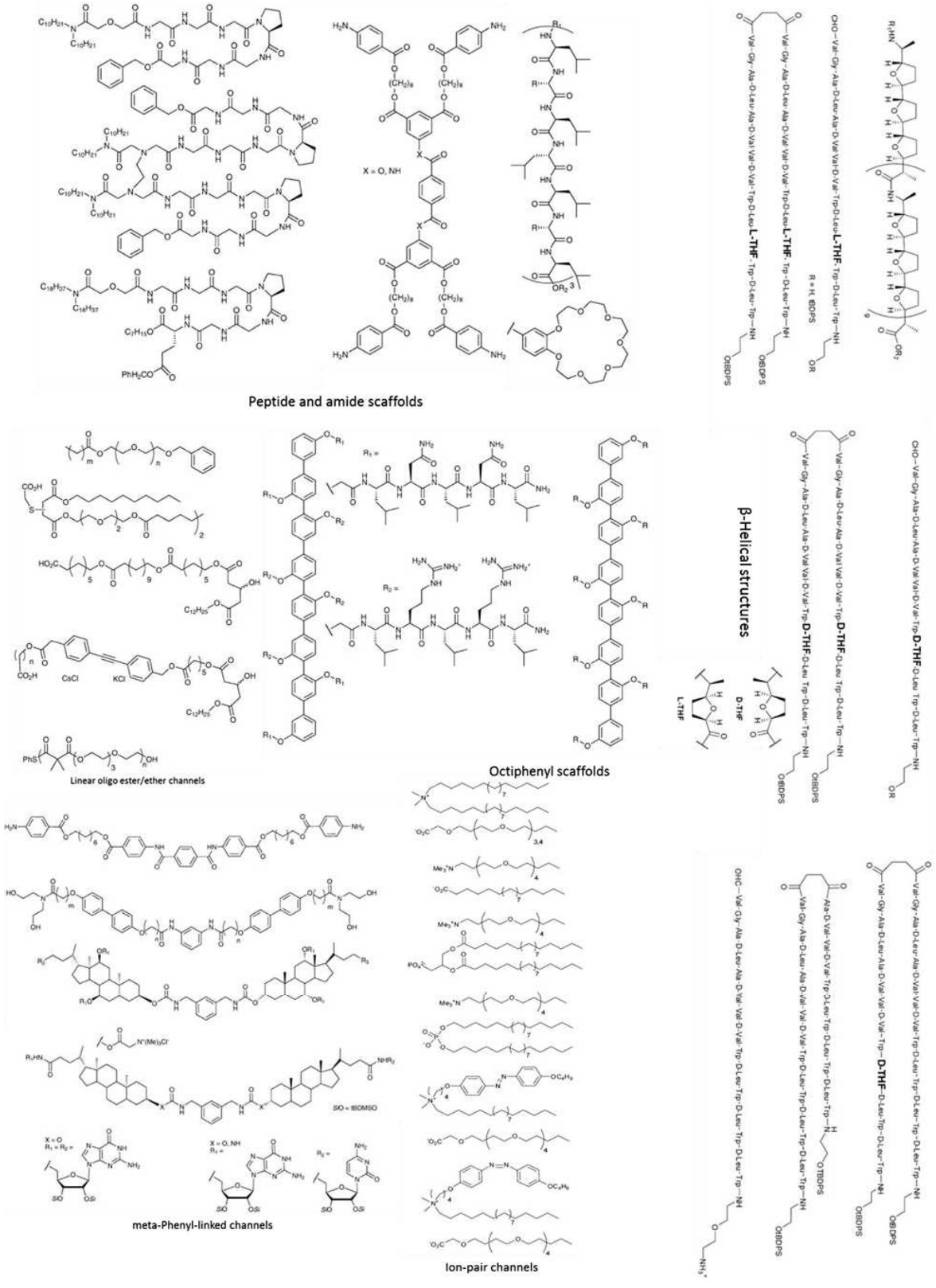


Figure 10: Third class of ion channels, displaying the tree morphology [53]

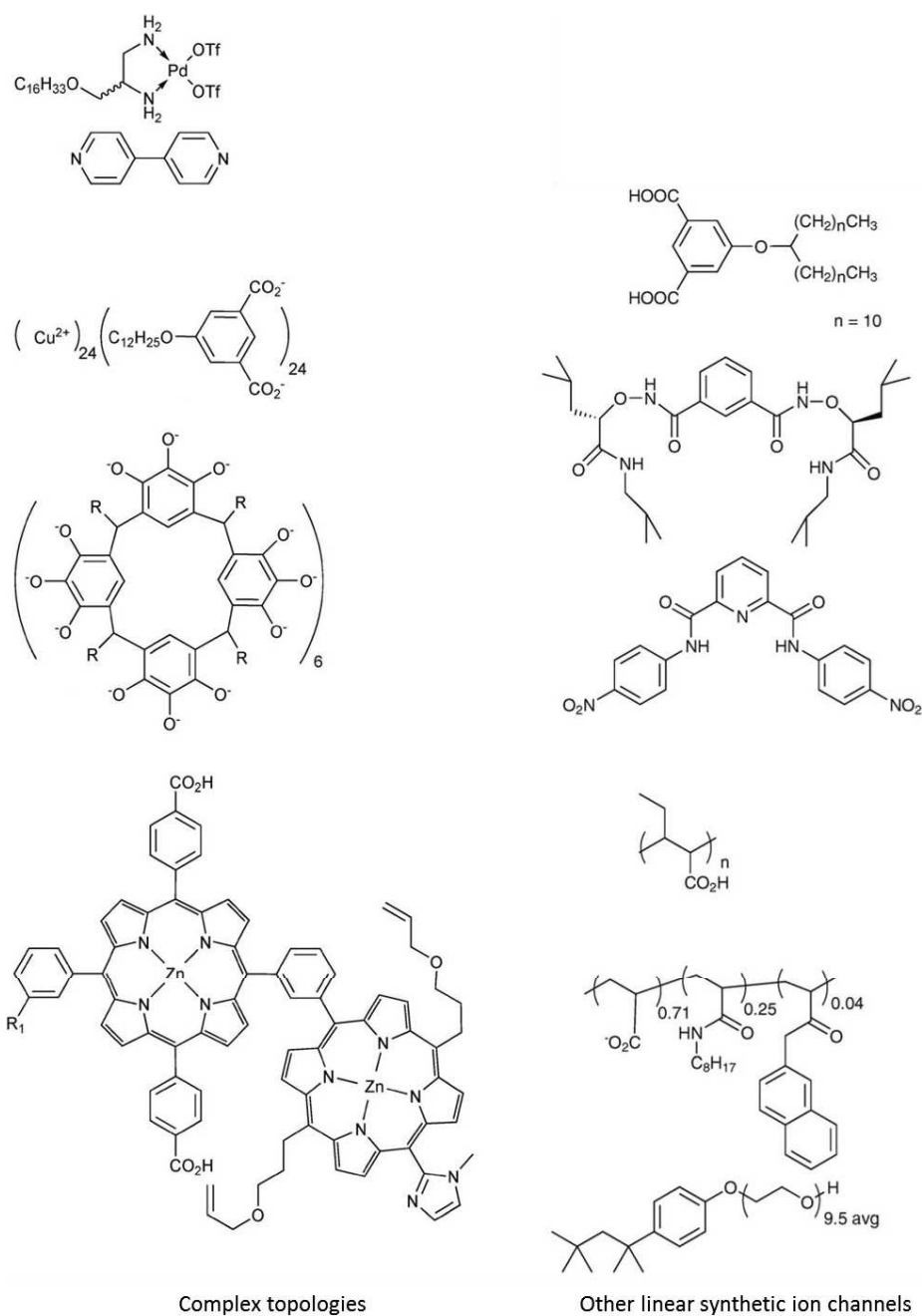


Figure 11: The fourth and fifth class, complex topologies and other linear synthetic channels [53]

In this paper the totality of molecules able to perform transport is split into five classes, each with subclasses. The first three of these can be easily compared to the natural ion channels gramicidin or amphotericin. Their constitutive skeletons either rely

on amidic/peptidic bonds (like the gramicidin), or on esters/ether macrocycles reminiscent of the amphotericin structure. The fourth class can be associated with metallo-proteins similar that present other transport functions (like porphyrins for example). The last class contains other compounds, unrelated structurally with natural channels. These have specific mechanisms and are not a unitary class.

Within group five we can find a class of dianilide derivatives[55], [56] reported as anion transporters. A library of compounds has been synthesized and is presented in Figure 12.

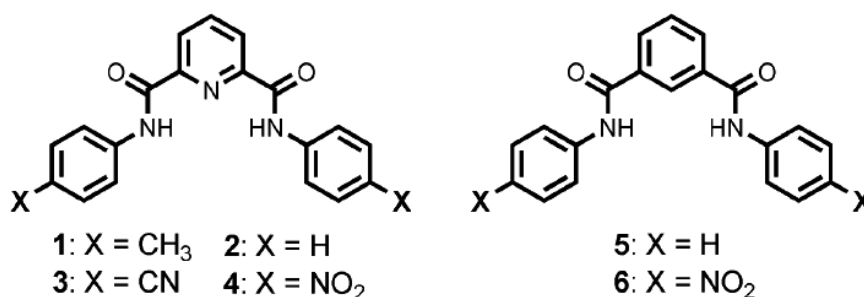


Figure 12: Structural modifications on the dianilide compounds as presented in [56].

The X-ray single crystal diffraction of self-assembling compounds, like the ones depicted here, provides important information on the spatial disposition of the molecules, and hints at possible conformations of a transporting suprastructure. The crystalline matrix of compound 4 and other related species were previously published [57], [58]. The packing of compound four displays that two molecules in a cell are stacked together, rotated at 60°, while maximizing the overlap between the electropositive and electronegative parts of the molecule.

By means of fluorescence, the compounds were tested for the transport of the Cl<sup>-</sup> on vesicle populations. The overall activity exhibited by the compounds towards transport is proven to be structure dependent. From the six analyzed compounds, the best activity was exhibited by compound 6 followed by compounds 4 and 3. Interestingly, the structural variation that increases activity is the presence of the strongly electron attractive group, -

NO<sub>2</sub> in the para position. Surprisingly the effect of the nitrogen atom of the pyridine presents a negligible influence in this matter. This result is presented in Figure 13.

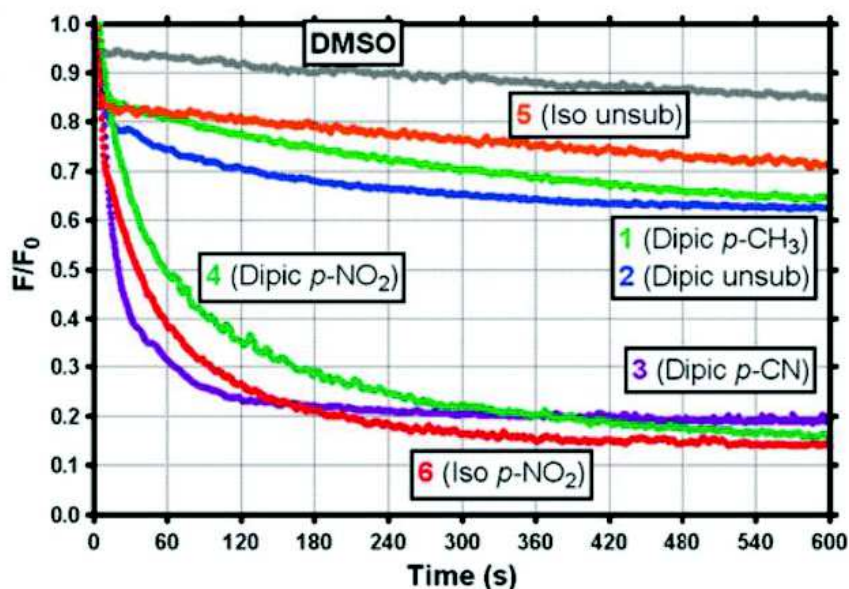
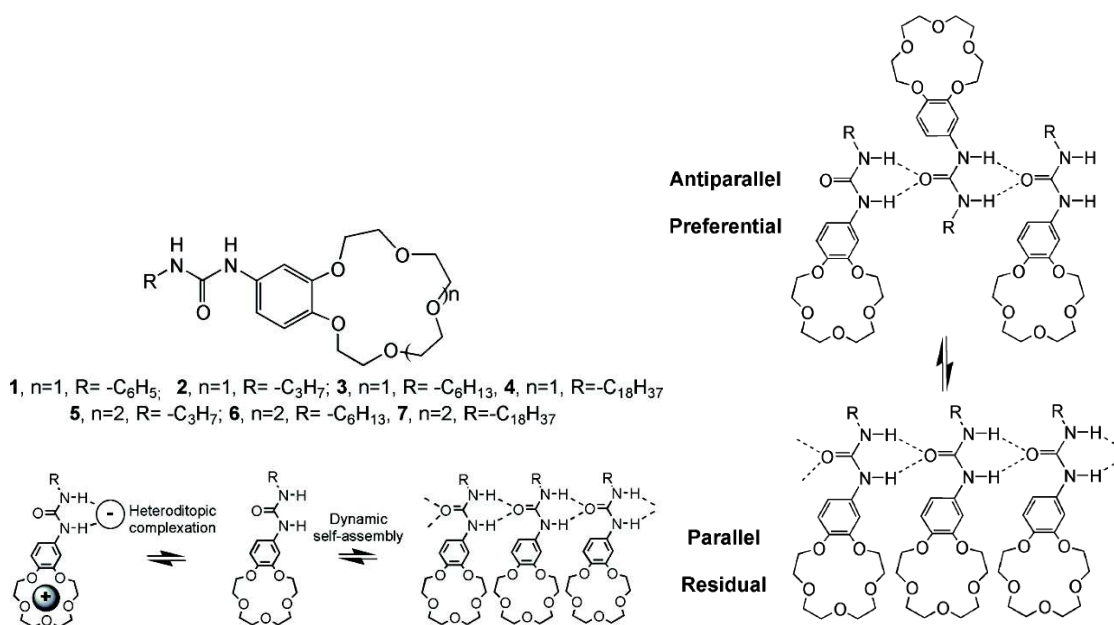


Figure 13: Chloride transport through DOPC vesicles mediated by dianilides 1–6. [56]

This result entices to believe that a phenyl nucleus which is poorer in electrons may have a significant impact on the transporting properties of molecules. This change in activity is related to the interaction which such a phenyl moiety is able to perform in terms of self-assembly and will be discussed further in chapter 1.2.1.

As mentioned in the general introduction, our group has previously worked on self-assembled functional transporting units. One monomolecular transporting system, previously investigated in our group, is that of ureido crown ether derivatives (Figure 14). In the design of the molecule three elements are necessary, each with its own role. Alkyl chains increase the lipophilicity of the molecule, the urea motif confers the directionality of the supramolecular assembly and the crown ether represents the active center towards cations.



**Figure 14: Dynamic self-organization in solution and in the solid state of the heteroditopic receptors 2-7 (left) and the two types of orientation of the receptors [16]**

This type of superstructure may present two types of relative orientation of crown-ethers within the ribbon, parallel and anti-parallel as seen in Figure 14. For example if the lateral R group is aromatic the parallel orientation is adopted, while the aliphatic R groups induce antiparallel conformation. In Figure 15 the X-ray crystallographic data is presented together with the conformation adopted by the structure in a lipid bilayer.

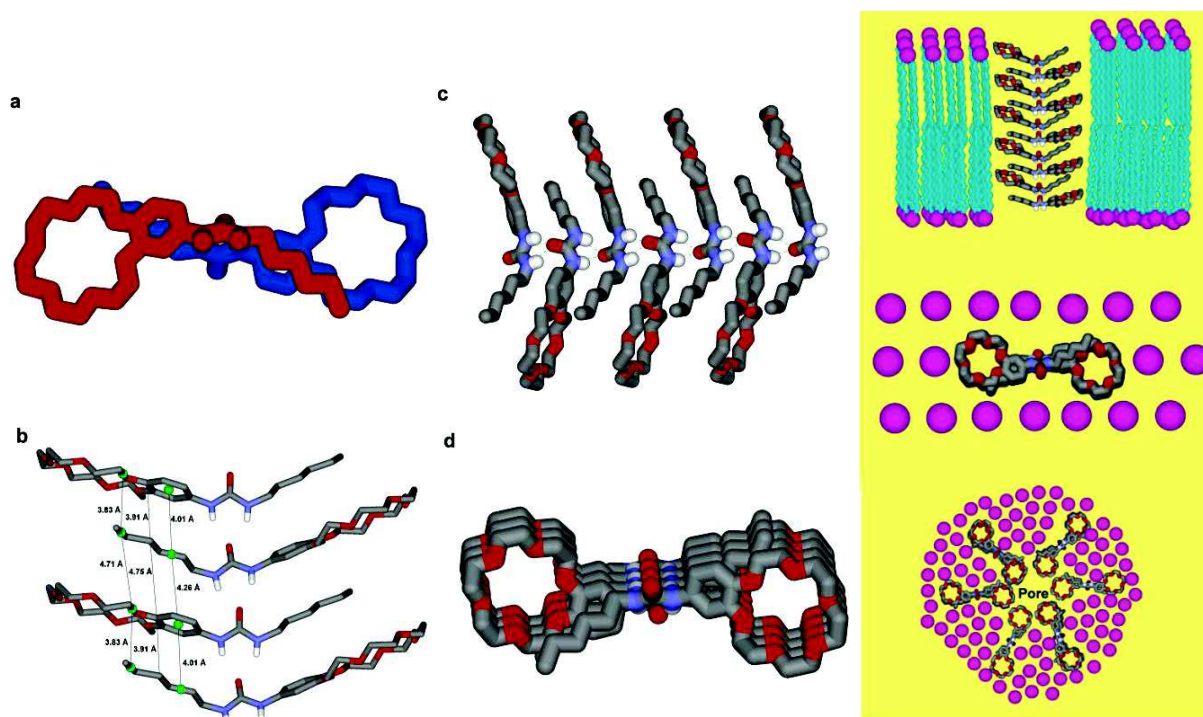


**Figure 15: Crystal structure of macrocyclic receptor 6 stick representation of (a) a single dimer, (b) dimer packing distances, (c) and (d) two side views of the crystal packing of 6 in the H-bond channel-type superstructures (left) and schematics of the double barreled model, lateral and top view and the possible organization of components in a toroidal model (right)[16].**

Bimolecular ion receptor systems were also designed [15]. This type system displays the two molecular components as pairs of receptors for both anions and cations. A urea based molecule acts as an anion interaction center, while a crown ether acts as the cation interaction center. Although the bicomponent type system is more complex to use practically in the translocation of charged species, it does shed light on the possible design of species able to perform transport based on  $\pi$ -cation interactions (Figure 16).

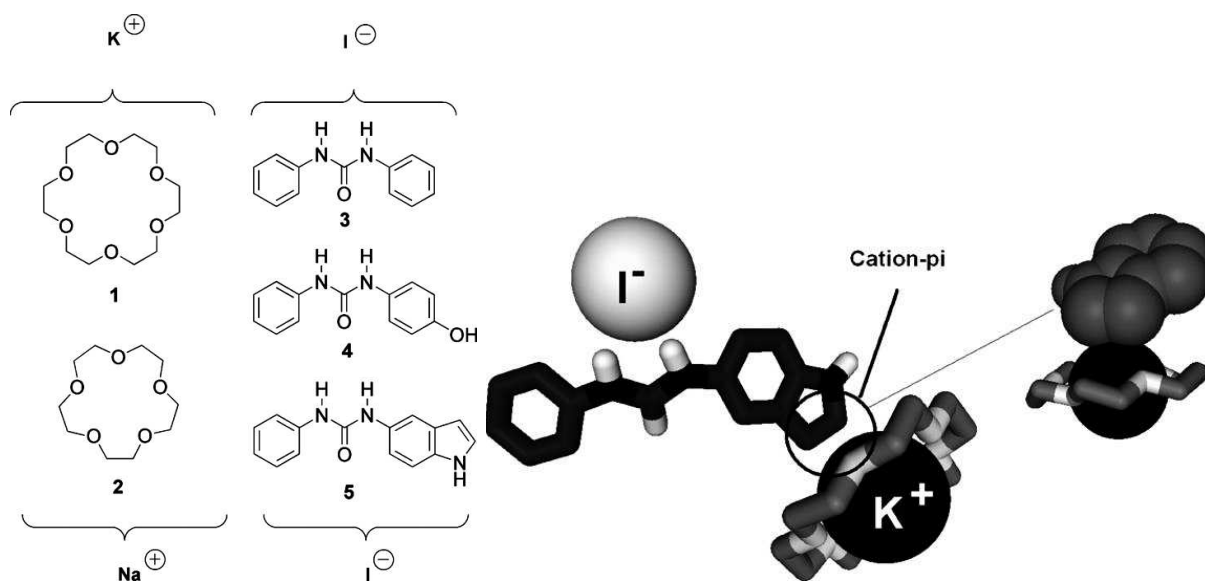
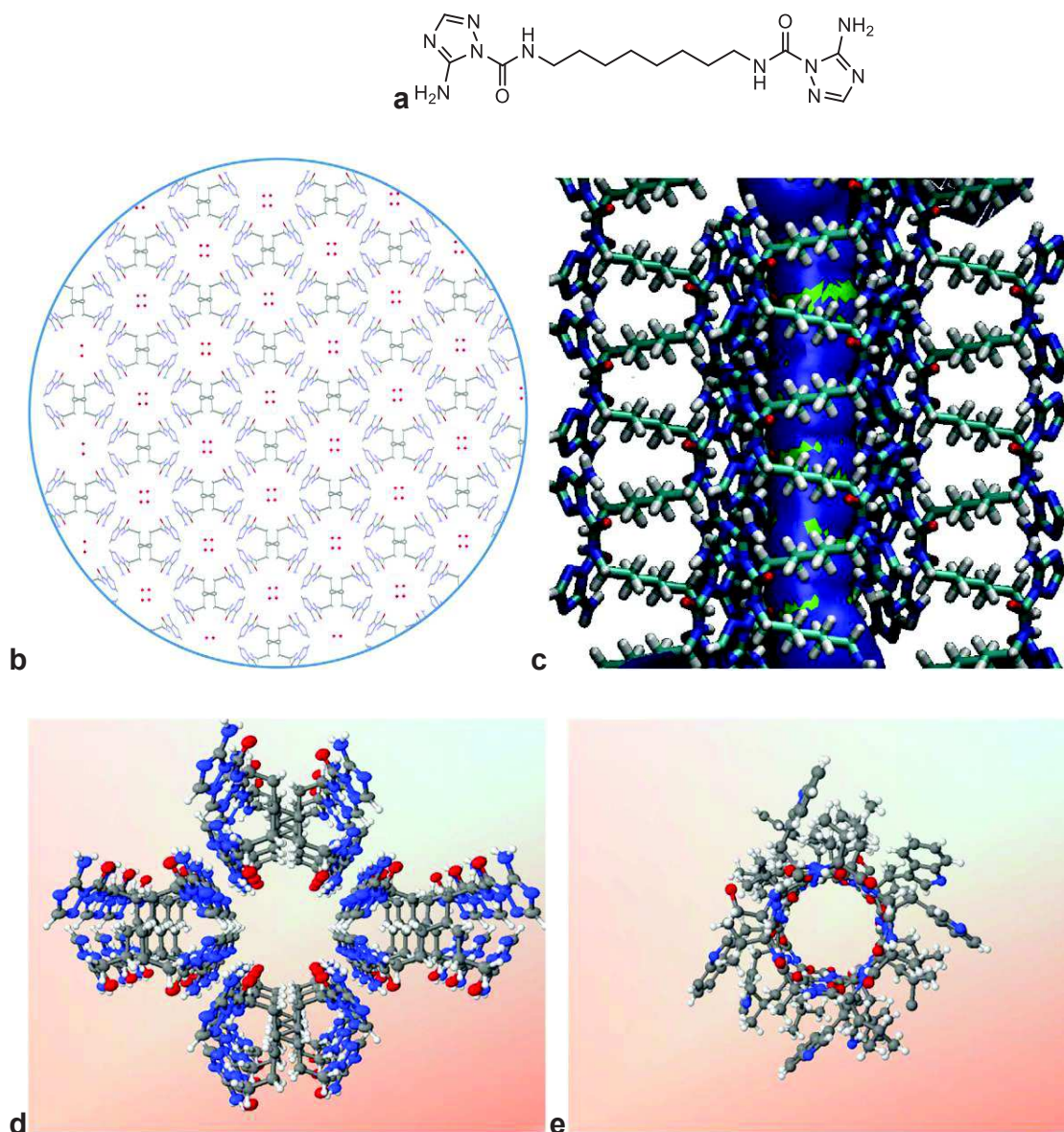


Figure 16: Structures of the cation-carriers 18-crown-6, 1 and 15-crown-6, 2M1–M3 and of the phenylureidoarene anion-carriers 3–5 (left) and crystal structure (stick representation) of the  $[1 \cdot K^+][5 \cdot I^-]$  complex showing clear cation– $\pi$  interactions between the macrocyclic complexed  $K^+$  cation and indole group of the phenylureidoindole 5.  $K^+$ : black and  $I^-$ : white spheres (right) [15]

Recently, a heterocycle based channel-like supramolecular assembly (a bola-amphiphile-triazole compound, referred as TCT) was published [19]. The self-assembled structure of TCT reveals intertwined strands of the monomer, which form a double helix. This, in turn, generates an internal pore throughout the channel, having a diameter of 5 Å. This size is very similar to the one exhibited by the gramicidin channel (Figure 17).





**Figure 17: Molecular structures and crystal packing. (a) Chemical formula of TCT. (b) Top and (c) side views in line and stick representation, respectively, of the T-channels; the water molecules are shown as (b) red dots and (c) the Van der Waals surface of the pore is shown as a blue surface. The latter was calculated by the HOLE program, which was first applied to the Gramicidin pore. Pore structures of (d) T-channel and (e) Gramicidin A (gA) at the same dimensional scale. The gA coordinates were taken from the literature. Red ellipsoids (for TCT) or balls (for gA) designate oxygen atoms, blue for nitrogen, grey for carbon and white for hydrogen.[19]**

The TCT channels were tested in conditions specific for water transport, proton transport, cation and anion transport. In the case of water transport, by using Dynamic

Light Scattering (DLS) methods, an increase in the average diameter of the population of large unilamellar vesicles (LUVs) was observed. The ion transport experiments were made using fluorescence methods on LUVs. The system's activity towards the transport of cations was also evaluated using Voltage Clamp techniques. The key results are shown lower in Figure 18.

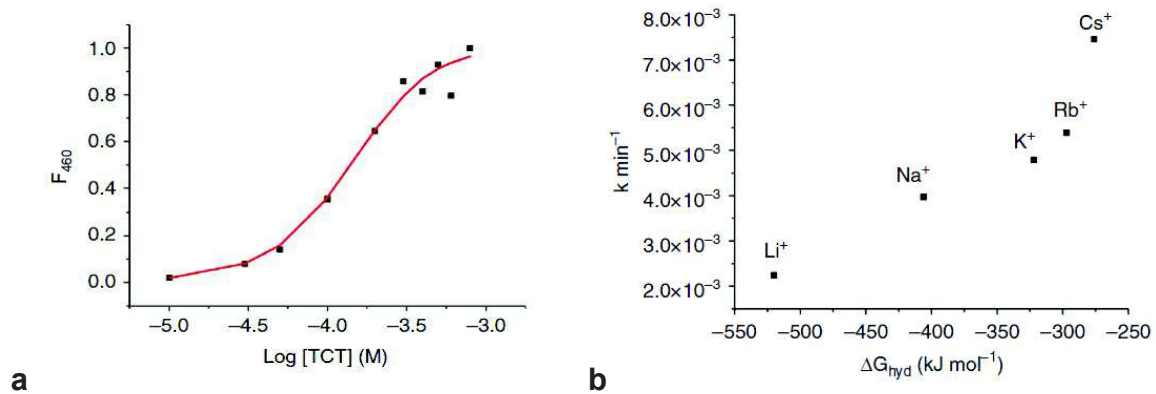


**Figure 18:** a) Transport of Na cations as determined in a pH gradient assay as a function of TCT concentration. b) The transport activity of T-channels versus dehydration energy of alkali cations show an increasing single-order exponential behavior. The abrupt change in transport of low hydration energy cations (Cs, Rb), not observed for cation-water single file gA channels, involves double file dipolar water wires and ion wires along the T-channel[19].

The nature of the TCT channels proves to be similar to the gramicidin natural channel in terms of size and in certain activity aspects. The structure allows the transport of water and ions while displaying a selectivity between cation and anions. Designing this type of bioinspired synthetic channels is useful in the sense of a better understanding of naturally occurring processes such as the transport of ions.

### 1.1.3. Objectives and Methods Employed

The objective of the work presented in this chapter is the creation and characterization of systems able to perform cation transport across lipid bilayers. The systems in question are generated by employment of self-assembly. The activity and

selectivity of the systems are assessed. The study was performed on a library of compounds in order to characterize in a systematic fashion the variation of activity as a function of structural modifications.

The methods employed during this study are the most commonly used and best described in the field of ion channels, namely fluorescence methods on large unilamellar vesicles (LUVs). LUVs (or liposomes) are spherical elements, constituted by an internal medium of buffer, which is separated from the external solution by a lipid bilayer. LUVs have been described as mimic cells, in the sense that they provide this membrane separation between the two media. Their membrane is much simpler than that of living cells, but still provides comparable conditions when it comes to the transport of ions. The advantages are related to cost, uniformity of size and characteristics, but most of all convenience: the LUVs can be varied in size during extrusion, the lipid composition can be modified according to experimental requirements and also, the content of the LUVs (in this case fluorescent dye) can be subject to modification.

## 1.2. Experimental Results

### 1.2.1. Description of Compounds

In order to describe the influence of structure over the transporting properties of compounds, a library was created and is presented in Table 1. This library contains several modifications on the same general backbone. The compounds present a phenyl ring as hydrophobic moiety, a urea bond as structuring agent and a heterocycle derivative which constitutes the hydrophilic head.

As presented in the introduction, the types of molecules presenting ion channels properties are very varied [53], though the simplest common feature is the presence of substituted heteroatoms, capable of generating weak bonds. For this reason two heterocycles were chosen in this case as the active center for our species, namely imidazole and 3-aminotriazole.

Another variation was the introduction of a chiral center in the molecules. Since lipids present chiral centers, the assessment of the effect of a compound's absolute configuration on its activity, could provide interesting results.

The last modification made on the structure was to vary the electron richness of the phenyl nuclei. By the introduction of a fluorine atom in the para position the respective nuclei become poorer in electrons. As Yamnitz et al. [56] showed in the case of their library in the case of anion transport, this small modification has a great effect on the activity of compounds. Moreover, the dianilide structures proposed by Yamnitz are similar on more accounts to the compounds designed for this project. The dianilides present three phenyl-like flat moieties bound by the fixed amidic bond. The compounds used in the project present flat moieties, the phenyl and the heterocycle linked through a urea directional bond. In both cases the supramolecular assemblies are responsible for activity.

The compounds were synthesized using either scheme (1) for the histamine derivatives or scheme (2) for the 3-amino triazole derivatives, presented in Figure 19. These are simple, one-step reactions, with almost quantitative yields. The protocol for the synthesis is presented in the annexes. The chiral modifications of the structures were introduced by using chiral isocyanates. The isocyanates may present a fluorine atom in the para position, leading to variations of the electron density of the phenyl ring in the resulting structures. The resulting compounds are presented in Table 1.

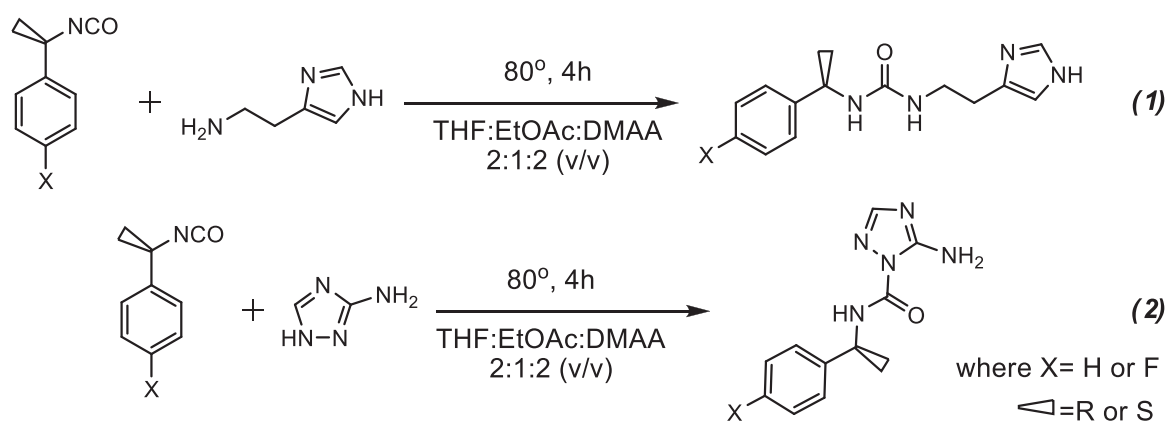
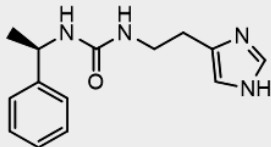
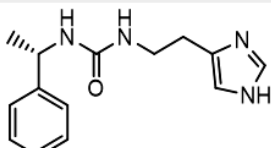
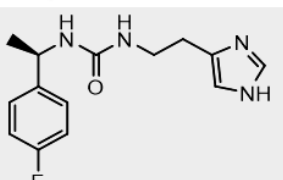
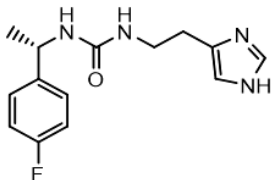
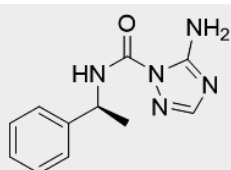
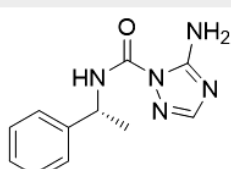
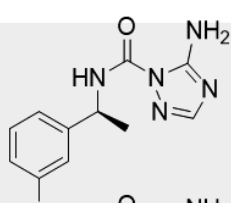
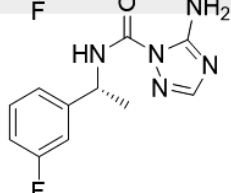


Figure 19: Synthetic route used in the synthesis of the compounds

Table 1: Library of compounds used for the construction of self-assembled transporters

| Nr. | Structure   | Structure name  | Chemical formula                                  | Molecular weight |
|-----|---|---|---|------------------|
| 1   |    | (R)-1-(2-(1H-imidazol-4-yl)ethyl)-3-(1-phenylethyl)urea                 | C <sub>14</sub> H <sub>18</sub> N <sub>4</sub> O  | 258.32           |
| 2   |    | (S)-1-(2-(1H-imidazol-4-yl)ethyl)-3-(1-phenylethyl)urea                 | C <sub>14</sub> H <sub>18</sub> N <sub>4</sub> O  | 258.32           |
| 3   |    | (R)-1-(2-(1H-imidazol-4-yl)ethyl)-3-(1-(4-fluorophenyl)ethyl)urea       | C <sub>14</sub> H <sub>17</sub> FN <sub>4</sub> O | 276.31           |
| 4   |   | (S)-1-(2-(1H-imidazol-4-yl)ethyl)-3-(1-(4-fluorophenyl)ethyl)urea       | C <sub>14</sub> H <sub>17</sub> FN <sub>4</sub> O | 276.31           |
| 5   |  | (R)-5-amino-N-(1-phenylethyl)-1H-1,2,4-triazole-1-carboxamide           | C <sub>11</sub> H <sub>13</sub> N <sub>5</sub> O  | 231.25           |
| 6   |  | (S)-5-amino-N-(1-phenylethyl)-1H-1,2,4-triazole-1-carboxamide           | C <sub>11</sub> H <sub>13</sub> N <sub>5</sub> O  | 231.25           |
| 7   |  | (R)-5-amino-N-(1-(4-fluorophenyl)ethyl)-1H-1,2,4-triazole-1-carboxamide | C <sub>11</sub> H <sub>12</sub> FN <sub>5</sub> O | 249.24           |
| 8   |  | (S)-5-amino-N-(1-(4-fluorophenyl)ethyl)-1H-1,2,4-triazole-1-carboxamide | C <sub>11</sub> H <sub>12</sub> FN <sub>5</sub> O | 249.24           |

All the compounds have been characterized by the appropriate methods,  $^1\text{H}$  NMR and mass spectrometry in order to confirm the structure. This data can be found in the annexes.

Single crystal structures were obtained for five of the compounds tested. These can be considered as models for the self-assembly of the molecules in membranes. The weak interactions (hydrogen bonding,  $\pi$  stacking, hydrophobic interactions, etc.) between different atoms are at the origin of packing patterns and may provide information on the possible assemblies that the molecules can adopt in bilayers.

For compounds 3 and 4 the displayed structure contains a head to tail arrangement of the polar part of the molecules. The urea by hydrogen bond extends to the imidazole moiety and not to other ureas in this case. The polar part is bordered by stacks of phenyl rings. The presence of hydrogen bonds made by the fluorine atom towards two slightly acidic hydrogen atoms generates a distortion of the stack, the phenyl rings are not found in the same plane. The structure does not present channel type structures in solid state, which does not imply the inactivity of the compound in transport experiments. Through the presence of multiple weak bonds as well as an amphiphilic character of the suprastructure permits a possible interaction with ions. The crystal packing of compound 3 is presented in Figure 20.

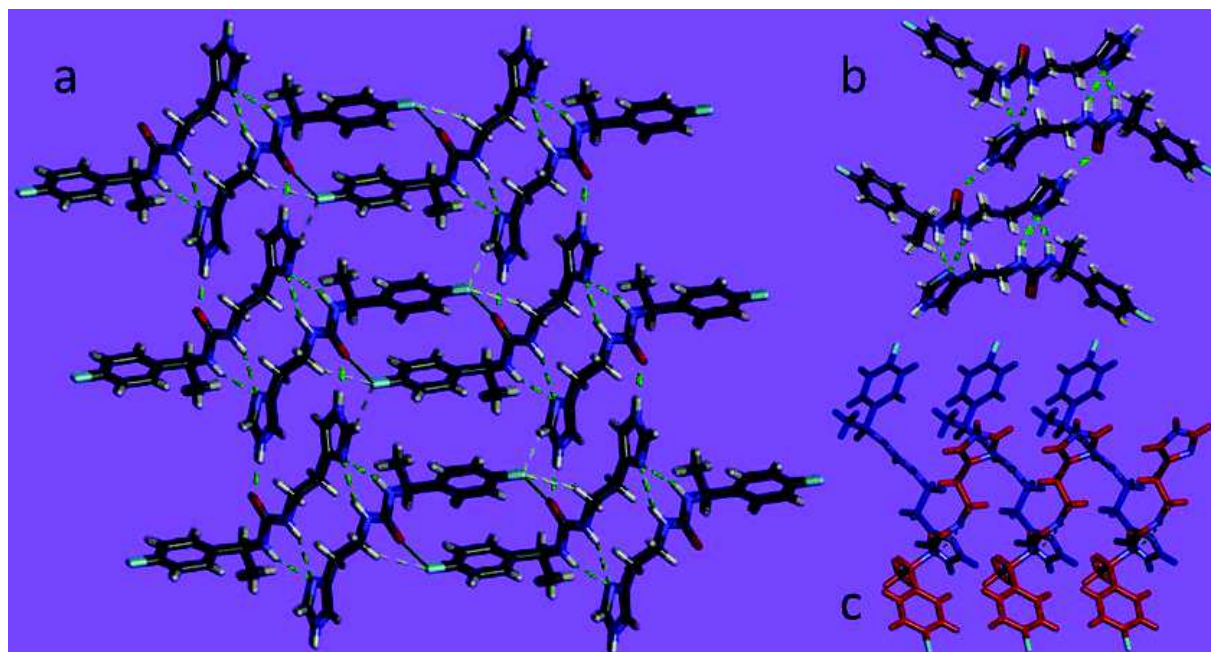


**Figure 20: Crystal packing of compound 4. Crystals obtained in water. a) crystal packing along b axis; b) head to tail packing of the polar part of the molecule; c) spatial representation of the urea self-assembly, red – front plane, blue – back plane**

A very similar arrangement is displayed by compound 7. The grouping of polar/non-polar regions follows the same pattern as in the case of compound 4. The phenyl moieties stack over each other, again under an angle. The amino-triazole heterocycles generate hydrogen bonding towards another heterocycle moiety, while the urea generates the directionality of the structure. The packing of this molecule can be seen in Figure 21. It is important to note that this structure is much closer to that of compounds 3 and 4 (presented in Figure 20), than that of compounds 5 and 6 (presented in Figure 22). This underlines the greater influence of the fluorine atom in the para position compared to the variation of the heterocycle moiety.



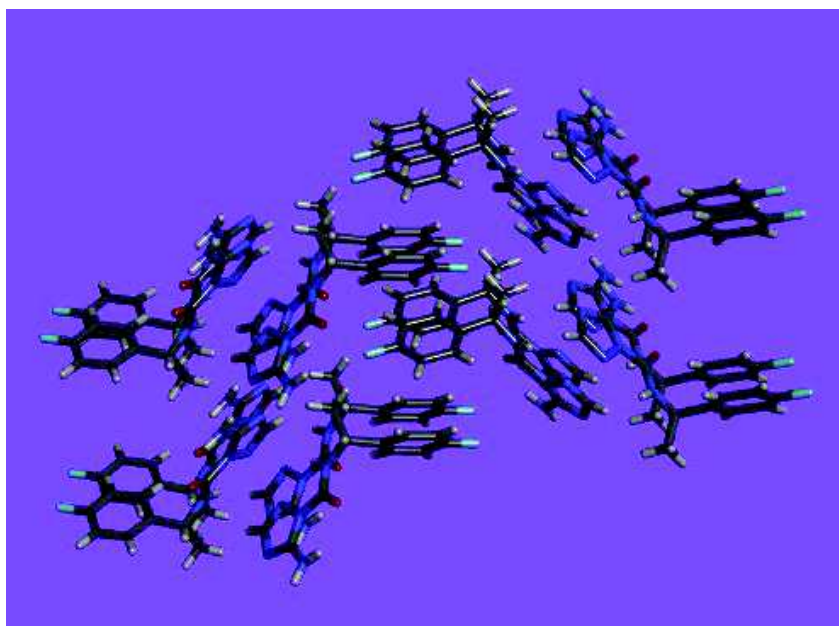


**Figure 21: Crystal packing of compound 7 along the b axis. Crystals obtained in water.**

The structures for compounds 5 and 6 display a very tight packing, as a consequence of the absence of the two carbon atom spacer found in histamine derivatives. Hydrogen bonds are extended between the urea oxygen, the available urea NH and the amino group of the triazole of the same molecule. The phenyl ring is almost perpendicular to the 3-amino triazole moiety, with an angle of  $83.44^\circ$  between the triazole NH, the urea oxygen and the para hydrogen of the phenyl ring. Moreover, the molecules have an embraced disposition, hydrophobic pockets being plugged by a perpendicular triazole moiety. The structure is less labile than in the case of compounds 3 and 4, the packing being overall tighter. The structure of compound 5 is presented in Figure 22.

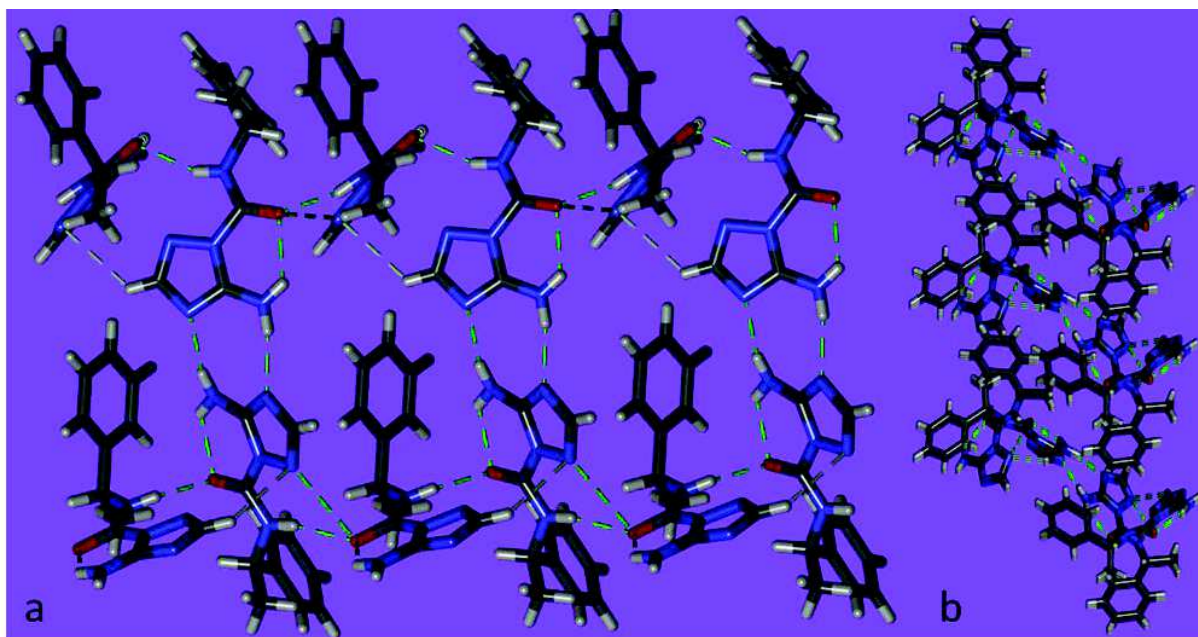


**Figure 22: Crystal packing of compound 5. Crystals obtained in water. a) Crystal packing along b axis; b) Crystal packing along a axis**

Although the X-ray single crystal data is very valuable, it does not give a complete representation of the interaction of a system in a complex environment such as a lipid bilayer. The absence of channel-like molecular associations does not give a definite verdict on the activity towards the translocation of ions across lipid membranes. As mentioned in the introduction, two possible mechanisms are employed by artificial ion channels, a carrier transport mechanism or a facilitated diffusion mechanism for the transport of ions.

The transport capabilities of the synthesized compounds have been assessed. However, the specifics of the transport mechanism cannot be fully described by the available methods in the case of supramolecular structures. The dynamism of the systems and the complexity of the vesicular methods prevent the in situ characterization. This does not hinder the possibility of both quantitative and qualitative studies on the transport effect which the compounds manifest.

### 1.2.2. Fluorescence Assays

As presented previously, in the case of ionic transport across lipid bilayers, the most common methods employed are fluorescence related. These techniques can provide both a quantitative and a qualitative result for this phenomenon.

One of the strengths of the method is the possibility to test multiple ions on the same vesicle substrate in order to describe the selectivity of a certain compound. The other one is that this method allows a wide scale concentrations of the same chemical species. The concentration assays are particularly important in this case since the channels are generated by using the compounds' property of self-assembly, which, of course, benefits from an increase in concentration.

For a better understanding of the experiments involving self-assembled transporting units on LUVs, monitored by means of ratiometric fluorescence techniques, a simplified scheme is presented in Figure 23. The method will be presented in detail in the following section, covering the principles, as well as, the data processing and interpretation.

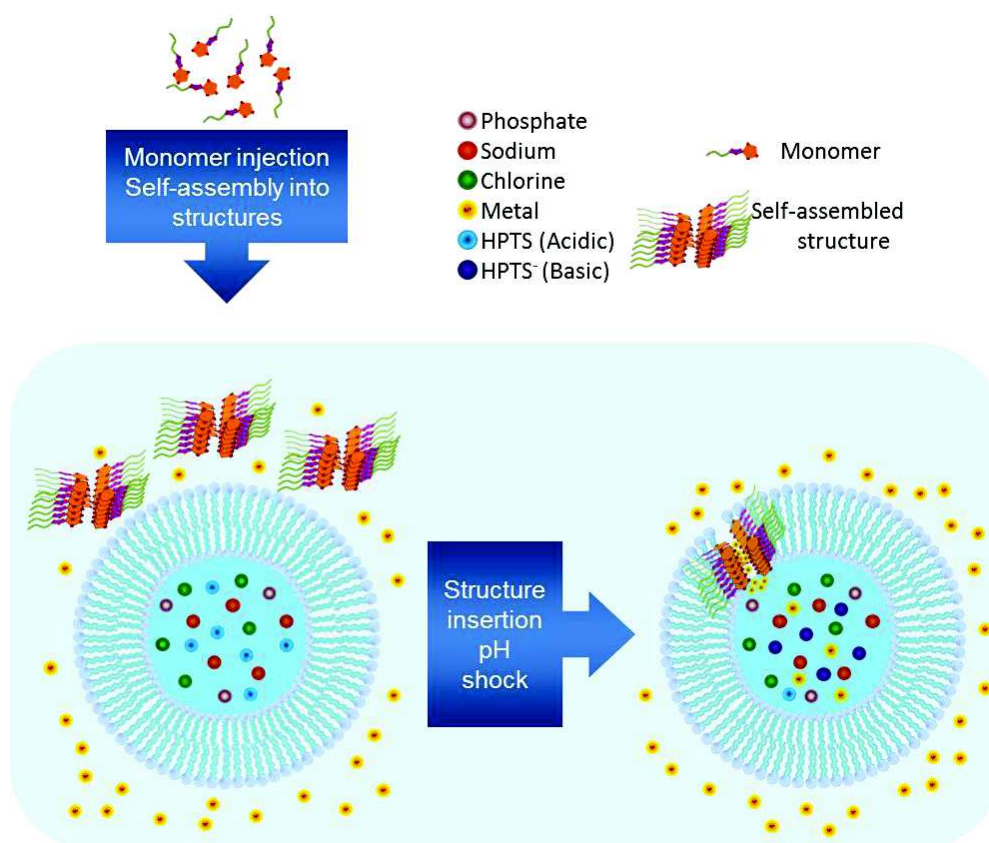
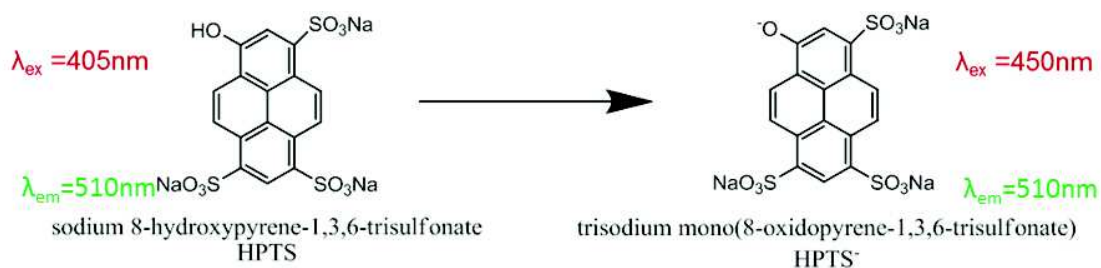


Figure 23: Simplified scheme of ionic transport using vesicular methods

The ratiometric method employed is based on the equilibrium between the acidic form of **HPTS** “pyranine” (8-Hydroxypyrene-1,3,6-Trisulfonic Acid, Trisodium Salt) and its basic form **HPTS<sup>-</sup>**. The acidic form is predominant at a pH value of 6.4 while the basic form is to be found at a pH value of 7.4 (Figure 24). This method is very well described in the literature [59]–[63] in relation to evaluating the transport capabilities of supramolecular self-assembled channels. The two forms of the fluorescent dye have two different excitation wavelengths, namely 405 nm for the acidic form and 450 nm for the basic form, while sharing the emission wavelength of 510 nm. The instrument measures alternatively the excitation at 405 nm and 450 nm and divides one signal to the other, thus revealing their relative amount, also correlated with the change in pH.



**Figure 24: HPTS, the fluorescent probe used in the ratiometric measurements**

By enclosing the acidic form of HPTS inside the LUVs (in a PBS buffer that has the value of 6.4 pH units), the acidic form is prevalent. The exterior pH is suddenly increased to a value of 7.4 (pH shock to the suspension of vesicles), creating the conditions in which the basic form of pyranine, HPTS<sup>-</sup> is found. Still, the two pH media are isolated by the lipid membrane. Therefore the basic form can only appear if positive ions, metals, are transported across the membrane. An injection of a compound, which might present transport capabilities in the fluorimetric cell (containing the pyranine loaded cells), will generate a quantifiable modification in the signal, proportional to its activity in translocating ions across the bilayer.

The transport activity of the entire library was tested using the ratiometric fluorescence method. The large unilamellar vesicles were suspended in a PBS buffer solution (10mM) containing a concentration of 100 mM of the respective alkali salt ( LiCl, NaCl, KCl, RbCl, CsCl). Each of the salts was used in order to transport the corresponding ion. As previously stated, the change in ratio between the two forms of HPTS, acidic and basic, can be attributed to the influx of cation ions through the lipid bilayer. In order to be able to compare different experiments, the recorded signal was normalized from 0 to 1, using the following formula:

$$N_t = \frac{(I_t - I_0)}{(I_\infty - I_0)}$$

Where  $I_t$  is the value of the intensity at a given moment,  $I_0$  is the value of the intensity before the transport occurs and  $I_\infty$  is the value of the intensity after the lysis of

the vesicles (where all of the dye spills in the exterior medium, with a pH of 7.4), considered to be the maximum value.

As seen from Figure 25 the two raw signals of HPTS and HPTS<sup>-</sup> are transformed to a ratio, which represents the transport curve. The transport curve presents the following events: the initial signal  $N_i=0$ , the injection of the compound, the pH shock, the transport interval, the vesicle lysis and the final signal  $N_f=1$ . The initial signal in the ratiometric data is normalized to 0. At this moment, it is considered that all the HPTS is in its acidic form. The injection of the compound is done at a moment in time (ex.  $t=-50s$  compared to the start of the transport) in order to allow the self-assembly of the compound in the lipid bilayer. This is followed by the pH shock generated by the injection of an experimentally determined amount of NaOH at time  $t=0$ . The amount of NaOH injected is previously calibrated for each batch of vesicles in order to provide an exact pH variation of 1 unit. A pH jump of 1 unit from 6.4 to 7.4 in the external solution is sufficient to change the entire HPTS amount into its basic form.  $t=0$  represents the moment when transport starts. The transport takes place over an interval of time, chosen to be long enough that the system reaches and equilibrium. At the end of this interval, the LUV population is lysed. The lysis is done by means of a surfactant, Triton 100, which breaks up the vesicles and releases the HPTS in the solution. The 7.4 pH of the solution forces the remaining HPTS to turn to its basic form. This produces a jump on the ratio curve, due to the sudden disappearance of the acidic HPTS signal. Therefore, in the ratiometric data the final signal is normalized to 1, corresponding to the signal of the basic HPTS.

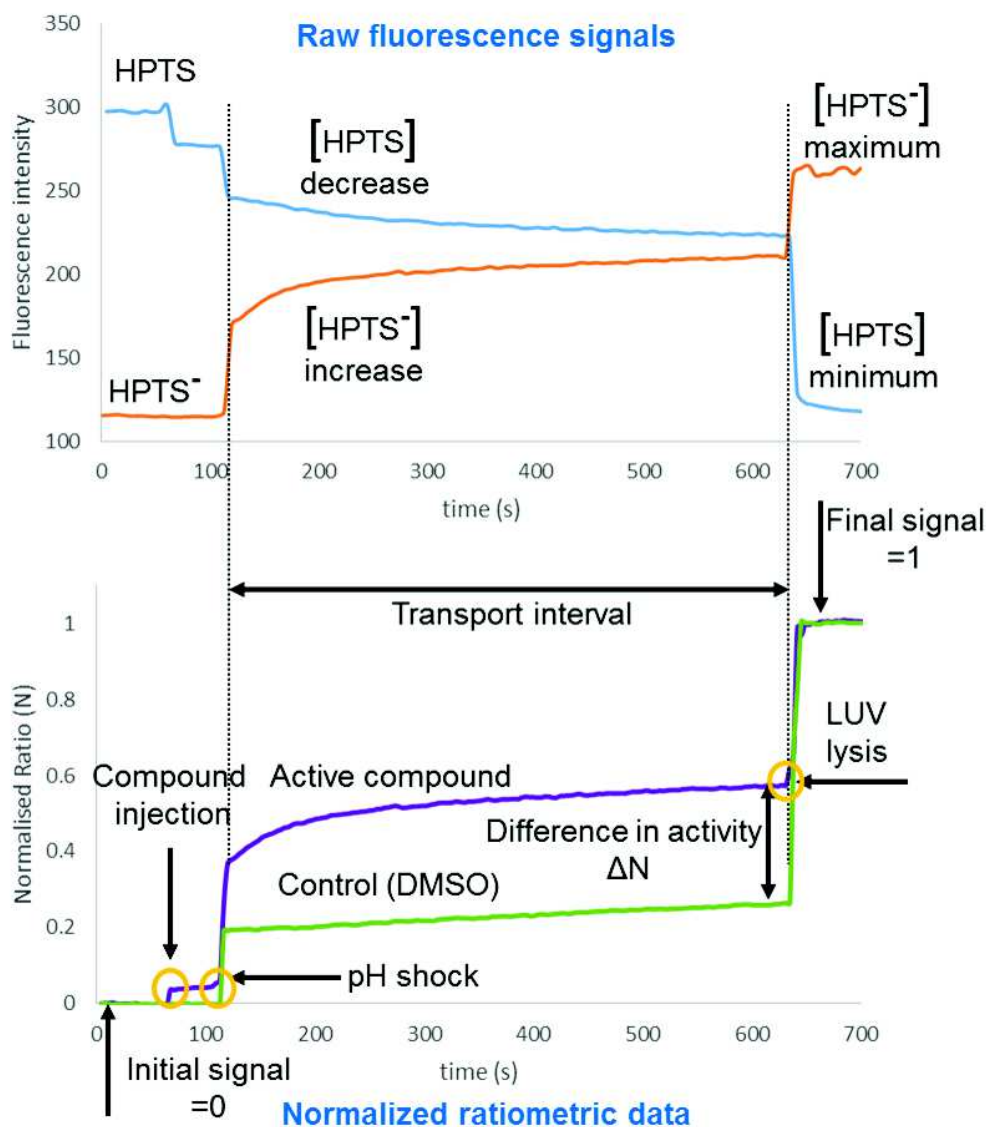


**Figure 25: Sample fluorescence curves in ionic transport. (Up) raw signals of HPTS and HPTS<sup>-</sup> in the fluorescence spectrum. (Bottom) ratiometric normalized curves for an active compound and for a control experiment using DMSO. The events over the course of the experiment are marked.**

The most important criterion in interpreting the results is the shape of the curve. When employing vesicular methods, the liposomes and their properties vary from one batch to the other, therefore one must always keep in mind that the method is referential to self. When analyzing the curves, the first aspect that is relevant is the amplitude of the normalized signal compared to the blank sample, as seen in Figure 25. A second aspect

is the curvature. In general, a sigmoidal shape represents transport, but, it is not always the case [64]. An ascending signal is also a good indication of transport as seen in Figure 25. However, depending on the nature of the compound, one species may promote a very fast and active transport, therefore reaching a maximum and followed by a signal descent, with a final point that is lower than the maximum. Working with self-assembled supramolecular structures in the role of the transporter also implies that the concentration must have a positive effect on the rate of transport. In other words, by increasing the concentration, one should observe an increase in transport. The absence of coherence in the signal distribution of specific concentrations is a strong indication of the absence of activity towards the ion. One last observation is that, in the case of very active compounds, one can talk about a saturation of transport. In this case increasing the concentration over the effective necessary concentration, does not have any other effect than a more accelerated increase of the curve.

The mathematical interpretation of the results was made using a Hill type plot [65]. This method, though more complex than the pseudo first order interpretation [22] provides a better understanding of the complex process of transport when employing self-assembled channels. The main difference is that instead of presuming a pseudo first degree constant, the Hill interpretation considers an “n” degree system, without imposing restrictions. This interpretation proves to be more accurate, since self-assembled channels do not present a finite number of molecules in constructing the channel, while the behavior changes from one compound to the other. So, instead of simplifying the system in a reductionist manner, it’s considered and treated as a whole.

The Hill analysis provides three parameters, Y- activity, EC<sub>50</sub> and the Hill number. The calculation method is presented lower.

$$Y = \frac{1}{1 + \left[ \frac{(\text{conc})}{EC_{50}} \right]^n}$$

Where **Y** is the activity of the channels, **(conc)** is the molar concentration of the monomer and **EC<sub>50</sub>** is the concentration at which 50% of the transport is performed and **n** is the Hill number.



This equation can be linearized in the following form:

$$\log Y = n \log(\text{conc}) - n \log K_D$$

Where  $Y$  is the activity of the channels,  $\log(\text{conc})$  is the 10 base logarithm of the molar concentration of monomer  $K_D$  is the dissociation constant and  $n$  is the Hill number.

In order to calculate the  $EC_{50}$  value the following formula is applied:

$$F_t = \frac{(N_{conc} - N_{min})}{(N_{max} - N_{min})}$$

Where  $F_t$  is the signal at a given time, in our case 500 seconds,  $N_{conc}$  is the normalized signal for a certain concentration,  $N_{min}$  is the normalized signal for the minimum concentration, in our case for the blank sample, DMSO, and  $N_{max}$  is the signal for the highest concentration tested. By plotting the  $F_t$  values over the range of tested concentrations, the  $EC_{50}$  value can be obtained through interpolation for a corresponding value of  $F=0.5$ .

The significance of  $EC_{50}$  is, by definition, the concentration of compound for which one half of the total number of ions are transported through the membrane. This is directly tied to the total possible transport done by a particular species in the given interval. So, for example, if a certain system is able to do a 0.6 transport rate the  $EC_{50}$  value will be the concentration of monomer for which a transport rate of 0.3 occurs.

The Hill analysis provides information on the type of channel that is being formed. There are two types of channels, type I and type II. Each of which can be either A or B, namely stable or unstable. The difference between type I and type II channels is the known stoichiometry of the formed structure. While type I channels consist from a known number of molecules, type II does not. A Hill number greater than 1 is specific for a type I channel. One that is lower or equal to 1 corresponds to a type II channel. For type I channels standard analyses (like NMR or spectrometry) do not provide any useful information on the structure. In the case of type II they do, for example shifts in a proton NMR based on concentration. One last difference between the two channel types is that type II formation is exergonic ( $\Delta G < 0$ ), while type I formation is endergonic ( $\Delta G > 0$ ) [65].

All the alkali metals have been tested, with a strong emphasis on sodium and potassium, the ones most common in living systems. The proton transporting capabilities of the compounds were also assessed because of similarities between this ion and the alkali metals. All the fluorescence data has been interpreted using a Hill model.

### 1.2.2.1. Sodium Transport Experiments

The fluorescence spectra were recorded over a period of 800 seconds, out of which, the active transport took place over 500 seconds. The resulting transport curves are therefore presented expressed in N500 as function of time as can be seen in Figure 26. The direct interpretation of the curves is presented lower in Table 2.

Table 2: Sodium transport activity

| <i>Compound</i>           | <i>1</i> | <i>2</i> | <i>3</i> | <i>4</i>  | <i>5</i> | <i>6</i> | <i>7</i> | <i>8</i> |
|---------------------------|----------|----------|----------|-----------|----------|----------|----------|----------|
| <i>N<sub>max500</sub></i> | 0.50     | 0.50     | 0.72     | 1         | 0.52     | NA       | 0.78     | 0.60     |
| <i>Activity</i>           | Weak     | Weak     | Good     | Excellent | Weak     | No       | Good     | Weak     |

From a structural point of view, we can observe that the presence of the fluorine atom in the para position has a strong and positive effect on the activity of compounds towards the transport of the sodium ion. Both the amino triazole and the histamine derivatives outperform the corresponding compounds that are lacking the fluorine atom. As a general rule, the R isomers present a better activity compared to the S isomers with the exception of compound 4 which is the most active.

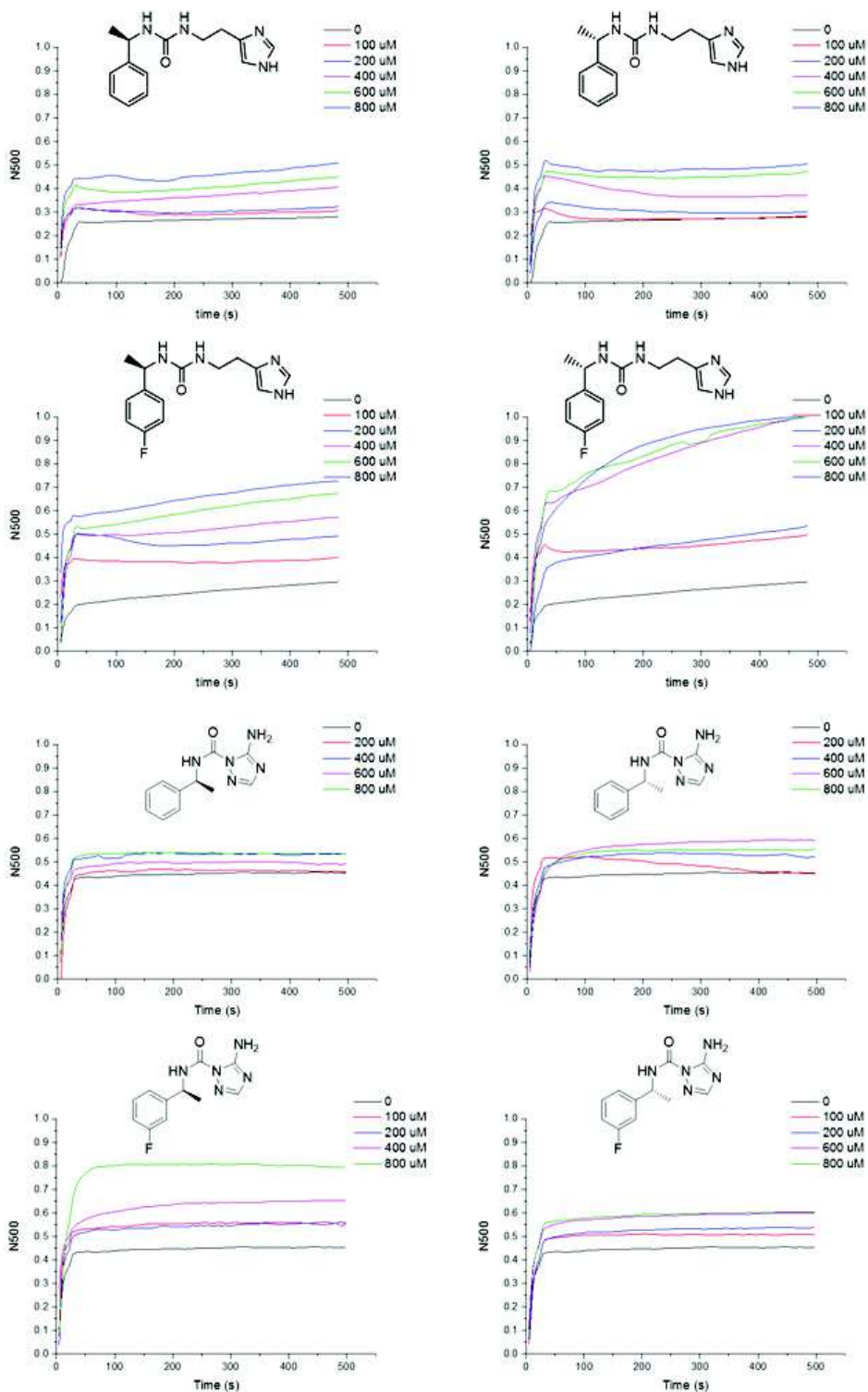
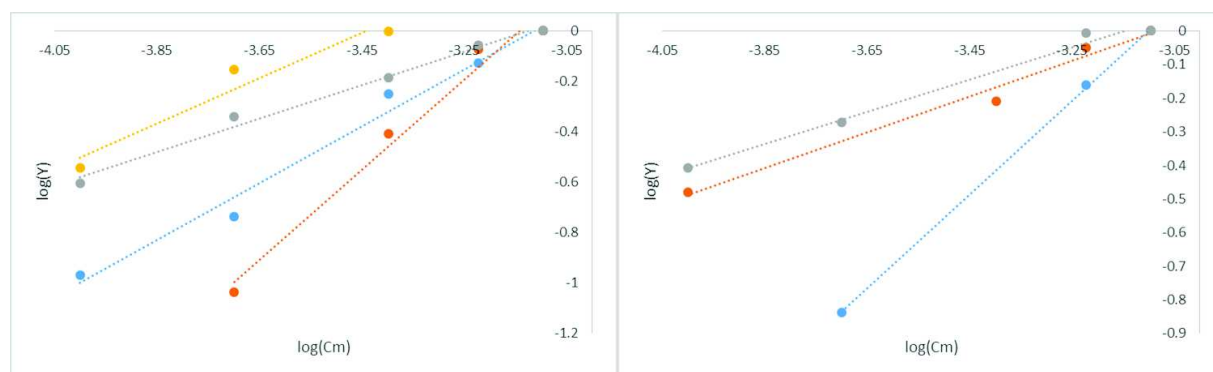


Figure 26: Ratiometric normalized fluorescence sodium transport curves of compounds 1-8. LUV suspension in PBS pH=6.4 (10mM), NaCl 100mM. N500 normalized transport over 500 seconds. Compound insertion at time=-50s, NaOH (25  $\mu$ l, 0.5M) added at t=0. Fluorescent probe HPTS  $\lambda_{1ex}$ =405nm,  $\lambda_{2ex}$ =460nm,  $\lambda_{em}$ =510nm.

The Hill plots, representing the logarithm of Y versus the logarithm of molar concentration, are first order curves with R<sup>2</sup> coefficients of 0.95. The slope of these curves represents the Hill number, determining the type of channel that is formed. The Hill plots for the tested compounds are presented in Figure 27.



**Figure 27: Hill plots for sodium transport. (Left) Blue – compound 1; Red – compound 2; Gray – compound 3; Yellow – compound 4. (Right) Blue – compound 5; Red – compound 7; Gray – compound 8**

By application of fitting methods, the Hill number is obtained. The results are presented, in Table 3. As it can be seen, the type I channels, with a Hill number value greater than 1, are attributed to the compounds that do not contain a fluorine atom in the para position. One hypothesis is that the compounds self-assemble in a similar fashion as in the X-ray single crystal structures, and they remain as stable and fixed moieties. The compounds containing the fluorine atom (that probably offers higher fluidity and better compatibility within the membrane), have probably a more dynamic structure and are able to form a cavity where they can accommodate ions.

**Table 3: Hill number and type of channels**

| <i>Compound</i>         | <i>1</i> | <i>2</i> | <i>3</i> | <i>4</i> | <i>5</i> | <i>6</i> | <i>7</i> | <i>8</i> |
|-------------------------|----------|----------|----------|----------|----------|----------|----------|----------|
| <i>Hill number</i>      | 1.124    | 1.790    | 0.662.   | 0.899    | 1.396    | NA       | 0.534    | 0.477    |
| <i>Type of channels</i> | Type I   | Type I   | Type II  | Type II  | Type I   | No       | Type II  | Type II  |

Finally, the EC<sub>50</sub> value can be calculated and is represented in Figure 28. The NA (not available) is used for the cases in which the compound does not present activity.

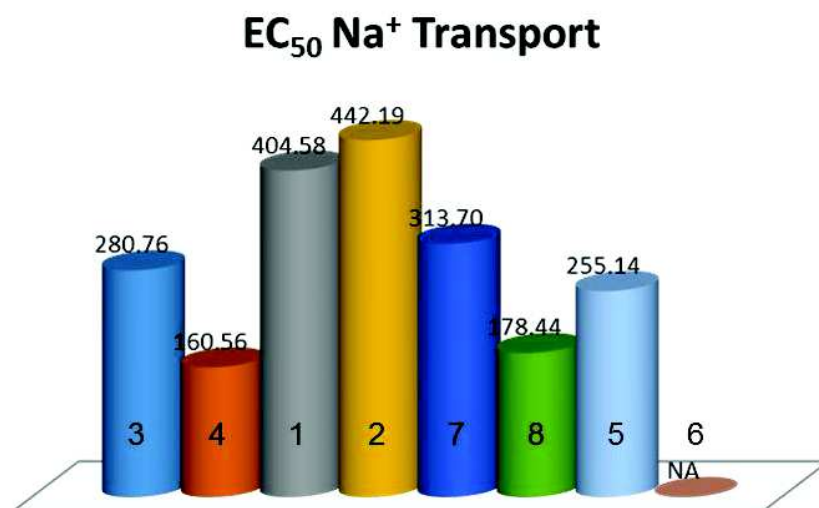


Figure 28: EC<sub>50</sub> values for sodium transport. Blue – compound 3; Red – compound 4 ; Gray – compound 1; Yellow – compound 2; Dark blue – compound 7; Green – compound 8; Light blue – compound 5; Pink – compound 6

The EC<sub>50</sub> value provides interesting information. These values should be referred to the total amplitude of the signal, and not to each other, as explained in the introductory part. Namely they represent, a “critical concentration” for which 50% of the total possible transport occurs. So, for example, between compounds 7 and 8 the lower value is for compound 8, which is weaker transporter. This value represents the fact that compound 8 reaches half transport at lower concentration values compared to compound 7, though the better transporter is compound 7.

#### 1.2.2.2. Potassium Transport Experiments

The potassium transport method is very similar to the sodium method, with the sole exception that the exterior solution contains potassium chloride with a concentration of 100mM instead of sodium chloride. The ratiometric fluorescence curves are presented in Figure 29.

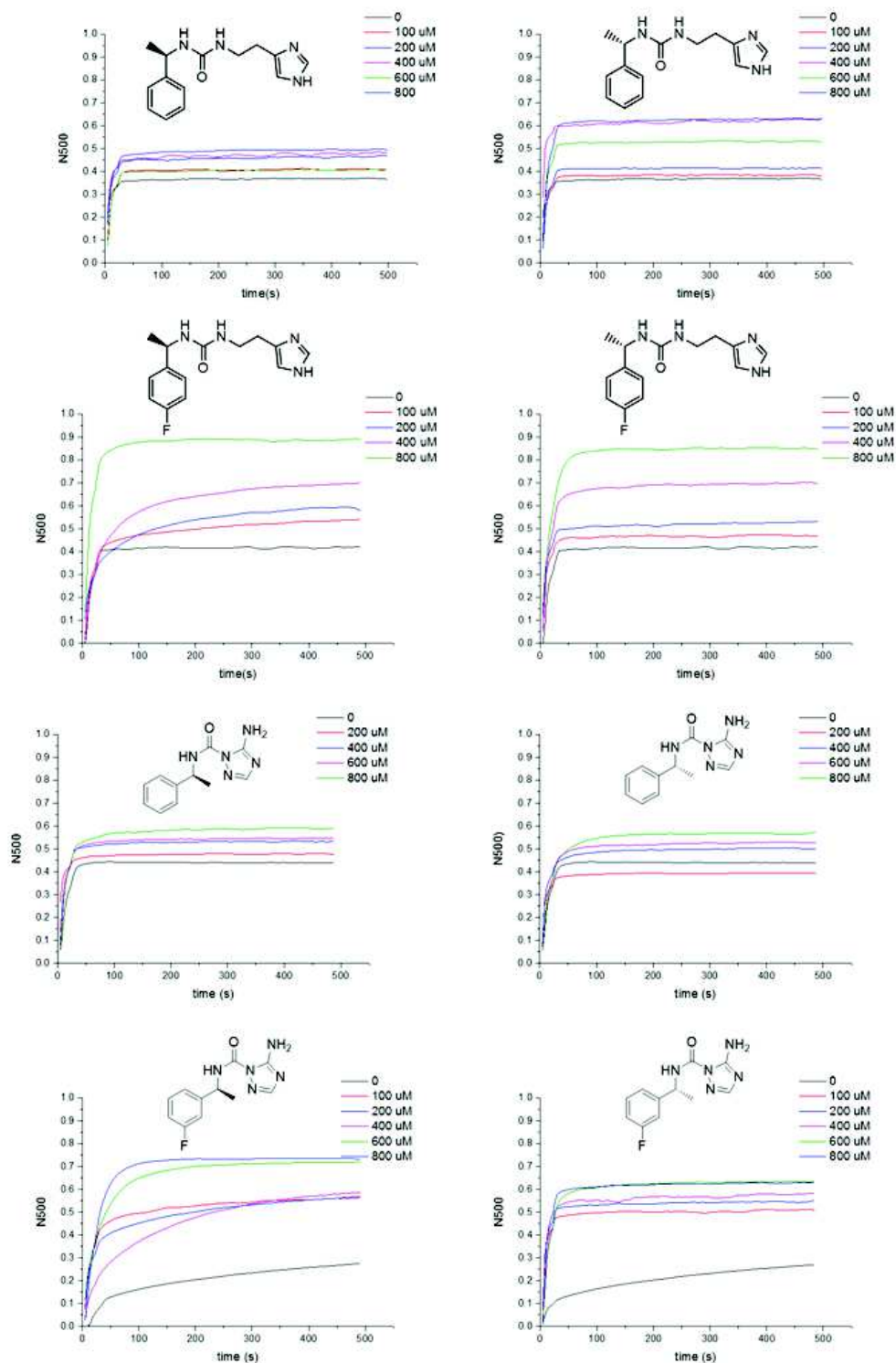


Figure 29: Ratiometric normalized fluorescence potassium transport curves of compounds 1-8. LUV suspension in PBS pH=6.4 (10mM), KCl 100mM. N500 normalized transport over 500 seconds. Compound insertion at time=-50s, NaOH (25  $\mu$ l, 0.5M) added at t=0. Fluorescent probe HPTS  $\lambda_{1ex}$ =405nm,  $\lambda_{2ex}$ =460nm,  $\lambda_{em}$ =510nm.

The curves have been interpreted using the principles presented for sodium transport. The direct interpretation of the curves is presented lower in Table 4.

**Table 4: Potassium transport activity**

| <i>Compound</i>           | 1    | 2    | 3         | 4         | 5    | 6    | 7    | 8    |
|---------------------------|------|------|-----------|-----------|------|------|------|------|
| <i>N<sub>max500</sub></i> | 0.49 | 0.63 | 0.88      | 0.84      | 0.59 | 0.57 | 0.73 | 0.62 |
| <i>Activity</i>           | No   | No   | Excellent | Excellent | Weak | Weak | Good | Good |

Similarly to the case of sodium, the fluorinated compounds present better activity. Especially the histamine derivatives perform an excellent transport. Compounds 1 and 2 don't display any type of activity towards the transport of potassium, while compounds 5 and 6 are very weak transporters. This also tends to confirm the crystallographic observations related to the very inflexible structure of compounds 5 and 6.

The Hill analysis was performed on the fluorimetric data in the same manner as in the case of sodium. The results are presented in Figure 30.

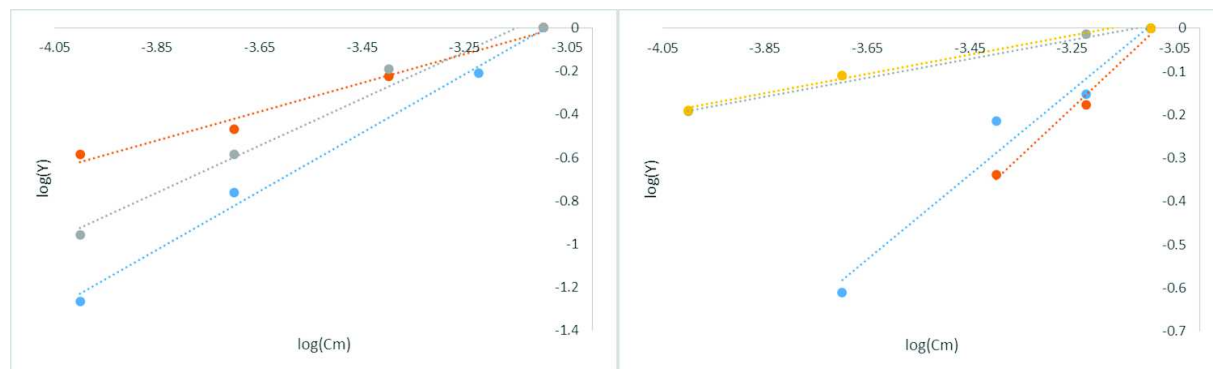


**Figure 30: Hill plots for potassium transport. (Left) Blue – compound 2; Red – compound 3; Gray – compound 4. (Right) Blue – compound 5; Red – compound 6; Gray – compound 7; Yellow – compound 8**

As in the case of sodium, the weak transporters have the tendency to form type I channels, while the fluorinated compounds generally favor type II channels. One exception is compound 4 which has a Hill number of 1.086, this value however, still is too low to be considered a type I channel (Table 5).

Table 5: Hill numbers and types of channels for potassium transport

| Compound         | 1  | 2      | 3       | 4       | 5       | 6      | 7       | 8       |
|------------------|----|--------|---------|---------|---------|--------|---------|---------|
| Hill number      | NA | 1.354  | 0.6647  | 1.086   | 0.977   | 1.113  | 0.219   | 0.223   |
| Type of channels | No | Type I | Type II | Type II | Type II | Type I | Type II | Type II |

The EC<sub>50</sub> values have been calculated for the active compounds. These reveal higher overall activity for compounds 3 and 4, while compounds 7 and 8 have much lower EC<sub>50</sub> values (one order of magnitude) at the expense of 15-20% activity. This provides the interesting option of choosing between the amount of compound used and the total provided activity. Compounds 1 and 2, which underperformed, in the transport of sodium present no activity towards potassium. Compounds 5 and 6 have a better affinity for potassium than sodium, but are overall very weak transporters (Figure 31).

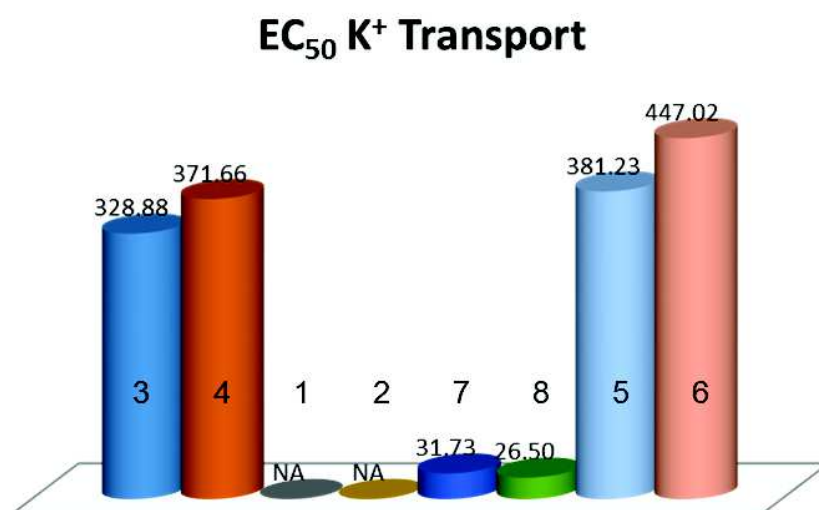


Figure 31: EC<sub>50</sub> values for sodium transport. Blue – compound 3; Red – compound 4 ; Gray – compound 1; Yellow – compound 2; Dark blue – compound 7; Green – compound 8; Light blue – compound 5; Pink – compound 6



The EC<sub>50</sub> values display very low critical concentrations for compounds 7 and 8, two good transporters. On the other hand, the most active transporters compounds 3 and 4 display this at the expense of a higher EC<sub>50</sub> concentration.

In order to valorize these differences in activity, the preference towards certain cations was further tested.

### 1.2.2.3. Ion Selectivity Transport Experiments

In the case of self-assembled artificial ion channels, the selectivity towards ions is a very important feature. Each type of transporter, based on its structure and disposition, favors the transport of certain species. This behavior is closely tied to the dehydration energy, volume and charge exhibited by each ion. By testing our library towards the transport of the monovalent metals of the first group, we can assess this intrinsic preference towards certain species. For this reason, one intermediary concentration of each type of compound was injected in transport conditions. The testing protocol was described in the sodium transport section, the variation being the solutions used, each containing a 100 mM chloride solution of the tested ion. A medium concentration (400µM), was chosen to avoid both capping effects and extreme behaviors characteristic of high concentrations of active system. Low concentrations were avoided in order and to obtain sufficient transport for reliable data. For each experiment a blank injection of DMSO (concentration=0) was also recorded. The fluorescence curves are presented lower in Figure 32.

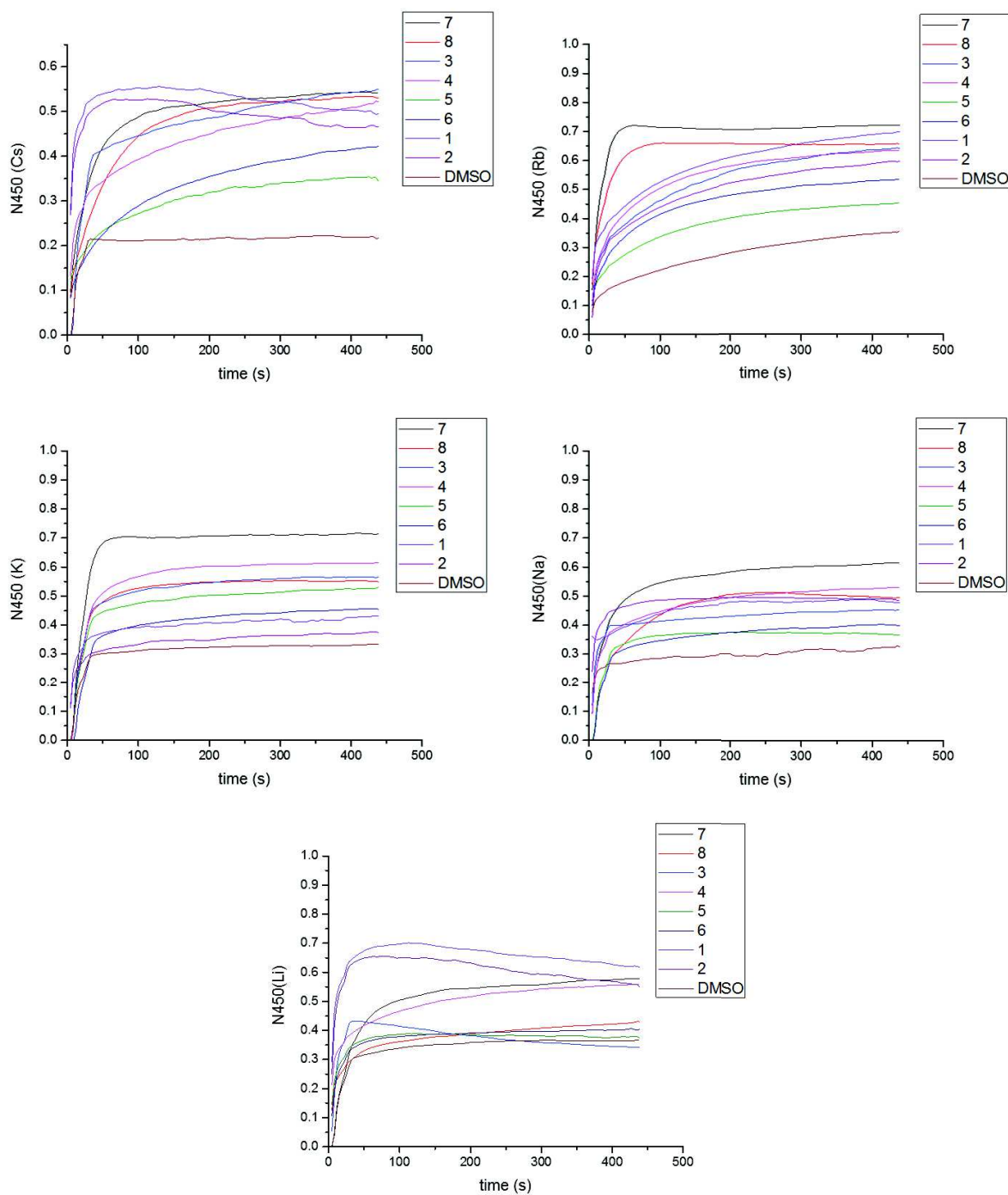


**Figure 32: Ratiometric normalized fluorescence transport curves of compounds 1-8 towards first group cations at a fixed concentration of 400  $\mu$ M. LUV suspension in PBS pH=6.4 (10mM), for each transport experiment a solution of 100mM the corresponding chloride of the transported cation was used. N450 normalized transport over 450 seconds. Compound insertion at time=-50s, NaOH (25  $\mu$ l, 0,5M) added at t=0. Fluorescent probe HPTS  $\lambda_{1ex}$ =405nm,  $\lambda_{2ex}$ =460nm,  $\lambda_{em}$ =510nm.**

The experimental curves were fitted using a Hill sigmoidal curve. Hill functions represent dose-response curves, thus applicable to this type of experiment. This was done because, in the absence of a range of concentrations, the Hill number and the EC50 cannot be determined. The Hill function is presented lower in Figure 33 as a sample curve. Applying this fit, with a chi square value better than  $10^{-9}$ , we can obtain the theoretical calculated values of activity in order to compare them to experimental results.

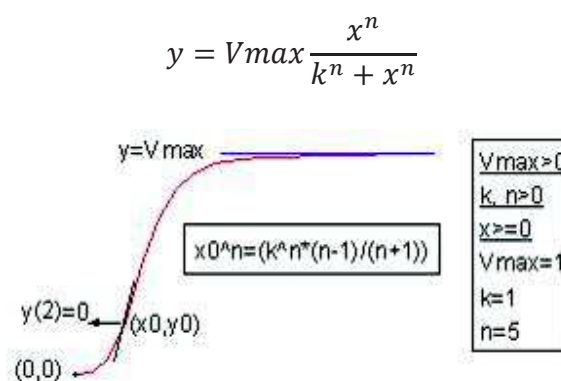


Figure 33: Sample Hill function curve [<http://www.originlab.com/>]

Where  $y$  is the normalized signal,  $Vmax$  is the maximum  $y$ ,  $x$  is the time,  $k$  is the slope for the initial increase and  $n$  is the exponent of the function, presuming an “ $n$ ” degree system.

This method was successfully applied to the curves with a few exceptions. In the case of compound 1 for the Rubidium ion, although the fit is good, the result has no physical sense ( $Y$  larger than 1). For some other particular cases, the fit gave a much larger activity value than the experimental one, but as a general observation, the calculated values (Table 6) are similar to the experimental ones (Table 7).

**Table 6: Calculated maximum values of activity**

| Comp.            | 1      | 2      | 3       | 4       | 5      | 6       | 7      | 8      |
|------------------|--------|--------|---------|---------|--------|---------|--------|--------|
| <b>Cesium</b>    |        |        |         |         |        |         |        |        |
| <b>Vmax</b>      | 0.530  | 0.497  | 0.540   | 0.867   | 0.527  | 0.666   | 0.556  | 0.571  |
| <b>k</b>         | 4.386  | 4.431  | 22.267  | 159.048 | 82.322 | 160.405 | 19.341 | 33.131 |
| <b>n</b>         | 2.017  | 2.069  | 1.187   | 0.373   | 0.452  | 0.559   | 1.170  | 1.097  |
| <b>Rubidium</b>  |        |        |         |         |        |         |        |        |
| <b>Vmax</b>      | 1.233  | 0.789  | 0.949   | 0.736   | 0.648  | 0.637   | 0.717  | 0.665  |
| <b>k</b>         | 214.10 | 64.729 | 104.439 | 33.616  | 83.343 | 41.266  | 9.992  | 10.883 |
| <b>n</b>         | 0.3839 | 0.589  | 0.535   | 0.727   | 0.527  | 0.701   | 1.965  | 1.506  |
| <b>Potassium</b> |        |        |         |         |        |         |        |        |
| <b>Vmax</b>      | 0.423  | 0.387  | 0.559   | 0.610   | 0.514  | 0.443   | 0.710  | 0.551  |
| <b>k</b>         | 7.279  | 7.146  | 18.42   | 21.173  | 18.511 | 25.217  | 18.388 | 18.355 |
| <b>n</b>         | 1.037  | 0.728  | 1.758   | 1.879   | 1.781  | 1.913   | 2.729  | 1.982  |
| <b>Sodium</b>    |        |        |         |         |        |         |        |        |
| <b>Vmax</b>      | 0.731  | 0.495  | 0.444   | 0.566   | 0.371  | 0.393   | 0.624  | 0.522  |
| <b>k</b>         | 17.408 | 4.434  | 6.777   | 15.687  | 16.333 | 20.033  | 16.064 | 29.915 |
| <b>n</b>         | 0.227  | 1.191  | 1.136   | 0.761   | 2.213  | 1.442   | 1.070  | 1.417  |
| <b>Lithium</b>   |        |        |         |         |        |         |        |        |
| <b>Vmax</b>      | 0.664  | 0.612  | 0.379   | 0.734   | 0.385  | 0.403   | 0.576  | 0.478  |
| <b>k</b>         | 5.332  | 5.626  | 8.382   | 24.875  | 6.788  | 9.057   | 26.236 | 13.972 |
| <b>n</b>         | 1.939  | 2.347  | 3.660   | 0.411   | 1.465  | 1.193   | 1.489  | 0.577  |

**Table 7: Experimental maximum values of activity**

| Comp./Ymax       | 1     | 2     | 3     | 4     | 5     | 6     | 7     | 8     |
|------------------|-------|-------|-------|-------|-------|-------|-------|-------|
| <b>Cesium</b>    | 0.495 | 0.466 | 0.551 | 0.522 | 0.345 | 0.423 | 0.542 | 0.531 |
| <b>Rubidium</b>  | 0.698 | 0.598 | 0.641 | 0.634 | 0.455 | 0.535 | 0.723 | 0.655 |
| <b>Potassium</b> | 0.432 | 0.375 | 0.566 | 0.616 | 0.530 | 0.454 | 0.715 | 0.549 |
| <b>Sodium</b>    | 0.475 | 0.484 | 0.452 | 0.529 | 0.366 | 0.396 | 0.613 | 0.495 |
| <b>Lithium</b>   | 0.617 | 0.550 | 0.342 | 0.558 | 0.375 | 0.403 | 0.578 | 0.430 |

By comparing the two values (Figure 34), the calculated one, based on the initial rate of transport, and the experimental one, we can differentiate between ideal and practical conditions. In this case of a good correlation between the two, we can conclude that the experimental activity is validated.

For all compounds, the experimental activity was plotted for each ion tested (Figure 35). For the systems that displayed good activity towards sodium and potassium (compounds 3, 4, 7 and 8), the preference vs ions follows the order  $Rb > K \geq Cs > Na \geq Li$ . For the less active systems, compounds 1, 2, 5 and 6, a certain order can't be fully established. For example, the first two compounds present a strong activity towards Lithium, which is not true for compounds 5 and 6. These differences in behavior can be attributed in the different types of channels that the compounds form. In the case of compounds 3, 4, 7 and 8, which were proven to be type II channels in the experiments for sodium and potassium transport, we can attribute a self-assembled labile and adaptive structure. Since these don't have a determined number of molecules forming the functional supramolecular structure, they are better accommodating for larger ions like rubidium, cesium and potassium. In the case of the other compounds, the supposedly rigid structures they form, better accommodates the smaller size of lithium. Their overall activity is lower. This fact, besides underlining once again that they are weak transporters, also hints at some selectivity differences towards certain cations.

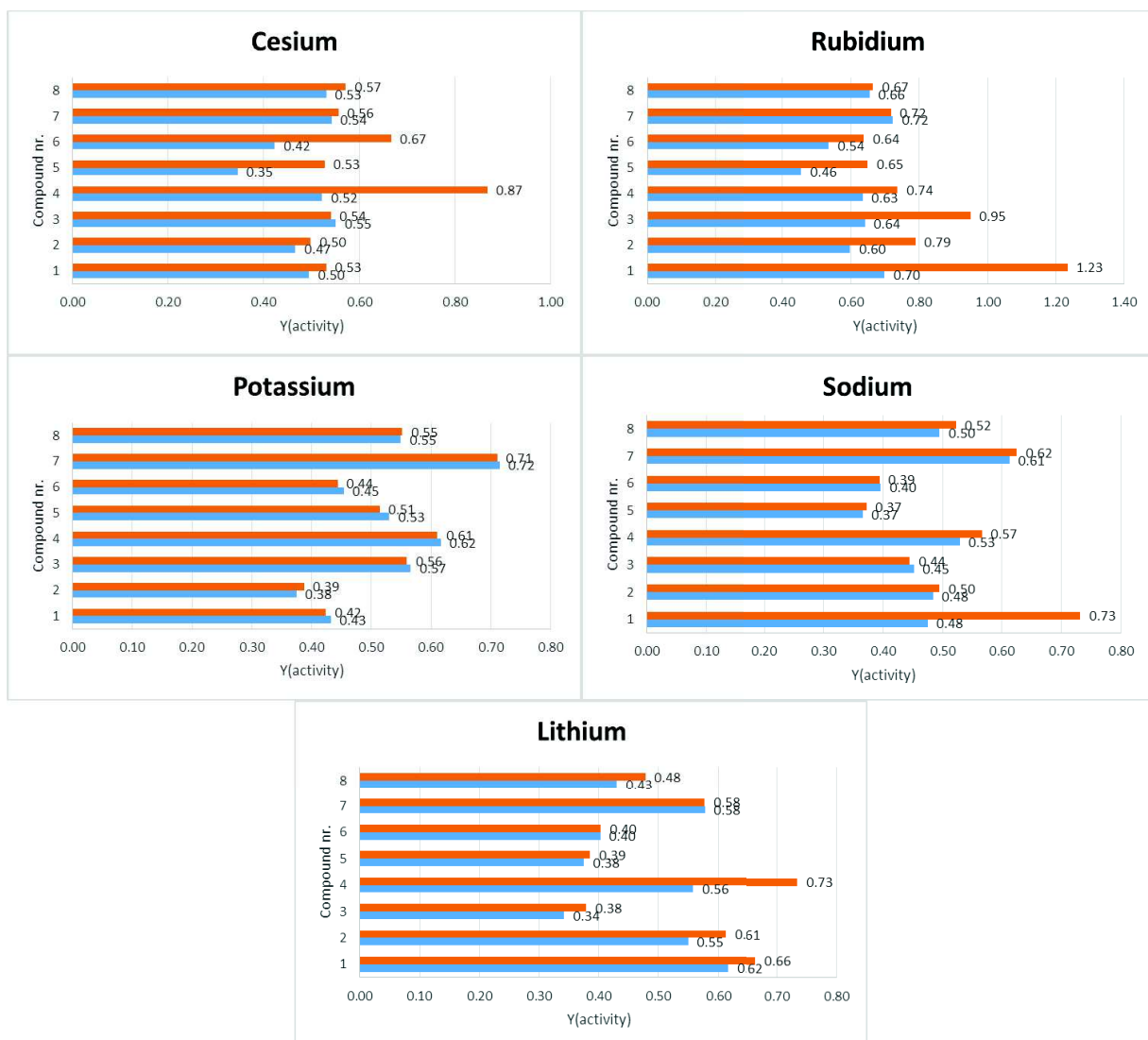
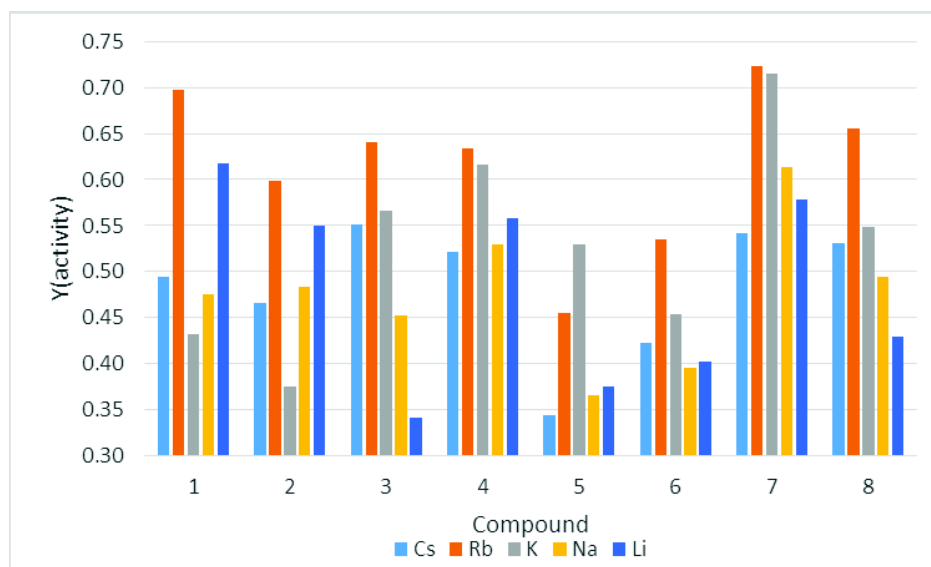


Figure 34: Correlation between the experimental values of transport (blue) and the fitted ones (red).



**Figure 35: Activity of compounds towards alkaline metals as revealed from the experimental data**

Although each compound presents preferences towards certain cations, the term selectivity is a bit restrictive in this case. Indeed, compound by compound, one could make some observations, like in the case of compound 3, where the activity towards the rubidium ion is twice that for lithium ion. The general behavior of the compounds could be classified as a percentage based favoritism towards certain ions. The results are plotted in Figure 35.

#### 1.2.2.4. Proton Transport Experiments

In the case of proton transport experiments, the principle of transport is different, although the data is treated in the same way as in the case of ion transport. In ionic transport conditions, for each ion that is transported through the membrane a proton must leave the liposome, in order to have a fixed charge. In this case, the proton transfer is achieved through simple diffusion. In proton transport conditions the proton is transported through a functional structure. For this to happen, a transporter is inserted in the bilayer of the liposomes, a non-selective potassium carrier valinomycin. The LUVs are suspended in a potassium solution and valinomycin is injected over the LUV population. This generates ideal transport conditions for the potassium ion, from the external solution towards the interior of the vesicles. In order to balance the charge out, protons must be transported from the interior of the vesicles towards the exterior. A compound is injected over the vesicle population, in order to verify its activity. If the compound self-assembles in transporting structure, the signal in ratiometric fluorescence will change in comparison to a blank experiment. The blank experiment only contains DMSO and its signal can be attributed to the simple diffusion of protons across the lipid bilayer. Thus the difference in activity between the compound and the blank experiment can be attributed to the direct transport effect of the active system.

This method uses the same pH-sensitive fluorescent dye, HPTS. The increase of pH inside the vesicle is given by the active carrier system, valinomycin. This is translated to an overall higher signal than in the case of the ion channels. The second influence on the spectra is the speed at which the protons leave the LUVs, equilibrating the system. In order to have a clearer picture Figure 36 illustrates the differences between ionic transport and proton transport.



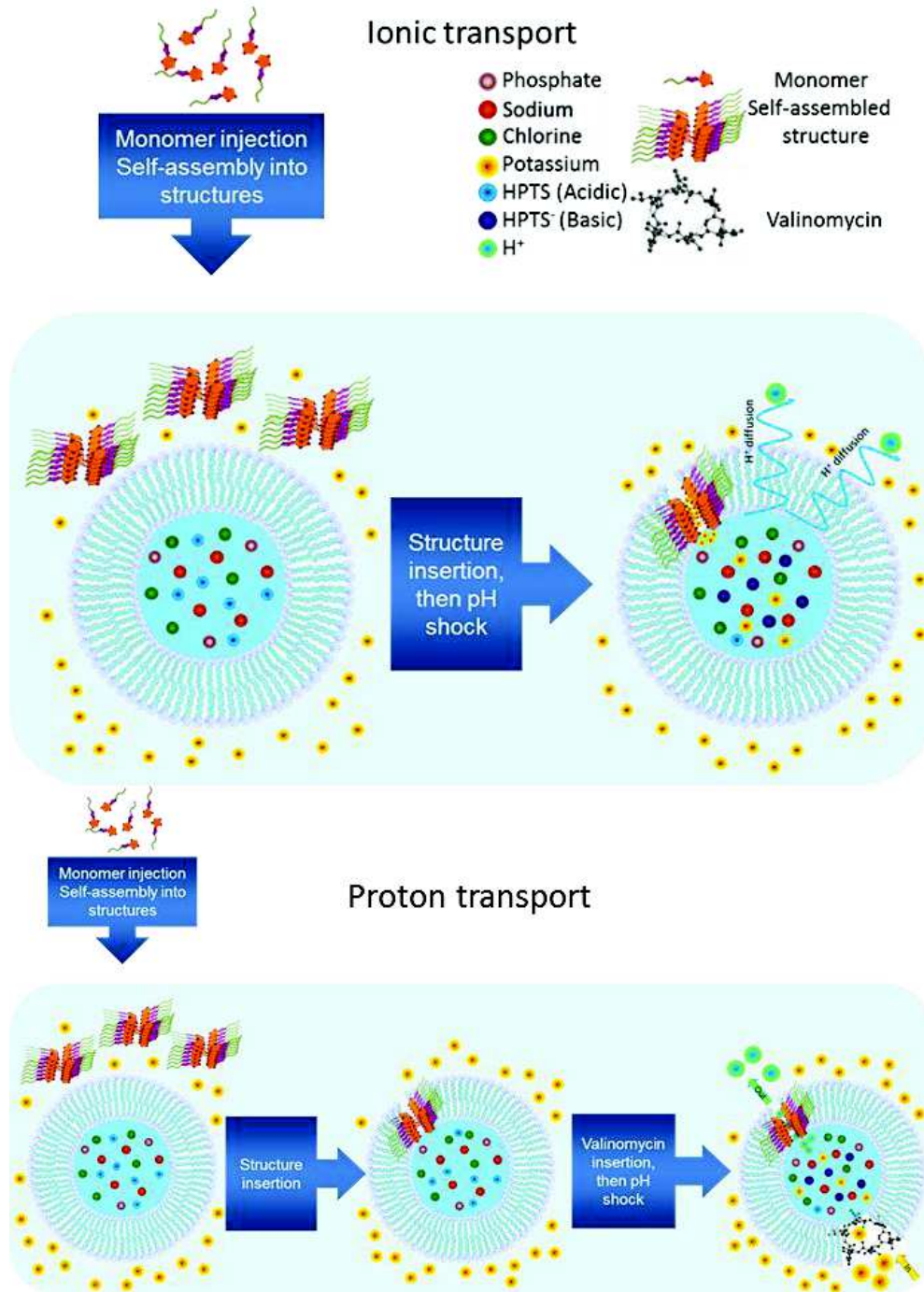


Figure 36: Differences between ionic and proton transport

The proton transport was monitored over a 500 second interval. The ratiometric fluorescence curves are presented lower in Figure 37.

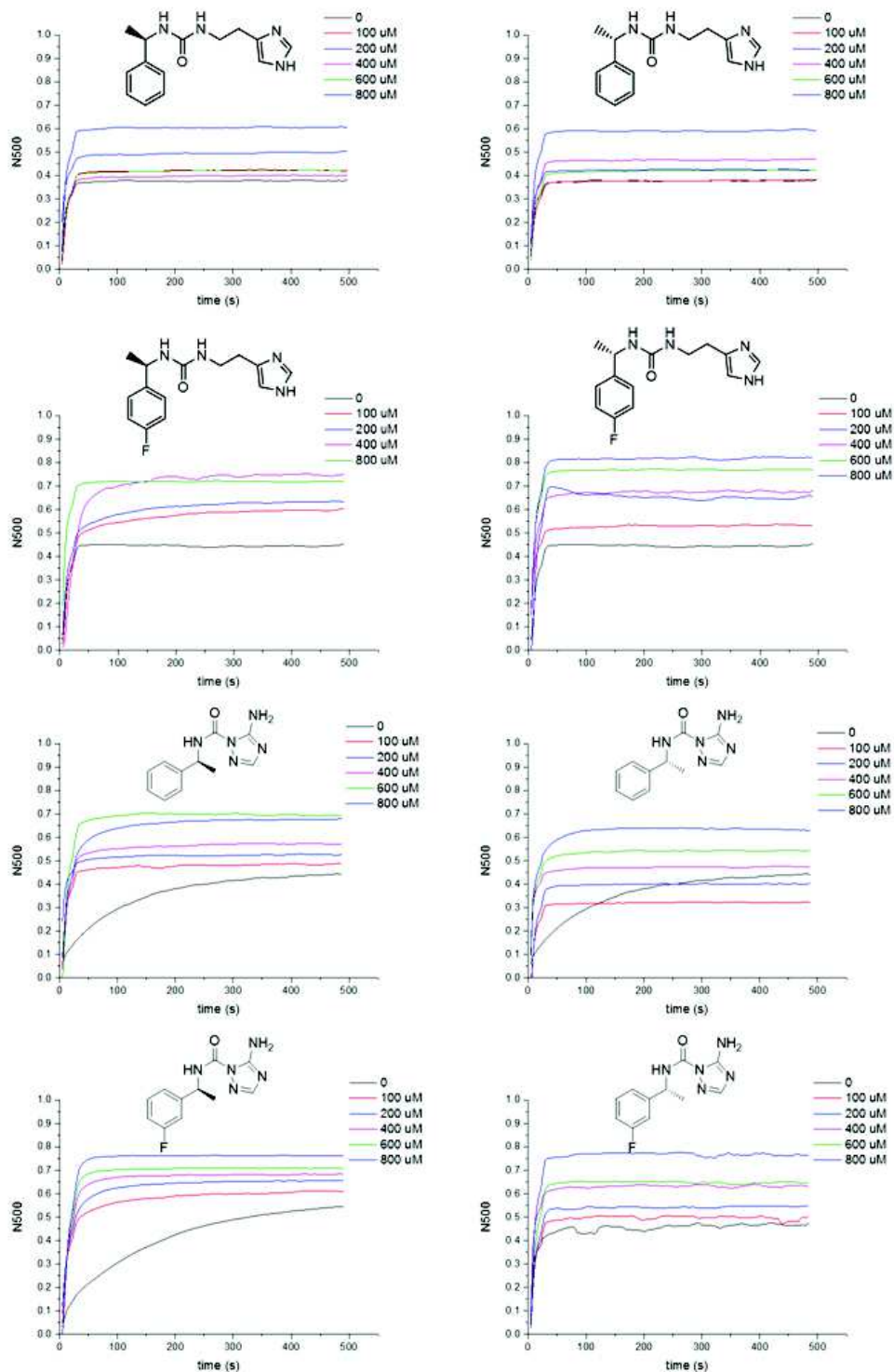


Figure 37: Ratiometric normalized fluorescence potassium transport curves of compounds 1-8. LUV suspension in PBS pH=6.4 (10mM), KCl 100mM. N500 normalized transport over 500 seconds. Compound insertion at time=-100s, valinomycin (1nM) insertion at time=-50s, NaOH (25  $\mu$ l, 0.5M) added at t=0. Fluorescent probe HPTS  $\lambda_{1ex}$ =405nm,  $\lambda_{2ex}$ =460nm,  $\lambda_{em}$ =510nm.

As in the case of ionic transport, the compounds containing the fluorine atom in the para position displayed much higher activity than the other systems tested. The histamine compounds proved to be particularly efficient, especially the S isomer (Table 8).

**Table 8: Proton transport activity**

| <i>Compound</i>           | 1  | 2  | 3         | 4         | 5    | 6    | 7         | 8         |
|---------------------------|----|----|-----------|-----------|------|------|-----------|-----------|
| <i>N<sub>max500</sub></i> | NA | NA | 0.75      | 0.82      | 0.67 | 0.62 | 0.76      | 0.76      |
| <i>Activity</i>           | No | No | Excellent | Excellent | Weak | Weak | Excellent | Excellent |

The Hill interpretation of the results was applied to the proton tests. In this case, compounds 1 and 2 present no activity and compounds 5 and 6 weak activity. The minimal activity of compounds 5 and 6 is not due to the amplitude of the signal, which is high, but to the lack of correlation between concentration and activity.

The Hill plots are presented in Figure 38 together with the calculated Hill numbers (Table 9). Consistent with the ions transport tests, the best transporters present type II channels while compounds 2 and 6 present type I channels as seen in Table 9.

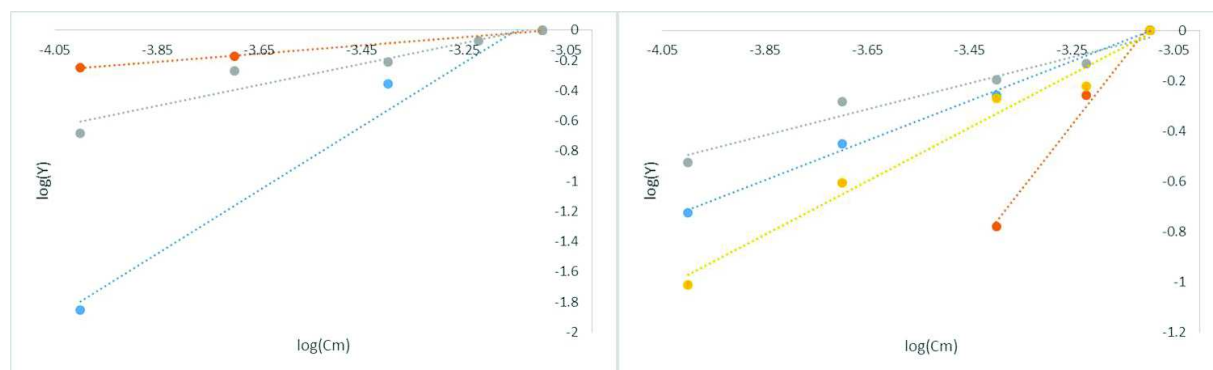


**Figure 38: Hill plots for proton transport. (Left) Blue – compound 2; Red – compound 3; Gray – compound 4. (Right) Blue – compound 5; Red – compound 6; Gray – compound 7; Yellow – compound 8.**

Table 9: Hill numbers and types of channels for proton transport

| Compound         | 1  | 2      | 3       | 4       | 5       | 6      | 7       | 8       |
|------------------|----|--------|---------|---------|---------|--------|---------|---------|
| Hill number      | NA | 2.11   | 0.276   | 0.693   | 0.786   | 2.615  | 0.520   | 1.062   |
| Type of channels | No | Type I | Type II | Type II | Type II | Type I | Type II | Type II |

The EC<sub>50</sub> values are presented in Figure 39.

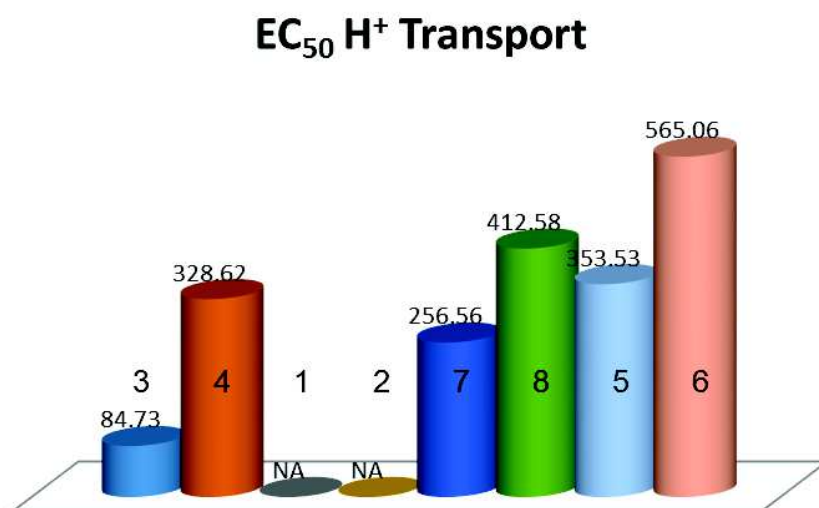


Figure 39: EC<sub>50</sub> values for proton transport. Blue – compound 3; Red – compound 4 ; Gray – compound 1; Yellow – compound 2; Dark blue – compound 7; Green – compound 8; Light blue – compound 5; Pink – compound 6

Compounds 4 and 5 presented the best activity towards protons. In this case, the EC<sub>50</sub> values are correlated directly with the activity. Namely, the critical dose for the best transporters are also the lowest critical concentrations. This observation is in contrast with the potassium transport experiments where the best transporters did not display the lowest EC<sub>50</sub> values.

### 1.3. Conclusions and Perspectives

A library of small molecules was synthesized and characterized. The compounds in the library were varied based on three features: the heterocycle moiety used, absolute configuration and the electronic density of the phenyl ring. By inserting self-assembling a motif in the molecules, urea, functional supramolecular structures were obtained. These modifications were generated so that a systematic study of ionic transport could be performed, while assessing the structure-activity relation.

The single crystal structures obtained did not present channel structures in the crystal matrix. However, transport experiments on these systems proved to be active, with variations based on their constituting atoms. The systems that present a fluorine atom have a less condensed structure, with grouped hydrophobic and hydrophilic parts. Opposed, the compounds lacking this feature, present a very compact interlocked structure.

From the eight systems tested, four proved to be better transporters over most tests. These were the compounds containing the fluorine atom on the phenyl ring. Out of these, the histamine derivatives displayed better activity towards all applications. However, the selectivity of the systems was low. The better activity of the histamine compounds is a particularly interesting observation, since it's contrary to the other observations of our group in this field. Namely, for similar structures that only differ through the heterocycle moiety, the amino triazole containing compounds were considered more active in the case of ion transport than their histamine counterparts [19], [22].

As perspectives, complementary experiments have to be done. From a supramolecular perspective, NMR titration experiments could provide valuable information regarding the interaction of the compounds with ions. The transport activity should also be described using Voltage Clamp techniques. This method, initially used in

electrophysiology, measures the potential of a planar lipid bilayer. The transport of ions through the membrane causes a change in membrane potential, which is recorded by the instrument. The resulting conductance-time plot describes the activity of a given compound. The strong suits of this method are the very good sensibility and high time resolution.

Another point that must be further investigated is the influence of the chirality of the isomers on the insertion in the lipid bilayers. No pair of enantiomers ever reached the same rate of transport for any of the given ions, suggesting a different behavior based on their conformation (R or S). In this work, these differences has been underlined for different species, when interacting with optically active substrates like lipids. In Chapter 2 an experiment involving circular dichroism techniques is presented on other compounds, in an attempt to better understand the particularity of these interactions. This behavior, related to the easiness of insertion through the membrane, could prove to be a powerful tool in optimizing the potential activity of synthetic ion channels.

# Chapter 2: Water and Proton Translocation across Vesicular Lipid Bilayers

## 2.1. Introduction

As the planet's needs for freshwater increase, the availability of this resource decreases. As such, one plausible solution would be sea the desalination of sea water. For this reason, the topic of water transport and purification becomes increasingly more important and present in the scientific community.

The technologies today are able to produce fresh water by the desalination of sea water, through industrial processes like reverse osmosis. The problem associated with these processes is the large amount of energy required for pressure filtration and thus its cost. A new approach is needed within this context, related to the use of selective water permeation or facilitated transport. Naturally occurring proteins, Aquaporins, are able to transport water through lipid membranes in mild conditions of temperature and pressure. Besides their efficiency, the selectivity of these proteins is also remarkable [40], [66].

By using the principles of supramolecular chemistry, self-assembled channels can be designed in order to replicate partially the function of aquaporins. This bioinspired approach envisions avoiding the cost related issues of the industrial water purification by taking advantage of the available natural solutions. Thus, an artificial water transport system operating on mimic cells, is a good first step towards large scale applications.

Surprisingly enough, the amount of literature on the subject of function replication of Aquaporin family is scarce. Only a few publications produced by several groups treat this subject, and will be assessed in the following sections.

### 2.1.1. Natural Water Channels: Aquaporins

Aquaporins are a distinct class of proteins which handle the transport of water through the cells' membranes. The first Aquaporin was discovered and purified by Peter Agre in 1992 [67]–[70], a discovery for which he received the Nobel prize in 2003. The first identification, however, of a mixture of proteins containing Aquaporin 1 was done in 1986 by Gheorghe Benga and his group, but who were unable to isolate it [71].

These proteins are ubiquitous in all living organisms, from bacteria to humans [70]–[74]. In mammals there are 13 distinct proteins, but more are expected to be discovered in the near future. In plants, there are five groups of Aquaporins, each with subgroups and isomeric forms [71]. To give a figure of the importance of this protein family, the human kidney filters every day 180L of dilute urine, which is then concentrated, and the metabolites are removed, while the purified water is then recirculated through the body. All this is done by Aquaporins, the kidney being the place where most types of these proteins can be found, within the cellular walls, where the largest concentration of these proteins is placed [70].

AQP1 (Aquaporin 1), is found in the cellular membrane as a group of four units, a tetramer (Figure 40) which permeates from one side to the other of the lipid bilayer. Each of the protein monomers presents one water channel. One monomeric unit contains 269 amino acid residues. Both the NH<sub>2</sub> and the COOH heads are highly hydrophilic and can be found in the cytosol of the cell.



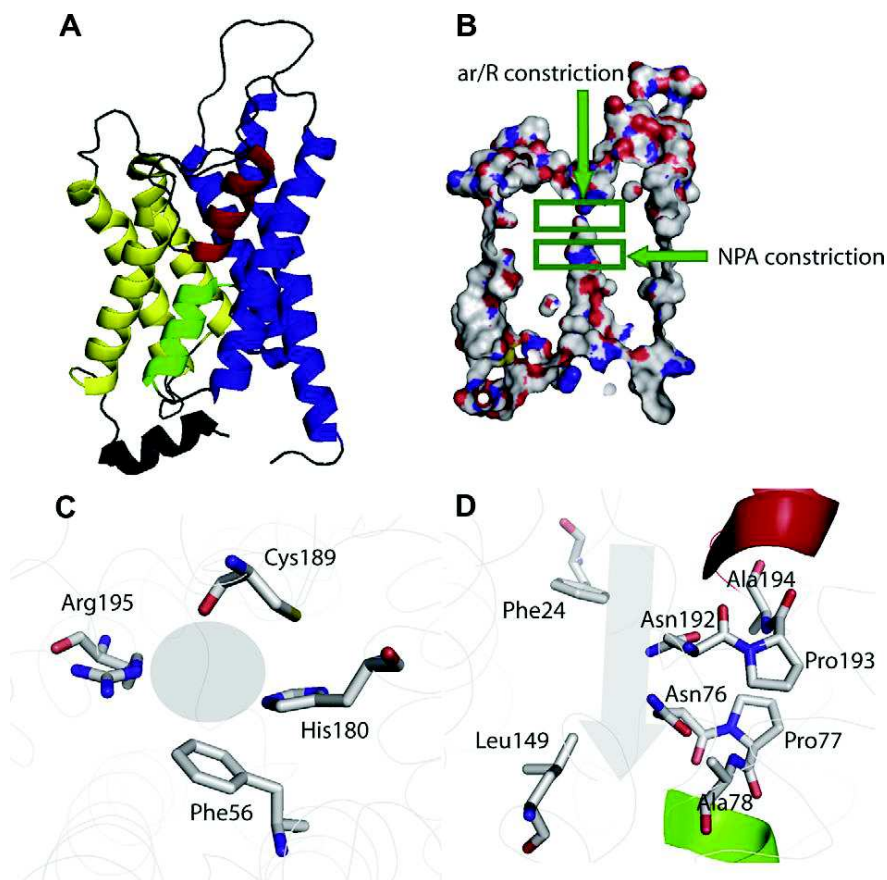


**Figure 40: Aquaporin structure: Various views of the prototypical Aquaporin (AQP1) crystal structure. (a) Cartoon of an AQP1 monomer as viewed from the side depicting the two repeated protein halves (blue and yellow helices) and the two short pore forming helices HB (green) and HE (red). The connecting loops are shaded in gray. (b) Vertical cross-section of AQP1 showing the location of the conserved aromatic/arginine (ar/R) constriction and the Asn-Pro-Ala (NPA) region. The arrows indicate the viewing direction on (c), i.e., residues of the ar/R constriction, and (d), the NPA Pharmaceutical and Medicinal Chemistry, Pharmaceutical Institute, Univ. Kiel, Germany) after the original [75]**

One monomeric unit has a structure of six  $\alpha$ -helices bundled together and five inter helical group regions, named A through E (Figure 41). Two of these loops, namely B and E contain what is called the NPA motif, a succession of asparagine-proline-alanine, to which the transporter properties are attributed. These two loops, B and E are hydrophobic, permitting a spatial arrangement in the form of a channel, through which the water circulates across the cellular membrane. The succession of amino acids in Aquaporins varies from case to case, but the active function of the NPA motif remains the same[71]. A monomer unit has a diameter of 30 Å and a height of about 60 Å.

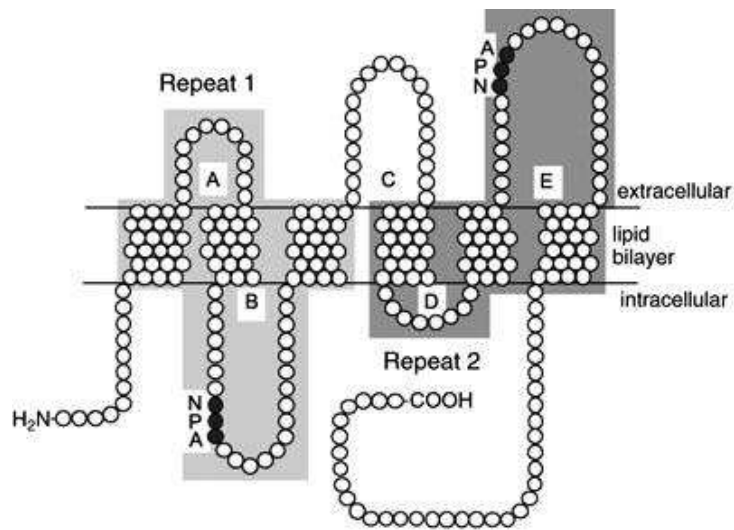


**Figure 41: Membrane orientation of AQP1 predicted from primary amino acid sequence. Two tandem repeat units of the protein each have three bilayer-spanning domains and are oriented 180° with respect to each other. The loops B and E each contain the conserved motif Asn-Pro-Ala (NPA). [70]**

It is important to note that the water transfer is made through the protein in a single file line, which implies that the channel formed through the protein's fold has to be of a precise diameter. In the case of AQP1, the channel has an hourglass shape, at its narrowest 3 Å. The size of the pores does vary from one Aquaporin to another but, in the case of AQP1, the channel is selective enough to totally block the transport of protons even, not only of ions or other chemical species.

It is also important to note the presence of the ar/R filter which confers the extraordinary selectivity of the Aquaporins. In AQP1 the filter is constituted from Arg 195, His 180, Phe 56 and Cys 189. The way in which these residues are arranged, with the arginine and histidine on one side (hydrophilic) and the phenylalanine on the other (hydrophobic) generates the 3 Å wide channel, only slightly larger than the 2.8 Å diameter of a water molecule.

As stated previously the objective is to obtain **specific** and **efficient** transport through lipid bilayers. By investigating natural solutions for the transport of water, synthetic

systems can be envisioned. These mimic the function of the natural active factors but remove their complex and fragile forms.

Evaluation of the Aquaporin channels:

- Specificity: For Aquaporins, in particular for AQP1, the specificity is very high. This is generated by the residues of amino acids called the ar/R (aromatic/arginine) filters which block all other species except for water from passing through the channel [71]. By comparison, in the case of gramicidin channel (which allows with the transport of water together with ions) specificity is very low [40]. Thus, in order to replicate the function of AQPs, steric restraints and an arrangement which can form a single file water channel, a “water wire” must be present.
- Efficiency: The active site of Aquaporins contains the NPA motif asparagine–proline–alanine. AQP1 has a calculated Arrhenius energy of less than 5kcal/mol [70] and a permeability of about  $3 \times 10^9$  water molecules per subunit per second. For comparison, the gramicidin channel’s active site is constituted of four tryptophan units. The diffusion of water through the channel is known to be of about  $9.3 \times 10^{-5} \text{ cm}^2\text{s}^{-1}$ , of which a significant part is proton conduction ( $3 \times 10^{-5} \text{ cm}^2\text{s}^{-1}$ ). The conduction of ions is done through a gramicidin channel through a column of water, differently from the single file mechanism of Aquaporins [76]. In conclusion we can attribute the activity to an effector, which is a plurality of amine functionalities, and a structure which spatially defines the molecule, that has to be hydrophobic.

### 2.1.2. Synthetic Approaches

The interest on the selectively enhanced water transport subject is growing, since the sources of fresh water are limited and desalination processes are usually expensive. A synthetic approach offers, of course, the advantages of industrial production and of better stability compared to the naturally occurring proteins. Yet little progress has been made, literature mentioning only very few approaches. These will be presented lower [13]-[14]. The aim of this research is a channel that displays an efficiency as close as possible to that of the proteins, while maintaining the selectivity towards metallic ions [21], [70], [77]–[92].

It should be mentioned that there are several attempts on integrating proteins into artificial matrixes. Yang et al [93] reviewed these and underlined the two major constraints of this approach: finding a suitable matrix and the practical amounts in which the protein can be isolated. Kumar et al [94], [95] have explored this route and published in 2012 the results of this type of assay. By replacing a lipid bilayer membrane with amphiphilic block copolymers (BCPs), they were able to successfully and functionally insert the less-specific Aquaporin, AQP0. It must be noted that the performance per molecule of AQP0 is much lower ( $2.5 \times 10^{-15} \text{ cm}^3/\text{s}$ ) than that of AQP1 ( $1.17 \times 10^{-13} \text{ cm}^3/\text{s}$ ) or AQPZ ( $\sim 1 \times 10^{-13} \text{ cm}^3/\text{s}$ ) in terms of water permeability. The BCP vesicles presenting functioning AQP0 channels had a water permeability of  $1409 \pm 409.5 \times 10^{-6} \text{ m/s}$  up from  $189.7 \pm 61.3 \times 10^{-6} \text{ m/s}$  for the vesicles without the protein channels. Thus the concept has been proven, however the applications are yet very limited.

### 2.1.2.1. Dendritic Peptides

One of the first successful attempts of creating artificial water channel was published in 2007 by Kaucher et al.[80]. They used a stabilized dendritic peptide (6Nf-3,4-3,5)12G2-CH2-Boc-L-Tyr-L-Ala-OMe, which, in bulk is able to form channels in lipid bilayers. The structure formed is reported to be 82.3 Å with a pore diameter of  $14.5 \pm 1.5$  Å. The methods employed to prove transport were: fluorescence techniques and a microscopy technique applied to GUVs (giant unilamellar vesicles). This technique consists in filming the evolution of the volume of water in a micropipette tip in contact with the lipid bilayer of the GUV containing the active compound. These channels are described as being selective against metallic ions like sodium and potassium but permeable to water and protons (which are excluded by Aquaporins) (Figure 42). It also must be noted that, since the date of this paper, the methods employed in measuring water transport across lipid bilayers have become more standardized.

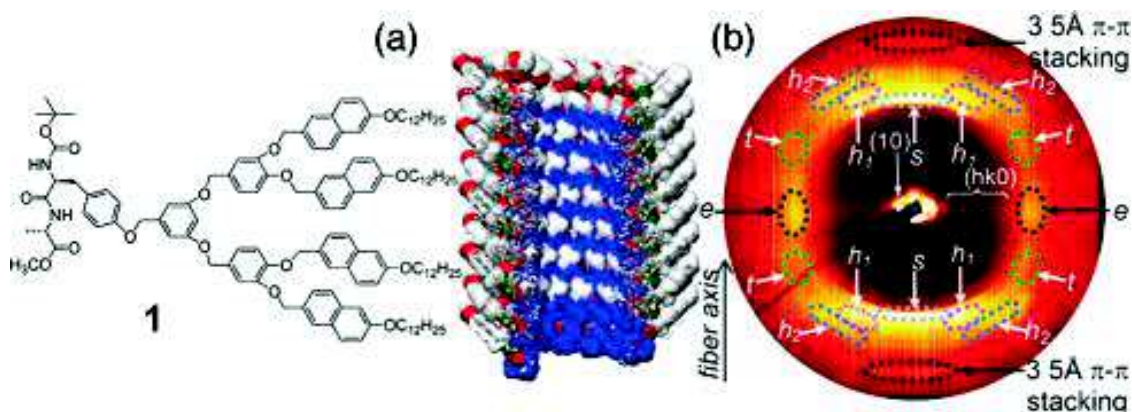
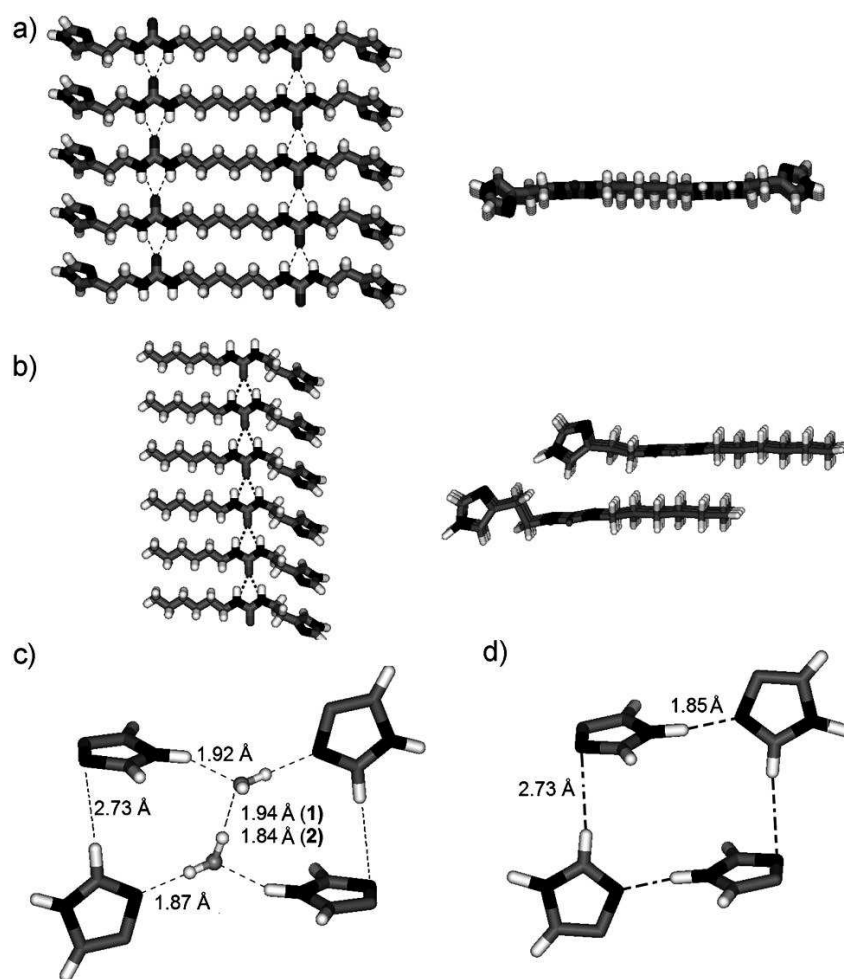


Figure 42: (6Nf-3,4-3,5)12G2-CH2-Boc-L-Tyr-L-Ala-OMe (1). (a) Cross section of the helical pore assembled from 1. Color code: -CH<sub>3</sub> of the protective group of Tyr, blue; -CH<sub>3</sub> of the methyl ester of Ala, white; C, gray; O, red; N-H, green. (b) Wide angle XRD of an oriented fiber of the helical pores assembled from 1. [80]

### 2.1.2.2. Imidazole Quartet

Barboiu et al. [22] reported a simple supramolecular structure able to perform water transport across lipid bilayers. This is achieved by using a urea motif and imidazole moieties as active parts of the system. The urea motif generates hydrogen bonds, organizing so called “urea ribbons”, while the imidazole self-organizes in units of 4, an I4 quartet. Alkyl chains are present on the opposite head of the molecule in order to generate an amphiphilic character to the species. The resulting self-assembled structure is in fact a supramolecular water channel. This system has a good compatibility with lipid bilayers through its hydrocarbon chain backbone (lipophilic part) and hydrophilic heads through the imidazole moieties (lyophobic part). The published systems are displayed in Figure 43.

The channel diameter is calculated to be 2.6 Å, very similar to the selective AQP 1 channel pore dimensions. This also implies that, as is the case of the Aquaporins' channels, it is not permeable by ions, which present larger radii than water. These findings were supported by X-ray single crystal diffraction, dynamic light scattering and fluorescence assays. The constants for water transport are  $k_{I4}=1.2 \times 10^{-3}$  for the active compound versus  $k_{DMSO}=8.7 \times 10^{-5}$  for the DMSO blank sample. The similarity to the AQP channel presumes ion selectivity, fluorescence studies proved a rejection effect over cations.



**Figure 43: Solid-state structures of a) 1 and b) 2: side and top views in stick representation (N, black, C, gray, O, light gray, H white) of continual planar arrays of the H-bonded urea ribbons. c) Water assisted formation of I-quartet “open form” through CH $\cdots$ N and NH $\cdots$ O H-bond interactions. Water molecules in ball-and-stick representation are H-bonded through OH $\cdots$ O interactions. d) Formation of I-quartet “off form” through CH $\cdots$ N and NH $\cdots$ N H-bond interactions in the absence of water. [22]**

### 2.1.2.3. Hydrazide Functionalized-[5] Pillar Arene Derivatives

Xiao-Bo Hu et al[96] reported in 2012 that hydrazide-appended pillar- [5] arenes are species able to form unimolecular water channels. The molecules display the propriety of coiling in the form of a tube using supramolecular interactions like hydrogen bonds. Through this a channel is formed. The resulting channels are selective against

protons, similar to natural occurring Aquaporins. However the mechanism is quite different, as single file transport of water is not possible along the channel. Discontinuous files were observed along the tubular structures. The methods employed for the characterization of the water channels are fluorescence based vesicular methods (LUVs), while the interactions with water are characterized through X-ray single crystal diffraction.

The performance of these channels is reported to be  $8.6 \times 10^{-10}$  cm/s in terms of water permeability. This is achieved at relatively low compound concentrations, which vary from 0.027%-0.45% (mol %) vs. lipids amount. The above permeability was obtained for a concentration of 0.3% mol (Figure 44).

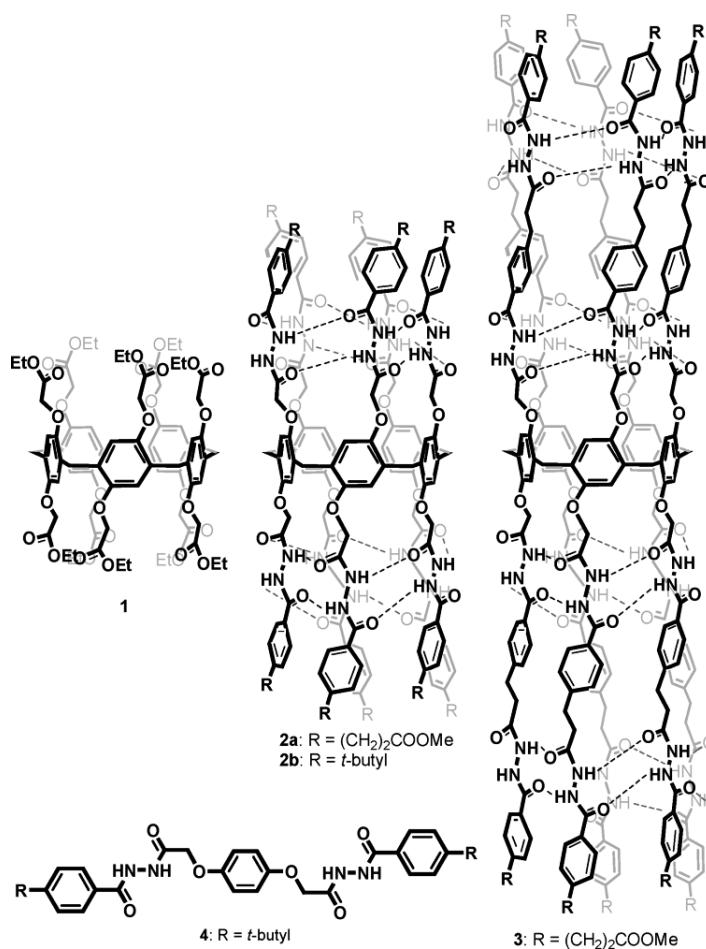


Figure 44: Structures of compounds constituting the water channels. [96]



### 2.1.3. Objectives and Methods Employed

As stated before, the objective of this project is the design of a functional class of self-assembled water channels. These should display efficiency and selectivity as close as possible to that of Aquaporins.

The compounds synthesized kept the general structure and observations made previously by our group. A library was designed around the concept of the I4 quartet. These molecules self-assemble using the urea-ribbon motif into supramolecular structures. By varying the constituent elements of the molecules, the resulting supramolecular structures are different, allowing a study of activity as a function of them. The chain length and the absolute configuration were varied throughout the library, allowing for a more systematic study of the matter at hand.

For the characterization of the compounds, NMR and mass spectrometry were used in the determination of the chemical structure and composition. X-ray single crystal diffraction was employed for describing the supramolecular self-assembled structures of the species and as a theoretical model.

In the case of water transport two methods were used, dynamic light scattering (DLS) and light-scattering stopped flow techniques. The proton transport experiments and the ion selectivity were performed using fluorescence methods as well as through fluorescence stopped flow techniques. Supporting tests were done using circular dichroism. Large Unilamellar Vesicles (LUVs) were used in correlation with all these techniques in order to provide a similar assay to that of using real, natural cells. The composition of the LUVs was changed according to the experiment undertaken. While for fluorescence methods simple PC was used in the case of all stopped flow techniques a composition of L- $\alpha$ -phosphatidylcholine (PC): L- $\alpha$ -phosphatidylserine (PS): Cholesterol (Chl) [97] in a ratio of 4:1:5 was used.

## 2.2. Molecular Simulations on the HC6 Channel

The HC6 system previously reported by our group [22] was very recently described using computational chemistry methods. These simulations were performed by Marc Baaden and Samuel Murail at Université Denis Diderot Paris 7.

They investigated the I4 water channel formed from HC6 molecules over 250ns with variations of the lateral pressure on the channels. These pressures were of -10, 0, 10 and 100 atm. The starting structure chosen for the calculations was based on the atom positioning of the crystal structure of HC6. A small system was used (about 61000 atoms), in a model membrane with a composition of phosphatidylcholine (POPC): phosphatidylserine (POPS): cholesterol (Chl) of 4:1:5. The results of these simulations are presented in Figure 45.

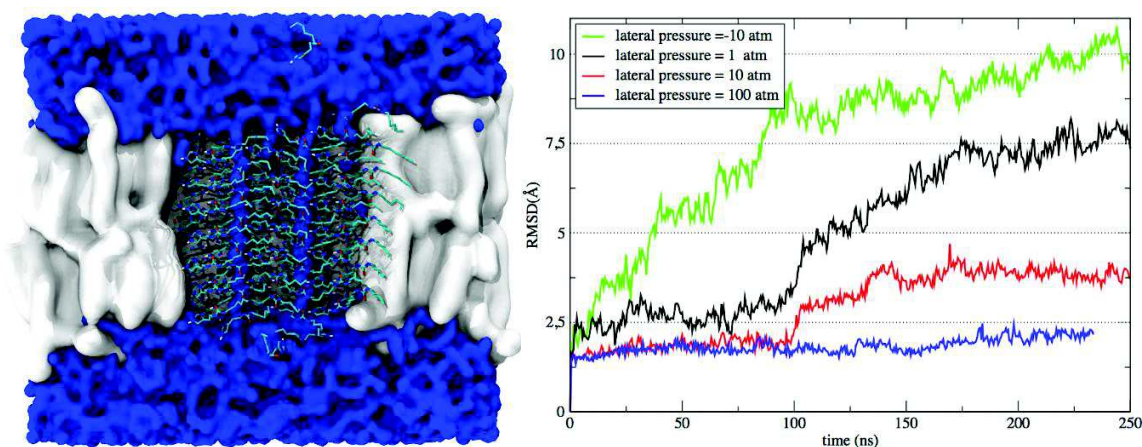


Figure 45: On the left, a typical cross-section of the HC6 simulation systems illustrates how water (blue surface) connects through artificial channels traversing the HC6 aggregate (atom-colored licorice representation) held together by the membrane (white surface). On the right, the structural drift measured as RMSD is shown for the first 250 ns of the pressure-dependent simulations at -10, 1, 10 and 100 atm. Courtesy of Marc Baaden and Samuel Murail

Figure 46 shows the theoretical aspect of the water channels formed by the HC6 in simulations, laterally sealed by the membrane. The higher the applied pressure, the closer the simulation remains over time (250ns) to its starting structure. Only half of the HC6 molecules are shown, concentrating on the « stable » ones and discarding the very mobile second half of these molecules.

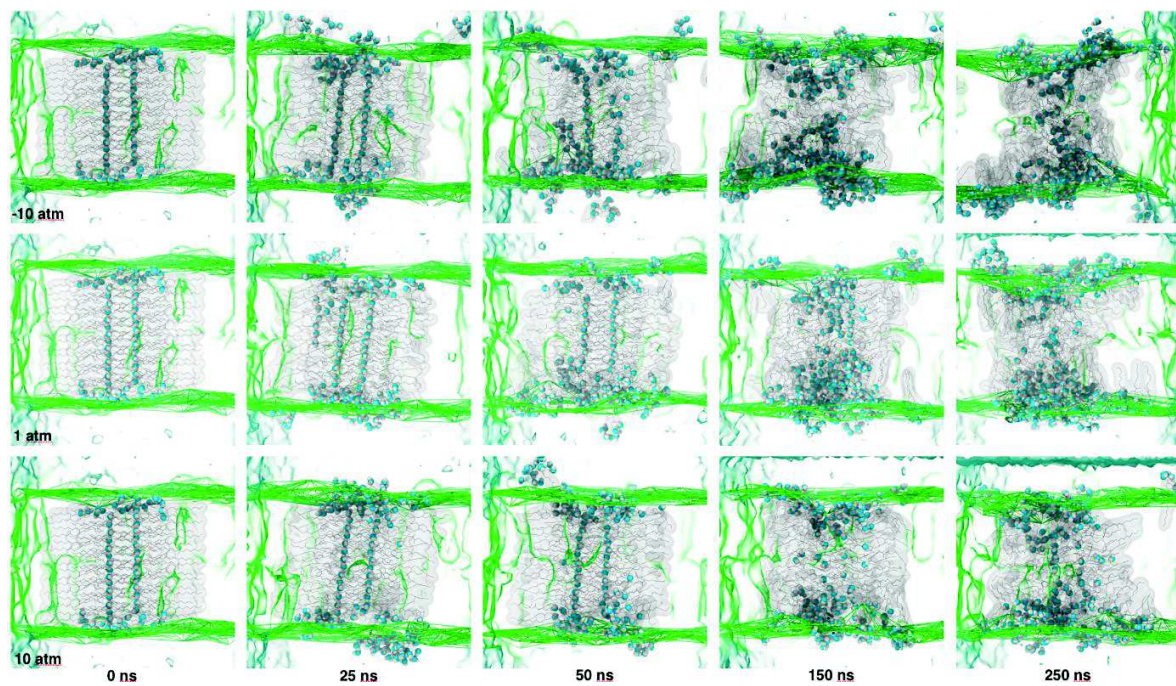
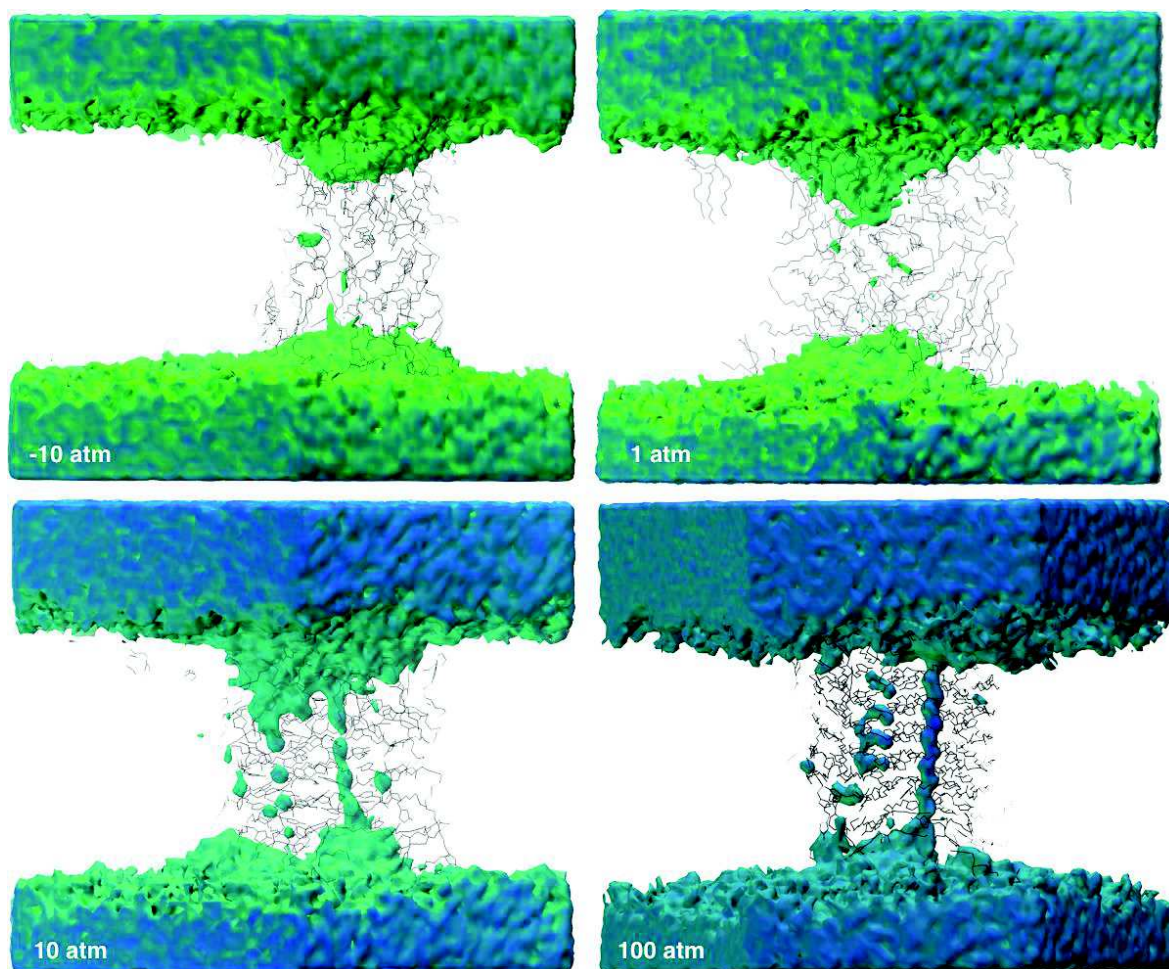


Figure 46: Temporal snapshots of the three pressure-dependent simulation systems at -10, 1 and 10 atm. Data for 100 atm is not shown.



**Figure 47: Water density in the 200-250 ns period of the pressure-dependent simulations shown as isosurface. The HC6 aggregate is shown as black lines. The membrane is omitted for clarity.**

Figure 46 shows initial, intermediate and final structure snapshots for three simulations. Visual inspection shows that both initial water channels are lost after around 90, 103 and 109 ns, for the systems at -10, 1 and 10 atm pressure, respectively. Still, in the simulation at 10 atm, a distinct planar area remains water filled with renewing formation of water wires. In the simulation at 100 atm (not shown) the channels are much better preserved, one is fully intact at the end of the simulation, the other has started to unstructure and loose some of its water. This is nicely visible in Figure 46.

Figure 47 depicts the water density during the 200-250 ns period of each simulation and confirms that increasing pressure stabilizes water within the HC6

assembly. While one water wire density is clearly visible in the simulation at 10 atm, both wires are still identifiable at 100 atm, with one of them being perfectly formed. Although the simulation at 1 atm has less water structure, it contains globally more water molecules than at other pressures but these water molecules are more dispersed than at 10 or 100 atm, where internal structuring is visible.

Water flow, i.e. single water molecules crossing the membrane completely by traversing the I4 assembly, was observed on a few occasions in these simulations, yet is difficult to characterize quantitatively.

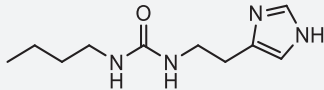
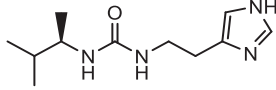
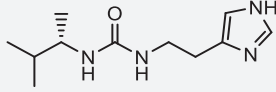
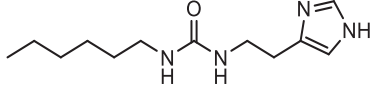
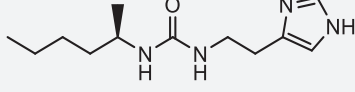
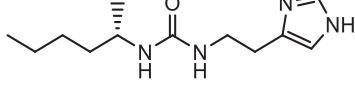
In conclusion the HC6 structure stays confined within the membrane region throughout all simulations, even though a few HC6 molecules may diffuse away in the bilayer. The system stabilizes water within the membrane environment only at higher pressure values. The stability of the system is influenced by the size (surface-to-volume ratio) of aggregates, by lateral pressure on the membrane and possibly by the peripheral packing of cholesterol molecules. Higher pressure favors structuring of water wires and stabilizes the structure of the aggregate. The observed cholesterol stabilization effect is not sufficient to hold together the small aggregates studied in this exploratory study. Under the conditions (size of aggregates, pressure, etc.) tested here, the tubular I4 structural arrangement is not preserved within bilayers. The aggregates tested here are probably too small (and hence unstable) to reproduce the real water permeation phenomenon measured experimentally. Much larger assemblies should be tested for this. However the physicochemical observations for it acting as a pressure-dependent water reservoir, eventually with structured water wires traversing the membrane, should hold. Even for the small systems tested here (<65000 atoms), the several hundred nanosecond timescale seems not sufficient to fully stabilize. The characteristic timescale for this system must therefore lie in the microsecond range or beyond. The simulations provide first insight about the dynamic behaviors of water molecules under confined conditions.

## 2.3. Experimental Results

### 2.3.1. Description of Compounds

Based on the initial findings presented in Leduc et al [22], homologous structures have been designed varying the chain length and their optical activity in order to have a systematic study over the transport proprieties they display. Along with HC6 and HC4 which have been synthesized and characterized by Yann LeDuc, the compound library was extended with related compounds. These are presented in Table 10.

**Table 10: List of compounds synthesized**

| NR. | STRUCTURE   | NAME   | MOLECULAR FORMULA                                | CODE |
|-----|---|--|--|------|
| 1   |  | 1-(2-(1H-imidazol-4-yl)ethyl)-3-butylurea                    | C <sub>10</sub> H <sub>18</sub> N <sub>4</sub> O | HC4  |
| 2   |  | (R)-1-(2-(1H-imidazol-4-yl)ethyl)-3-(3-methylbutan-2-yl)urea | C <sub>11</sub> H <sub>20</sub> N <sub>4</sub> O | RHC5 |
| 3   |  | (S)-1-(2-(1H-imidazol-4-yl)ethyl)-3-(3-methylbutan-2-yl)urea | C <sub>11</sub> H <sub>20</sub> N <sub>4</sub> O | SHC5 |
| 4   |  | 1-(2-(1H-imidazol-4-yl)ethyl)-3-hexylurea                    | C <sub>12</sub> H <sub>22</sub> N <sub>4</sub> O | HC6  |
| 5   |  | (R)-1-(2-(1H-imidazol-4-yl)ethyl)-3-(hexan-2-yl)urea         | C <sub>12</sub> H <sub>22</sub> N <sub>4</sub> O | RHC6 |
| 6   |  | (s)-1-(2-(1H-imidazol-4-yl)ethyl)-3-(hexan-2-yl)urea         | C <sub>12</sub> H <sub>22</sub> N <sub>4</sub> O | SHC6 |

|   |  |  |           |      |
|---|--|--|-----------|------|
| 7 |  | 1-(2-(1H-imidazol-4-yl)ethyl)-3-octylurea            | C14H26N4O | HC8  |
| 8 |  | (R)-1-(2-(1H-imidazol-4-yl)ethyl)-3-(octan-2-yl)urea | C14H26N4O | RHC8 |
| 9 |  | (S)-1-(2-(1H-imidazol-4-yl)ethyl)-3-(octan-2-yl)urea | C14H26N4O | SHC8 |

The synthetic route for the compounds in question is quite simple and straight-forward, a one-step synthesis between the corresponding isocyanate and the amine, histamine, as seen in Figure 48. The yields are practically quantitative. The protocol for their synthesis is presented in the annexes.

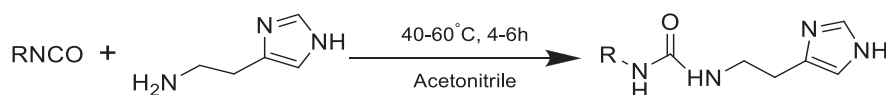


**Figure 48: General reaction scheme. R= corresponding hydrocarbon chain**

All compounds tested were characterized through the appropriate methods, NMR and mass spectrometry and the results of these analyses are presented in the annex. These compounds were described by single crystal X-ray diffraction and were subjected to appropriate methods in order to describe their transport capabilities for water and protons.

The X-ray single crystal structures provide a very good understating on the active system throughout the library of compounds. All the crystals in the library were obtained in pure water, in order to maximize the chances of obtaining suprastructures that present sterically hindered water. As stated, the amphiphilic nature of the molecules is given by the lipophilic tail as well as the polar imidazole head. The urea motif is generated in order to assist the self-assembly of the molecules in supramolecular structures. As presented earlier, imidazole containing compounds display the I4 quartet, made of four individual units. These do present a type of polymorphism when it comes to the spatial orientation of the units when water molecules are found in the formed channels. The infinite packing

of a compound forming a channel with the I4 motif, reveals a continuous file of water molecules, the so called water wires. The water molecules present a type of pseudo permanent dipole, meaning that their orientation is the same throughout the channel. This forces the imidazole moieties to adapt in order to accommodate this polarized water, adding a supplementary degree of order to the supramolecular structure. Depending on the system several conformations can be achieved as seen in Figure 49.

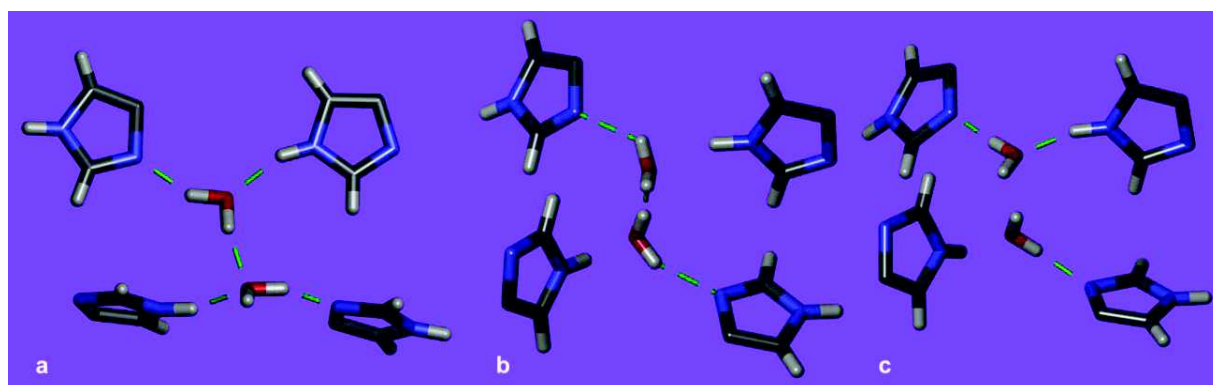


**Figure 49: polymorphism of the I4 quartet. a – I4 generated by HC6 specie; b – I4 generated by RHC8 packing (type I, majoritarian); c – I4 generated by RHC8 (type II, minoritarian). Crystals obtained in pure water.**

Crystals of the members of the library can be used to give an initial hint on the link between structure and activity. Starting from the shortest member, HC4, we can see a packing pattern that is entirely composed of urea-imidazole hydrogen bonding. The molecules have a head to tail arrangement creating a very dense structure. The binding doesn't create an I4 quartet but a semi-dimeric pseudo-polymeric structure. This type of semi-dimeric structure provides unfavorable conditions for the insertion of other species. The X-ray packing of HC4 can be observed in Figure 50.



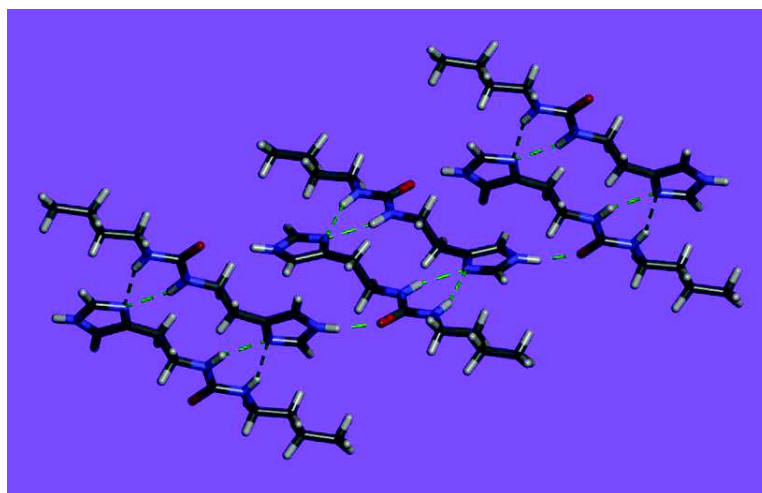


**Figure 50: X-ray single crystal structure of HC4, packing. Crystals obtained in pure water.**

The next compounds in the series, RHC5 and SHC5 present a different type of packing. Here the urea motif generates a ribbon type structure on the c axis, while the imidazole moieties are hydrogen bonded to each other. The optical center forces hydrophobic interactions in the form of an arrow-like pattern. The packing here is also very condensed, and the I4 quartet is not formed, or we could assume its structural collapse based on the ramified hydrocarbon chain. This structure could be considered the opposite of the systems that form channels, as a consequence of the hindrance generated by aliphatic part of the molecule. The X-ray packing of SHC5 can be observed in Figure 51.

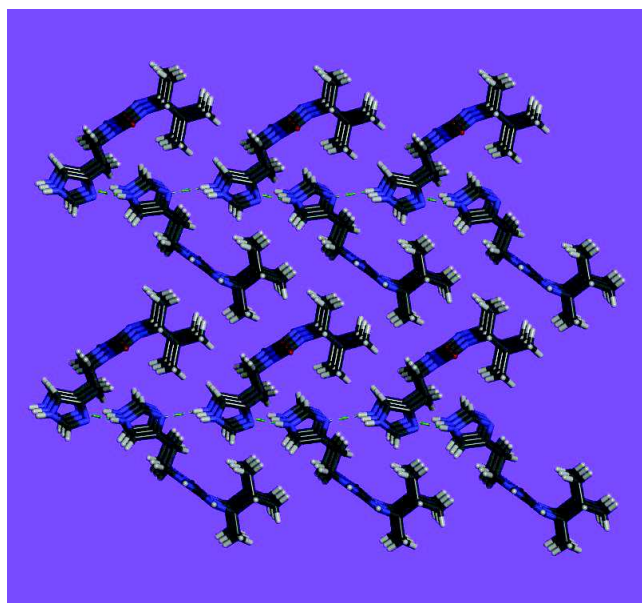


Figure 51: X-ray single crystal structure of SHC5, packing. Crystals obtained in pure water.

The X-ray structure of HC6 was discussed in detail in reference [22]. It is worth mentioning that HC6 is the shortest member that generates a water channel. This channel is presented transversally in Figure 52. The water is hydrogen bonded by four imidazole units, the I4 quartet.

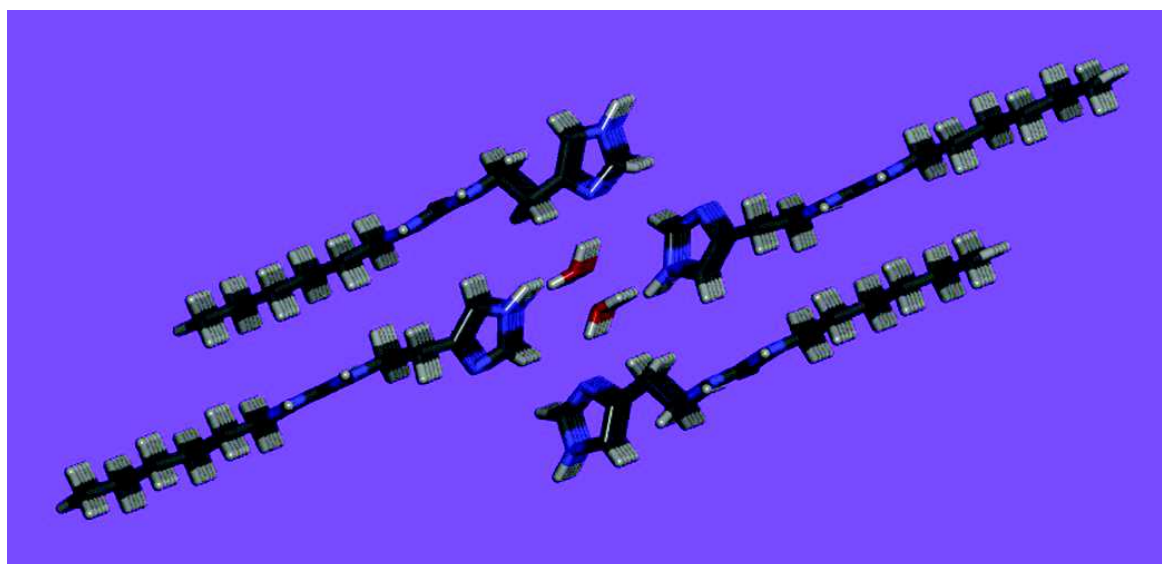
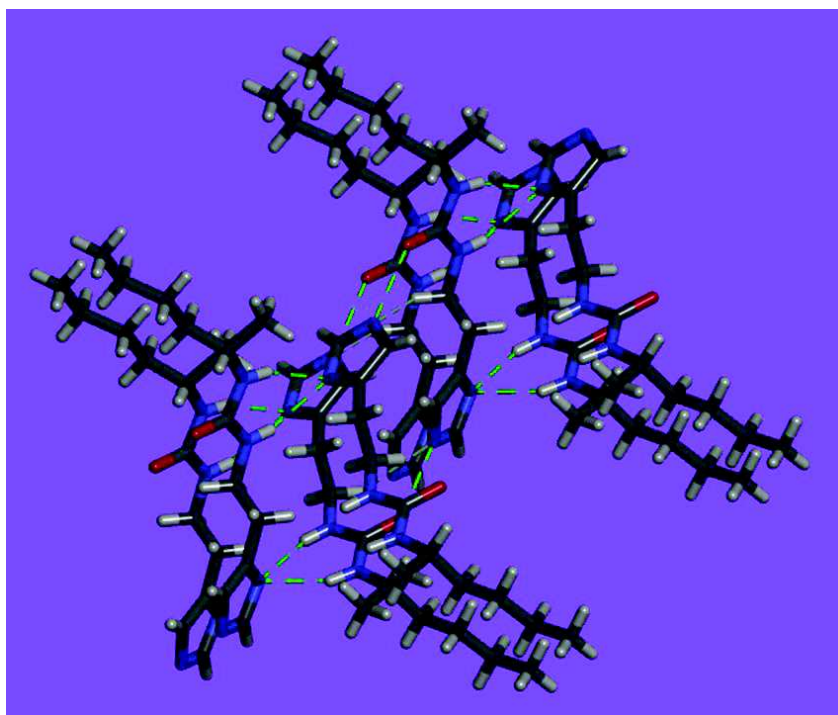


Figure 52: X-ray single crystal structure of HC6, packing. Crystals obtained in pure water.

R and SHC6 present a head-to tail packing, with imidazole-urea hydrogen bonding. Although the alkyl chain has the same length as in the case of HC6, the interactions between the elements of the molecule are completely different. The optical center acts like a spacer elongating the distance between two molecules, with a succession up/down of the methyl groups between two neighboring molecules. The resulting packing has a zig-zag shape and does not present the I4 quartet. As a consequence of the length of the chain the structure is less crowded, but no cavities are formed. The packing of SHC6 is presented in Figure 53.



**Figure 53: X-ray single crystal structure of SHC6, packing. Crystals obtained in pure water.**

The linear HC8 molecule present a pattern very similar to the HC6 structure. Here, the I4 quartet is formed and the water is entrapped within it. As in the case of HC6 the hydrophobic tails are arranged linearly opposite of the I4 quartet. The water wires generated are oriented with a permanent pseudo-dipole moment. This structure can be seen in Figure 54.

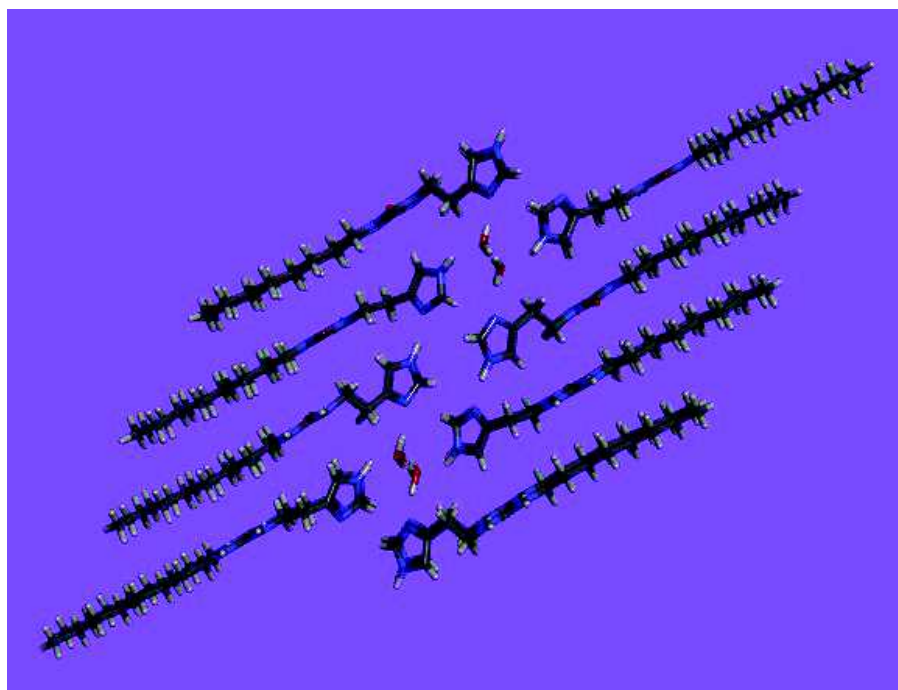
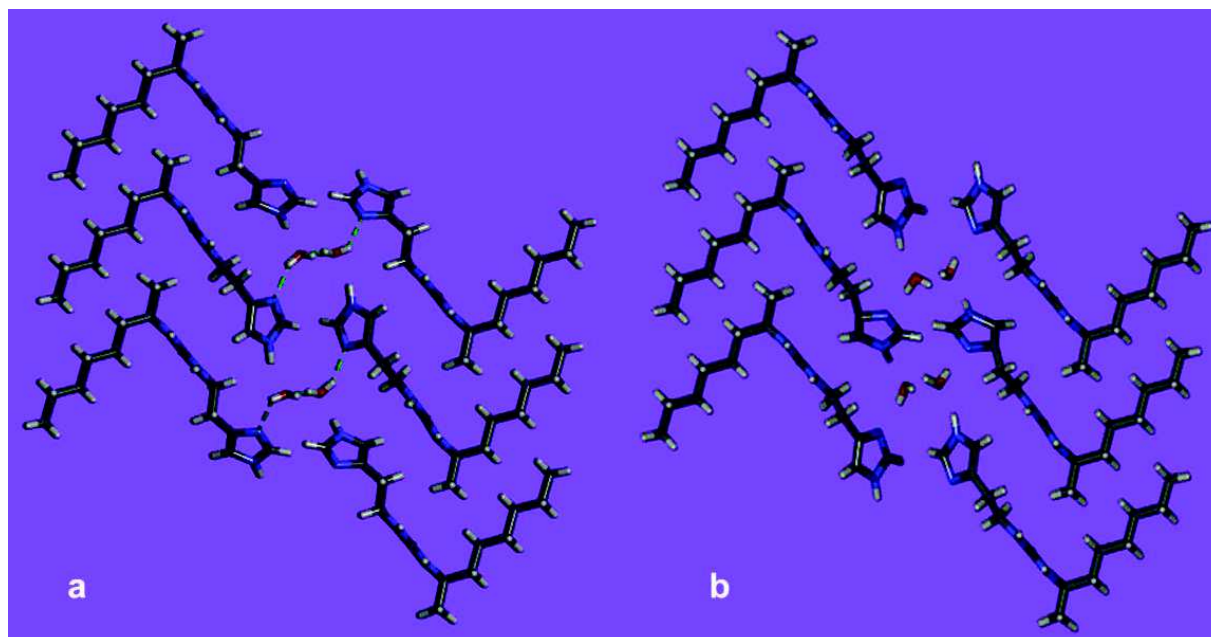


Figure 54: X-ray single crystal structure of HC8, packing. Crystals obtained in pure water

S and R HC8 present a channel type structure. The packing of RHC8 is presented lower, with its two isomorphous forms. In comparison to the SHC6 structure there are differences worth pointing out. The packing is comprised by two chains of molecules, one ascending and one descending. The chiral centers go along this trend being on either one or the other side of the channel, as opposed to the alternating positioning of the SHC6 structure. The I4 quartet is well represented in both morphologies containing two oriented molecules of water per quartet. Compared to the HC6 and HC8 channels in which the I4 quartet is almost plane, the I4 displayed by RHC8 is spatially distributed on the three axes. The two morphologies are different by the relative position of the imidazole moieties, the first one accounting for 80% and the second for 20%. In both, the water molecules present fixed orientations, leading to the conclusion that the polymorphism encountered is a form of the system to adapt to the guest molecule. The packing of the two RHC8 morphologies is presented in Figure 55.



**Figure 55: X-ray single crystal structure of RHC8, packing along b axis. (Left) the first morphology, 80% of the structure and (Right) the second one 20% of the structure. Crystals obtained in pure water.**

Regarding the compatibility with the structure of a lipid bilayer, it's intuitive why a structure like the one displayed by RHC8 would be favored for insertion, compared to HC6 and HC8. The angle, described by the hydrophobic chain, is compressing the total width of the structure in the case of RHC8 while, for HC6 and HC8 the modifications that the membrane should adopt would be significantly greater in order to fit the completely linear structure.

While the X-ray diffraction data does not provide certainties regarding the interaction of the supramolecular channels with the LUVs, it does constitute a good starting point for theoretical considerations.

The affinity between a specific compound and the bilayer is a primary consideration that must be taken into account. For example, the amphiphilic nature of the membrane would better suit species that have a longer hydrocarbon chain. On the other hand, the length of the chain limits the compound's solubility in aqueous solutions, where the experiment concerning the suspension of LUVs takes place. The dynamic nature of

the channels implies that they can be formed and unformed within the bilayer. As a consequence, just like in the case of the ionic channels, the formation of the channels can't be specifically characterized. In turn, the effect of the channels over the substrate, in other words, its effect, can be registered and well described. This principle is applied to all the methods used, where the activity of the supramolecular structures is observed and calculated, as the formation of such structures cannot be.

### 2.3.2. Water Transport Experiments

Our initial attempt was to describe the water transport phenomenon by means of Dynamic Light Scattering (DLS). DLS is a very useful technique in describing the size (and not the charge, or the surface rugosity, etc...) of small particles (between 5 nm & 1 $\mu$ m) in suspension.

In DLS, a laser is passed through the probe contained in a cell. When a polarized beam of light passes through a medium containing particles, these are subsequently hit and the light diffracts in all directions. This diffraction is then registered on a screen. By repeating this process at known intervals of time the images formed on the screen become a pattern.

The mathematics behind the method is quite complex. The interpretation of the result relies on Rayleigh scattering (when the particles are small compared to the wavelength of the laser). The system also accounts for the Brownian movement of the molecules. The auto correlation function of the system is a single exponential decay in the case of a monodisperse population. In the case of polydisperse populations a sum of exponential decays is applied for each population. The processing of this data is then done using either a cumulant method, or a CONTIN algorithm. The first method is applied for a population with high homogeneity and involves the summing of the exponentials, while the CONTIN analysis is done through an inverse Laplace transform, and is used for very heterogeneous samples. The latter is a high resolution method. For our experiments

the CONTIN analysis was used in order to determine the heterogeneity of the sample (if any).

$$g^2(q, \tau) = \frac{\langle I(t)I(t + \tau) \rangle}{\langle I(t) \rangle^2}$$

The equation describes the autocorrelation function at a particular wave vector,  $g^2(q, \tau)$ ,  $q$  is the wave vector,  $\tau$  is the delay time,  $I$  is the intensity,  $\langle \rangle$  denote the expected value operator.

The experiments were performed according to the following protocol. In 1880  $\mu$ l of pure MilliQ water, 100  $\mu$ l of LUVs, containing 10mM PBS and 100mM NaCl, were added directly in the cell. An initial measurement was performed in order to have a referential of the size, before the adding of any modifier. After the first measurement, 20  $\mu$ l of DMSO containing the channels solution or just DMSO (as a blank sample) were injected in the cell. Immediately after the sample was measured. Timed experiments were performed over the course of 1500s, registering the modification of the diameter of the LUVs. The samples were mixed between experiments in order to maintain homogeneity.

By exposing the vesicle suspension to a hypotonic solution (pure water) the transport of water inwards is expected to work against the concentration gradient. The inflow of water leads to an increase in volume and thus an increase in diameter. The diameters of the vesicles were referenced to the initial diameter (%D/D0) both for the active compounds and for the blank sample. The entire library was tested in this fashion and in Figure 56 the results of the HC8 series are presented.

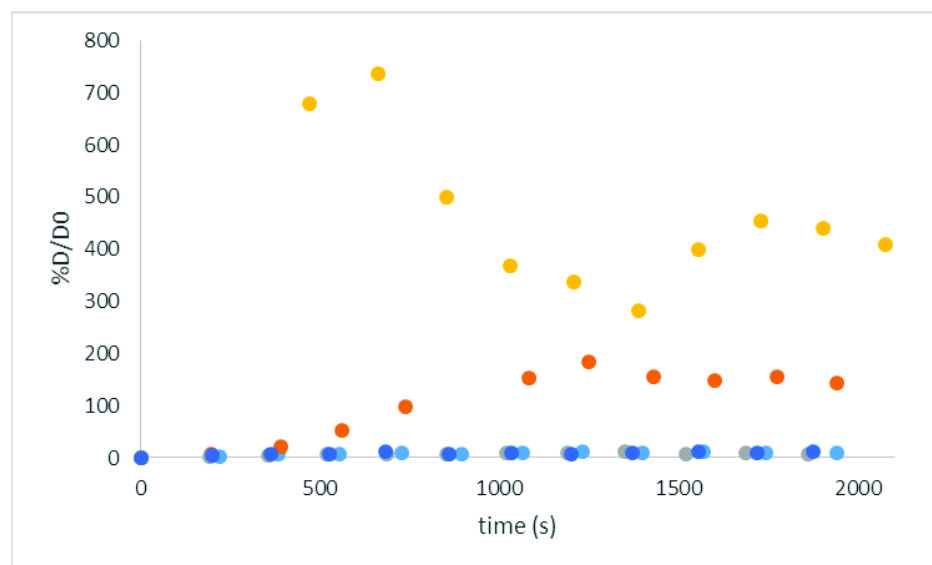


Figure 56: Variation of LUV size over time using DLS methods for HC8 and its isomers. Internal solution PBS pH=6.4 NaCl 100mM, 10 mM, external solution MilliQ water. Light blue – RHC8; Orange-SHC8; Gray – racemic mixture of R&S HC8; Yellow - HC8, Dark blue – blank sample, DMSO (CM=0). Compound concentration in solution 300 $\mu$ M

As expected, a sharp increase is observed for the linear HC8 species, as well as for the S isomer of the series. However, by repeating the measurements it became clear that the increase is not constant in each experiment series, and thus the technique is not suitable as a quantitative method. This method only provides a qualitative merit. A similar observation was also recently reported [98]. The results of two experiments made on the same date and on the same batch of vesicles for HC8 are presented in Figure 57. Both series of measurements present an increase in diameter, but since the reproducibility is low, a quantitative calculation becomes unsuitable.



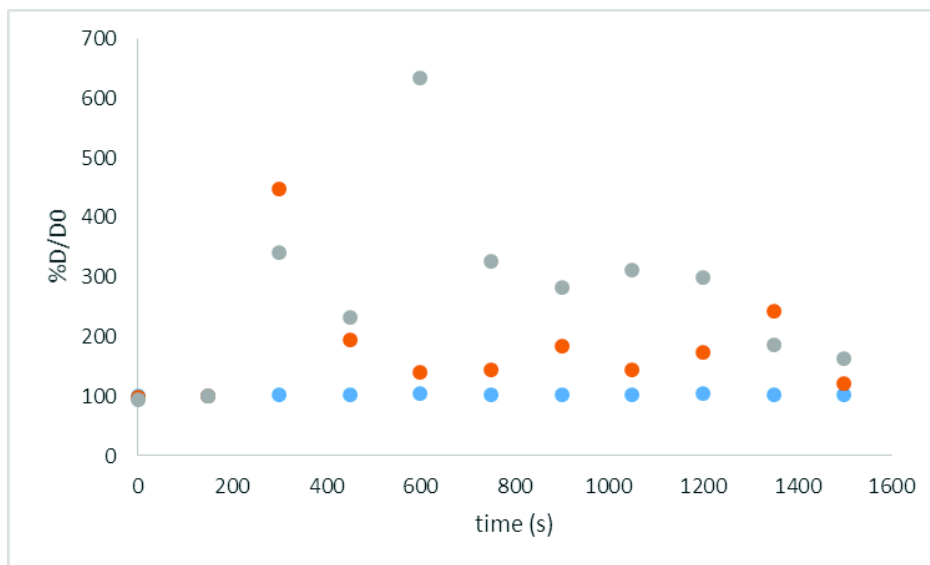
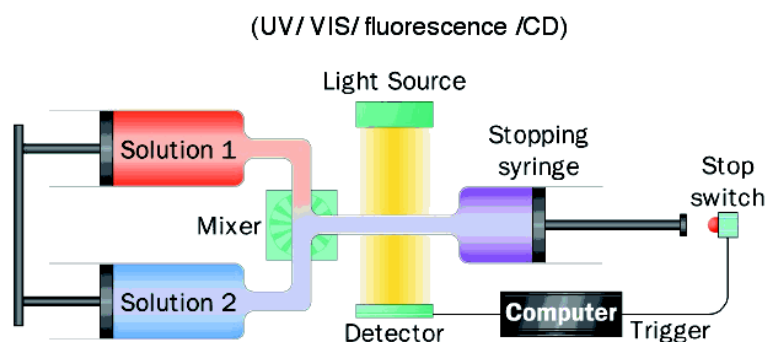


Figure 57: DLS experiments performed on HC8. Internal solution PBS pH=6.4 NaCl 100mM, 10 mM, external solution MilliQ water. Light blue – DMSO; Orange- HC8, series I; Gray – HC8 series II. Compound concentration in solution 300 $\mu$ M

A new method of describing the phenomenon was needed, and it was found in the form of light scattering stopped flow techniques.

Stopped flow techniques present the advantage of having very good temporal resolution, of millisecond scale. The central aspect of the method is the very quick, accurate and controlled mixing of two solutions. This is done using pistons, which provide, in combination with a hard stop valve, the instant insertion of the solutions in the mixing chamber. When the mixing chamber is filled, the flow is abruptly stopped. A schematic of this type of system is presented in Figure 58.



**Figure 58: Schematic of a stopped flow system connected to a spectrometer**

As this is not a physical method of its own, it can be associated with other detection techniques (spectrometric or light scattering). The name of the method is related to this trigger, which allows the recording of the signal over very short periods of time, at the moment when the flow is stopped and the solutions are present in the mixing chamber. The method is widely employed in the study of proteins in order to observe folding [99], [100]. Kinetic studies of chemical reactions are also described using this technique, both in the original form, as well as a quenched flow instrument form. The latter implies that the reaction is stopped by exterior means.

Because of its good temporal resolution (ms), stopped flow was widely used as a technique in measuring water transport on various substrates, such as different types of vesicles (block copolymer and lipids of various compositions) [94], [95], [101].

In our case the stopped flow system was coupled to a spectrometer in light scattering mode. By having the vesicles in a buffer solution and quickly subjecting them to an osmotic shock, the transport of water can be investigated. In the case of a positive osmotic shock, the vesicles have the tendency to shrink, with the water coming out, while in the case of a negative shock the vesicles have a tendency to swell, the water going inside as presented in Figure 59.

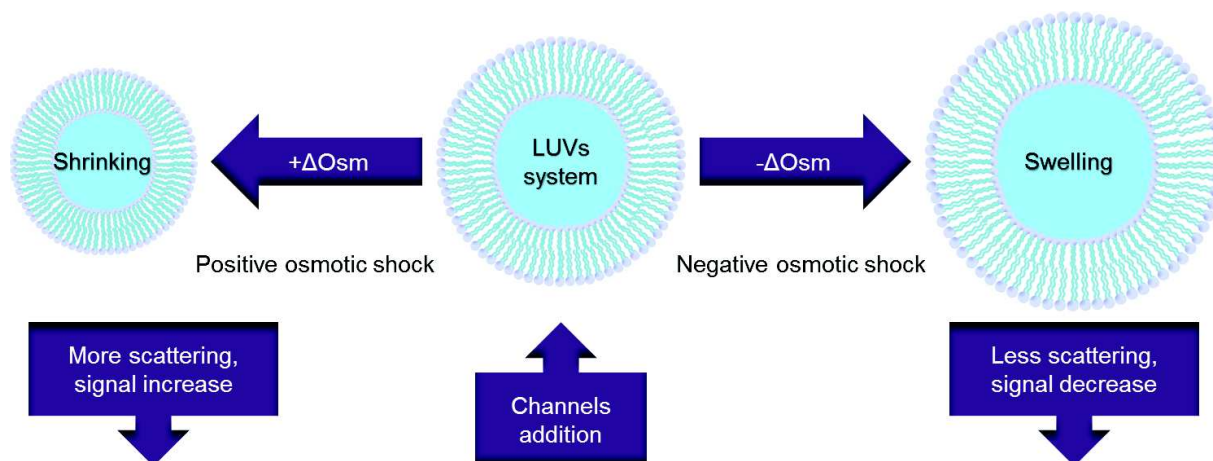


**Figure 59: Simplified schematic of scattering stopped flow on LUVs systems**

This work has been performed in collaboration with Dr. Manish Kumar from Penn State University. Because of this, we were able to elaborate two strategies. The water transport was measured under two different sets of conditions, by inserting the compounds on the outside of the vesicles (part made here at IEM) and by mixing the molecules directly in the lipid bilayer (part done by Yuexiao Shen at Penn University). In both cases the goal was to obtain the water permeability of the system. The calculation is explained in the following section.

The abrupt change of the vesicle size leads to variation in the light scattering at 90°. According to the Rayleigh-Gans theory applied to this system, the signal can be fitted in the form a sum of two exponential functions. The osmotic permeability ( $P_f$ ) was calculated by the following expression:

$$P_f = \frac{k}{(S/V_0) \times V_w \times \Delta_{osm}}$$

Where  $k$  is the exponential coefficient of the change in the light scattering.  $S$  and  $V_0$  are the initial surface area and volume of the vesicles, respectively;  $V_w$  is the molar volume of water, and  $\Delta_{osm}$  is the osmolarity difference. Two types of  $k$  can be determined,  $k_1$  and  $k_2$ , depending on the light scattering response of the vesicles compared to the control liposomes. This interpretation of the results will be explained further.

The entire library was subjected to this type of testing in order to assess the variation of activity vs. the modifications on the structures, namely chain length and absolute configuration. The first modification taken into account was the chain length, the results are presented lower. The results are presented in Figures 60-62, while the processed data is presented in Figure 63.

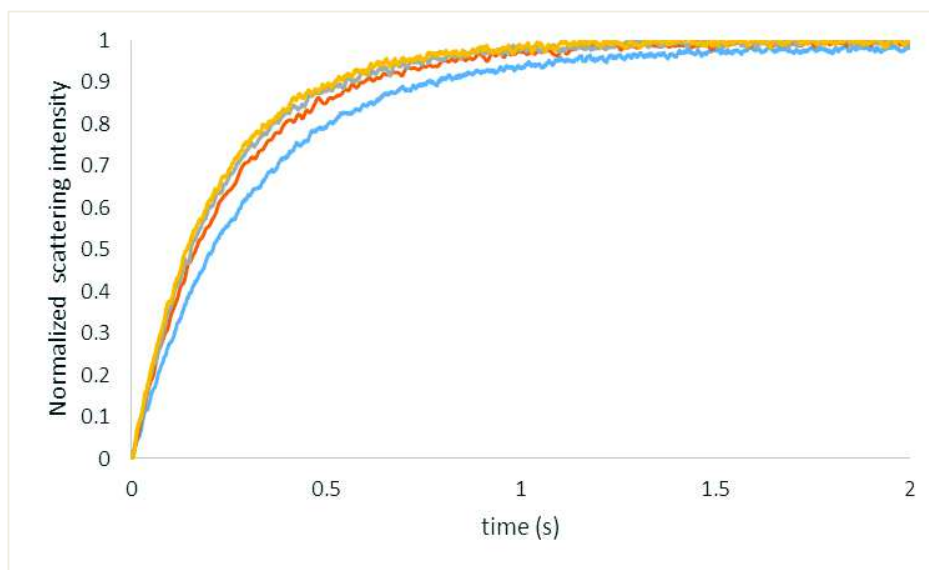


**Figure 60: Stopped-flow traces from experiments on liposomes with different imidazole derivatives in the shrinkage mode. All the liposomes were abruptly exposed to a shock solution of +200 mM sucrose. Light blue – blank; Red – HC4; Gray – HC6; Orange – HC8**

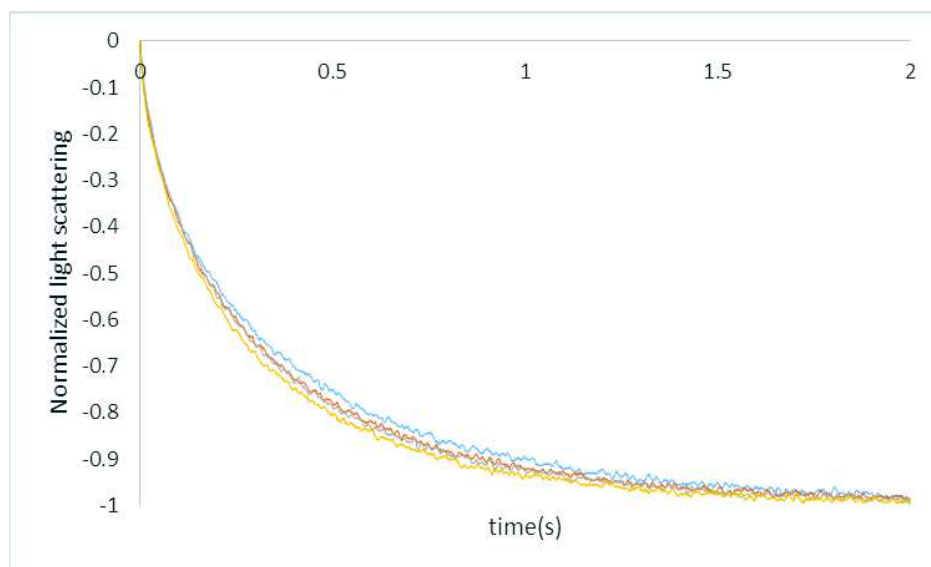


Figure 61: Stopped-flow traces from experiments on liposomes with different imidazole derivatives in swelling mode. All the liposomes were abruptly exposed to a shock solution of - 200 mM sucrose. Light blue – blank; Red – HC4; Gray – HC6; Orange – HC8

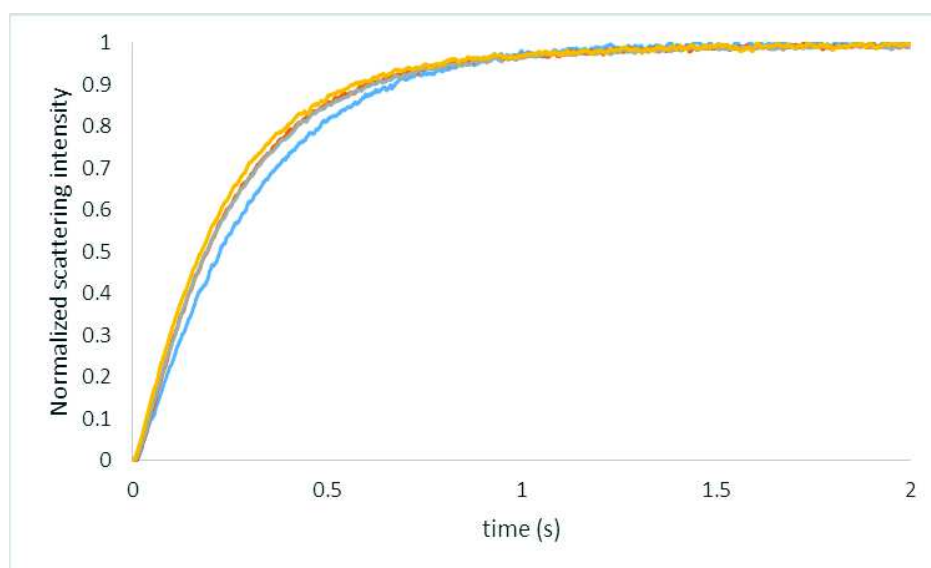
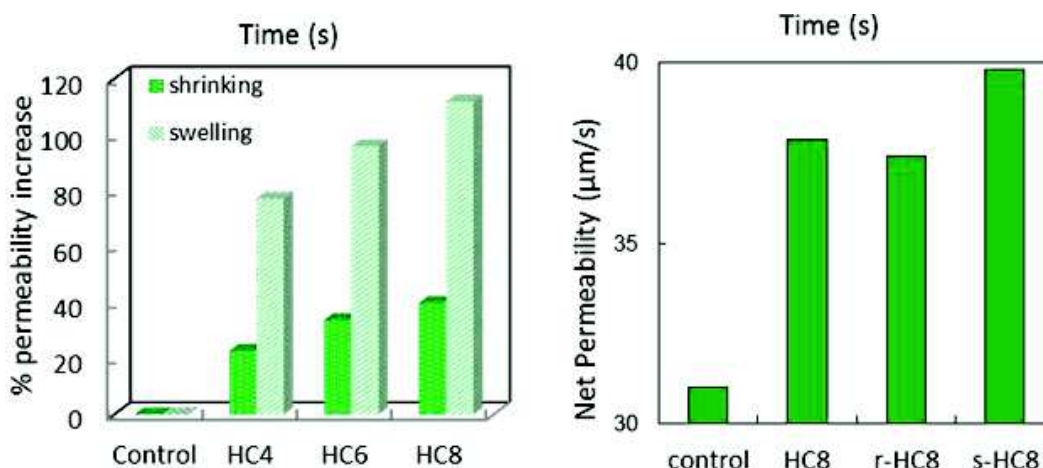


Figure 62: Stopped-flow traces from experiments on liposomes with different imidazole derivatives of the same chain length and different chirality in the shrinkage mode. All the liposomes were abruptly exposed to a shock solution of +200 mM sucrose. Light blue – blank; Red – HC8; Gray – RHC8; Orange – SHC8



**Figure 63: (Left) The percentage based permeability increase of the channels assembled by different imidazole compounds in the shrinkage and swelling mode. (Right) The net permeability of the channels assembled by different imidazole compounds in the shrinkage mode.**

Both hypertonic and hypotonic conditions were undertaken, which yielded significantly different results. In shrinkage mode, the light scattering signal increased and could be fitted in the form of a single exponential function, like in the case of HC8 and its chiral isomers (RHC8 and SHC8). There, a significant increase of the larger exponential coefficient ( $k_1$ ) was observed after the channels' insertion in the liposomes, while the second exponential coefficient ( $k_2$ ) was almost null. In swelling mode, the fitting yielded two shrinkage rates characterized by two exponential constants and thus two permeability values: a larger value constant ( $k_1$ ) and a smaller value constant ( $k_2$ ). The net permeabilities increased, in both modes, with the increase of the carbon chain length. The permeability values were comprised, in shrinkage mode between 30 and 40  $\mu\text{m/s}$  while in swelling mode between 70 and 150  $\mu\text{m/s}$ . The water transport rates of the HC8 channels were found to be 39% higher in swelling, while in shrinkage mode it was 111% higher versus the control experiments. With this method, the net permeability of HC8 channels was found to be 38  $\mu\text{m/s}$ , while for its chiral isomers RHC8 and SHC8, their permeabilities were of 37.5  $\mu\text{m/s}$  and of 39.9  $\mu\text{m/s}$ , respectively.

The second approach, consisting in the direct mixing of the compounds in lipid composition (prior to the LUV formation), was performed at Penn State University. The artificial channels constituted by the imidazole compounds assembled within PC/PS/Chl

liposomes were water permeable. The water transport rates greatly differed for compounds based on the different carbon chain lengths. Due to the shrinkage of the liposomes, driven by outwardly directed osmotic gradients, the light scattering signal increased and could be fit in the form of a sum of two exponential functions. The fitting yielded two shrinkage rates characterized by two exponential constants and thus two permeability values: the larger value constant ( $k_1$ ) and the smaller value constant ( $k_2$ ). For HC4 and HC6,  $k_1$  was found to be independent of channel concentrations and  $k_2$  increased when the channel to lipid ratio was increased (see Figure 64 a and b). This result indicated that the contribution to the overall liposome's permeability by the channels assembled by HC4 and HC6 was less than lipid background. Thus the smaller exponential coefficient ( $k_2$ ) was used to calculate the channels' permeabilities for HC4 and HC6. This approach has also been suggested in a recent study with the low-water-permeability Aquaporin, AQP0 [102]. For HC8 and its chiral isomers RHC8 and SHC8, there was a significant increase of the larger exponential coefficient ( $k_1$ ) after the addition of the channels into the liposomes. In this case the second exponential coefficient ( $k_2$ ) was almost null for liposomes with different channel ratios (see Figure 64 d, e and f). The permeabilities of these higher efficiency channels were thus calculated using  $k_1$ . The net permeabilities of HC4 and HC6 channels at a lipid to channel weight ratio of 1 (LCR1) were  $0.012 \pm 0.003 \mu\text{m/s}$  and  $0.027 \pm 0.015 \mu\text{m/s}$  respectively. The water transport rates of the HC8 channels were found to be 1~2 orders of magnitude higher than those of HC4 and HC6. The net permeability of the HC8 channels at LQR1 was  $0.989 \pm 0.306 \mu\text{m/s}$ , while for its chiral isomers RHC8 and SHC8, the permeabilities were  $2.771 \pm 0.738 \mu\text{m/s}$  and  $4.120 \pm 0.152 \mu\text{m/s}$  respectively.

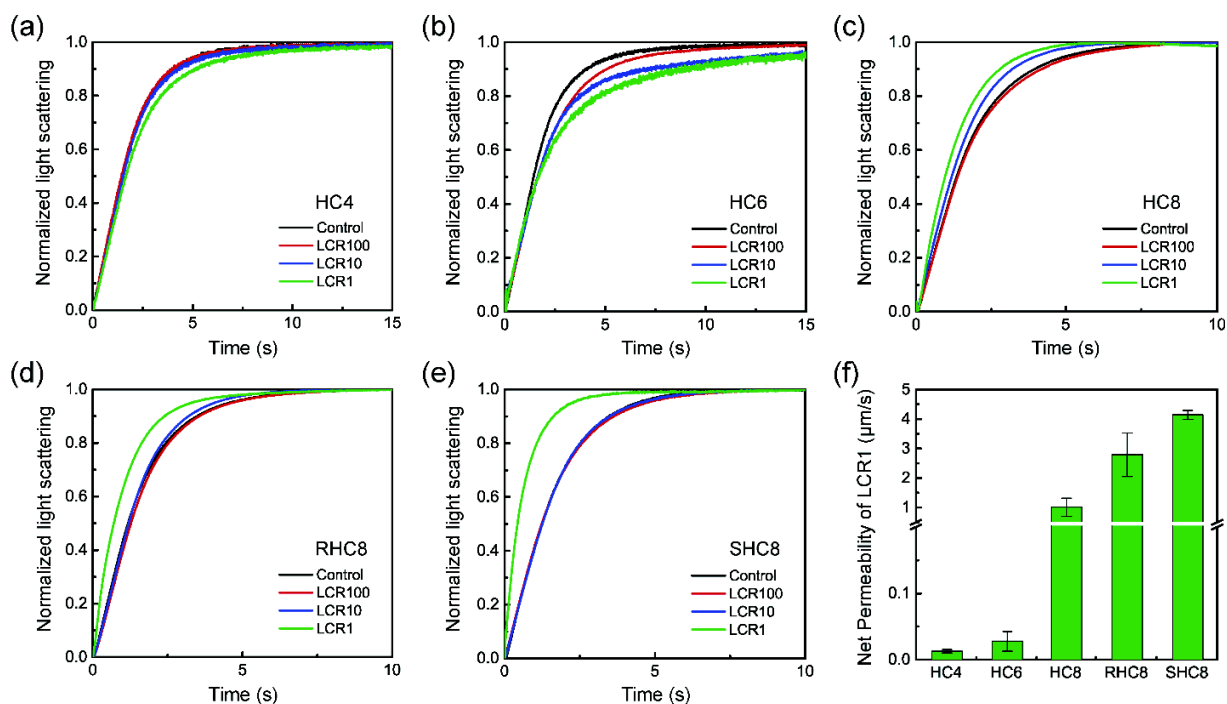


**Figure 64: Stopped-flow data shown are single traces. (a-e) Stopped-flow traces from experiments on liposomes with different weight lipid to channel ratios (LCRs: 1, 10 and 10). All the liposomes were abruptly exposed to a hypertonic solution of 200 mM NaCl. (f) The net permeability of the channels assembled by different imidazole compounds at LCR of 1. Experiments done by Yuexiao Shen at PENN State University**

In conclusion, these experiments showed a significant increase in activity in relation with the increase of chain length and with the presence of the chiral center. For the shorter species, HC4 and HC6 the calculations are made using the second transport constant,  $k_2$ , a mark of weak transporters (compared to the blank samples). HC8 and its isomers are calculated using the constant  $k_1$ , since they present significant modifications in the first step of transport compared to the control experiments. The permeabilities obtained using both approaches are several fold larger in the case of HC8 and its isomers. This observation is particularly striking in the second protocol, where the channel forming compounds are added directly in the lipid mixture. On account of chirality, a difference can be observed between RHC8 and SHC8. While this difference is not as impressive as in the case of chain length variation, the S isomer does present a 25% better activity in terms of permeability to its counterpart. The possible reasons for this will be presented in chapter 2.3.4.



### 2.3.3. Proton Transport Experiments

The formation of water containing supramolecular structures provides a very promising start in applications as proton channels. The high degree of order exhibited by the channels due to the I4 quartet [22] influences directional transport in a very similar way to that of natural proton pumps. Having a pillar of water in the center of the transmembrane channel, provides an ideal mean of proton communication between the intravesicular environment and the external solution. Moreover, the pseudo-permanent dipole moment given by the chiral orientation of the water molecules, provides pathways that are less labile (less degrees of freedom), and thus faster for proton circulation.

As in the case of water, in the case of proton transport, two complementary methods were employed, both relying on fluorescence as the principle of measuring the transport of protons across the lipid bilayer.

The first method employed is the standard HTPS/Valinomycin ratiometric fluorescence method [60], [103]–[105]. It was used to assess the proton conduction of each system, at equilibrium, over a long period of time (500 sec), and is characterized by N500, as described in the ion transport experiments. This systematic study over the entire library of compounds allowed for a better understanding of the influence of the structural motifs varied, namely chain length and absolute of the compounds. The fluorescence curves are presented in Figure 65 and Figure 66.

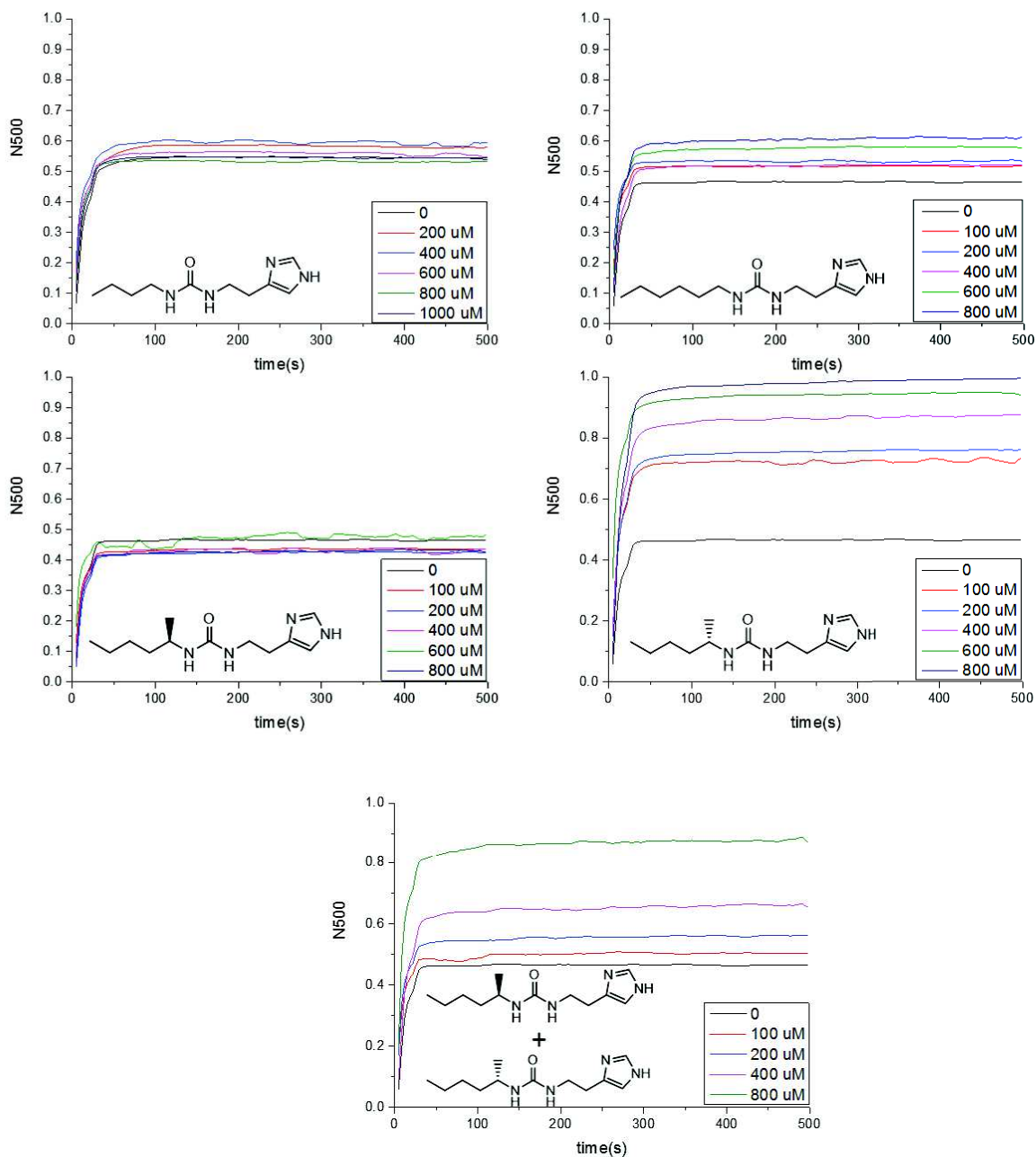


**Figure 65: Ratiometric fluorescence transport curves of HC4 (up-right); HC6 (up-left); RHC6 (middle-left); SHC6 (middle-right); racemic mixture of RHC6 and SHC6 (down). LUV suspension in PBS pH=6.4 (10mM), NaCl 100mM. N500 normalized transport over 500 seconds. Compound insertion at time=-100s, valinomycin (20 $\mu$ l, 1nM) injected at time=-50s, NaOH (25  $\mu$ l, 0,5M) added at t=0. Fluorescent probe HPTS  $\lambda_{1ex}$ =405nm,  $\lambda_{2ex}$ =460nm,  $\lambda_{em}$ =510nm.**

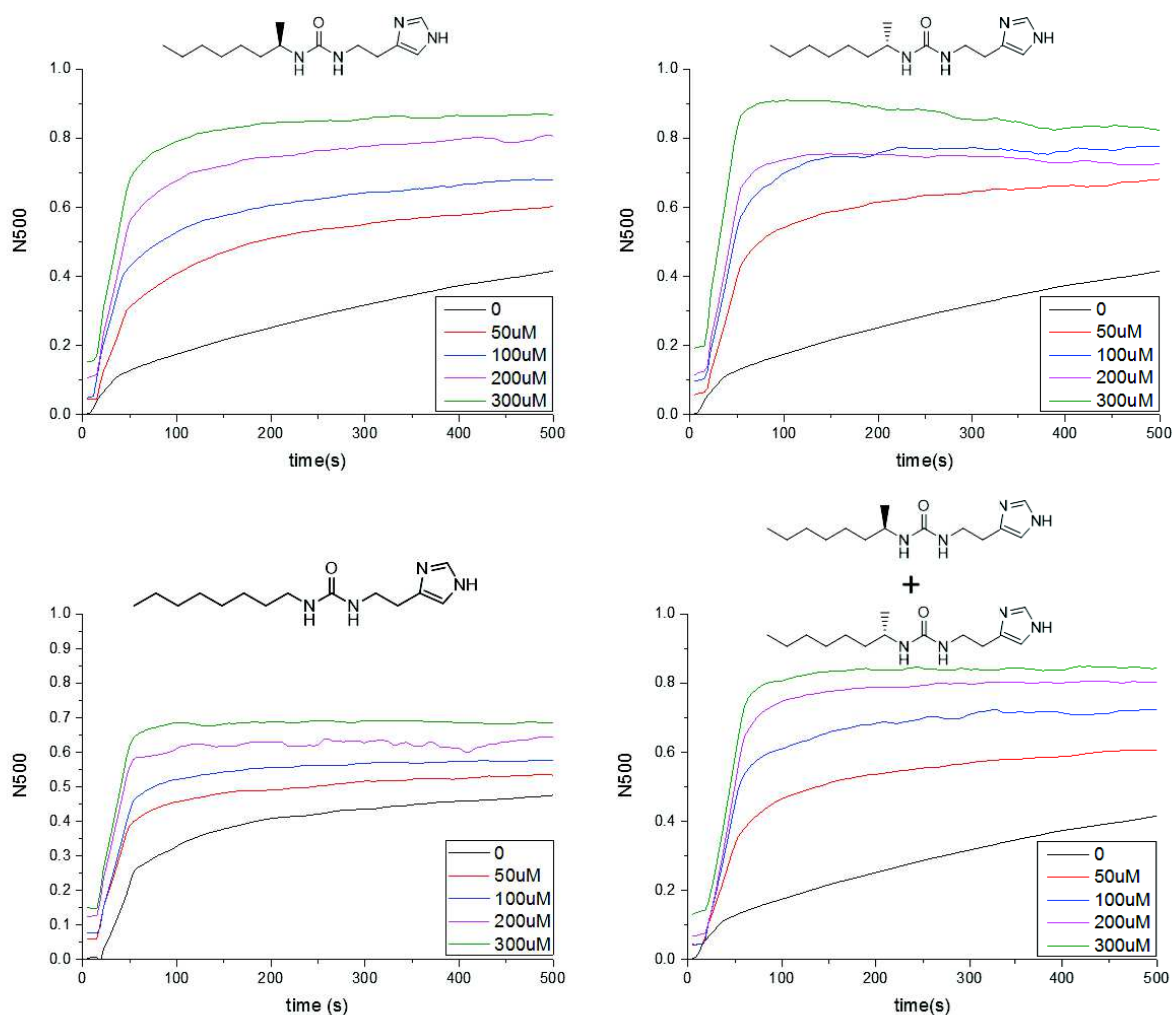


**Figure 66: Ratiometric fluorescence transport curves of RHC8 (up-right); SHC8 (up-left); HC8 (down-left); racemic mixture of RHC6 and SHC6 (down-right). LUV suspension in PBS pH=6.4 (10mM), NaCl 100mM. N500 normalized transport over 500 seconds. Compound insertion at time=-100s, valinomycin (20 $\mu$ l, 1nM) injected at time=-50s, NaOH (25  $\mu$ l, 0,5M) added at t=0. Fluorescent probe HPTS  $\lambda_{1ex}$ =405nm,  $\lambda_{2ex}$ =460nm,  $\lambda_{em}$ =510nm.**

The curves were interpreted accounting for total amplitude, comparison to the blank sample and shape of the curve. The structure-activity relation is positively influenced by the increase in chain length, varying from no activity for HC4, to weak activity for HC6 and good activity for HC8. Regarding the activity of enantiomers, the S and the R isomers might present different means of interacting with the LUVs, which, of course, affect their overall activity in the transports of protons. For the shorter C6 isomers,

the R doesn't present any activity, while the S presents a strong activity. In the case of the longer C8 isomers, both configurations present good activity better than the linear structure. This implies that the effect of chain length is much more important than the effect of enantiomer. Tests over an equimolecular mixture of the isomers were also performed the results displaying a weak synergistic behavior in both cases. This finding is supported by the shape of the curves and by the EC<sub>50</sub> values.

A Hill type interpretation of the results was performed. The Hill numbers and the EC<sub>50</sub> values were calculated by fitting the experimental results for each of the active compounds in a linear manner. The results are presented in Table 11

**Table 11: Hill numbers and EC50 values**

| <b>CODE</b>   | <b>HILL NUMBER</b> | <b>EC<sub>50</sub>(<math>\mu</math>M)</b> |
|---------------|--------------------|---|
| <b>HC8</b>    | 0,735              | 121,47                                    |
| <b>RHC8</b>   | 0,496              | 69,53                                     |
| <b>SHC8</b>   | 0,205              | 11,20                                     |
| <b>RACHC8</b> | 0,424              | 28,20                                     |
| <b>HC6</b>    | 0.493              | 269.41                                    |
| <b>RHC6</b>   | NA                 | NA  |
| <b>SHC6</b>   | 0.347              | 85.01                                     |
| <b>RACHC6</b> | 1.133              | 92.97                                     |
| <b>HC4</b>    | NA                 | NA  |

As in the case of the of ion transport, the EC<sub>50</sub> value represents the concentration at which, one given compound is able to perform half of its total transport potential, taking into account the compounds' intrinsic transport capabilities. Thus, a general comparison is inapplicable (presented in Figure 67). However, the much lower values of the C8 isomers point to the general conclusion of better activity. One other important observation is that the S isomer reaches this critical concentration sooner than its R counter counterpart. In spite of this, the overall transport is better for the R compound. The Hill numbers determine also the type of channel formed. All of the presented channels belong to the type II class,  $n < 1$ , and their formation is exergonic ( $\Delta G < 0$ ). Type two channels are

made up of a variable number of molecules, number which can't be precisely determined. One possible exception is the racemic mixture of R&SHC6 which presents a Hill number of 1.13, though the difference is not large enough to be conclusive. One possibility is that the two enantiomers form a self-standing finite structure that behaves as a unitary channel.

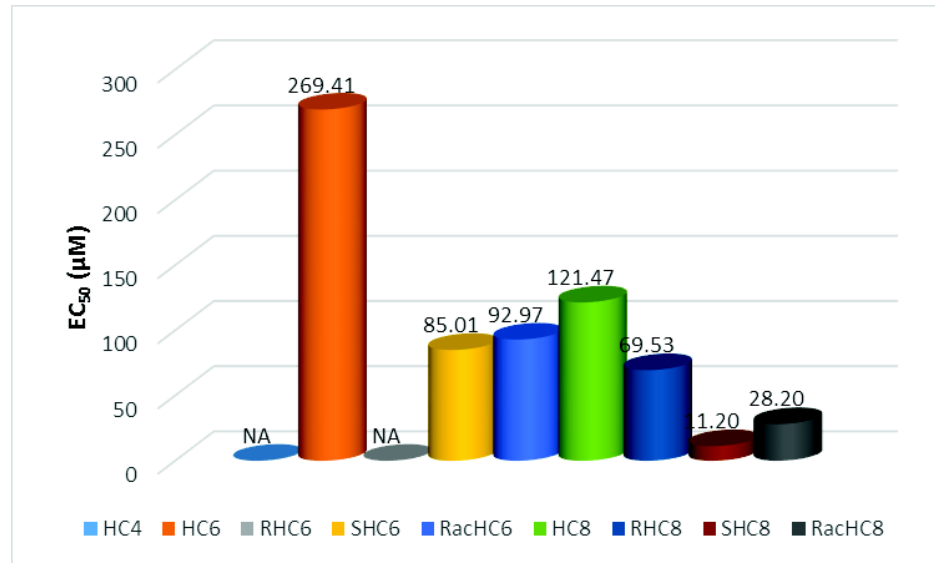


**Figure 67: Calculated EC<sub>50</sub> values in μM for the library of compounds**

The Hill plots are presented in figure 68. They display a linear dependency  $\log(Y)$  vs.  $\log(C_m)$  as predicted.

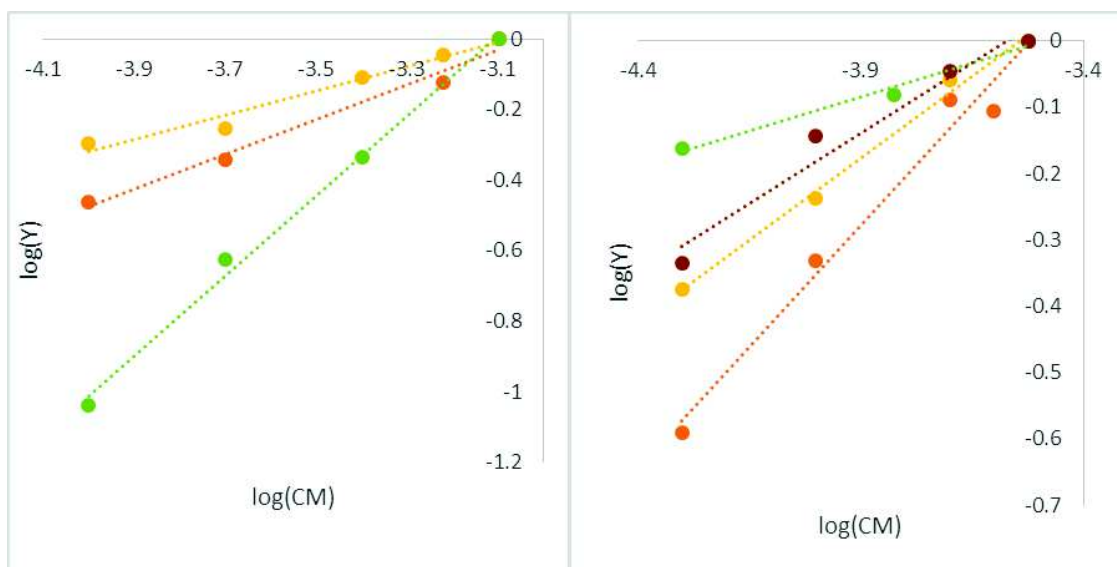


**Figure 68: Hill plot for species that display activity. (Left) Yellow – SHC6; Orange – HC6; Green – Racemic mixture of RHC6 and SHC6; (Right) Yellow – RHC8; Orange – HC8; Green – SHC8; Green – Racemic mixture of RHC8 and SHC8. Linear dependency displayed.**

As part of our ongoing collaboration with the group of Manish Kumar at Penn University, non-equilibrium (kinetic) measurements of proton transport were performed using stopped flow techniques. The compounds were assessed in different molar ratios related to the lipid substrate. The behavior of the system was determined with high resolutions over short time spans over some of the compounds of the library. The resulting curves are presented in Figure 69.

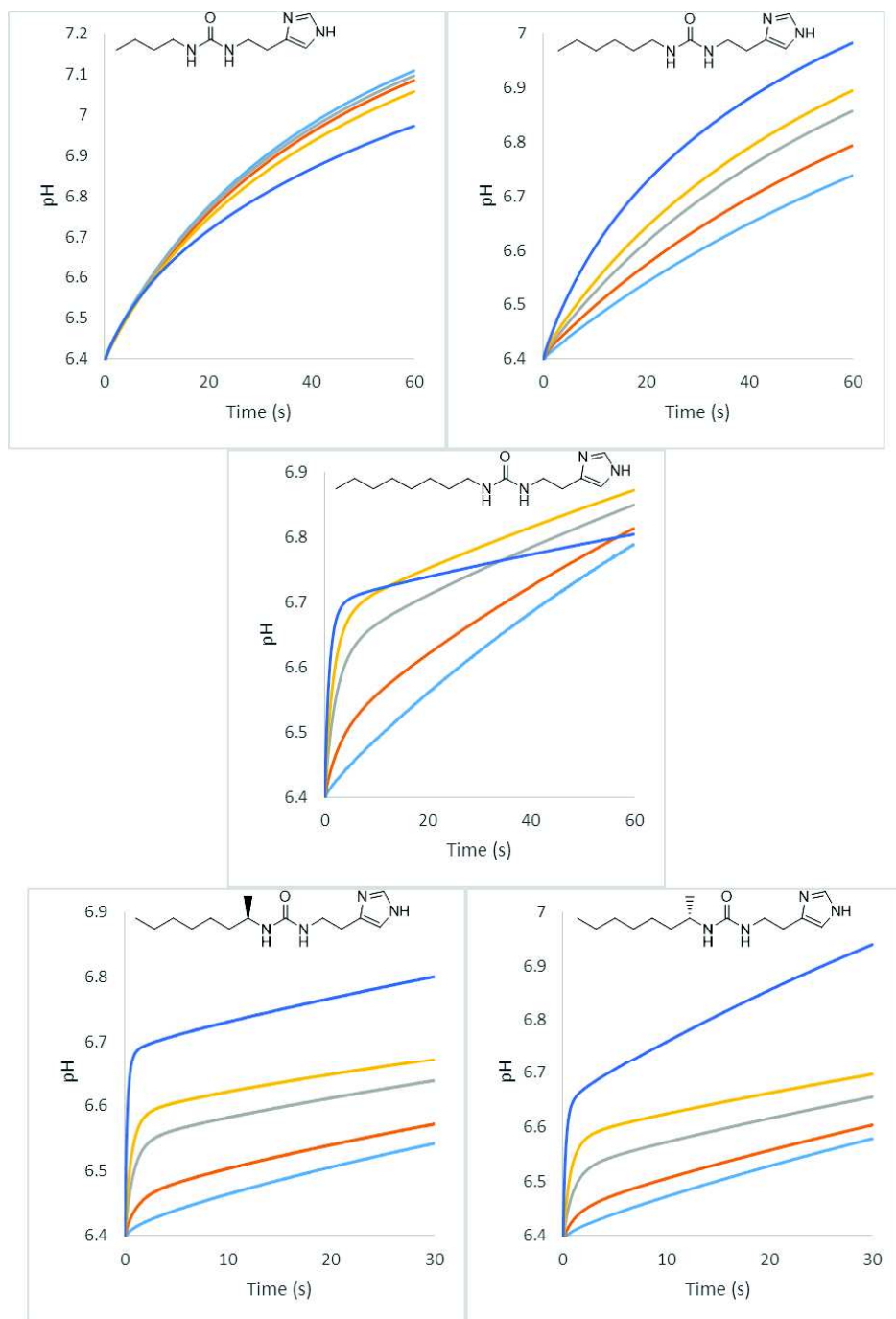


**Figure 69: Kinetic proton transport curves.** Fluorescently labeled dextran as the fluorescent probe  $\lambda_{ex}=494$  nm,  $\lambda_{em}=521$ nm. LUV suspension in 10 mM Hepes, 100 mM KCl, pH=6.4. Transport starts by applying a pH shock with the same buffer, pH=8.4. Light blue – control; Red- compound/lipid molecular ratio 1/500; Gray- compound/lipid molecular ratio 1/100; Yellow- compound/lipid molecular ratio 1/50; Dark blue- compound/lipid molecular ratio 1/10. Experiments done by Yuexiao Shen at Penn State University.

This high resolution method allows the actual calculation of the number of protons that are transferred across the membrane in the unit of time. The results confirm the measurements made in equilibrium conditions: the lack of activity of HC4 and the positive influence of chain length over activity. For example HC8 transports 4.75 times more protons in unit of time and of surface than HC6. Truly remarkable results were obtained for the enantiomers RHC8 and SHC8 that exhibit 3 to 4 times more proton conduction than the linear isomer. The increased efficiency of the enantiomers versus the linear isomer could be attributed to the different packing of the crystal matrix in the case of these species. This observation corresponds to the initial presumption formulated on the crystal packing of the species, in which a tightly packed linear structure has more difficulty in inserting itself in the lipid bilayer.

The proton flux ( $J_{H^+}$ ) is determined according to the following equations:

$$J_{H^+} = \frac{dpH}{dt} \times \beta$$

Where  $dpH$  is the evolution of pH,  $dt$  is the evolution of time and  $\beta$  is the buffer capacity:

$$\beta = \frac{dn}{dpH} = 2.303 \left( \frac{K_w}{[H^+]} + [H^+] + \frac{cK_a[H^+]}{(K_a + [H^+])^2} \right)$$

Where  $K_w$  is the water constant,  $[H^+]$  is proton concentration,  $K_a$  is the acidity constant. Therefore the proton transport rate ( $\#/s \cdot \mu m^2$ ) can be calculated as  $J_{H^+} = N_A V_0 / S$ . Where  $N_A$  is the Avogadro's number,  $V_0$  the initial volume and  $S$  the surface of the vesicle. The results are presented in Figure 70.



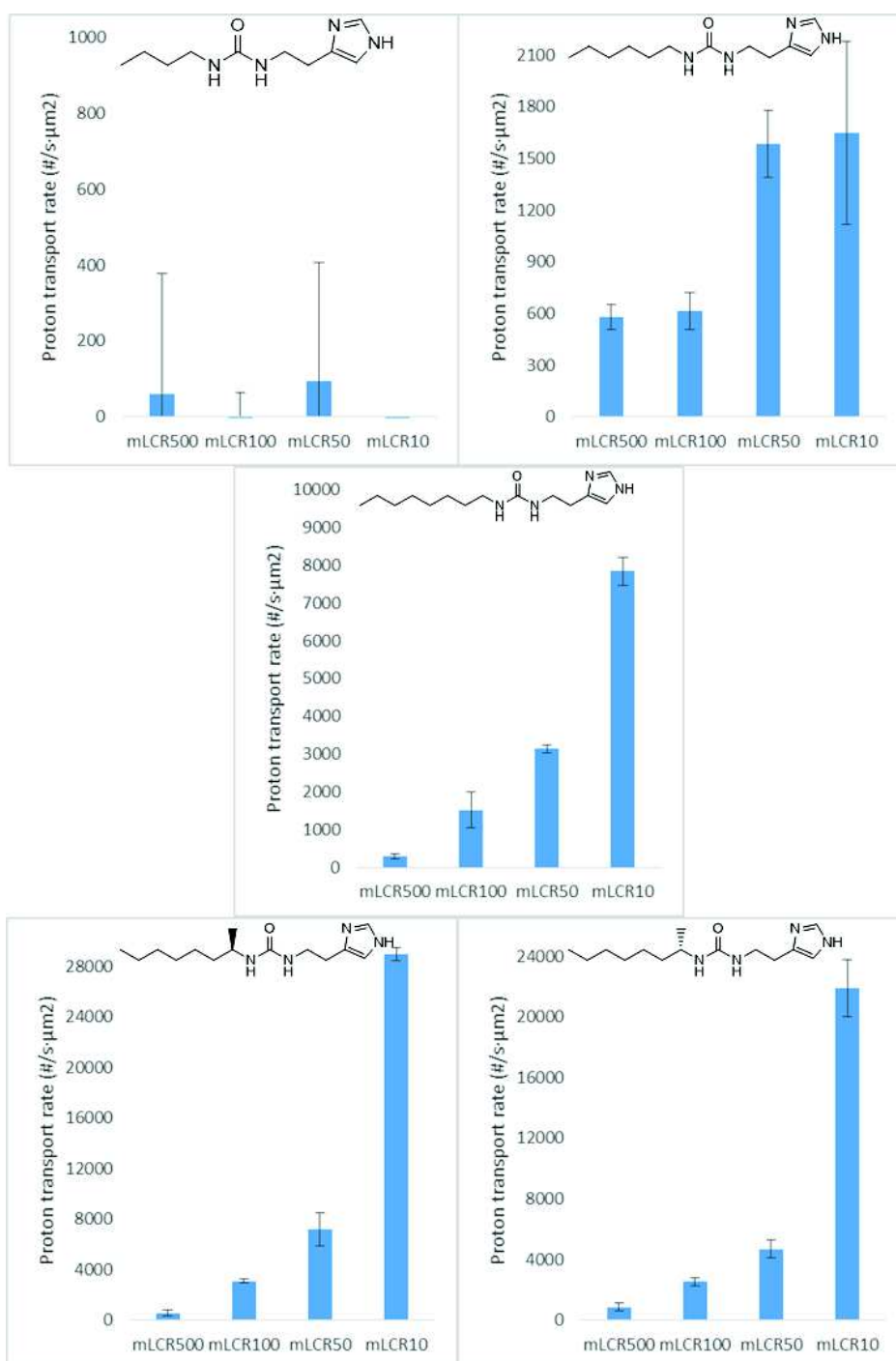
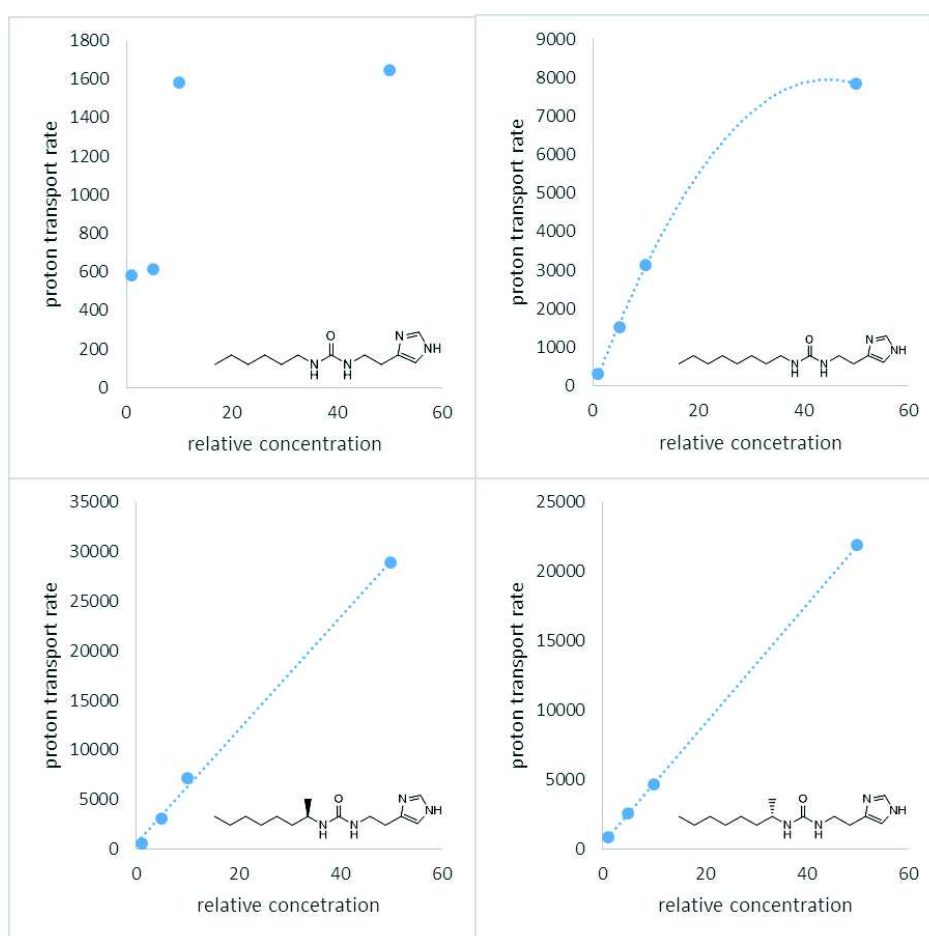


Figure 70: Proton flux through the lipid bilayer as calculated from the kinetic experiments performed at Penn University. up-right - HC4, up-left - HC6, middle - HC8, bottom left - RHC8, bottom right - SHC8

By plotting the values of the proton conduction vs. concentration, the tested systems can be better defined (see Figure 71). As such, the linear isomers, HC6 and HC8 prove to present a capping effect, probably given by a partition function of affinity for the lipid bilayer. This restricts the efficiency of the system to a certain concentration over which, any increase does not further increase the conduction of the system. On the contrary, the RHC8 and SHC8 isomers have perfect linear profiles, implying that all increases in concentration will lead to an increase in activity.



**Figure 71: Types of mathematical dependencies of transport as a function to relative concentration vs. lipids amounts for HC6 (up-left) - capping effect, HC8 (up-right) – second degree dependency capping effect, RHC8 (left-low)- linear dependency, SHC8 (right-low) – linear dependency.**

In order to explain the different activity exhibited between the HC8 enantiomers, the initial slope of the transport curves can be compared. The linear increase domain of

the signal was isolated, immediately following the initial jump. This slope represents the difference in behavior between the two isomers. The S isomer presents the steeper slope, representing a better overall transporter after the initial moment.

Our hypothesis is that the speed or degree of insertion in the lipid bilayer varies between the R and the S isomer. POPC ( $\alpha$ -L-Phosphatidylcholine) similarly to natural vesicles presents an absolute configuration and, as a consequence, a preference towards one of the isomers, in this case S. This could imply a much faster insertion of the species in the membrane as a possible explanation for the steeper slope of the proton transport curves (as visible from the stopped flow experiments). So, while the R formed structure inserts itself from the outer interface inwards, the S isomer inserts itself very quickly (and probably as a monomer) that self-assembles in a channel structure in the bilayer. For the S isomer this promotes a very quick initial transport followed by a slow decrease (see fluorescence curves, in Figure 66). Therefore, the transport mechanism is quite different between the two isomers. This presumption is also supported by the fact that in the case of the HC6 isomers, the R does not present any activity while the S is a better transporter than the linear isomer of same length, HC6.

#### 2.3.4. Effect of Chirality on Transport

This difference in behavior between enantiomeric species is very present in real biological systems, for example in the preference for the L isomer when it comes to amino acids and the D when it comes to sugars [106]–[108]. Recently this property was also proven for artificial systems such as vesicles[109], [110]. In these cases the different rate of penetration across a lipid bilayer for pairs of enantiomers is harnessed as a method of purification and separation. We made an attempt to prove the different type of interaction between RCH8 and SCH8 using circular dichroism (CD) techniques. The experiments were made in conditions similar to those of the fluorescence transport condition, in a PBS buffer containing 100mM NaCl. The CD spectrum of a suspension of vesicles was first

registered, followed by the addition of the species RHC8 and SHC8 as well as an equimolecular mixture of the two. The spectra of the two compounds by themselves, could only be obtained in a simple dilution in pure methanol, and not in the buffer system. This was caused by weak optical activity and solubility issues. The results are presented in Figure 72 and Figure 73.

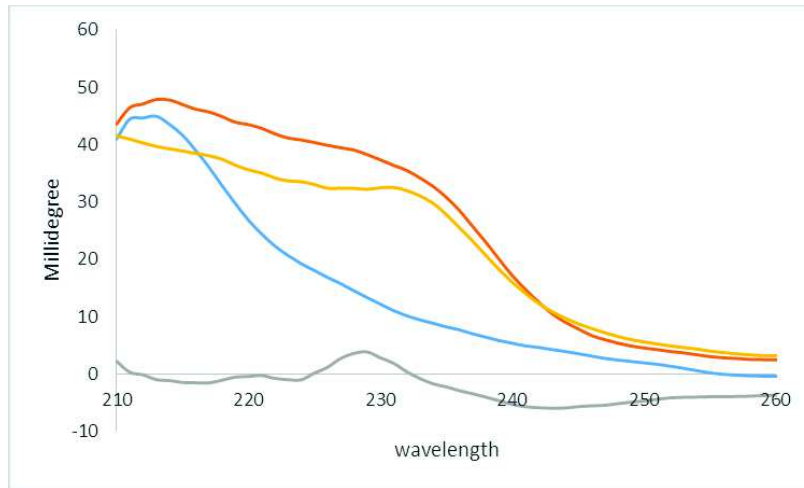


**Figure 72: CD spectra of vesicle systems made in PBS buffer (10mM, pH=6.4) NaCl 100mM. Light blue - LUVs solution, Red - LUVs solution with RHC8; Gray - LUVs solution with SHC8; Orange - LUVs solution with a racemic mixture of RHC8 and SHC8. Compound concentration 600µM. Step size 0.5nm.**



**Figure 73: CD spectra of RHC8 and SHC8 in pure methanol (high concentration, 50mM). Step size 0.5nm.**

The CD spectra of the vesicles show a strong signal between 210 and 220 nm. By adding the active compounds some differences in interaction become visible. In the case of the S isomer, the signal disappears entirely, probably signifying a strong rearrangement of the membrane due to the quick insertion of the compound. In the case of R, the signal is amplified and broadened over a large interval 210-250 nm. This could mean that the R isomer is interacting with the membrane from the exterior medium, possibly creating multiple structures that modify the intrinsic signal of the vesicles through binding. By adding the racemic mixture, we see an intermediate result that accounts for the decrease in the 210 peak of the vesicles, but also for the broadening of the signal generated by the R isomer. By comparing these results with the CD spectra of the two isomers in solution, we can observe a large increase in signal (from millidegrees to tens of millidegrees), as a consequence of the interaction with the lipid substrate.

Although this experiment does not completely elucidate the difference in activity between the enantiomer pairs, it is a starting point for a better understanding of their interaction differences. Although the entire mechanism is not completely elucidated, our hypothesis is that the R isomer probably forms channels in the external solution, structures that then insert themselves in the bilayer, while the S isomer penetrates the membrane and forms channels in that exact spot, leading to a modification the self-assembly of the lipid bilayer. The activity of the enantiomers, in all cases, is better than that of the linear isomer, suggesting a conformational preference of the liposomes towards the types of structures formed by these optically active compounds.

### 2.3.5. Cation Transport

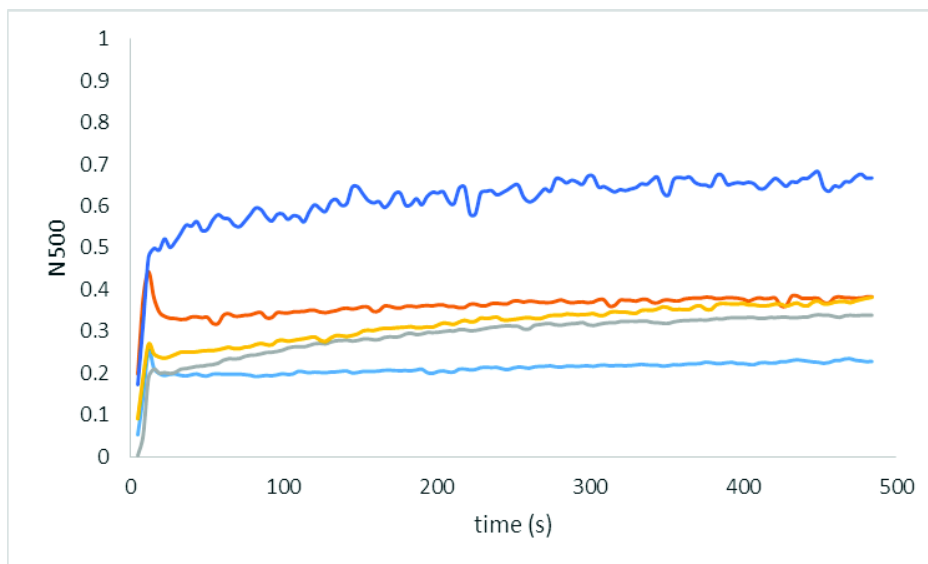


**Figure 74: Sodium transport curves for HC8 (Orange), RHC8 (Yellow), SHC8 (Gray), Compound 8 Chapter I (Dark blue), DMSO (Light blue). LUV suspension in PBS pH=6.4 (10mM), NaCl 100mM. N500 normalized transport over 500 seconds. Compound insertion at time=-50s, NaOH (25  $\mu$ l, 0,5M) added at t=0. Fluorescent probe HPTS  $\lambda_{1ex}$ =405nm,  $\lambda_{2ex}$ =460nm,  $\lambda_{em}$ =510nm.**

The selectivity of the compounds was tested using fluorescence methods. An active compound was chosen as comparison (compound 8 from chapter 1). The ion picked for this experiment was sodium, for its very general and common behavior. The concentrations chosen were moderate (200 $\mu$ M), in order to obtain data without any trace of interference from extreme concentrations. The fluorescence curves are presented in Figure 74. The curves were interpreted on the same principles applied for ion transport curves. The conclusion is that the compounds are not active towards the transport of sodium, based on the following criteria: small response versus the blank and versus the witness and the lack of variation of activity with concentration (data not presented here). The selectivity of the channels is manifested by their ability to discriminate between protons and sodium. Opposed to the compounds presented in chapter one, which do display some similarities to this library (small molecules, same heterocycle unit), these compounds do not perform ionic transport. This could be a very useful feature in

applications such as water purification, where the presence of protons, contrary to ions, does not have bad implications.

## 2.4. Conclusions and Perspectives

A library of compounds was assessed as self-assembled supramolecular transporters, based around the concept of the I4 quartet. The direct link between structure and activity was evaluated through modifications of both chain length and chirality of the species. The larger members of the series presented water transport and proved to be very efficient proton transporting units, while displaying a good selectivity towards monovalent ions.

The water transport capabilities of the tested systems were assessed through multiple methods: computational chemistry, dynamic light scattering and stopped flow light scattering measurements. For the latter two different approaches were used, with the characterization of the systems, either introduced on the exterior of the LUVs, either through direct incorporation in the bilayer. This very thorough set of experiments constitutes a very accurate description of the synthetic water channels tested.

A positive influence on activity was found to be the enlargement of the chain length. This is probably due to a better affinity to the lipid bilayer but also, as the crystal structure packing revealed, the way in which the species self-assemble. Starting from HC4 (the shortest member), through HC8 (the longest member), derivatives the structures become less crowded and the linked structure effect is lessened, going from a continuous structure for HC4 and the two HC5 isomers towards the water channels exhibited by the HC8 isomers.

The influence of the enantiomeric effect was also addressed. For the long RHC8 and SHC8, in all accounts, the activity presented was higher than for their linear counterpart, HC8. Here, a discussion is needed to optimize the water channels. Given

the fact the lipids are optically active, one new strategy could be, the modification of molecules by adding favorable optical centers which, that would affect the speed of insertion through the bilayer. This may be an alternative to other structural modifications in order to increase the activity of a given species. One other observation is that in the case of the enantiomers, R and S, the activity vs. concentration dependency is linear, which makes solubility is the limiting factor, as opposed to intrinsic affinity. This also implies that, on a reasonable domain of concentration, there is not capping effect which would affect total efficiency of the system.

Structurally speaking, the chiral water molecules that present a pseudo-permanent dipole, should be further investigated. The passage of species, cations, protons and anions, is strongly affected by the number and exact positioning of the water molecules in a supramolecular structure, and, as such, these effects over the speed of transfer should be assessed.

The field of artificial water channels is still underdeveloped and thus many contributions are still needed. The goals of obtaining the efficiency and selectivity of proteins is far from being reached. However, advances in regards to self-assembled structures able to perform water transport, while also manifesting certain types of selectivity are being made.



## Chapter 3: Molecular Electrodes Systems

### 3.1. Introduction

Silica is a very well-known and characterized “wonder” material. The multiple and various applications of mesoporous silica stretch from separation and catalysis to biosensors, bioimaging, drug delivery and enzyme immobilization. This is due to the very well controlled, narrow distribution, size of pores it creates[111]–[119]. The issue to overcome in the creation electroactive devices is the isolating nature of the silica.

Walcarius et al.[120] proposed methods based on electrochemically deposited thin silica films on the surfaces of conducting surfaces. The resulting structures are controlled by using a surfactant template, which generates well-ordered pores on conductive surface supports. Hexagonal in shape, these pores connect the conducting under layer of the support to the external medium. Conductive assemblies can be inserted in the resulting perpendicular pores. Towards this target the silica must be modified in changing its hydrophilic nature. This type of system has been previously designed, in which supramolecular structures of interest have been introduced in confined space systems.[23], [24], [121]–[124]. By combining these concepts, nanoscale electrode systems could be designed, under the condition of finding suitable conductive species.

In order to obtain metal-like conduction using organic species there are a few known candidates. One of these is the “metallic” carbon nanotubes, which are allotropes of carbon presenting a cylindrical nanostructure with a very small diameter (1-3 nm) and very well defined structure as a crystal lattice. Because of these very strict requirements they are very difficult to use [125]–[127]. One other better known solution is that of conjugated polymers which can then be doped (polyaniline for example)[128]. These

ones have been known for some time. Multiple methods of production are employed with an adequate control over the resulting material.

A newer approach is that of supramolecular self-assembled structures. The most promising of these are the  $\pi$ -conjugated systems[129]–[136]. One such system is that of triaryl amines (TAAs). Although TAAs are not conductive on their own, some species of the family of compounds display the property of generating a cation radical on the nitrogen atom. This promotes a non-covalent polymerization, in which the charged molecule self-assembles with its neutral counter parts, generating a structure with a delocalized charge [137] (Figure 75)

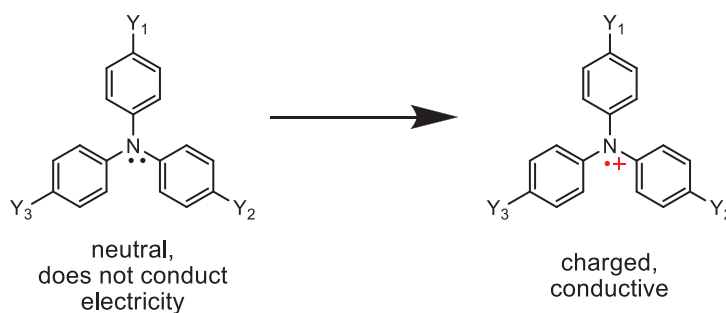


**Figure 75: Neutral and charged TAA.  $Y_1$ ,  $Y_2$ ,  $Y_3$  generic substituents**

Combining these concepts opens the possibility to design and obtain an electrically active device. This device would present molecular self-assemblies in a mesoporous silica matrix. Because of the very good electrical properties of TAAs the devices would act as an array of nanoscale electrical contacts, which would perform electron translocation.

### 3.1.1. Electrodeposited Templated Mesoporous Silica and Functionalized Silica

Silica is a universally used material because of its properties. Just to mention some of the most important ones [23], [24], [111]–[124], [132]:

- Relatively cheap to produce. Silica is synthesized from industrially made precursors, making the cost of the material low.
- Almost chemically inert and good mechanical properties. The Si-O-Si bond is unbreakable by aggressive media such as acids, bases or organic compounds. It is dissolved by hydrofluoric acid and sodium hydroxide, but aside from that, it is not reactive towards species in general. Silica's density can be adjusted in the fabrication process and thus its mechanical properties can be adapted.
- Easily modifiable. Since silica is made out of precursors, by changing the precursor, functionalized silica can be obtained. The most interesting aspect of this is the possibility of obtaining so called hybrid materials, made of silica that have organic chains with functions such as, alcohols, amines, thiols, double bonds, long alkyl chains etc. This opens the possibility of producing materials which are tuned for specific purposes. While retaining the robustness of the silica matrix, a hydrophobic material can be obtained by attaching a long alkyl chain. Other possibilities include dynamic systems that could be manufactured using a reversible bond such as an iminic bond, by inserting amines in the matrix.
- Many synthetic procedures. Silica can be obtained through numerous methods: sol-gel protocols, CVD (chemical vapor depositions), or electro-assisted depositions just to name the most common. All the methods can be used by themselves or as a combination.

Alain Walcarius has pioneered the field of mesoporous silica films in electrochemical applications[120], [138]–[140]. The generation of the film can be done by spin coating, dip coating or by electro-generation. This approach is based on the surfactant-assisted hydrolysis/condensation of precursors, which is a sol-gel procedure.

From a chemical point of view, silica is made by using as precursors the alkoxy silanes (Figure 76). These species present hydrolysable alkane-oxygen bonds, which free up derivatives of the silicic acid, which can then condense, in order to obtain the polymerized silica network. Besides the typical tetra alkoxy silanes, like tetraethoxy silane (TEOS) and tetramethoxy silane (TMOS) that present four hydrolysable bonds, derivatives containing functional groups (on non-hydrolysable hydrocarbon chains linked to the silicon atom), can be added to the sol-gel in order to alter its properties. In this work, (3-Mercaptopropyl)trimethoxysilane (MPTMS) was used for this purpose.

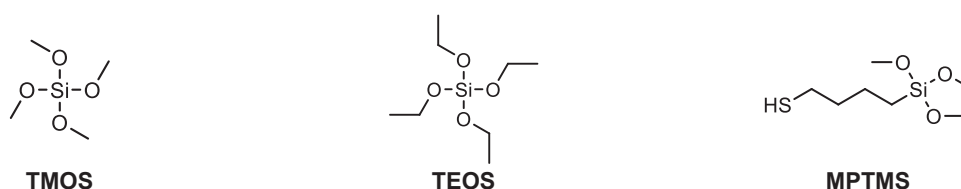
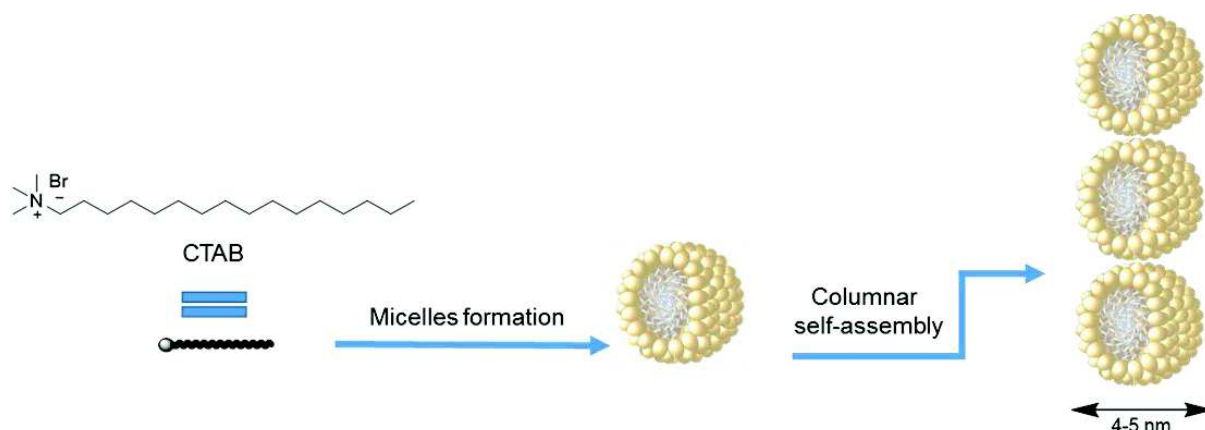


Figure 76: Silica precursors

In turn, the resulting films must be templated by employing a surfactant. For this purpose either CTAB (cetyltrimethylammonium bromide), a cationic surfactant, or, the neutral pluronic triblock copolymer can be used. The resulting mesoporous silica has well defined pores with constant diameters. For this project CTAB was chosen because of its compatibility with the electrodeposition technique. CTAB self-assembles in column like structures, with a diameter of 4-5 nm, when inserted in the silica sol-gel. When the surfactant is removed, pores of the mentioned diameter are generated. A schematic of the CTAB self-assembly is presented lower in Figure 77.



**Figure 77: CTAB self-assembly**

The templated mesoporous silica obtained by this method can serve as a host for various species. A previous project developed at IEM has used similar concepts[124]. In that project, a mesoporous layer of silica was electrodeposited on ITO electrodes. These electrodes were then modified with the assistance of chlorosilanes in order to entrap C60 fullerenes in the modified pores. The schematic of the process is presented in Figure 78.

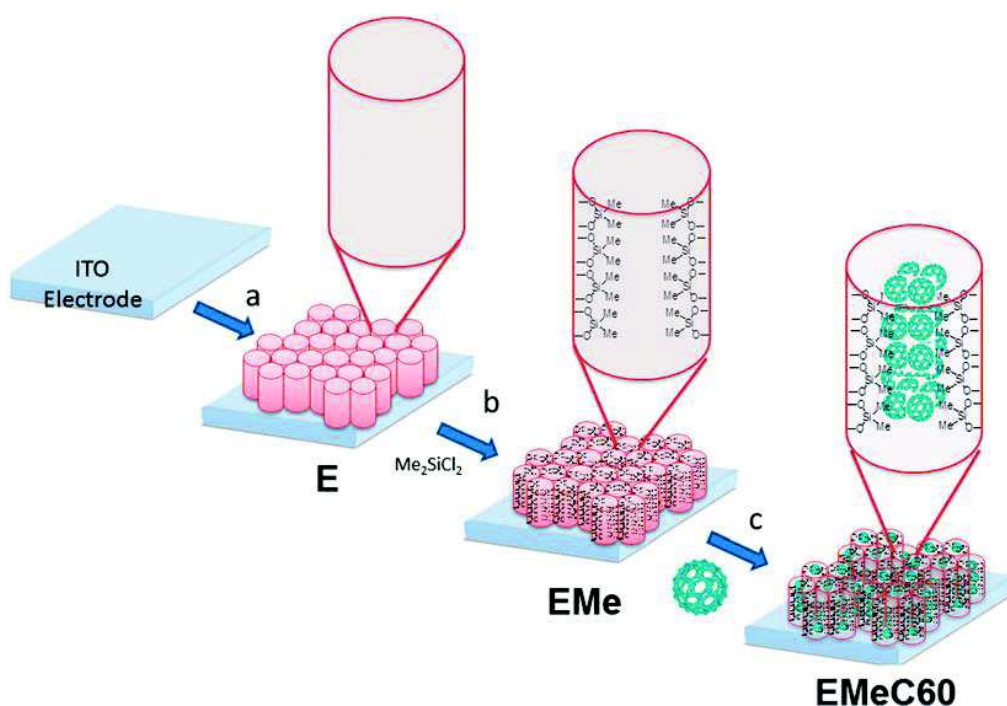


**Figure 78: Schematic representation of the synthetic route to obtain thin-layer mesoporous silica ITO electrodes: (a) electrochemical deposition of mesostructured silica-CTAB and then washing with HCl to generate E, (b) reaction with  $\text{Me}_2\text{SiCl}_2$  to generate hydrophobic EMe and (c) physical filling with the fullerene, resulting in the formation of an EMeC60 system [124]**

The key aspect of the project was the physical entrapment of the fullerenes in the pores, which relies only on the hydrophobic interactions and affinity for the medium in order to generate the confined space system.

The system was characterized by all appropriate methods, scanning electron microscopy and transmission electron microscopy to describe the silica morphology while X-ray diffraction and electrochemical methods were used to evidence the presence of the fullerenes in the mesoporous system. The porous electrode (E), the modified electrode (EMe) and the fullerene doped electrode (EMeC60) were investigated via cyclic voltammetry. These results are presented in Figure 79. In the case of EMeC60 two reduction peaks are observed, corresponding to two successive steps of the fullerenes' reduction,  $C_{60}/C_{60}^-$  and  $C_{60}^-/C_{60}^{2-}$ . These signals were not observed for the other the two types of electrodes, thus confirming the presence of the fullerenes in the confined system.

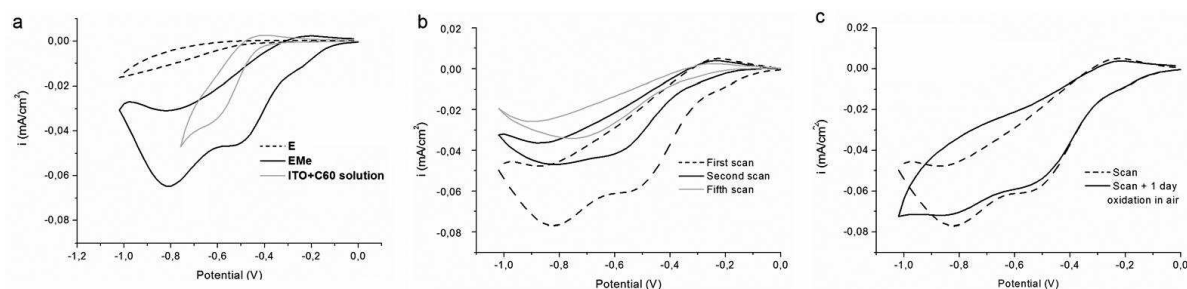


**Figure 79: Cyclic voltammograms (CV) in 0.1 MTBAPF<sub>6</sub> acetonitrile–toluene (1/1) of: (a) E and EMe after immersion in a 0.5 mM fullerene solution for 1 h. The light grey curve features a bare ITO electrode immersed in 0.5 mM fullerene solution; (b) continuous scanning procedure of a EMeC60 electrode at different intervals of time; (c) comparison of the first scanning CV and the CV of an EMeC60 electrode kept in air for one day at  $v = 100 \text{ mV s}^{-1}$  [124]**

The reduction of the fullerenes in the pores is a slow kinetic process, so the lifespan of the modified electrode is short. However this system may work as an excellent capacitor, while the system also tends to re-oxidize in contact with the atmospheric oxygen. These properties shed light on the possibilities to use it as a long time electron donor system for biological applications. Still, this result leaves room for improvement in the sense of stability and repeated use.

### 3.1.2. Triaryl Amines and Their Properties

The use of triaryl amines as conductive nanofibrils was recently discovered in 2010 [141]. By irradiating a TAA solution in a chlorinated solvent with white light, the aspect of the solution changed, because of the formation of supramolecular assemblies [137], [141]–[145]. These findings were confirmed by means of proton NMR and a study was conducted order to describe the structure modifications of the TAA. The self-assembly proprieties were found to be in correlation with the substituents on the phenyl rings of the TAAs. It was shown that the modifications in the NMR spectrum were generated by the presence of the radical-cation (Figure 80). By means or electron paramagnetic resonance (EPR) the amounts of TAA radicals generated could be measured (Figure 81). By irradiation for an hour with 20W of power the maximum number of radicals was achieved and measured at about 11%. Further the generated structures were described by DLS and AFM techniques. It was concluded that the radical species pull together the neutral TAA species resulting in nanoscale fibers (10-50 nm in width and 50-1000 nm in length).

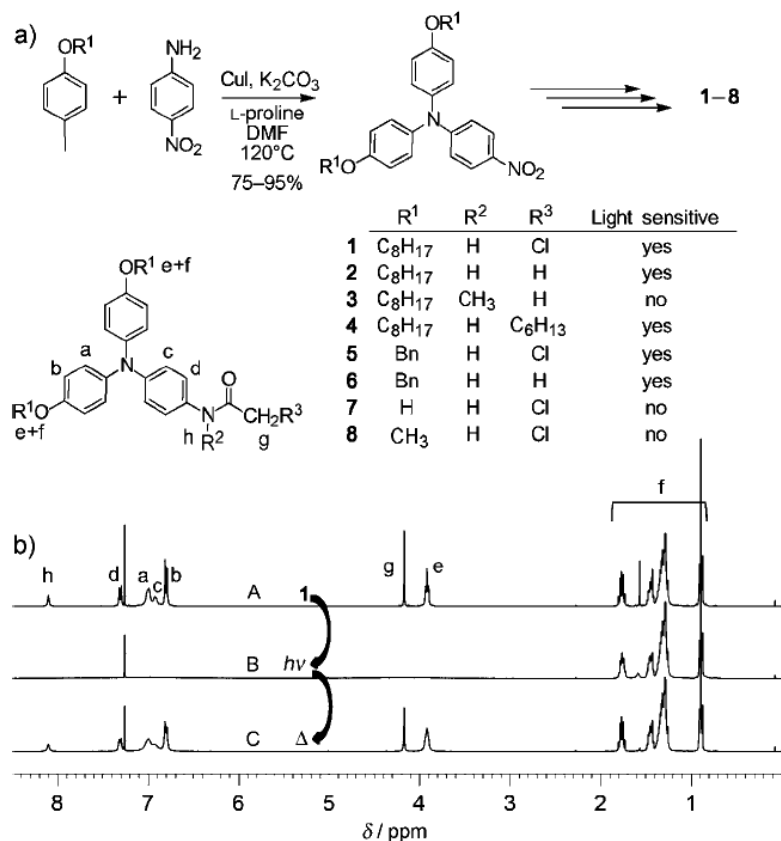


Figure 80: a) Structures and key synthetic step to access triarylamines 1–8. b) Typical <sup>1</sup>H NMR spectra (CDCl<sub>3</sub>) of 1 obtained immediately after purification (A); after 10 min exposure to visible light, (B); and after subsequent heating overnight at 60°C (C); [1]=10 mM [141]

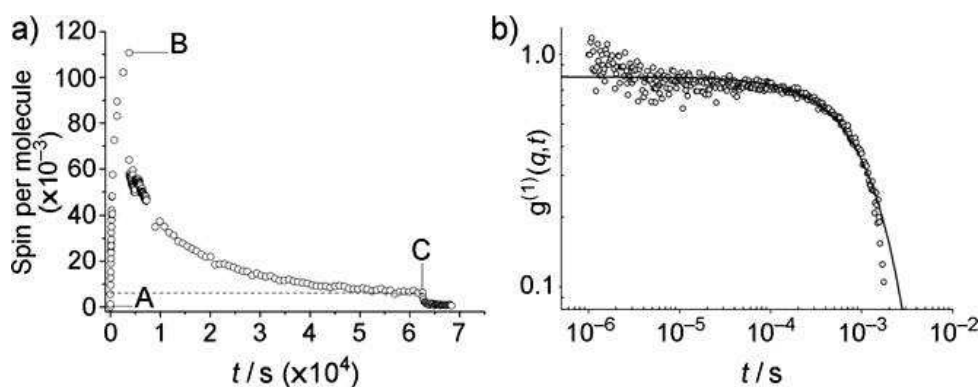


Figure 81: Quantitative EPR data as a function of time, showing the evolution of the ratio of the triarylammonium radical 1<sup>+</sup> over neutral 1: without visible light excitation at RT (point A); upon visible light excitation (A–B); in the absence of light at RT (B–C); and after subsequent heating (60°C) in the dark (from C; [1]<sub>init.</sub>]=10 mM). Dotted line: y-axis value of 6x10<sup>-3</sup>. b) Time autocorrelation function of the scattered electric field vector for an irradiated solution of 1 ([1]<sub>init.</sub>]=7.5 mM in chloroform at T=20°C) and for a scattering angle q=90°. Solid line: exponential fit. [141]



The property of having very well defined charged organic assemblies mandated another experiment to be conducted. A groove of about 80 nm was made between two metals, gold and nickel, to avoid the contact between the two metallic surfaces not being in contact. In the trench, a TAA solution was drop casted and was irradiated in order to produce assemblies, Supramolecular Triaryl Amine Nanowires (STANWs). The current had increased six orders of magnitude compared to the blank experiments of the circuit immersed in a solution of not irradiated TAAs. The conclusion was that the nanofibrils have very good electrical properties, comparable to those of metals. In the STANWs the charge is probably dislocated throughout the whole “roll of coins” but unidirectional through the middle. The experiment also showed that the resulting structures adapt themselves to a finite space (the trench in the case). The very good electrical properties recommend the TAAs as organic components in electrical devices (Figure 82).

Besides, due to their unique self-assembly process that can be achieved in situ, these molecules are promising for implementing numerous devices in which conducting nanochannels are needed.

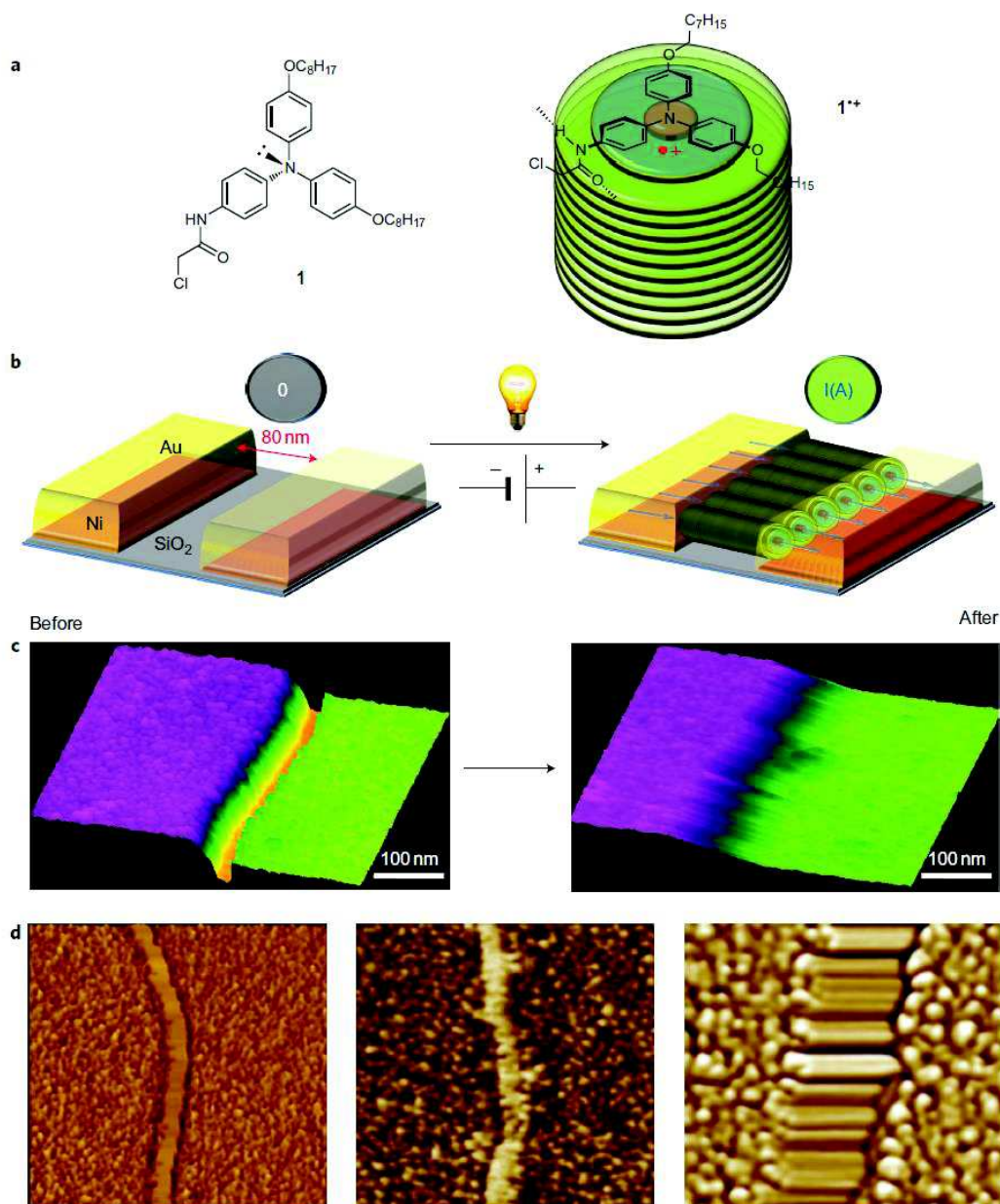


Figure 82: Triggered self-construction process for STANWs in a nanotrench geometry together with corresponding AFM imaging. a,b A solution of triarylamine 1 (a, 1 mg ml<sup>-1</sup> in C<sub>2</sub>H<sub>2</sub>Cl<sub>4</sub>) is drop-cast, in the dark, on nanopatterned gold/nickel electrodes (b: trench width, 100 μm; length, 0.08 μm; ΔV=0.3–0.8 V). The device is then submitted to white light irradiation (power density, 10 Wcm<sup>-2</sup> for 10 s), which enables the production of a catalytic quantity of radicals 1<sup>•+</sup>. The triarylammonium 1<sup>•+</sup> induces a supramolecular polymerization with neutral 1 that results in the self-assembly of STANWs aligned in the direction of the electric field and strongly connecting the two electrodes. c, Left: topography of the opened gap seen by AFM before light irradiation. Right: topography of the closed gap filled with STANWs after light irradiation. d, Left: AFM phase image of a fibre-free gap (surface scale, 1,500 × 1,500 nm<sup>2</sup>) before light irradiation. Middle: AFM phase image of a gap filled with STANWs (surface scale, 1,500 × 1,500 nm<sup>2</sup>) after light irradiation. Right: AFM zoom into the gap, which is filled with STANWs after light irradiation (surface scale, 250 × 250 nm<sup>2</sup>).<sup>[137]</sup>

The process of generating supramolecular STANWs by employment of radical TAA species was further investigated [146]. The radicals can be generated by three methods, namely irradiation with visible light, by employment of a chemical oxidant 2,3,5,6-tetrabromobenzoquinone (TBQ), or by seeding the solution of TAAs with fibril fragments. All these methods of promoting self-assembly have been characterized and studied in detail by multiple, adequate techniques (NMR, UV spectroscopy, EPR, X-Ray diffraction, AFM etc). In the case of the irradiation triggered assembly, a very prerequisite of the self-assembly is constituted by a solvent able to generate a negative charged counter ion. In this case chloroform was used, and the counter ion generated was Cl<sup>-</sup>. The growth and morphology of the TAA systems were measured and the processed results are presented in Figure 83, together with proposed mechanisms.

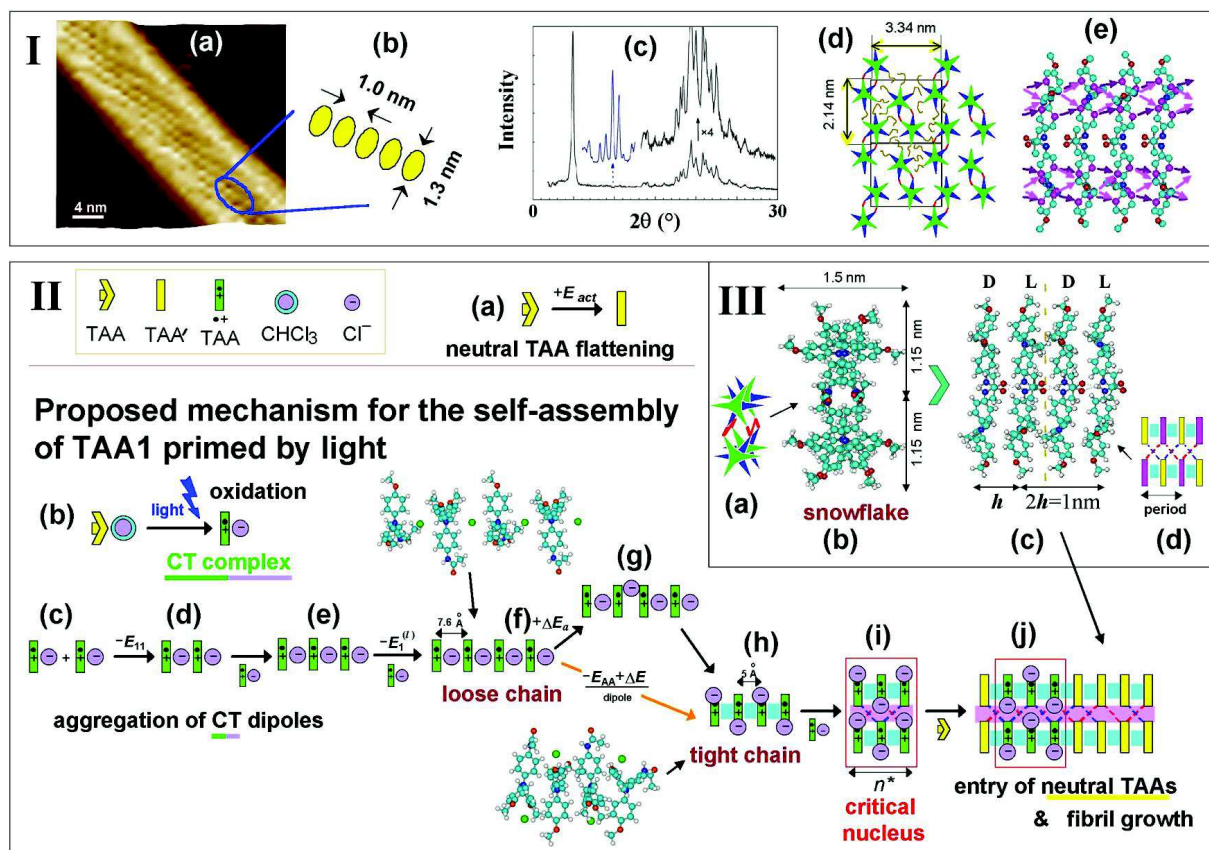


Figure 83: TAA fibrils in chloroform after 1 h exposition to white light. (I) (a,b) AFM height image (dry phase) of maize-like structures formed in 1 mM solution of TAA1 in chloroform. (c) The original XRD pattern from 10 mM TAA1 sample (bottom, black) accompanied by its magnification in the WAXS range (top, black) and in the SAXS range (top, blue) registered on the high-flux line. (d) The proposed internal molecular organization of TAA1 fibrils (in the plane normal to the c-axis) based on the XRD: the lattice cells are shown by rectangles; each crystalline cell consists of 8 molecules and includes two layers (TAA molecules belonging to different layers are shown with green and blue colors, respectively). Amide bonds are shown with red segments, and alkyl side chains with brown curly lines. (e) The simulated all-atomic structure of snowflake double column: the conducting pathways formed between nearest-neighboring carbons (marked with violet color) of adjacent TAA molecules (RCC = 0.36-0.37 nm) are marked with violet arrows (hydrogens are not shown). (II) Light-induced aggregation kinetics in TAA solutions. (a) Highly improbable spontaneous flattening of isolated neutral TAA molecule (transition TAA → TAA'). (b) Light induces oxidation of a neutral TAA molecule producing TAA<sup>•+</sup> radical and Cl<sup>-</sup> anion. (c,d) Two free radicals TAA<sup>•+</sup> complexed with the Cl<sup>-</sup> counter ions attract each other head-to-tail. (e,f) A growing stack of radical dipoles. (f,g,h) Tightening of the stack: chloride ions move sideways (g); aromatic rings of TAA molecules benefit from closer contacts, while chloride anions are finally accommodated in the gaps between ether tails of TAA molecules (h). (i) Formation of double-columnar nuclei stabilized by H-bonds between the columns. (j) Growth of the structure by attachment of neutral TAA molecules. (III) Molecular arrangements in bicolumnar “snowflake” stacks of neutral TAA3: (a) A cartoon showing alternating molecular orientation in the columns. (b) The top view (along the main axis), and (c) the side view of the structure. (d) A cartoon with zigzag chain of H-bonds connecting the columns. [146]

From these findings, one is of particular importance for this project, the “snowflake” pattern of the STANWs. The fibrils present a double columnar assembly, based on dipole-

dipole interactions and  $\pi$ - $\pi$  stacking, while the side chains generate van der Waals interactions also required for this type of self-assembly.

A novel application could be the insertion of these supramolecular assemblies in a confined medium. Mesoporous silica is such a medium, in which this application could be developed. It would take advantage of the good electrical contacts the TAA self-assemblies provide. In order to demonstrate the functioning of such device, bioelectrodes can be designed starting from the mesoporous electrodes.

### 3.1.3. Laccase Biocathodes

Biocathodes are electrodes modified with a biological component, an enzyme or a yeast typically, that is able to perform the role of a cathode in an electrochemical cell. A lot of research has been put in this application, since by adapting an enzyme to a support, an eco-friendly bioinspired fuel-cell could be obtained. Although this field is quite new there are several comprehensive publications on this subject [147]–[149].

On the account of oxygen reducing enzymatic cathodes, there are two main enzymes used, namely Bilirubin oxidase and Laccase, the differences between the two being a higher current output of Laccase, versus a better overall stability of Bilirubin oxidase. N. Mano [150] had a major contribution on the subject of Bilirubin oxidases, but also on Laccase biocathodes [151]. He proposed a very interesting redox hydrogel as a compliment to the enzyme. The use of an osmium pyridine complex as a doping on a poly(benzimidazobenzophenanthroline) derivative polymer, allowed the gain of a  $2^+/3^+$  redox charge in the mentioned polymer. The redox doped polymer as well as an undoped one were mixed with Laccase and applied to carbon nanofibers as a support. The resulting biocathodes were then compared to a platinum wire, which served as a model electrode. The doped electrode outperformed the undoped one and provided the reduction of oxygen at lower potentials vs. the platinum wire. It was concluded that the redox complex provided the much needed electrons for the laccase active centers, thus

influencing the potential where the oxygen was reduced and bringing it to as low as 0.07 V.

The access of electrons to the Laccase enzyme is quite slow and all applications based on this enzyme have to overcome this short coming. One simple solution is the adding of a chemical mediator, that transfers the electrons from the electroactive surface of the electrode to the enzyme. One such mediator is 2,2'-azino-bis(3-ethylbenzthiazoline-6-sulphonic acid) (ABTS) [152], [153] (Figure 84).

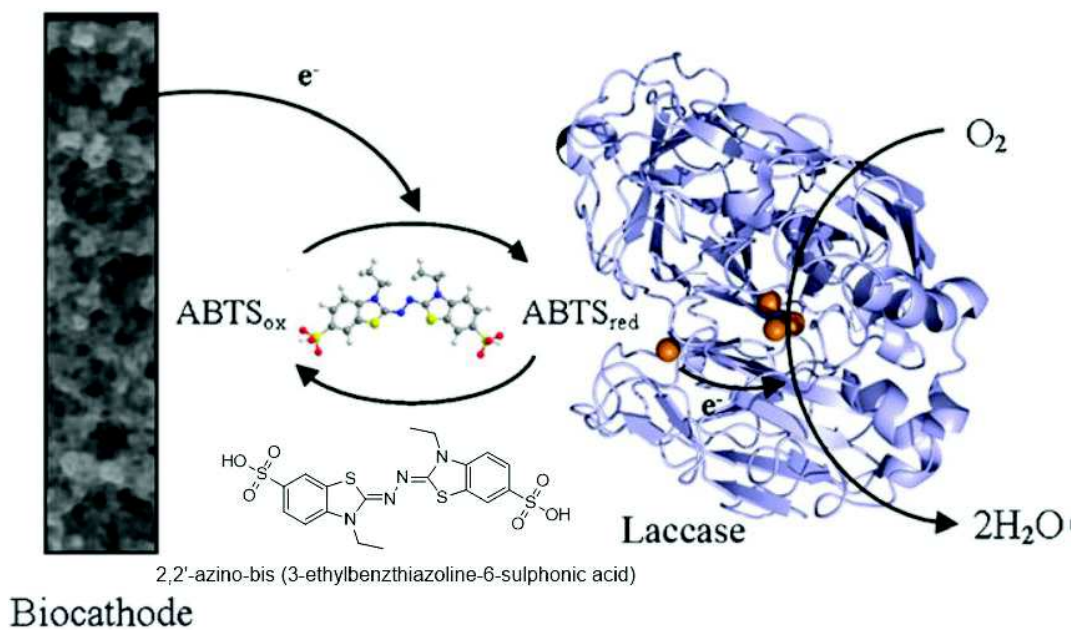


**Figure 84: Electron transfer processes at the biocathode. [153]**

Another important aspect, in preparing biocathodes, is the available surface. One solution comes in the form of electrospun PAN fibers (polyacrylonitrile). These form a 3D structure, while their parameters (thickness and surface area) can be closely controlled. Since they don't present conductivity, they must be modified accordingly.

The first approach could be the thermal treatment of such material until the material becomes carbonized and conductive[153]. The advantage of this approach is that the resulting electrode are self-standing, not requiring a support. The resulting material had a surface are of 11.8 m<sup>2</sup>/g and a conductivity of between 26-70 S/cm<sup>2</sup>. The enzyme was

then incorporated in the fibrous mass. A film of pyrrole was electropolymerized over the electrode.

The resulting cathodes through this method displayed high efficiency in terms of current output of  $950\mu\text{A}/\text{cm}^2$ . This is attributed to the direct interlocking of the enzyme in the electrode. Compared to the values reported in literature for laccase with ABTS as mediator on various supports the system is several times more performant, as seen in Table 12.

**Table 12: Current densities of various cathodes prepared with the Laccase/ABTS couple**

| <b>Electrode type</b>  | <b>Current density<br/>(<math>\mu\text{A}/\text{cm}^2</math>)</b> | <b>pH<br/>value</b> |
|--|---|---------------------|
| <b>Silica on porous carbon paper</b>                           | 450[154]  | 5                   |
| <b>Carbon ceramic electrodes</b>                               | 150[155]  | 4.8                 |
| <b>Modified carbon nanotubes with Nafion/glassy<br/>carbon</b> | 120[156]  | 5.2                 |
| <b>Polypyrrole on porous carbon tubes</b>                      | 300[157]  | 4.8                 |
| <b>Carbonized PAN fibers covered in polypyrrole</b>            | 950   | 3                   |

A second approach is the sputtering of gold on the spun fibers[152]. This modification makes the electro spun fibers conductive while keeping their macroporous structure. A support of silica wafer was used in order to perform the gold sputtering. The thickness of the gold layer was controlled during the deposition procedure.

The electrodes designed in this procedure had the enzyme immobilized on their surface and protected by a layer of Nafion. The output of the electrodes was very high, of  $3\text{ mA}/\text{cm}^2$ . Due to the leaching of the ABTS, as well as the natural inactivation of the enzyme, this current density decreased to half of its initial value over the course of 6 days (Figure 85).

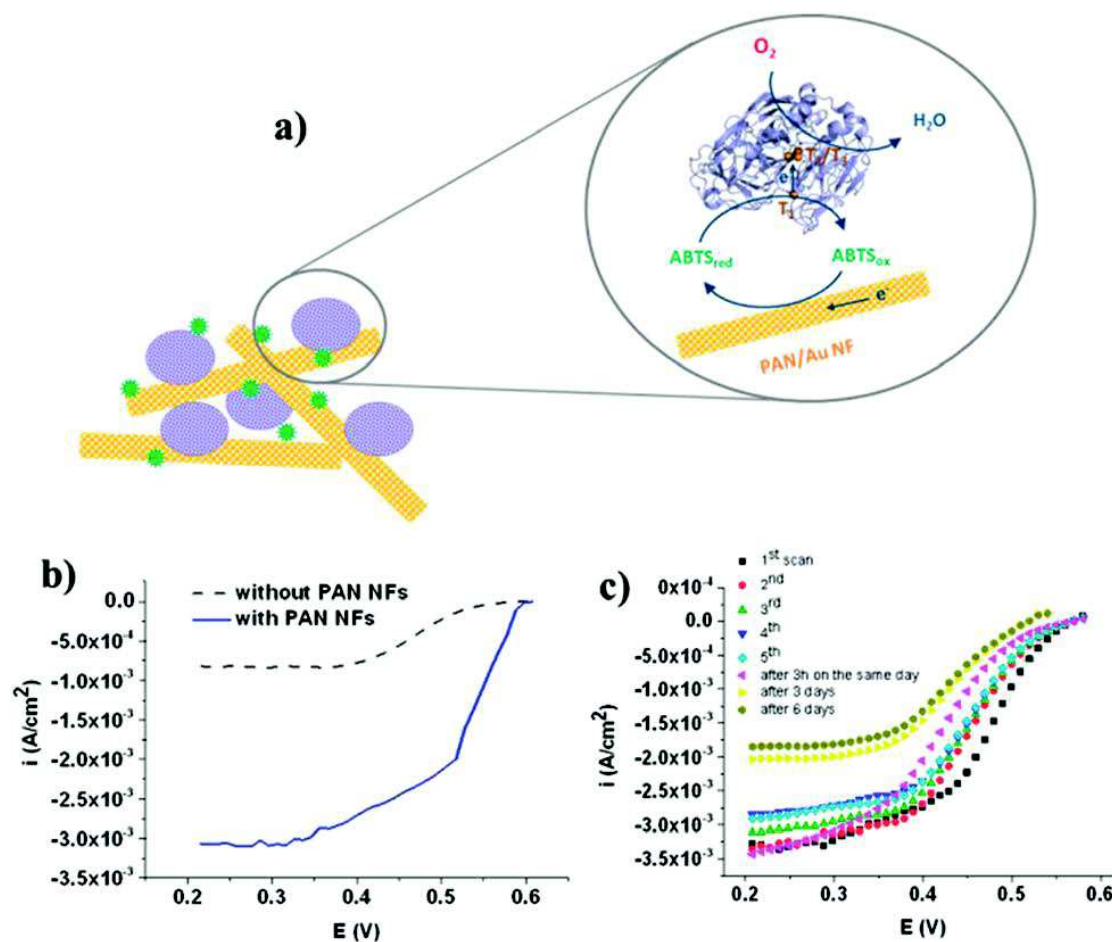


Figure 85: a) Schematic pathway for electron transfer between the PAN/ Au NFs and O<sub>2</sub>. (b) Polarization curves of a biocathode with and without PAN NFs in O<sub>2</sub>-saturated phosphate solution (pH 5, 0.1 M). Scan rate 3.3 mV s<sup>-1</sup>. (c) Stability of the PAN/Au NFs bioelectrode evaluated from polarization curves plotted the 1st day after repeated scans, after 3 h, and the 3rd and 6th days [152]

In conclusion, there are a few key aspects to keep in mind concerning the improvement of the performances of Laccase biocathodes. Firstly, a large surface area, which increases significantly the performance of the cathode. Supports that present large specific areas, like fibers, carbon nanotubes or carbon powder, have a positive effect on the efficiency of the electrode. Secondly, the used chemical mediator, ABTS, has a tendency to diffuse in the solution. This can be partially circumvented by coating the surface with a fluorinated ion-exchange polymer, Nafion, which slows down this leakage of mediator. However, this can't be mitigated totally. Lastly, when considering bioelectrodes, one must take into account the natural inactivation of the enzyme, meaning a limited life span for the resulting electrodes.



### 3.1.4. Project Objectives

The objective of this chapter is the design and application of a system composed from the self-assemblies of conducting species, inserted in an oriented mesoporous matrix.

The concept is to go from the angstrom size of a molecule, to the nanoscale size of the supramolecular structure of the molecule. Then, to integrate these structures with conductive properties in a macroscale device, resulting in an array of nanocontacts (Figure 86). These will be able to perform electron translocation and will be suitable for applications such as biocathodes. This project is a collaboration with the SAMS team from Institut Charles Sadron, Strasbourg, as part of the DYNANO Marie Curie ITN.

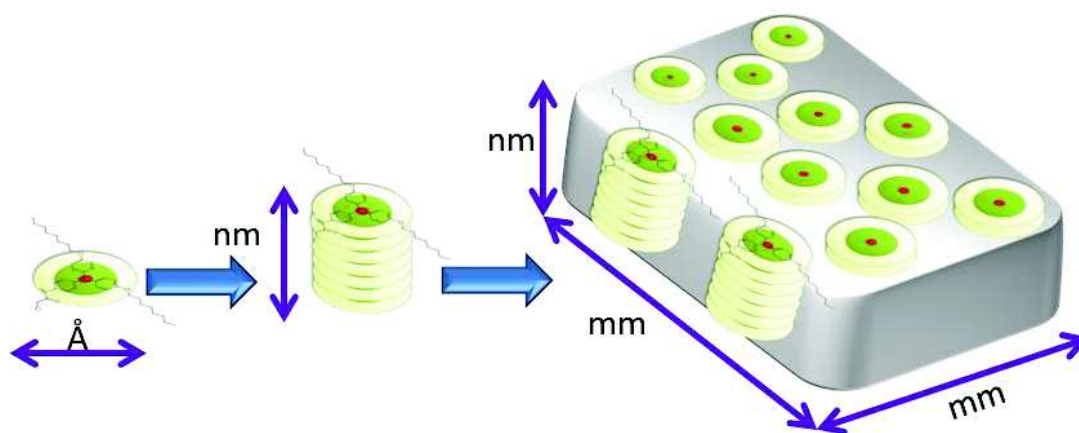


**Figure 86: Concept of the device. Individual nanoscale contacts are spread and distributed in the silica matrix**

Oriented mesoporous silica was chosen as the matrix which holds the TAA nanostructures for several reasons. The confined medium is needed in order to keep the nanofibrils in place. Moreover, silica is isolating, offering the perfect support in which the individual structures constitute the only means of electron transport between the gold

surface and the external solution, ensuring the criteria of generating nanoscale contacts. Another reason is the easiness of modification presented by silica, in order to be able to accommodate the TAAs in the mesoporous structure through hydrophobic interactions.

The silica was generated through a process of templated electrodeposition. This method allows a very good control over the type of silica created, while the surfactant template generates well defined and relatively uniform pores. The deposition was done on gold electrodes (glass plated with a layer of deposited gold).

The successive modifications of the generated device were followed by means of electrochemical measurements, cyclic voltammetry and impedance spectroscopy. These techniques are very accurate, present very good sensitivity and have high reproducibility. The surfaces of the electrodes were characterized both morphologically through electronic microscopy (Scanning Electron Microscopy (SEM) and Atomic Force Microscopy (AFM)) and composition wise through X-ray photoelectron spectroscopy (XPS).

The compounds used were two triaryl amine derivatives (TAA1 and TAA2) kindly provided by our collaborators at ICS Strasbourg (Figure 87).

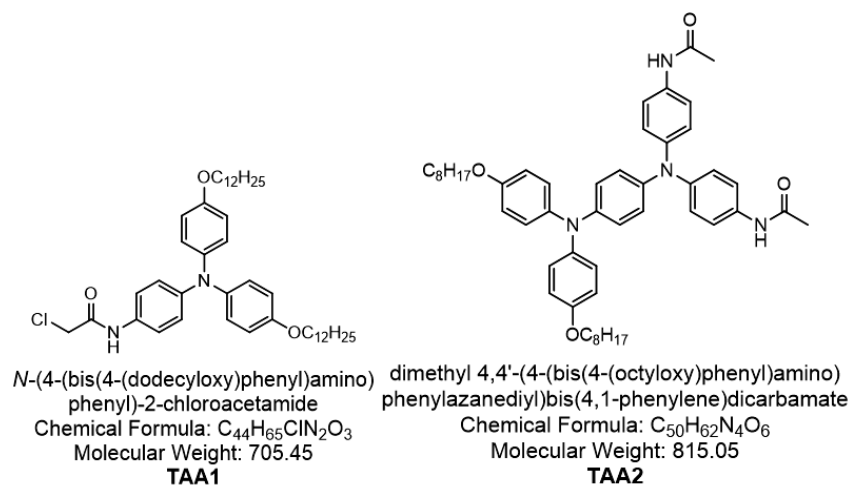


**Figure 87: Structures of TAA1 and TAA2**

## 3.2. Experimental Results

### 3.2.1. Electrode Manufacturing

The electrodes were made via a 5 step procedure presented in the scheme (Figure 88). The first step is the templated condensation of silica on the gold plate using an applied negative potential. The surfactant is then removed in step 2 in order to obtain the mesoporous thin layer; with the pores perpendicularly oriented to the surface. In step 3 the pores are modified to be more hydrophobic and suitable for step 4 the doping of the electrode with the active agent, the triaryl amines (TAA). In order to obtain the functioning biocathodes another step is required, the enzyme immobilization on the electrode surface. All these steps will be presented in detail in the following sections.

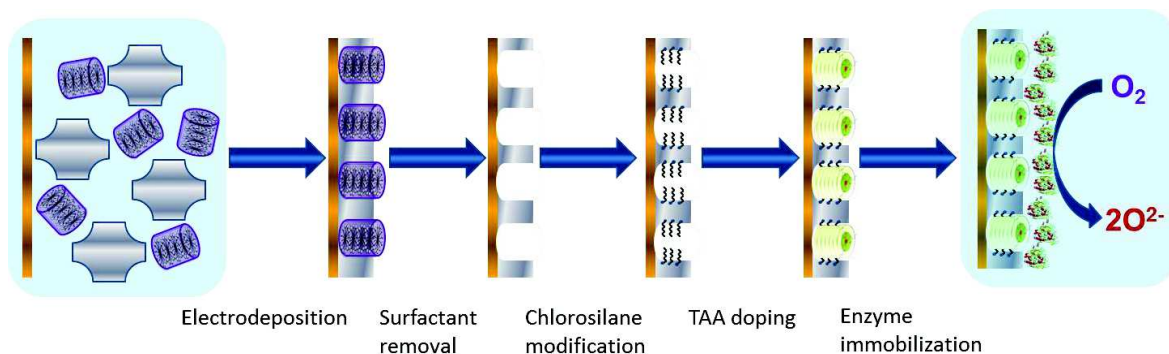


**Figure 88: Electrode manufacturing process**

The gold electrodes used are glass plates, with a layer of 60 nm of chromium over which a 300-400 nm layer of gold is deposited. The electrodes are cleaned, both chemically and electrochemically (Annexes), prior to the electrodeposition of the silica layer.

The mesoporous layer of silica is made of a sol-gel mixture containing the surfactant, which acts a templating agent. The sol-gel is a mixture of two solutions, one of which is alcoholic and one that is aqueous. The aqueous one contains NaNO<sub>3</sub> (0.1M) in which CTAB (cetyl trimethylammonium bromide) is dissolved. CTAB is commonly used in silica synthesis to generate controlled pore sizes of 40-50 Å. The NaNO<sub>3</sub> serves both as electrolyte but also is required in the condensation of the silica. The alcoholic phase contains TEOS (tetraethoxy orthosilicate), MPMTS (3-thiopropyl trimethoxy silane), both dissolved in absolute ethanol, the two components being in a molar ratio of 4:1. The TEOS is the main precursor for silica, while the MPMTS is necessary in order to make the silica adhere to gold, via a thiol bond. When the two solutions are homogenous, they are mixed together and HCl (0,1M) is added to obtain a final pH of 3. The sol-gel is left to hydrolyze for 2.5 hours.

The pH is important since the condensation of silica from siloxanes is a two-step process. The first step is the hydrolysis of the precursor and takes place in an acidic pH (ideally pH=3), while the second in a basic medium (pH=8) (Figure 89). Since the polymerization of the silica must be controlled and done electrochemically, the pH must remain acidic until a negative potential is applied to the gold electrode.

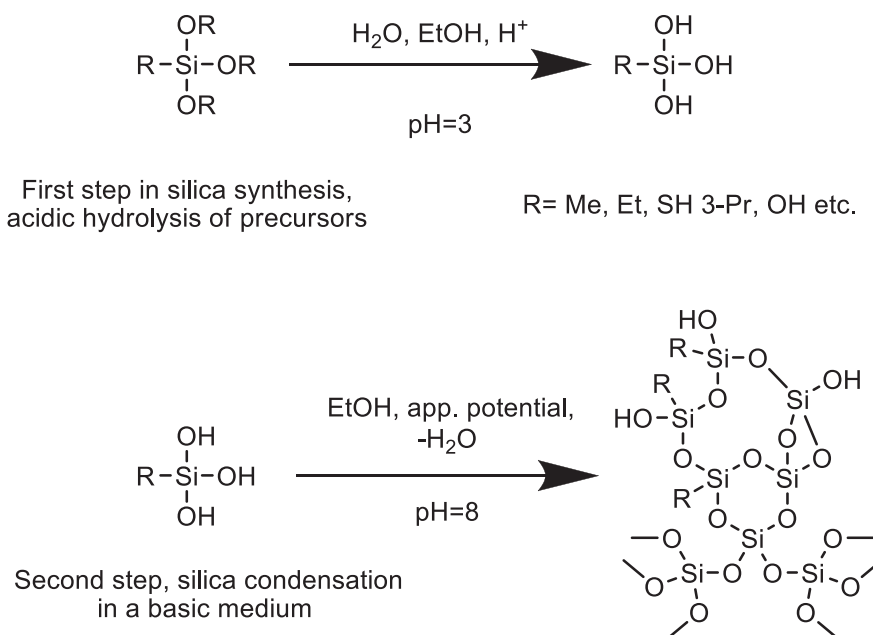


Figure 89: Silica polymerization from precursors

The electro-deposition is made in a standard 3-electrode system electrochemical cell. The reference is an Ag/AgCl standard electrode, the counter electrode is a steel plate electrode and the working electrode, on which the silica will be deposited, is the gold on glass plate.

To obtain the silica film on the gold surface, a negative potential is applied on the working electrode that induces the production of hydroxide ions, according to the reaction (1):



This results in a locally increased pH at the interface, to a value which promotes the polymerization of the silica. It also makes the cationic surfactant to stick electrically to the gold surface, which, in turn, forces the silica to condense around it. Through this process the templated mesoporous structure is obtained.

The potentials tested were: -1.2V, -1.4V and -1.6V vs. the reference electrode. The deposition time was also varied, between 5 and 30 seconds, in concordance to previous work[124]. The optimal conditions were found to be a potential of -1.4V and a time of 10 seconds, in regards to the limitations, a uniform and homogenous deposition with a defined layer thickness. A layer too thick would not generate straight, perpendicular pores, while this method is not suited to produce layers that are extremely thin. The variation of these parameters resulted in a compact porous layer of an average thickness of about 100 nm.

Scanning Electron Microscopy (SEM) was employed in order to describe the surface of the electrodeposited layer and its thickness (Figure 90). As mentioned previously, several parameters were varied, namely the deposition time and the applied potential during the deposition. The micrographs presented here correspond to an electrode manufactured using the following conditions, an applied potential of -1.4V and a deposition time of 10 seconds. From the surface micrographs the standard pattern of the electrodeposited, amorphous silica can be distinguished. The layer fully covers the

gold surface, without defects to the structure. The section micrograph reveals the thickness of the layer of approx. 100 nm. This thickness is considered ideal for applications, as earlier stated.

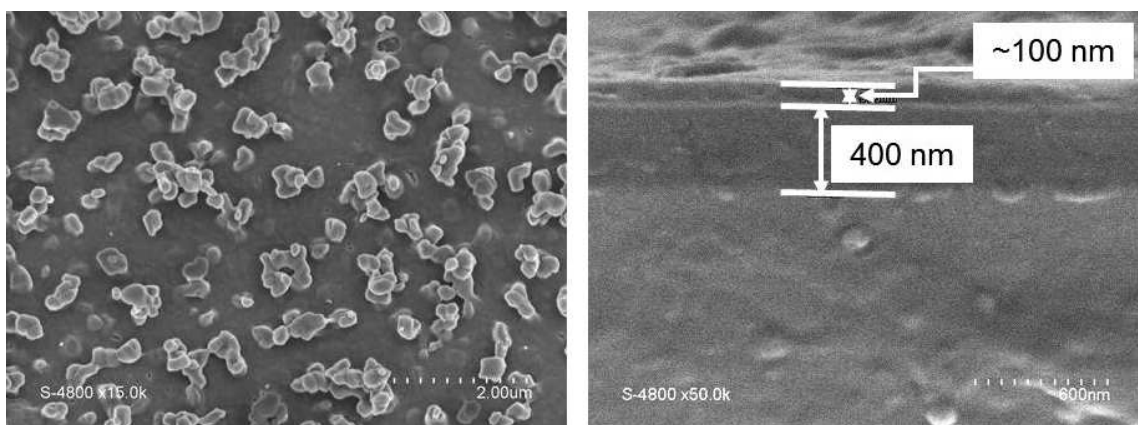


**Figure 90: SEM micrographs of the surface (left) and section (right) of an electrodeposited silica electrode. Scales: (left) - 2 $\mu$ m, (right) – 0.6 $\mu$ m. In section the thickness of the silica layer is seen 91.3 nm and of the gold layer 400 nm**

After the deposition the electrodes are cured overnight at 60°C to stabilize the polymeric silica network. The surfactant templating agent was then removed by washing the electrodes several times with distilled water and ethanol. The resulting porous surfaces are tested by electrochemical methods.

In order to create a suitable confined medium for the triaryl amines, the hydrophobicity of the silica must be modified. Silica is generally hydrophilic, while the TAAs are hydrophobic. This is achieved by treating the electrodes with a solution of chlorosilanes of different chain lengths (1 carbon atom, 6 carbon atoms and 18 carbon atoms) in toluene. Thus grafting on the inside of the pores hydrophobic alkyl chains that would act as anchors for the TAAs. Chlorosilanes are highly reactive species which can bind to the free hydroxyl groups of silica. This reaction is presented in Figure 91.

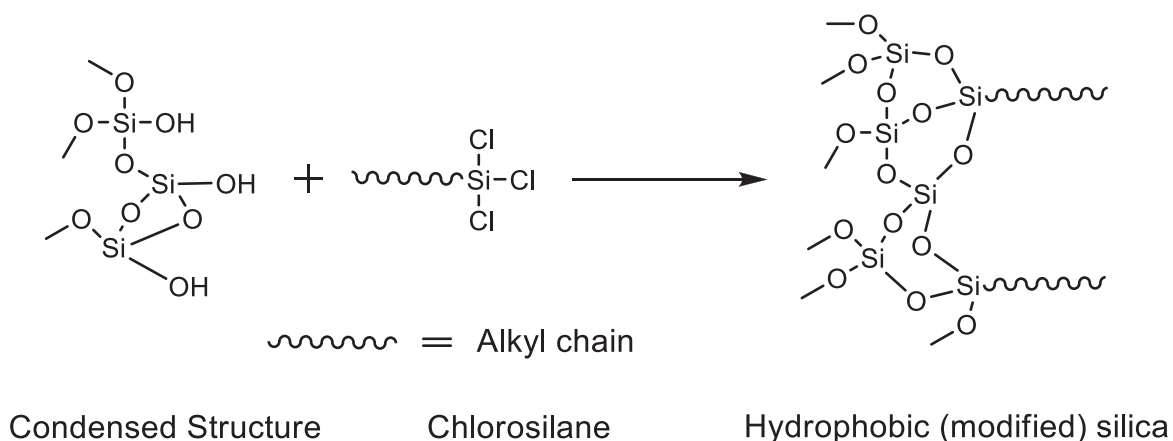


**Figure 91: Modification of silica with chlorosilanes**

The porous electrodes were immersed in a toluene solution of the respective chlorosilane (concentration of 50 mM) for 6 hours at a temperature of 60°C. After this time the hydrophilicity of the electrodes was drastically changed, as can be seen from the contact angle measurements (Figure 92).



**Figure 92: Contact angle measurements. Left: silica electrode, complete dispersion, angle =0°, middle C6 modified electrode, hydrophobic surface, angle=145.5°, right doped electrode, hydrophobic surface angle=149.3°.**

The hydrophilicity of unmodified silica causes the complete absorption of the water drop on the surface of the porous electrode. For the modified electrode an angle of 145.5° is obtained, confirming the change in surface properties. The hydrophobic interactions that would hold the TAAs in the pores are thus present.

The last step of the process is the doping using TAAs. As presented before, the modified TAAs have the unique property of generating a cationic radicals by irradiation, which then promote self-assembly, generating supramolecular structures. Their unidirectional conductive properties along the formed “fibril” have the purpose of connecting the gold from the bottoms of the pores to the electrolyte solution. The confined medium of the mesoporous silica will keep the fibrils intact. The doping procedure is performed by irradiating, with white light (approx.  $1\text{W}/\text{cm}^2$ ), a glass vial that contains the modified electrode, immersed in a chloroform solution of TAAs (1mg/ml). After an hour the self-association of the molecules is complete and it is considered that they have filled the pores. The resulting systems present very good stability, and are perfect working condition for at least a month in the presence of atmospheric oxygen. The protocol is described in the annexes.

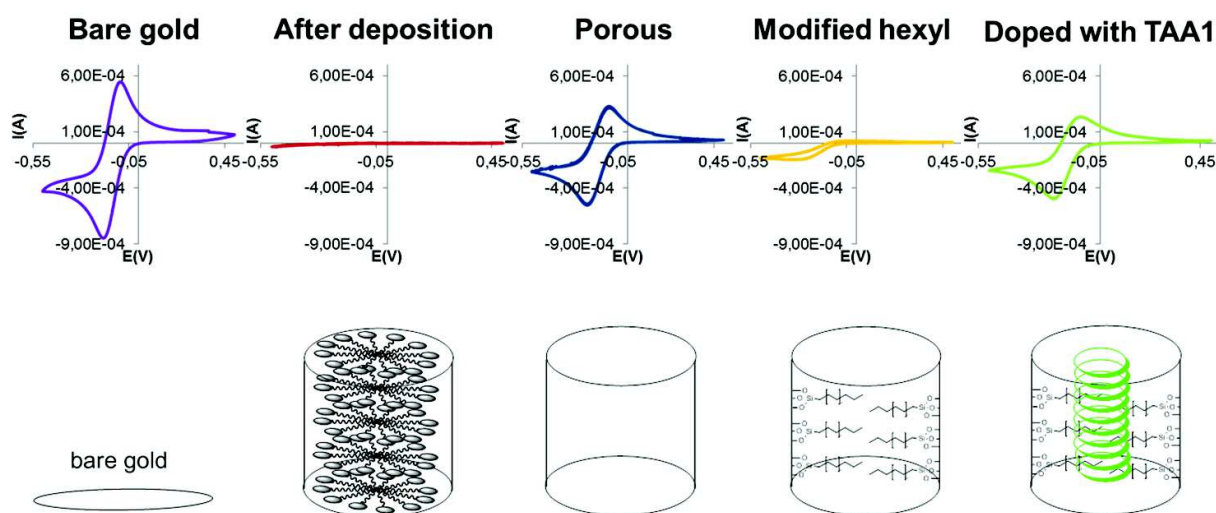
### 3.2.2. Characterization of the Electrode Manufacturing Process by Cyclic Voltammetry

Each step of the process was monitored by cyclic voltammetry. Cyclic voltammetry is a very reliable electrochemical analysis, which strongly relies on its good reproducibility. The method uses a redox probe, a compound that has well defined oxidation and reduction states, depicted by identified peaks. The potential values at which the redox probe exchanges electrons are called peak potentials ( $E_{ox}$ ,  $E_{red}$ ) and have an associated intensity of current ( $I_{p_{ox}}$ ,  $I_{p_{red}}$ ). From cyclic voltammetry the redox specie can be characterized by the peak current intensity and the separation of peak potentials ( $\Delta E_p$ ). The current intensity is directly proportional to the amount of reduced/oxidized species and thus, to the electroactive surface of the tested electrode. This property is essential in our case, since the modifications of the electrodes also, modify their electroactive surface.

The redox probe selected was the hexaamino ruthenium chloride,  $\text{Ru}(\text{NH}_3)_6\text{Cl}_3$ . Figure 93 depicts the electrode manufacturing process step by step, associating the



electrochemical signal of  $\text{Ru}(\text{NH}_3)_6^{3+}$  to the corresponding state of the pores. The cyclic voltammograms of  $\text{Ru}(\text{NH}_3)_6^{3+}$  (1 mM in  $\text{NaNO}_3$  100mM), using either a bare gold electrode or electrodes subjected to the successive steps of modification are presented on the same figure (Figure 94) for easier comparison. In this case, the doping of the mesoporous electrode was performed with TAA1



Successive surface modifications: (left to right) 1. bare gold, surface=electro-active surface, 2. after deposition, with the template inside, 3. after the removal of the template, 4. after the modification with chlorosilanes, 5. after the insertion of the TAAs

**Figure 93: Cyclic voltammograms of  $\text{Ru}(\text{NH}_3)_6^{3+}$  ( $c=1\text{mM}$  in  $0,1\text{M}$  aqueous solution  $\text{NaNO}_3$ ,  $v=20\text{mV/s}$  vs.  $\text{Ag}/\text{AgCl}$ ) at the electrodes subjected to the successive steps of modification**

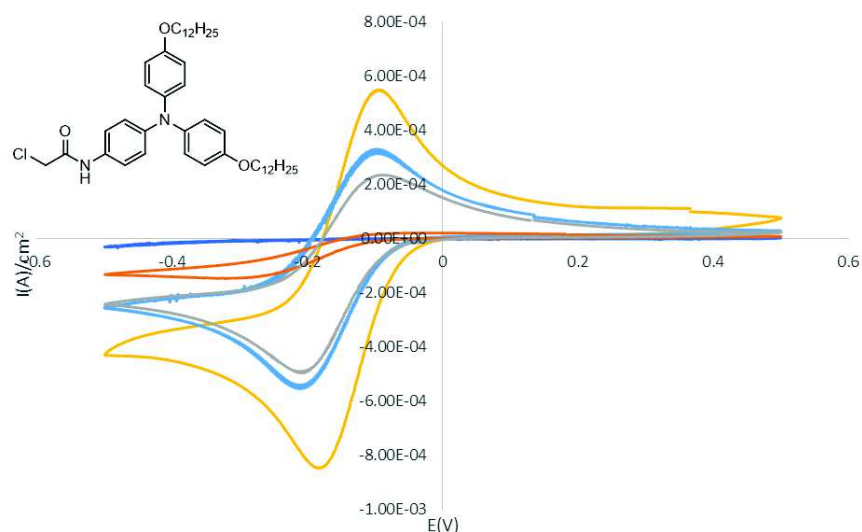


**Figure 94: Cyclic voltammograms of  $\text{Ru}(\text{NH}_3)_6^{3+}$  ( $c=1\text{mM}$  in  $0,1\text{M}$  aqueous solution  $\text{NaNO}_3$ ,  $v=20\text{mV/s}$  vs.  $\text{Ag}/\text{AgCl}$ ). Curves bare gold-yellow; after deposition-dark blue; porous-light blue; modified C6-orange; doped with TAA1-gray**

On bare gold, the redox probe is characterized by a well-defined  $\text{Ru}^{3+}/\text{Ru}^{2+}$  reduction and oxidation peaks ( $E_{1/2}=135\text{mV}$ ). Here, the electroactive surface corresponds entirely with the geometrical surface of the electrode. At this moment, the redox exchange can be done in any point on the gold. In the second step, the whole surface is covered by the electrodeposited silica, and the surfactant is still in the pores. It doesn't show any electrochemical signal, indicating that the silica structure generated is completely isolating. The third voltammogram depicts the behavior of the porous electrode, after the removal of the surfactant. Here the electroactive surface is much lower than the geometrical one, the redox exchange being done only through the gold on the bottoms of the pores. Since the intensity of the peak current is proportional to the surface, the actual electroactive surface can be determined. This was found to be around 66%. After the hydrophobisation of the pores, as seen in the fourth step, the weak electrochemical signal reveals hindered access of the redox probe in the hydrophobic, nano-sized, channels. However after the insertion of the TAAs in the pores the redox signal is restored, and is nearly equal to the one recorded for the empty pores system. This result shows that the

TAA assemblies are conductive, and are able to act as an electrical contact, between the ruthenium ions, and the gold surface on the bottom of the pores. Moreover the well-defined peaks as well as the total amplitude of the signal confirms the good conductivity of these structures.

The sol-gel procedure has the disadvantage of some reproducibility issues. On this account the electroactive surface can be calculated from the electrochemical peak currents. Both the intensity of the oxidation peak, and of the reduction peak, can be compared. Since a system is tested, entire intervals of current intensity are also evaluated. In conclusion, every system has to be compared to itself, since minor differences in the sol-gel composition, along with any electrochemical impurities on the electrode surface and charge uniformity issues during the electro-deposition, can result in a very strong effect on the surface obtained. A comparison between the geometrical surface (as in the case of gold equal to the electroactive surface), and the actual electroactive surface (in the case of porous electrodes) is presented lower. A large number of electrodes was tested and some of them are presented in Table 13. Although the available surface in the case of porous electrodes varies, we can conclude that it corresponds to 60-80% of the geometrical surface of the electrode. The calculations are made using the Randles–Sevcik equation (2).

$$i_p = 0.4463 nFAC \left( \frac{nFvD}{RT} \right)^{\frac{1}{2}} \quad (2)$$

With  $i_p$  = current maximum (A);  $n$  = number of electrons transferred in the redox event (1);  $A$  = electrode area (cm<sup>2</sup>);  $F$  = The Faraday Constant (C.mol<sup>-1</sup>);  $D$  = diffusion coefficient of Ru(NH<sub>3</sub>)<sub>6</sub><sup>3+</sup> (cm<sup>2</sup>.s);  $C$  = concentration (mol/L);  $v$  = scan rate in V/s.

For the same experimental conditions, it results from equation (2) that:  $I_{p \text{ gold electrode}}/I_{p \text{ porous electrode}} = A_{\text{gold}}/A_{\text{porous electrode}}$ . By considering that the diffusion coefficient of the Ru(NH<sub>3</sub>)<sub>6</sub><sup>3+</sup> species in NaNO<sub>3</sub> in water is similar at the gold electrode surface and within the pores of the porous electrodes. It results  $A_{\text{porous electrode}} = A_{\text{gold}} * I_{p \text{ gold electrode}}/I_{p \text{ porous electrode}}$ .

**Table13: Electroactive surfaces for porous electrodes estimated from the Randles–Sevcik equation**

| <b>Porous Electrode number</b> | <b>I<sub>OX porous</sub>/I<sub>OX bare gold</sub> (%)</b> | <b>I<sub>RED porous</sub>/I<sub>RED bare gold</sub> (%)</b> |
|--------------------------------|---|---|
| <b>1</b>                       | 60.21%  | 65.31%  |
| <b>2</b>                       | 46.25%  | 73.07%  |
| <b>3</b>                       | 63.71%  | 72.15%  |
| <b>4</b>                       | 72.77%  | 82.42%  |
| <b>5</b>                       | 63.16%  | 93.33%  |

TAA2 doped electrodes were also manufactured. Given the larger size of the molecule these systems were less efficient than the TAA1 ones. Probably due to the difficulties of obtaining the self-assembled structures in the pores, where the anchorage was designed for the TAA1 structure. Still, the resulting devices were functioning and well-defined signal was registered. By comparison to TAA1, where the doped system presented a peak current intensity of 82% vs. the porous system, in the case of TAA2, the signal was just 25% confirming a lower doping yield, as can be seen in Table 14. The TAA2 system is presented lower in Figure 95.

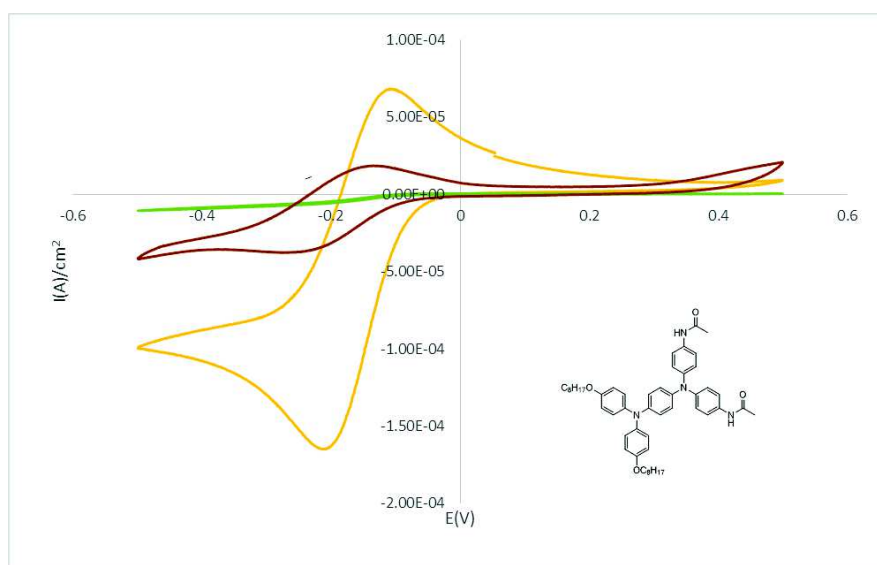


Figure 95: Cyclic voltammograms of  $\text{Ru}(\text{NH}_3)_6^{3+}$  ( $c=1\text{mM}$  in  $0,1\text{M}$  aqueous solution  $\text{NaNO}_3$ ,  $v=20\text{mV/s}$  vs.  $\text{Ag}/\text{AgCl}$ ). Curves: porous-yellow; modified C6-green; doped with TAA2-dark red. The first two steps of the process omitted for clarity.

Table 14: Comparison of the  $\text{Ru}^{3+/2+}$  signal at the doped electrodes with TAA1 and TAA2

| DOPED Vs. POROUS | $I_{\text{OX DOPED}}/I_{\text{OX POROUS}}$ (%) | $I_{\text{RED DOPED}}/I_{\text{RED POROUS}}$ (%) |
|------------------|--|--|
| TAA1 system      | 71.12%   | 89.59%   |
| TAA2 system      | 30.45%   | 22.78%   |

### 3.2.2.1. Electrochemical Detection of TAAs in the Pores

Cyclic voltammetry was also applied, to electrochemically detect the presence of the TAAs in the pores. Previously our colleagues from ICS Strasbourg were able to register the electrochemical signal for the TAA oxidation in a chlorinated solvent solution. The reported values of  $E_{1/2}$  were of approx.  $0.8\text{V}$  vs.  $\text{Ag}/\text{AgCl}$  for TAA1 and  $0.4\text{V}$  vs.  $\text{Ag}/\text{AgCl}$  for TAA2 (data not shown here). By conducting the experiment at very slow

scanning speeds (5mV/s) and in the absence of the Ruthenium redox probe, the electrochemical signal of the TAAs confined in the mesoporous electrode, can be registered in the NaNO<sub>3</sub> (0.1M) electrolyte solution.

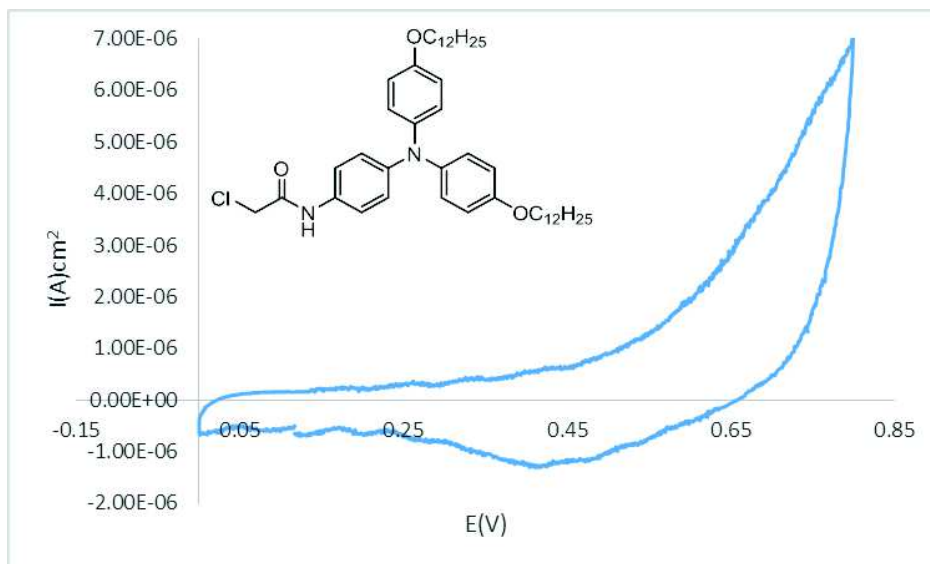


Figure 96: Electrochemical signal of TAA1. Electrolyte solution NaNO<sub>3</sub> (0.1M) scan speed 5mV/s ref. Ag/AgCl.

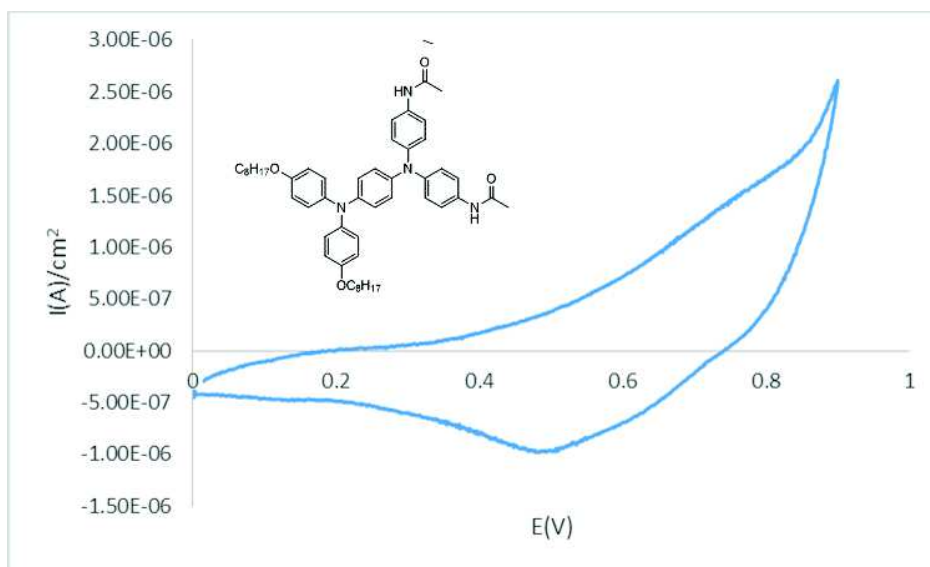
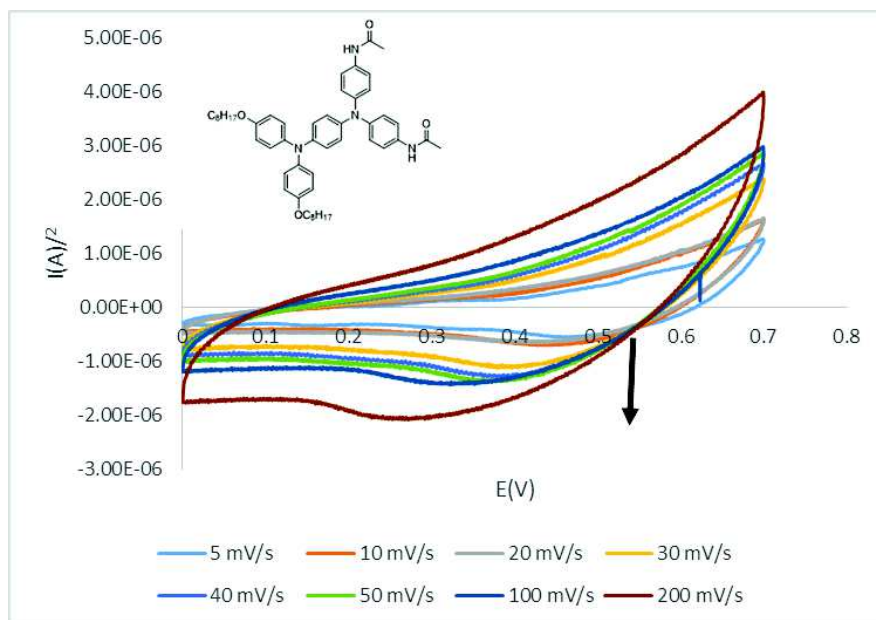


Figure 97: Electrochemical signal of TAA2. Electrolyte solution NaNO<sub>3</sub> (0.1M) scan speed 5mV/s ref. Ag/AgCl.

Figure 96 and Figure 97 illustrate the electrochemical detection of TAA1 and TAA2 in the pores. The current intensity for both TAAs is very feeble, and correlated directly with the very small amount of compound that is found in the pores. In the case of TAA1 the oxidation potential couldn't be reached without damaging the electrode. However the reduction potential was detected around 0.5V. In the case of TAA2 both potentials could be registered, due to the differences in structure this compound presents a lower oxidation potential, at 0.78V. The reduction potential for this species is encountered at 0.5V. By comparison to a porous electrode, the presence of the redox signal of TAAs, proves the confinement of these molecules in the pores.

One other test was performed on a TAA2 doped electrode, in order to verify further the presence of the TAA in the pores. The scan speed has been varied in order to see an increase in signal amplitude directly proportional to this increase. The expected result was obtained: the reduction peak current intensity, characteristic of TAA2 reduction, increasing with the scan speed, a mark of the presence of a chemical system. This result is presented in Figure 98.

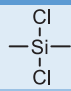
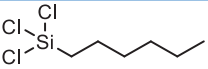
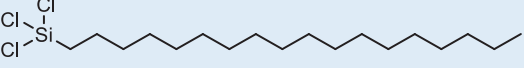


**Figure 98: Scan speed variation experiments of a TAA2 doped electrode. Electrolyte solution  $\text{NaNO}_3$  (0.1M) ref.  $\text{Ag}/\text{AgCl}$ . The peak current intensity and the peak potential vary with the increase of speed.**

### 3.2.2.2. Influence of Chain Length in Pore Modification

The incorporation of TAA1 in the pores was tested by varying the length of the alkyl chains within the silica mesopores. Three different chlorosilanes, that hold non-covalently the nanofibrils in place, namely chains of 1 (C1), 6 (C6) and 18 (C18) carbon atoms were applied (Table 15). The effect on the yield of doping was then monitored by cyclic voltammetry. Figure 99 compares the three types of modifications, and clearly shows that in the presence of C6 alkyl chains, the doping is one order of magnitude higher than the other types of functionalization, based on peak intensities. This higher affinity for the C6 modified pores is to be expected, given the two dodecyl chains present on TAA1 favoring hydrophobic interactions. The size of the pores decreases significantly by grafting the C18 modification, leaving very little space available for TAA1, while in the case of the C1 modification, the hydrophobic interaction is too weak to hold the TAA structures in place. The several fold difference in peak current intensity recommends the C6 modification to be optimal.

Table 15: Chlorosilanes used for silica modification

| Structure   | Name                             |
|---|----------------------------------|
|  | Dimethyldichlorosilane (C1)      |
|  | Trichloro(hexyl)silane (C6)      |
|  | Trichloro(octadecyl)silane (C18) |



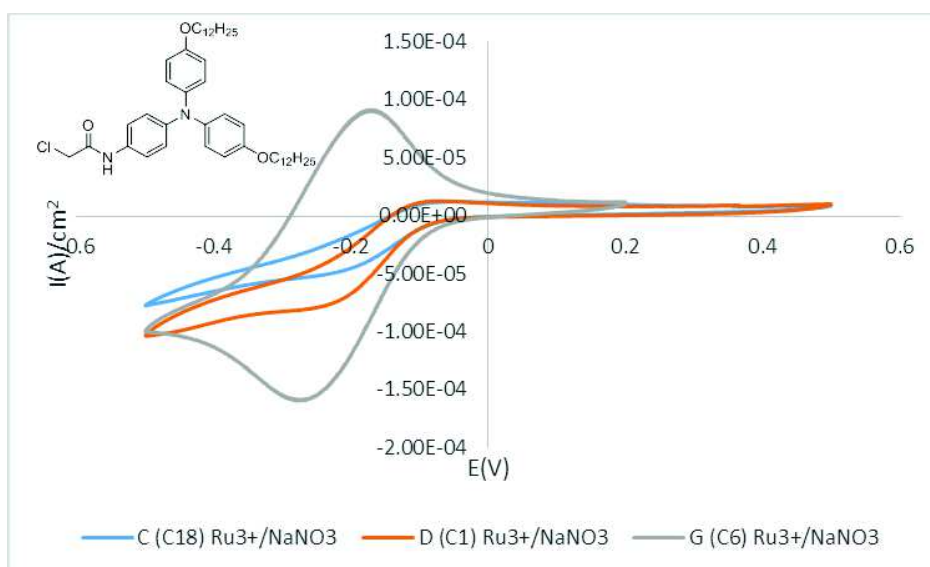


**Figure 99: Influence of chain length over doping. Cyclic voltammograms of  $\text{Ru}(\text{NH}_3)_6^{3+}$  ( $c=1\text{mM}$  in  $0,1\text{M}$  aqueous solution  $\text{NaNO}_3$ ,  $v=20\text{mV/s}$  vs.  $\text{Ag}/\text{AgCl}$ ). C18-blue, C6 gray, C1-orange, electrode doped with TAA1.**

### 3.2.2.3. Influence of irradiation

In a similar fashion, the influence of the irradiation on the doping process was evaluated. For this purpose, electrodes that were doped with the active compound under irradiation and in the dark were both prepared.

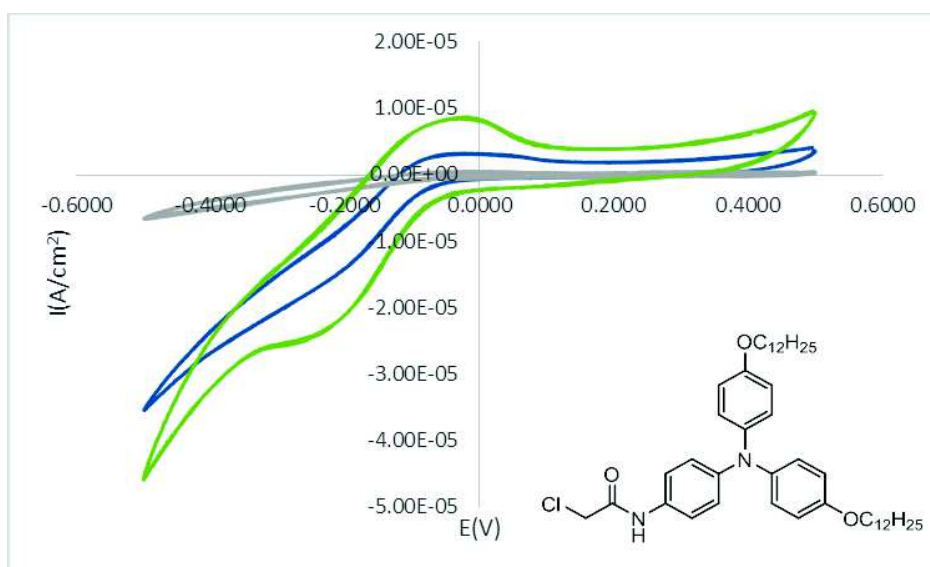


**Figure 100: Influence of irradiation on a TAA1 system. Cyclic voltammograms of  $\text{Ru}(\text{NH}_3)_6^{3+}$  ( $c=1\text{mM}$  in  $0,1\text{M}$  aqueous solution  $\text{NaNO}_3$ ,  $v=20\text{mV/s}$  vs.  $\text{Ag}/\text{AgCl}$ ). Gray- C6 modified electrode; Blue electrode prepared in the dark; Green- electrode prepared under irradiation.**

From the resulting cyclic voltammograms (Figure 100) of the redox probe, one can observe higher peak intensities for the system where the insertion of TAA1 was done under irradiation confirming, thus the importance of the self-assembling trigger.

#### 3.2.2.4. Influence of the Presence of TAAs

In order to display the electroactive characteristics of the TAAs, an electrode system containing tridodecyl amine,  $\text{C}_{12}\text{H}_{26}_3\text{N}$ , (TDA), was made in the same fashion as the TAA1 systems. The differences between the two chemical species is the absence of self-assembling and conductive properties in the case of TDA. Without the possibility to self-assemble in the form of charged nanofibrils, the resulting system is expected to not display any electrochemical properties. The process was monitored through cyclic voltammetry, and the result was the envisioned one as can be seen from Figure 101. This

also signifies that the electrode systems created only rely on the intrinsic properties of TAA in order to function.

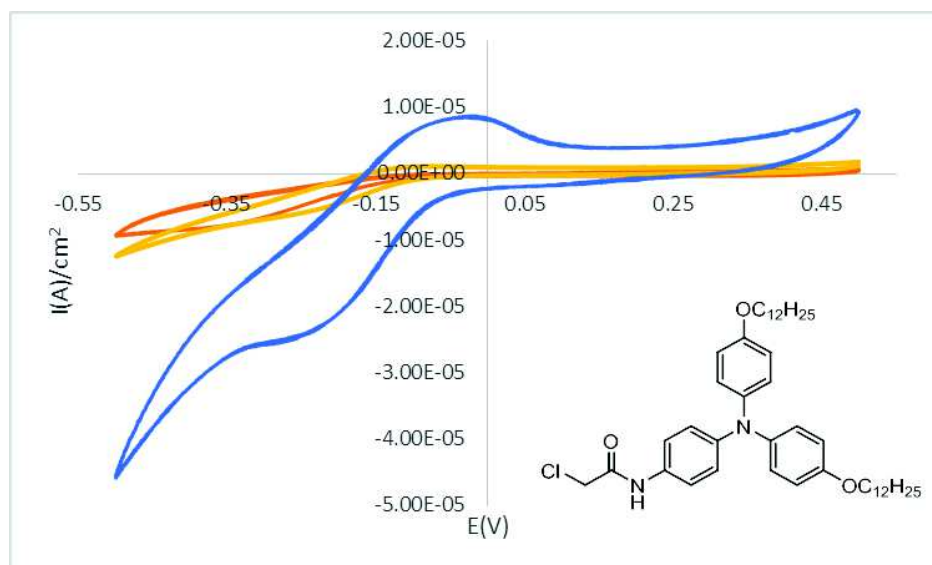


**Figure 101: Cyclic voltammogram of a TDA system, TAA1 system plotted for comparison. Cyclic voltammograms of  $\text{Ru}(\text{NH}_3)_6^{3+}$  ( $c=1\text{mM}$  in  $0,1\text{M}$  aqueous solution  $\text{NaNO}_3$ ,  $v=20\text{mV/s}$  vs.  $\text{Ag}/\text{AgCl}$ ). Orange- C6 modified system; Yellow- TDA doped system; Blue-TAA1 system.**

### 3.2.3. Impedance Spectroscopy

Electrochemical impedance spectroscopy (EIS) is used as an electrochemical method of characterizing systems. The measured parameter is impedance over a range of frequencies, practically registering the frequency response of the system. This reveals the energy storage and dissipation properties of the tested element. Since a theoretical model circuit can be attributed to a physical electrochemical system, a number of elements (like resistors and capacitors) and their connection type (series, parallel) are proposed. The experimental data is then fitted using this model circuit.

The resulting TAA1 electrode systems were characterized by impedance spectroscopy. EIS was performed in  $0.1\text{M}$  PBS (pH 7), containing the redox probe

potassium hexacyanoferrate trihydrate  $\text{Fe}(\text{CN})_6^{3-}/\text{Fe}(\text{CN})_6^{4-}$  10 mM. The frequency range on EIS was varied from 10 kHz to 0.1 Hz, with 10 points per decade, at the half wave potential ( $E_{1/2} = 0.208$  V). The EIS spectra are presented in Figure 102.

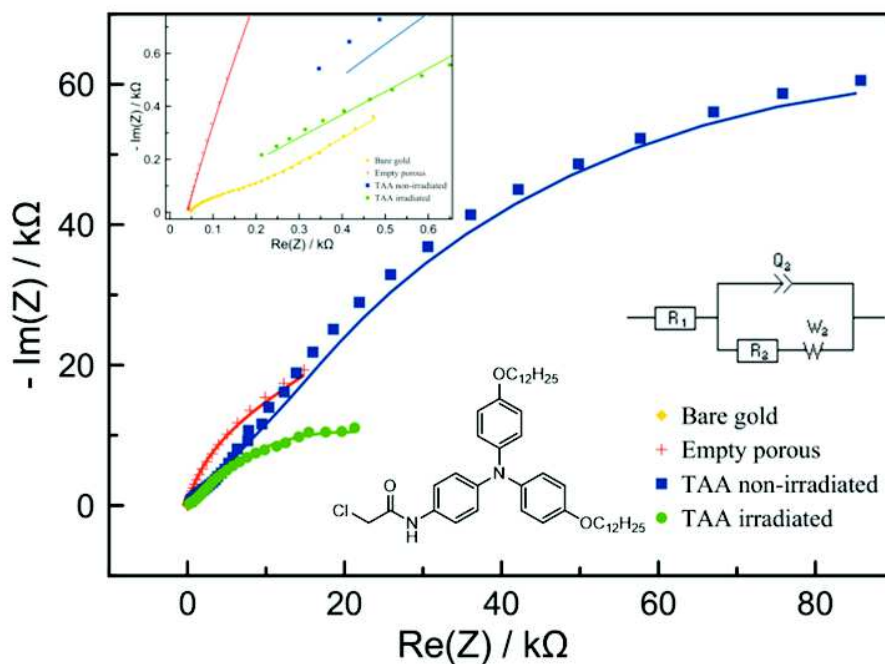


**Figure 102: EIS of the electrodes (frequency range 0.1-10 000 Hz) in a solution of 10 mM  $\text{Fe}(\text{CN})_6^{3-}/\text{Fe}(\text{CN})_6^{4-}$  in 0.1 M phosphate buffer, ref. Ag/AgCl**

A Randles circuit was proposed for the fitting of the results. The Randles circuit consists of an active electrolyte resistance  $R_s$ , in series with the parallel combination of the double-layer capacitance  $Q$ , and an impedance of a faradaic reaction. The impedance is associated to an active charge transfer resistance  $R_{ct}$  and an electrochemical element of diffusion, Warburg ( $R_{dif}$ ). This data is presented in Table 16.

**Table 16: The charge transfer resistance of modeled Randles circuit modeling was chosen to fit the impedance data.**

| Electrode                 | Rs/ $\Omega$ | Q       | A     | Rct / $\Omega$ | Rdif / $\Omega$ | Td   | Area  |
|---------------------------|--------------|---------|-------|----------------|-----------------|------|-------|
| <b>Bare gold</b>          | 46           | 7.3E-05 | 0.730 | <b>165.7</b>   | 1904            | 2.2  | 0.255 |
| <b>Empty porous</b>       | 39           | 5.0E-06 | 0.894 | <b>26733</b>   | 41037           | 0.76 | 0.35  |
| <b>TAA non-irradiated</b> | 0            | 1.8E-06 | 0.603 | <b>10385</b>   | 204223          | 0.10 | 0.331 |
| <b>TAA irradiated</b>     | 0            | 1.0E-05 | 0.480 | <b>156.8</b>   | 48182           | 0.07 | 0.336 |

The Randles circuit model fits the data quite well despite the 100nm silica layer. From the model, the charge transfer resistance should be a good approximation to the resistance provided by the wire. The bare gold charge transfer resistance can be used as the charge transfer resistance, intrinsic to the gold layer and to the transfer to the redox probe.

From the data obtained, a few conclusions can be drawn. The resistance (Rct) of the irradiated electrode is similar to that of the gold layer and both are two orders of magnitude under the control electrodes tested. This underlines the very good electrical properties of the TAAs. One last observation is linked to the importance of irradiation, the non-irradiated electrode strongly underperforming the irradiated electrodes.

By using the EIS data, the conductivity of the TAA can be determined. Assuming the silica layer thickness determined by SEM is the thickness of the path length of the TAA (91.3nm), and the determined polarization resistance is primarily from TAA charge transfer, the charge transfer resistivity of each layer can be determined by:

$$\rho = \frac{RA}{l}$$

Where  $\rho$  is the resistivity;  $R$  is the charge transfer resistance determined before,  $A$  is the surface of the electrode and  $l$  is the length of the layer. The calculations are presented in Table 17.

**Table 17: The charge transfer resistivity of modeled Randles circuit was chosen to fit the impedance data**

| Electrode                 | Rct / $\Omega$ | Area / $\text{cm}^2$ | Resistivity/ $\Omega \cdot \text{m}$ |
|---------------------------|----------------|----------------------|--------------------------------------|
| <b>Gold</b>               | 165.7          | 0.255                | 4.63E+04                             |
| <b>Porous Gold</b>        | 26733          | 0.35                 | 1.03E+07                             |
| <b>TAA non-irradiated</b> | 10385          | 0.331                | 3.77E+06                             |
| <b>TAA irradiated</b>     | 156.8          | 0.336                | 5.77E+04                             |

Assuming the surface area of the TAA determined by the XPS 25% (see chapter 3.2.4.), and the determined charge transfer resistance is primarily from the TAA wires; leads to a remarkable TAA wire conductivity of 0.39 mS/m (considering that the wires are not directly connected to the gold layer). In terms of resistivity the irradiated TAA has a very similar value to gold, confirming once again the metal-like conductivity exhibited by the species. Moreover if the resistivity intrinsic to the gold is removed and the charge transfer to the redox probe results in the resistivity of irradiated TAA layer alone of  $1.14\text{E}+04 \Omega \cdot \text{m}$ . By comparison in terms conductivity the other electrodes, are two times lower of the porous electrode and a five times lower for the non-irradiated TAA electrode.

### 3.2.4. Surface Characterization

The surface was characterized using three distinct methods scanning electron microscopy (SEM) which was presented in chapter 3.2.1., atomic force microscopy (AFM) and X-ray photoelectron spectroscopy. While the first two methods characterize the morphology of the surface on a micron and respectively nanometer resolution, the latter determines the chemical composition of the layer.

In order to describe the morphology of the layer on a nanometer level AFM methods were employed. These experiments were performed at Institut Charles Sadron, Strasbourg. This method can experimentally determine the size of the pores. This was found to be around 5nm, in concordance with the templated procedure used in the

fabrication of the electrodes and the theoretical data. The AFM topography of a porous electrode and a doped electrode are shown in Figure 103. The tips of the TAA1 fibrils are visible as coming out of the pores.

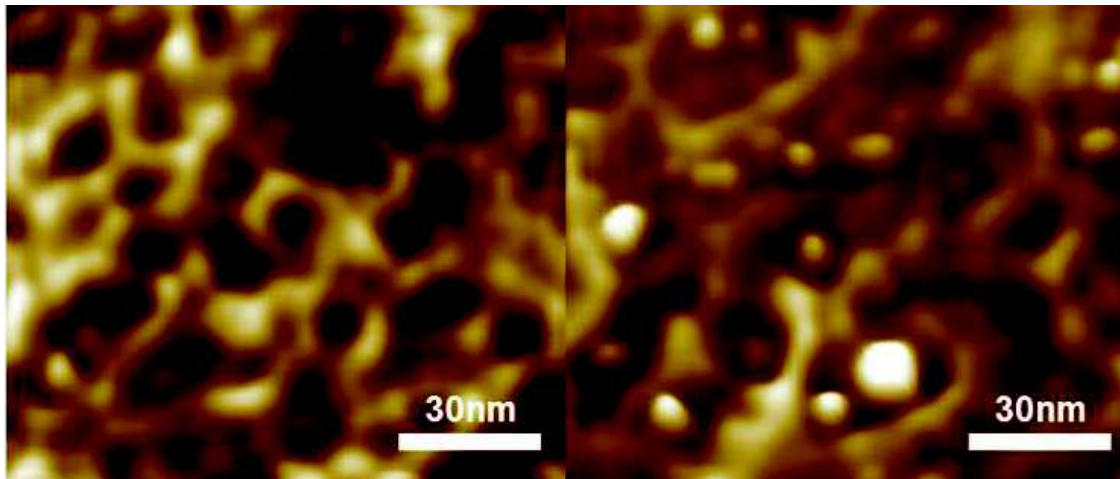


Figure 103: AFM topography of mesoporous silica electrodes. Left – before the insertion of the TAA; right – after the insertion of the fibrils. Courtesy of Prof. Mounir Maaloum SAMS team ICS Strasbourg.

By increasing the resolution to 5 nanometers, each individual pore can be characterized. At this scale the individual fibril tips can be described. The pictures reveal a bicolumnar arrangement of the TAA structures (Figure 104).

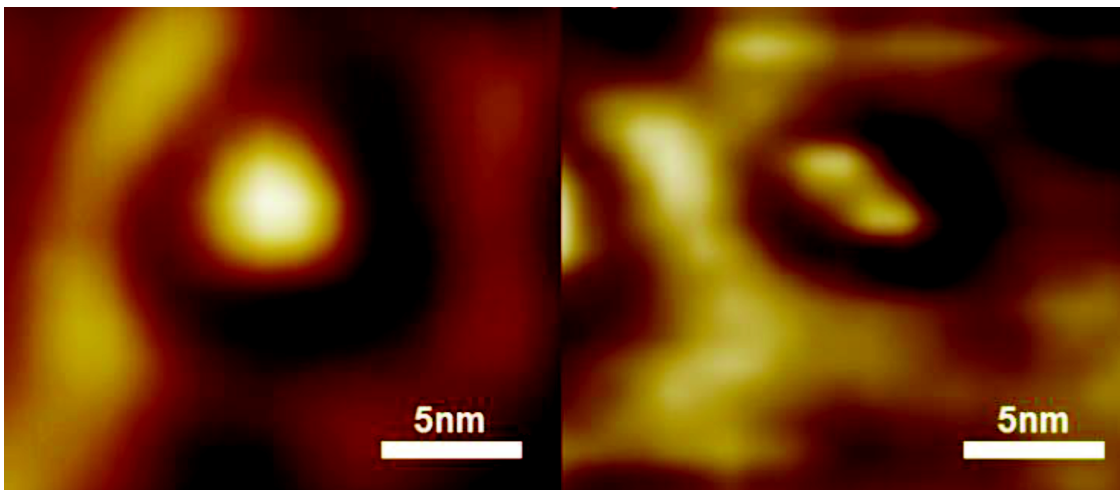
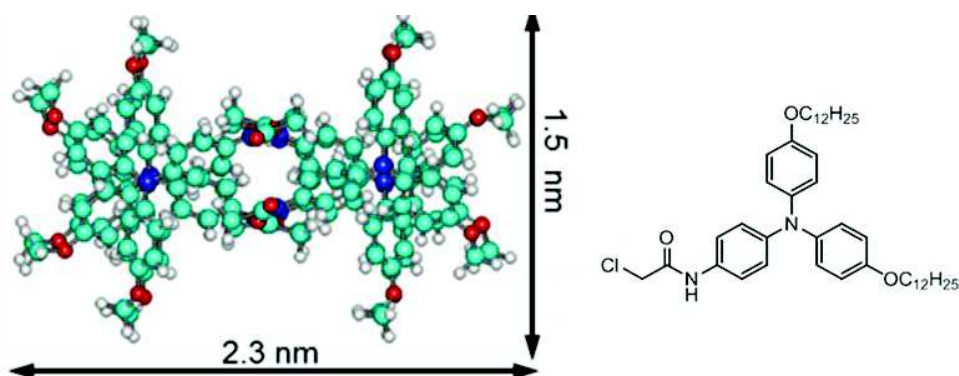


Figure 104: AFM topography of doped mesoporous silica electrodes. Doped individual pores are presented with fibril tips visible. Two interlocked structural units stick out of the cavity. Courtesy of Prof. Mounir Maaloum SAMS team ICS Strasbourg.

This finding fits well with the anterior published results on the self-assembly of TAA1 [146]. The generation of a cation radical pulls together other molecules generating a roll of coins-like structure. Taking into account the diameter of one molecule, which is equal to the diameter of an individual fibril, in a 5 nm pore two of these structures would fit. The two fibrils are held together by a zipper like hydrogen bonding. The representation of four molecules of TAA1 is presented lower (Figure 105)



**Figure 105: Model of 4 molecules of TAA1. Side chains not presented for clarity. Model elaborated at ICS Strasbourg**

XPS or X-ray photoelectron spectroscopy is a quantitative surface evaluating method. The modified the surface of the electrodes was evaluated using this technique. The results of the wide scan are presented in Table 18. By correlating the wide scan results with the high resolution results the chemical composition of the surface can be obtained. This then can be correlated with the information provided by the AFM study.



**Table 18: XPS results on modified silica electrodes**

| Sample      | Element (%)  | C     | O     | Si    | N    | S    |
|-------------|--------------|-------|-------|-------|------|------|
| Porous      | Atomic conc. | 43.28 | 34.69 | 15.68 | 4.25 | 1.5  |
|             | Mass conc.   | 31.62 | 33.76 | 26.79 | 3.62 | 2.92 |
| C6 Modified | Atomic conc. | 53.6  | 25.75 | 20.65 | 0.0  | 0.0  |
|             | Mass conc.   | 39.35 | 25.18 | 35.47 | 0.0  | 0.0  |
| TAA1 Doped  | Atomic conc. | 48.59 | 30.8  | 17.58 | 2.15 | 0.0  |
|             | Mass conc.   | 32.89 | 27.78 | 27.82 | 1.7  | 0.0  |

The results of the XPS analysis confirm the expected composition of the systems. The doped system in comparison to the C6 modified system contains nitrogen, from the presence of the TAA1 in the pores. Also the percentage of carbon decreases while the percentage of oxygen increases, as the insertion of the compound covers the C6 chains making them unavailable to be scanned. The porous system also contains traces of sulfur, from the silica precursor MTMPS, as well as some nitrogen and carbon from the surfactant template.

Moreover, the XPS data is complementary to the AFM findings, and makes available the calculation of the number of pores occupied by the TAA wires. Taking into account the dimensions of the two TAA molecules and considering that all the nitrogen signal comes from them, we can determine the area of  $1.5 \text{ nm} \times 2.3 \text{ nm} = 3.45 \times 10^{-18} \text{ m}^2$ . Since in this basic structure there are 4 nitrogen atoms per cell, the area can be divided by 4 giving a result of  $8.63 \times 10^{-19} \text{ m}^2$ . The ratio between the area of the TAA1 to a single nitrogen atom is  $8.63 \times 10^{-19} / 7.54 \times 10^{-20} = 11.5$ , where  $7.54 \times 10^{-20} \text{ m}^2$  is the area of the covalent radius of the circle defined by one single nitrogen atom. XPS determined a molecular percentage of 2.15% nitrogen, which makes the percentage of the TAA1 equals to  $2.15 \% \times 11.5 = 24.6 \%$ . This means that about one third of the pores are occupied by TAA1, taking into account that the porous surface compared to bare gold is between 60-80%, is in good correlation with the AFM observations. This relative percent further points at the very good electrical properties of the TAAs.

### 3.2.5. Design of Biocathodes

The doped electrodes were envisioned for an application as bioelectrodes. Bioelectrodes are components for biofuel cells, which oxidize a substrate at the anode using an oxidant generated at the cathode. The typical substrates are glucose, methanol or ethanol, while the oxidant is generally oxygen, making the byproduct of the biofuel cell water, a very attractive perspective. For this purpose the enzyme Laccase was used. The enzyme immobilization protocol is described in the annexes. This enzyme reduces oxygen to water in an acidic (pH=5) medium at high redox potentials. The chemical mediator, ABTS was used to provide quick electron transfer between the surface of the modified electrodes and the enzyme. Tests were performed to determine if the doping agents (TAAs) could also fill in the function of the chemical mediator, but were unsuccessful, meaning that the nanofibrils cannot access the electroactive core of the enzymes in these modified electrodes.

The electrochemical response of the electrodes (tested for each step of the process, doped or not with TAAs), are typical for the enzymatic reduction of O<sub>2</sub> in phosphate buffer at pH 5. The oxygen reduction current starts around 0.6 V vs Ag/AgCl and current densities feature a semi-plateau indicating a control of the electrocatalytic reaction by diffusion of O<sub>2</sub> to the active enzymes in the film. The presence of a peak around 0.3 V is attributed to the reduction of some weakly adsorbed ABTS molecules.

The modified electrodes were submitted to various tests, in order to characterize their efficiency. Bio-cathodes using TAA1 and TAA2 as doping agents were tested in terms of current intensity, initial potential and stability. For comparison reasons the same tests were done on porous and functionalized electrodes, as well as bare gold electrodes. For a TAA1 electrode, the open circuit potential ( $i=0$ ) was 590 mV and the current intensity was 240  $\mu\text{A}/\text{cm}^2$ . Bioelectrodes were also made using the other modified electrodes for

comparison reasons. One thing to point out is the case of the gold electrode, which presented an initial potential of 650mV and a current intensity of 220  $\mu\text{A}/\text{cm}^2$ . However this initial positive result is misleading, since the electrode couldn't be used after the first experiment. This is due to the lack of adherence of the enzyme mixture to the very smooth surface of the gold. These results are presented in Table 19

**Table 19: Current intensities and initial potential for the four types of bioelectrodes**

| <b>Electrode type</b> | <b><math>I_p(\mu\text{A}/\text{cm}^2)</math></b> | <b><math>E_{i=0}(\text{V})</math></b> |
|-----------------------|--|---------------------------------------|
| <b>Doped TAA1</b>     | 240  | 590                                   |
| <b>Modified C6</b>    | 140  | 490                                   |
| <b>Porous</b>         | 130  | 620                                   |
| <b>Bare gold</b>      | 220  | 650                                   |

The polarization curves are presented in Figure 106. In conclusion the TAA1 electrode displayed the largest current intensity, proving the importance of the TAA wires in the system. The stability of the electrodes was assessed by performing repeated scans on the biocathodes. These curves for the TAA electrode are also presented in Figure 106. The systems proved to stay within the parameters, the current intensity not varying significantly, with the sole exception of the bare gold electrode which had the adhesion issues.

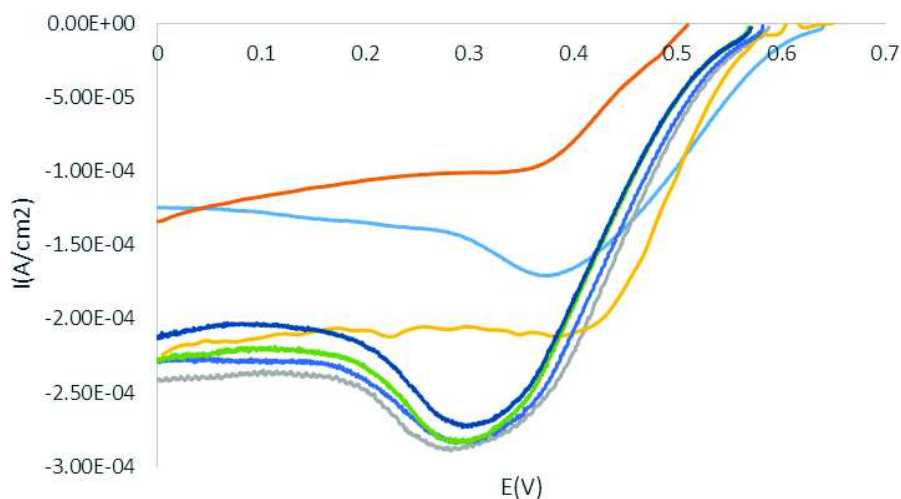


**Figure 106: Polarization curves of the biocathodes. Electrolyte solution PBS pH=5 (0.1M) scan speed 3.33 mV/s, ref. Ag/AgCl. Orange - c6 modified electrode; Light blue – porous electrode; Yellow – bare gold electrode; Gray, Dark blue, Blue and Green – TAA1 electrode.**

Since the enzyme Laccase loses its activity in time due to inactivation, as well as because of the leaching of the chemical mediator ABTS, several evaluations were made about this aspect. The conclusion was that the main cause of the decrease in activity was the diffusion of the chemical mediator ABTS from the enzyme containing layer. This was proven by adding ABTS to the electrolyte solution after two weeks, and performing the same experiment with and without ABTS. The results proved that the decrease in initial potential, and, to a somewhat extent, the decrease in current density is due to this factor. These experiments are presented in Figure 107 for a TAA1 electrode.

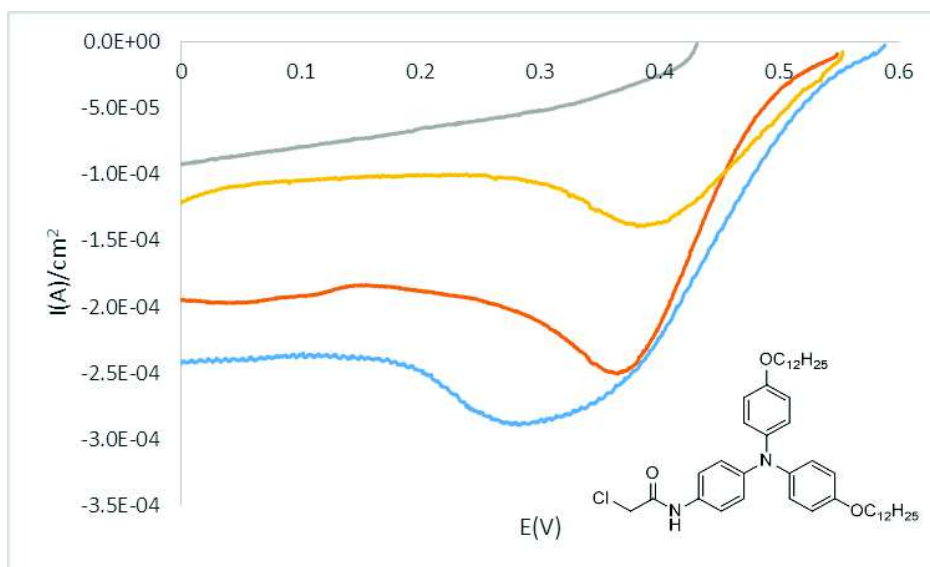


**Figure 107: Influence of the presence of ABTS.** Electrolyte solution PBS pH=5 (0.1M) scan speed 3.33 mV/s, ref. Ag/AgCl. Light Blue – day 1; Orange - day 5; Yellow – day 13 (added ABTS); Gray – day 13 (no ABTS); Green – day 21 (added ABTS); Blue – day 21 (no ABTS); Dark red – day 26 (added ABTS); Dark blue – day 26 (no ABTS).

The electrodes were tested over 4 weeks, in order to see the evolution of their performance in this period of time. The current efficiency was normalized to the initial activity (on day 1) and the results plotted in Figure 108. The conclusion is that the enzyme activity decrease isn't affected by the type of electrode used, the inactivation resulting in the same type of curve for all electrodes. After a period of four weeks, the electrodes retain a percentage of activity between 15-22% However, in absolute numbers the current intensity values are two fold greater for the TAA1 electrodes, compared to the other types of electrodes tested, as seen in the table in the annexes.

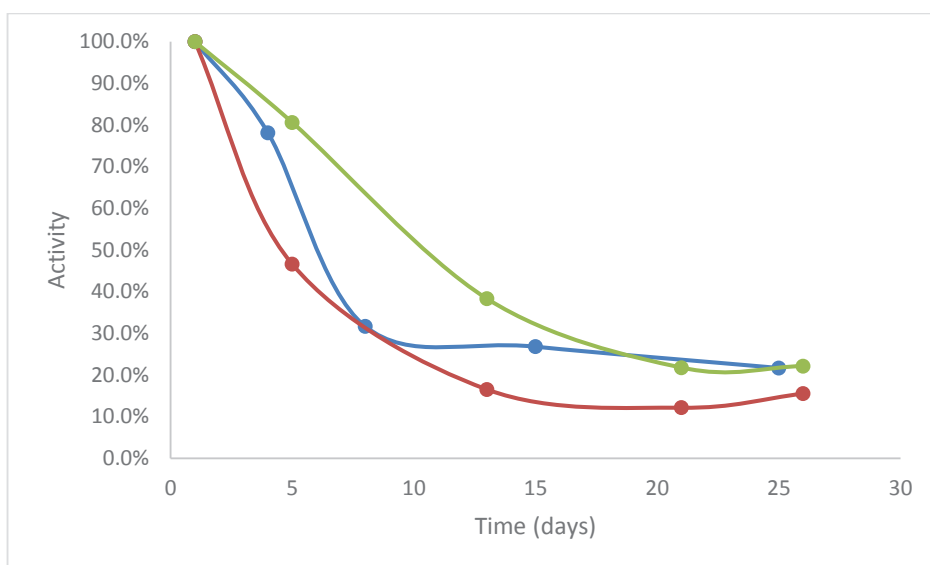


**Figure 108: current efficiency for the electrodes tested versus time. Values normalized to the initial current intensity of each biocathode. Blue – porous electrode; Orange – C6 modified electrode; Gray – TAA1 doped electrode.**

The results could be improved by other methods to immobilize the enzyme on the electrode surface, by avoiding the necessity of the chemical mediator, or by increasing the stability of the enzyme beyond 4 weeks, in order to increase the practical uses of the bioelectrodes.

### 3.3. Conclusions and Perspectives

A functioning system of nanoscale contacts has been designed and fabricated, based on growing supramolecular stacks of triaryl amine molecules inside the oriented mesopores of a silica layer. In the view of future applications, these systems were implemented towards the design of biocathodes.

The electrically charged nanofibrils which are generated by TAAs under irradiation have been successfully inserted in a templated mesoporous matrix. The resulting macroscale device is composed from an isolating silica layer that can transfer electrons only through the organic nano-assemblies. This array of nano contacts was characterized by electrochemical methods in order to verify both the presence of the TAAs in the pores, as well as, to monitor the preservation of the electrical properties of the supramolecular structures. The presence of the TAAs was evidenced also through AFM and XPS techniques, further describing structural factors, as well as the degree of the presence in the matrix. Throughout the project, comparison electrodes were used in order to test the effect of the presence of the electrical nano contacts. These tests showed that the system over performs on all criteria the comparison electrodes, and indeed the TAAs form efficient electrical contacts.

To take advantage of the resulting electric conduction of the doped electrodes, the manufactured electrodes were further implemented towards the construction of biocathodes. The resulting biocathodes based on enzyme immobilization, were applied to electrocatalytically reduce oxygen to water. The TAA doped biocathodes were two fold better in terms of current efficiency, compared to the control electrodes. The remarkable observation is the performance of the biocathodes, on the account of the very small amount of confined TAAs, and the very little specific surface .this, keeping in mind that the system is electroactive only through the tips of the nanofibrils.

From a perspective point of view the nano-sized electrode systems can be improved in several ways. From the practical point of view, the silica matrix can be modified in order to suit other types of TAAs. This could be done on the pore, by changing their diameter or shape, or on the hydrophobic anchor. Several other types of anchoring

systems could be envisioned, relying on stronger supramolecular forces, like hydrogen bonds for example. Other matrixes could also be designed, for example polymeric ones, the only criterion for a suitable matrix being the control over the structure, in the sense of a well-defined confined space to keep the TAA assemblies in place. From an application point of view, there are many opportunities in the field of organic electronics, taking advantage of the nanoscale of the electrodes in question, and their very good conductivity. Exploiting these two characteristics could lead us to envision a system that would act as an electrode, being able to permeate the lipid membrane of a cell, without having adverse effects on its integrity. This would provide a method to measure electrically such a complex unit as a living cell.



## General Conclusion

The transport process is a phenomenon ubiquitous in nature. Chemical species have to be translocated across living organisms, in order to maintain life through the balance of equilibria. Multiple mechanisms have been documented in regards to transport. These are both transporter specific and transported species specific. Natural transporters also display a remarkable efficiency as was reported in the introduction, i.e. Aquaporins.

This work approached the transport subject in a bioinspired fashion. It took a look at the natural solutions, as well as to previously reported synthetic solutions, in order to have an understanding of the key aspects. The first part, comprising the first and second chapters, applied the translocation of species on mimic cells, large unilamellar vesicles (LUVs). The LUVs are systems that emulate, in part, the complexity of a cell membrane. Through their tunable composition LUVs narrow the gap between natural occurring transport and entirely artificial transport.

The compounds used were small molecules. Their design was made in accord to the principles of supramolecular chemistry. The small molecules synthesized have three distinct segments: a hydrophobic part, constituted from an alkyl chain or an aryl moiety, which provides compatibility to the lipid substrate, an ordering structure in the form of the urea moiety, with its directional hydrogen bonding and multiple types of self-assembly presented in the introduction, and, finally a heterocycle moiety as the active center of the molecule. The species synthesized self-assemble in various supramolecular structures as a function of their structural variations.

The first chapter treated cation and proton transport across lipid bilayers. A library of 8 compounds was prepared and tested. X-ray single crystal diffraction did not reveal channel like self-assemblies, however the compounds proved to be active transporters. These highly dynamic small molecule systems have the inconvenient of being impossible to characterize in situ, in the lipid bilayer. Their transport effect was characterized by means of fluorescent ratiometric measurements. A structure feature that made a strong

impact on their activity was the presence of a fluorine atom in the para position of the phenyl ring. Versus all the species tested, the compounds that had this modification proved to be better transporters. The selectivity of the compounds proved to be low, and could be better characterized as a preference towards certain ions. This subject was not fully developed. Questions remain on the transport mechanism of these compounds, while a carrier type transport was proposed. One other feature to be exploited is the Voltage Clamp planar membrane transport experiments. This method has very good sensitivity and accuracy and would be a further confirmation of the fluorescence results.

The second chapter treated the transport of water and across lipid bilayers as part of a collaboration with Prof. Manish Kumar from Penn State University. Here also, a small library of compounds was created, presenting variations in chain length and chirality. One of the systems, HC6, was also described by molecular simulation techniques, for predicting its behavior in lipid membranes. This part of the project was done with the help of Marc Baden from Universite Paris Diderot. The supramolecular structure of the compounds, as was obtained from the X-ray single crystal diffraction, showed the strong influence of the hydrophobic tail on the formation of channel like structures. Namely, while the shorter members of the library present a very tight packing, the longer ones (HC6, HC8, RHC8, SHC8) present channels with hydrogen bonded water inside. The center of the channels is the I4 moiety, previously reported by our group. The water molecules are very well ordered and oriented in a continuous single file line, generating "water wires". The initial assumption, based on the X-ray diffraction data was confirmed from an activity point of view in regards to transport. Our collaboration allowed two approaches to be experimented in the transport of water, either by inserting the channels on the outside or, directly in the LUV membrane. The longer members of the library had better water transport capabilities. The two chiral HC8 isomers, R and S displayed different behaviors towards the translocation of species. This phenomenon was further investigated and the hypothesis of different insertion speeds was formulated. The promising water transport results encouraged further testing on protons and cations. The systems proved to be very good proton transporters. Moreover they present very good selectivity against sodium. This finding proposes this type of systems as suitable for applications in the field of water purification.

The third chapter treats the translocation of electrons through nanoscale organic electrical contacts. This work was done in collaboration with Professor Nicolas Giuseppone and his group, SAMS, from Institut Charles Sadron Strasbourg, as part of the DYNANO Marie Curie Actions ITN. Triaryl amines (TAAs) are organic species that don't present any conduction properties. However, some TAA structures are able, under irradiation and in a chlorinated solvent to produce a cation radical molecule. This molecule then pulls together its neutral counter parts, and self-assembles into a column like structure, a nanofibril. These nanofibrils are reported to present metal-like conduction properties. They transport electrons in a unidirectional fashion, only through the center of the fibril. This project's objective was the design and manufacturing of a confined medium system in which these structures could be kept intact in their self-assembled form, while being able to exploit their electrical properties. The solution was the fabrication of a mesoporous silica matrix on the gold surface of an electrode. This material was obtained through templated electrodeposition methods in order to control the size and shape of the resulting pores. The TAAs were inserted in the 5 nm pores and a working device was created. The central point of this project is that the resulting electrode communicates from an electrochemical perspective with the environment through the nano sized TAA contacts. The system was described through electrochemical methods like cyclic voltammetry and impedance spectroscopy. The conclusion of these was the retention of the good conductivity properties of the TAA self-assemblies. The presence of the TAAs in the porous matrix was detected electrochemically, through X-ray photoelectron spectroscopy and atomic force microscopy methods (AFM). The AFM study confirmed the presence of two fibrils in each pore. An application was envisioned for the resulting electrodes in the form of biocathodes. The enzyme Laccase was immobilized on the surface of the mesoporous silica, being connected to the gold underlay only through the TAA molecular contacts. The resulting biocathodes performed better in terms of current intensity over control electrodes, proving the positive effect of the presence of TAAs. This result encourages future pursuits in designing electronic devices containing organic species with very good conductive properties such as TAAs.

The translocation of species over different environments is as fascinating as it is wide. By using the principles of supramolecular chemistry transporters have been

designed with applications for water, ions, protons and even electrons. This transposition of theoretical notions into practical system conception is the very definition of materials' chemistry. I hope that this work will make a small contribution to this area of research and will help in its development.

# Annexes

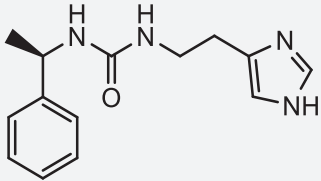
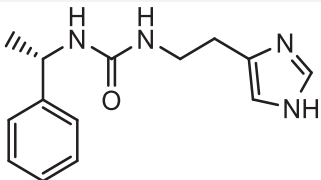
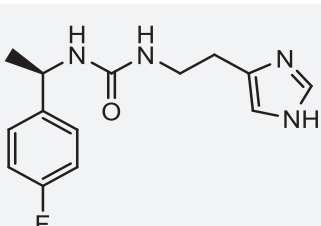
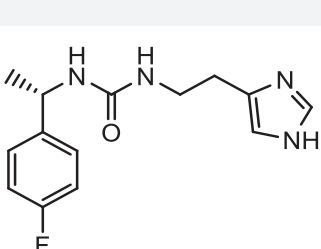
## Chapter 1 and Chapter 2

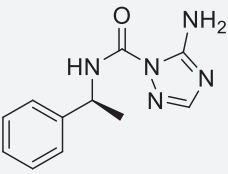
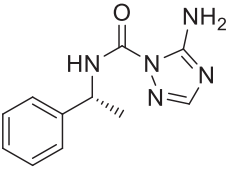
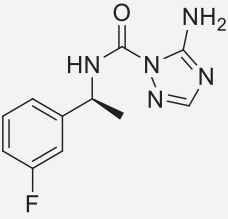
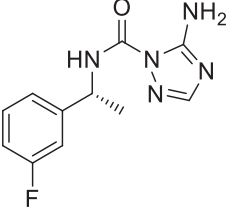
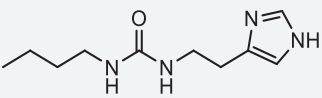
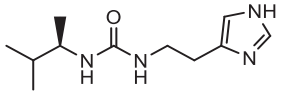
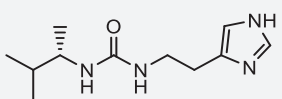
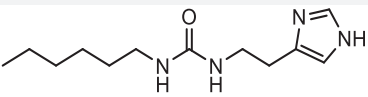
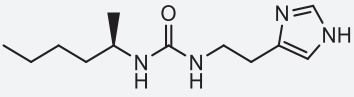
### Compounds' synthesis and characterization

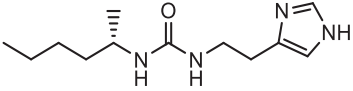
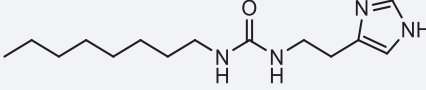
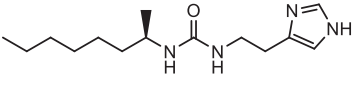
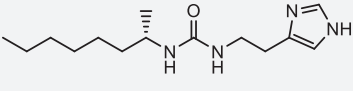
#### Synthesis

For this project the following compounds were synthesized and characterized:

Table 20: List of compounds synthesised

| <i>Nr</i> | <i>Structure</i>  | <i>Structure name</i>   | <i>Chemical formula</i>                           | <i>Molecular weight</i> |
|-----------|---|---|---|-------------------------|
| 1         |   | (R)-1-(2-(1H-imidazol-4-yl)ethyl)-3-(1-phenylethyl)urea           | C <sub>14</sub> H <sub>18</sub> N <sub>4</sub> O  | 258.32                  |
| 2         |  | (S)-1-(2-(1H-imidazol-4-yl)ethyl)-3-(1-phenylethyl)urea           | C <sub>14</sub> H <sub>18</sub> N <sub>4</sub> O  | 258.32                  |
| 3         |  | (R)-1-(2-(1H-imidazol-4-yl)ethyl)-3-(1-(4-fluorophenyl)ethyl)urea | C <sub>14</sub> H <sub>17</sub> FN <sub>4</sub> O | 276.31                  |
| 4         |  | (S)-1-(2-(1H-imidazol-4-yl)ethyl)-3-(1-(4-fluorophenyl)ethyl)urea | C <sub>14</sub> H <sub>17</sub> FN <sub>4</sub> O | 276.31                  |

|    |   |   |   |        |
|----|---|---|---|--------|
| 5  |    | (R)-5-amino-N-(1-phenylethyl)-1H-1,2,4-triazole-1-carboxamide           | C <sub>11</sub> H <sub>13</sub> N <sub>5</sub> O  | 231.25 |
| 6  |    | (S)-5-amino-N-(1-phenylethyl)-1H-1,2,4-triazole-1-carboxamide           | C <sub>11</sub> H <sub>13</sub> N <sub>5</sub> O  | 231.25 |
| 7  |    | (R)-5-amino-N-(1-(4-fluorophenyl)ethyl)-1H-1,2,4-triazole-1-carboxamide | C <sub>11</sub> H <sub>12</sub> FN <sub>5</sub> O | 249.24 |
| 8  |   | (S)-5-amino-N-(1-(4-fluorophenyl)ethyl)-1H-1,2,4-triazole-1-carboxamide | C <sub>11</sub> H <sub>12</sub> FN <sub>5</sub> O | 249.24 |
| 9  |  | 1-(2-(1H-imidazol-4-yl)ethyl)-3-butylurea                               | C <sub>10</sub> H <sub>18</sub> N <sub>4</sub> O  | 210.28 |
| 10 |  | (R)-1-(2-(1H-imidazol-4-yl)ethyl)-3-(3-methylbutan-2-yl)urea            | C <sub>11</sub> H <sub>20</sub> N <sub>4</sub> O  |        |
| 11 |  | (S)-1-(2-(1H-imidazol-4-yl)ethyl)-3-(3-methylbutan-2-yl)urea            | C <sub>11</sub> H <sub>20</sub> N <sub>4</sub> O  |        |
| 12 |  | 1-(2-(1H-imidazol-4-yl)ethyl)-3-hexylurea                               | C <sub>12</sub> H <sub>22</sub> N <sub>4</sub> O  | 238.33 |
| 13 |  | (R)-1-(2-(1H-imidazol-4-yl)ethyl)-3-(hexan-2-yl)urea                    | C <sub>12</sub> H <sub>22</sub> N <sub>4</sub> O  | 238.33 |

|           |   |  |  |        |
|-----------|---|--|--|--------|
| <b>14</b> |  | (S)-1-(2-(1H-imidazol-4-yl)ethyl)-3-(hexan-2-yl)urea | C <sub>12</sub> H <sub>22</sub> N <sub>4</sub> O | 238.33 |
| <b>15</b> |  | 1-(2-(1H-imidazol-4-yl)ethyl)-3-octylurea            | C <sub>14</sub> H <sub>26</sub> N <sub>4</sub> O | 266.38 |
| <b>16</b> |  | (R)-1-(2-(1H-imidazol-4-yl)ethyl)-3-(octan-2-yl)urea | C <sub>14</sub> H <sub>26</sub> N <sub>4</sub> O | 266.38 |
| <b>17</b> |  | (S)-1-(2-(1H-imidazol-4-yl)ethyl)-3-(octan-2-yl)urea | C <sub>14</sub> H <sub>26</sub> N <sub>4</sub> O | 266.38 |

The compounds were prepared according to the reaction schemes **(1)** or **(2)** in one-step reactions according to the protocol presented lower:

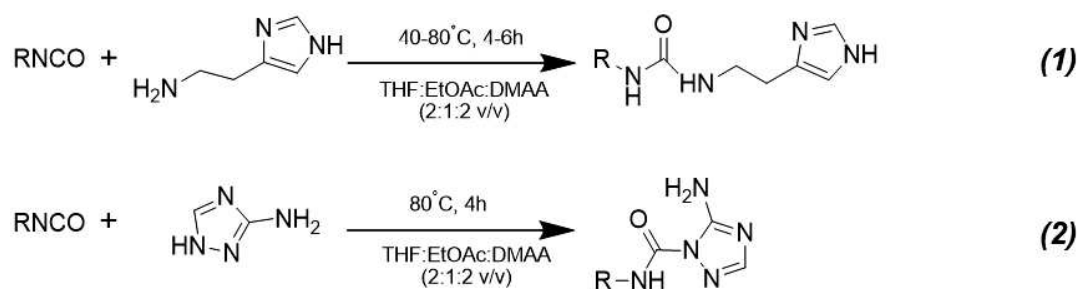


**Figure 106: Reaction schemes 1 and 2**

### Synthetic protocol

All of the compounds have been synthesized following either the scheme **(1)** for compounds 1-4 and 9-17 or scheme **(2)** for compounds 5-8. The amine (30 mmol) is mixed with the corresponding amount of isocyanate, under sonication (1 eq.: 1eq). The mixture was solubilized in 10 ml of THF (tetrahydrofuran), 5 ml of ethylacetate, and 10 ml of dimethylacetamide. The reaction mixture was heated to 80°C for 15 minutes. When the precipitation begins 5 ml of acetonitrile are added and the heating is maintained for another 4 hours. The resulting product will be a white powder which is then filtered and washed with methanol on the filter paper. The exceptions of the protocol are compounds

**9, 10** and **11** for which the reaction temperature is 40°C. Compounds **9, 10** and **11** are soluble in the reaction mixture and therefore the purification procedure is as follows. The reaction mass is evaporated under vacuum in a round bottomed flask and the compound is then recrystallized from CHCl<sub>3</sub>.

Alternatively a microwave reactor can be used. The procedure is the following: the isocyanate is dissolved in 5 ml of acetonitrile and added over the amine in the microwave reactor. The reaction is performed at 140°C under high stirring for 15 minutes. The product is then filtered and washed with acetonitrile. In the case of compounds **9, 10** and **11** the temperature is 70°C and for compounds **12, 13** and **14** is 90°C. For compounds **9, 10** and **11**, the purification method is the same.

The exact amounts of compounds used and the yields obtained are presented for a reaction between 30 mmols of each component in table 21:

**Table 21: Amounts and yields for a theoretical preparation of 30 mmols of compound**

| Compound number | Isocyanate name/ formula  | Isocyanate mass (g) | Amine name/ formula  | Amine mass (g) | Overall yield (%) |
|-----------------|---|---------------------|--|----------------|-------------------|
| <b>1</b>        | (R)-(1-isocyanatoethyl)benzene/<br>C <sub>9</sub> H <sub>9</sub> NO             | 4.41                | Histamine/<br>C <sub>5</sub> H <sub>9</sub> N <sub>3</sub> | 3.35           | 91                |
| <b>2</b>        | (S)-(1-isocyanatoethyl)benzene/<br>C <sub>9</sub> H <sub>9</sub> NO             | 4.41                | Histamine/<br>C <sub>5</sub> H <sub>9</sub> N <sub>3</sub> | 3.35           | 94                |
| <b>3</b>        | (R)-1-fluoro-4-(1-isocyanatoethyl)benzene/<br>C <sub>9</sub> H <sub>8</sub> FNO | 4.95                | Histamine/<br>C <sub>5</sub> H <sub>9</sub> N <sub>3</sub> | 3.35           | 92                |
| <b>4</b>        | (S)-1-fluoro-4-(1-isocyanatoethyl)benzene/<br>C <sub>9</sub> H <sub>8</sub> FNO | 4.95                | Histamine/<br>C <sub>5</sub> H <sub>9</sub> N <sub>3</sub> | 3.35           | 93                |
| <b>5</b>        | (R)-(1-isocyanatoethyl)benzene/<br>C <sub>9</sub> H <sub>9</sub> NO             | 4.41                | 3-amino-1,2,4-triazole                                     | 2.52           | 88                |



|           |   |      |  |      |    |
|-----------|---|------|--|------|----|
| <b>6</b>  | (S)-(1-isocyanatoethyl)benzene/<br>C <sub>9</sub> H <sub>9</sub> NO             | 4.41 | 3-amino-<br>1,2,4-<br>triazole                             | 2.52 | 91 |
| <b>7</b>  | (R)-1-fluoro-4-(1-isocyanatoethyl)benzene/<br>C <sub>9</sub> H <sub>8</sub> FNO | 4.95 | 3-amino-<br>1,2,4-<br>triazole                             | 2.52 | 90 |
| <b>8</b>  | (S)-1-fluoro-4-(1-isocyanatoethyl)benzene/<br>C <sub>9</sub> H <sub>8</sub> FNO | 4.95 | 3-amino-<br>1,2,4-<br>triazole                             | 2.52 | 91 |
| <b>9</b>  | Butyl isocyanate/ C <sub>5</sub> H <sub>9</sub> NO                              | 2.97 | Histamine/<br>C <sub>5</sub> H <sub>9</sub> N <sub>3</sub> | 3.35 | 99 |
| <b>10</b> | (R)-2-isocyanato pentane/<br>C <sub>6</sub> H <sub>11</sub> NO                  | 3.39 | Histamine/<br>C <sub>5</sub> H <sub>9</sub> N <sub>3</sub> | 3.35 | 98 |
| <b>11</b> | (S)-2-isocyanato pentane/<br>C <sub>6</sub> H <sub>11</sub> NO                  | 3.39 | Histamine/<br>C <sub>5</sub> H <sub>9</sub> N <sub>3</sub> | 3.35 | 98 |
| <b>12</b> | Hexyl isocyanate/<br>C <sub>7</sub> H <sub>13</sub> NO                          | 3.81 | Histamine/<br>C <sub>5</sub> H <sub>9</sub> N <sub>3</sub> | 3.35 | 99 |
| <b>13</b> | (R)-2-isocyanato hexane/<br>C <sub>7</sub> H <sub>13</sub> NO                   | 3.81 | Histamine/<br>C <sub>5</sub> H <sub>9</sub> N <sub>3</sub> | 3.35 | 97 |
| <b>14</b> | (S)-2-isocyanato hexane/<br>C <sub>7</sub> H <sub>13</sub> NO                   | 3.81 | Histamine/<br>C <sub>5</sub> H <sub>9</sub> N <sub>3</sub> | 3.35 | 96 |
| <b>15</b> | Octyl isocyanate/ C <sub>9</sub> H <sub>17</sub> NO                             | 4.65 | Histamine/<br>C <sub>5</sub> H <sub>9</sub> N <sub>3</sub> | 3.35 | 96 |
| <b>16</b> | (R)-2-isocyanato octane/<br>C <sub>9</sub> H <sub>17</sub> NO                   | 4.65 | Histamine/<br>C <sub>5</sub> H <sub>9</sub> N <sub>3</sub> | 3.35 | 95 |
| <b>17</b> | (S)-2-isocyanato octane/<br>C <sub>9</sub> H <sub>17</sub> NO                   | 4.65 | Histamine/<br>C <sub>5</sub> H <sub>9</sub> N <sub>3</sub> | 3.35 | 94 |

## Characterization of compounds

All reagents were obtained from commercial suppliers and used without further purification. <sup>1</sup>H NMR were recorded on an ARX 300 MHz Bruker spectrometer in d<sub>6</sub>-DMSO, with the use of the residual solvent peak as reference. Mass spectrometric studies were performed in the positive ion mode using a quadrupole mass spectrometer (Micromass). All the structures have been measured on an Agilent Technologies Gemini-S four circle diffractometer using Mo-K $\alpha$  radiation ( $\lambda$  0.71073 Å) and equipped with a Sapphire3 detector at 175 K at the joint X-ray scattering facility of the Pole Balard at the University of Montpellier, France.

### Compound 1

**(R)-1-(2-(1H-imidazol-4-yl)ethyl)-3-(1-phenylethyl)urea : (Mass spectrometry, ES M<sup>+</sup>=259.1)**

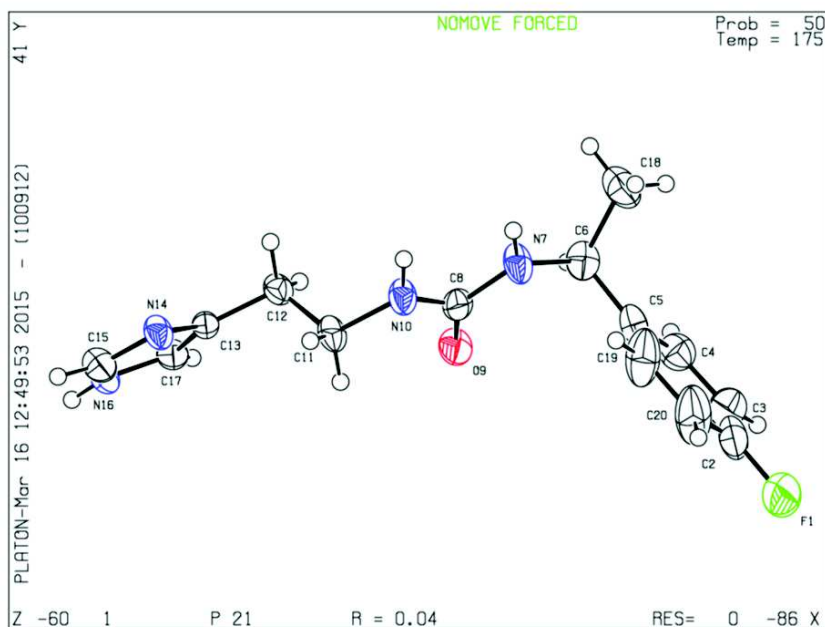
**RMN<sup>1</sup>H (DMSO-d<sub>6</sub>, 300 MHz)  $\delta$  (ppm) =**1.29 (d,3H, CH<sub>3</sub>) ; 2,57 (t, 2H, NHCH<sub>2</sub>CH<sub>2</sub>) ; 3,21 (q, 2H, CH<sub>2</sub>CH<sub>2</sub>NH) ; 4.70 (qv, 1H, CH<sub>3</sub>CHNH) ; 5,79 (s mod, 1H, NHCH<sub>2</sub>) ; 6,37 (d mod,1H,NH-CH-Ph) ; 6,77 (s,1H,C CHNH imidazole) ; 7.17-7.33 (m,5H, phenyl) ; 7,56 (s,1H,N CHNH imidazole)

### Compound 2

**(S)-1-(2-(1H-imidazol-4-yl)ethyl)-3-(1-phenylethyl)urea : (Mass spectrometry, ES M<sup>+</sup>=259.1)**

**RMN<sup>1</sup>H (DMSO-d<sub>6</sub>, 300 MHz)  $\delta$  (ppm) =**1.29 (d,3H, CH<sub>3</sub>) ; 2,60 (t, 2H, NHCH<sub>2</sub>CH<sub>2</sub>) ; 3,19 (q, 2H, CH<sub>2</sub>CH<sub>2</sub>NH) ; 4.72 (qv, 1H, CH<sub>3</sub>CHNH) ; 5,79 (s mod, 1H, NHCH<sub>2</sub>) ; 6,37 (d mod,1H,NH-CH-Ph) ; 6,80 (s,1H,C CHNH imidazole) ; 7.19-7.33 (m,5H, phenyl) ; 7,61 (s,1H,N CHNH imidazole)

### Compound 3

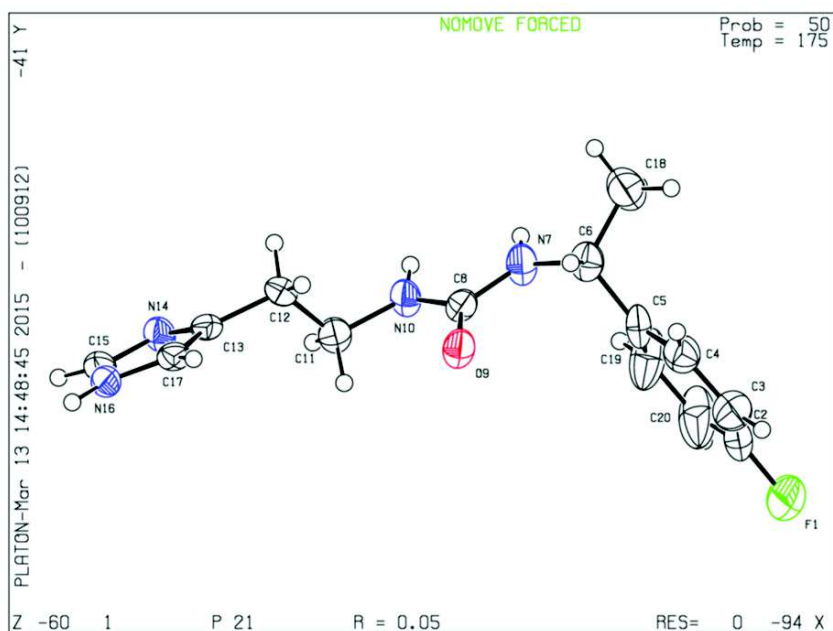


|             |                   |
|-------------|-------------------|
| compound    | 3                 |
| chemsum     | C14H17FN4O        |
| moiety      | C14H17FN4O        |
| SG          | P21               |
| a           | 9.1866(12)        |
| b           | 5.6564(6)         |
| c           | 14.2700(16)       |
| alpha       | 90                |
| beta        | 107.802(14)       |
| gamma       | 90                |
| volume      | 706.01(8)         |
| Z           | 2                 |
| size        | 0.010x0.030x0.100 |
| density     | 1.300             |
| resol       | 0.86              |
| nreflot     | 1756              |
| nrefls      | 820               |
| Rint        | 0.036             |
| sigma/overl | 0.0651            |
| npar        | 190               |
| R1          | 0.0426            |
| wR2         | 0.0401            |
| GOF         | 1.1798            |

### (R)-1-(2-(1H-imidazol-4-yl)ethyl)-3-(1-(4-fluorophenyl)ethyl)urea : (Mass spectrometry, ES M<sup>+</sup>=277.1)

**RMN<sup>1</sup>H (DMSO-d<sub>6</sub>, 300 MHz)** δ (ppm) =1.28 (d,3H, CH<sub>3</sub>) ; 2,58 (t, 2H, NHCH<sub>2</sub>CH<sub>2</sub>) ; 3,20 (q, 2H, CH<sub>2</sub>CH<sub>2</sub>NH) ; 4.78 (qv, 1H, CH<sub>3</sub>CHNH) ; 5,80 (s mod, 1H, NHCH<sub>2</sub>) ; 6,40 (d mod,1H,NH-CH-Ph) ; 6,80 (s,1H,C CHNH imidazole) ; 7.13-7.18 (m,2H, CHCCH phenyl) ; 7.27-7.32 (m,2H,CHCFCH phenyl) ; 7,52 (s,1H,N CHNH imidazole)

## Compound 4

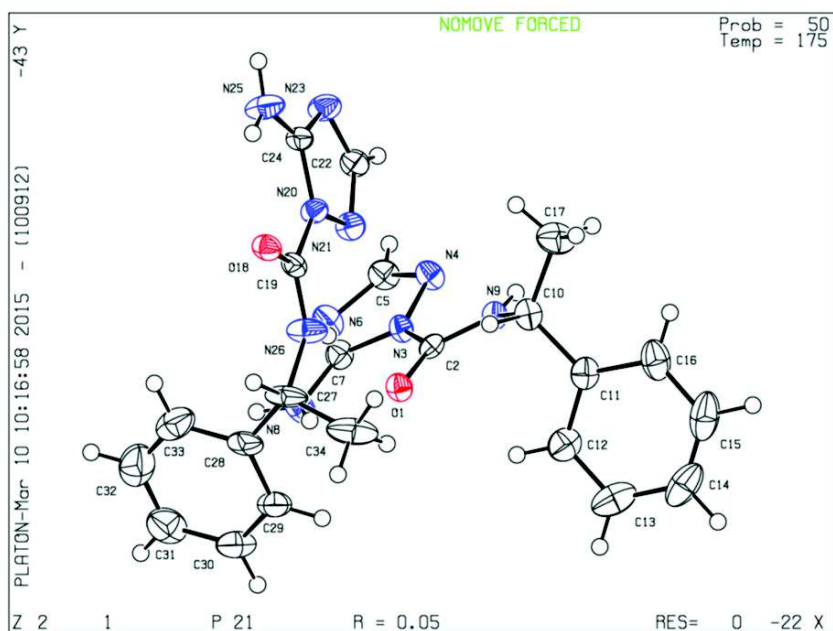


| Crystallographic table |                   |
|------------------------|-------------------|
| compound               | 4                 |
| chemsum                | C14H17FN4O        |
| moiety                 | C14H17FN4O        |
| SG                     | P21               |
| a                      | 9.181(2)          |
| b                      | 5.6412(8)         |
| c                      | 14.210(3)         |
| alpha                  | 90                |
| beta                   | 107.80(2)         |
| gamma                  | 90                |
| volume                 | 700.75(13)        |
| Z                      | 2                 |
| size                   | 0.020x0.040x0.120 |
| density                | 1.309             |
| resol                  | 0.85              |
| nreflot                | 3446              |
| nrefls                 | 959               |
| Rint                   | 0.046             |
| sigma/overl            | 0.0604            |
| npar                   | 190               |
| R1                     | 0.0475            |
| wR2                    | 0.0524            |
| GOF                    | 1.1142            |

**(S)-1-(2-(1H-imidazol-4-yl)ethyl)-3-(1-(4-fluorophenyl)ethyl)urea : (Mass spectrometry, ES M<sup>+</sup>=277.1)**

**RMN<sup>1</sup>H (DMSO-d<sub>6</sub>, 300 MHz) δ (ppm) =** 1.28 (d, 3H, CH<sub>3</sub>) ; 2,58 (t, 2H, NHCH<sub>2</sub>CH<sub>2</sub>) ; 3,22 (q, 2H, CH<sub>2</sub>CH<sub>2</sub>NH) ; 4.72 (qv, 1H, CH<sub>3</sub>CHNH) ; 5,79 (s mod, 1H, NHCH<sub>2</sub>) ; 6,39 (d mod, 1H, NH-CH-Ph) ; 6,79 (s, 1H, C CHNH imidazole) ; 7.09-7.15 (m, 2H, CHCCH phenyl) ; 7.27-7.31 (m, 2H, CHCFCH phenyl) ; 7,58 (s, 1H, N CHNH imidazole)

## Compound 5

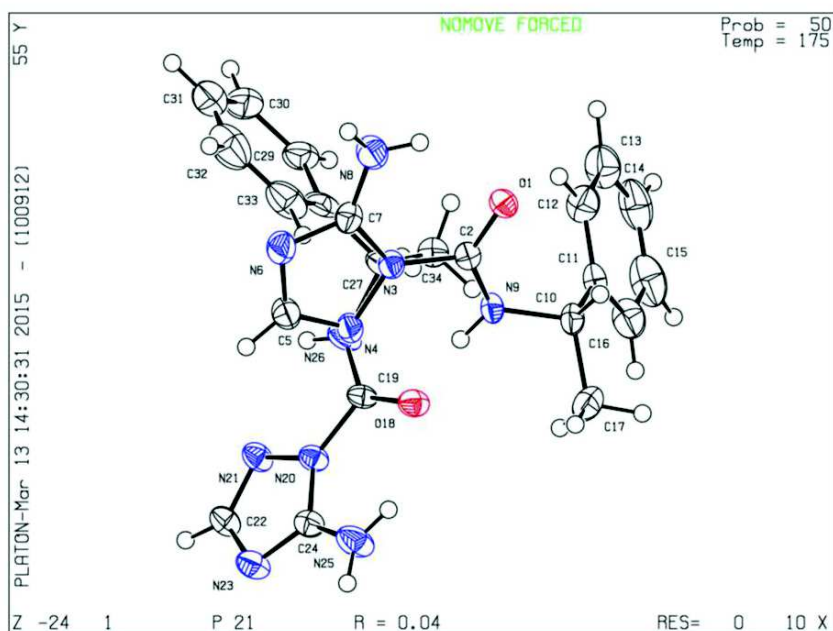


| Crystallographic table |                   |
|------------------------|-------------------|
| compound               | 5                 |
| chemsum                | C11H13N5O         |
| moiety                 | C11H13N5O         |
| SG                     | P21               |
| a                      | 8.5348(4)         |
| b                      | 14.7899(6)        |
| c                      | 9.8094(4)         |
| alpha                  | 90                |
| beta                   | 105.886(4)        |
| gamma                  | 90                |
| volume                 | 1190.94(5)        |
| Z                      | 4                 |
| size                   | 0.060x0.120x0.230 |
| density                | 1.290             |
| resol                  | 0.73              |
| nrefot                 | 5537              |
| nrefls                 | 2457              |
| Rint                   | 0.035             |
| sigma/overl            | 0.0509            |
| npar                   | 325               |
| R1                     | 0.0465            |
| wR2                    | 0.0464            |
| GOF                    | 1.1215            |

**(R)-5-amino-N-(1-phenylethyl)-1H-1,2,4-triazole-1-carboxamide : (Mass spectrometry, ES M<sup>+</sup>=232.1)**

**RMN<sup>1</sup>H (DMSO-d<sub>6</sub>, 300 MHz)** δ (ppm) =1.52 (d,3H, CH<sub>3</sub>) ; 4.98 (qv, 1H, CH<sub>3</sub>CHNH); 7.19-7.23 (m,1H, CHCH phenyl) ; 7.31-7.35 (m,2H,CHCHCH phenyl) ; 7.39-7.41 (dm,2H,CHCCH phenyl) 7.56 (s,1H,N CHN triazole), 8.52-8.56 (d, 1H, CH-NH-C)

## Compound 6



|            |                   |
|------------|-------------------|
| compound   | 6                 |
| chemsum    | C11H13N5O         |
| moiety     | C11H13N5O         |
| SG         | P21               |
| a          | 8.5277(7)         |
| b          | 14.8001(11)       |
| c          | 9.8121(6)         |
| alpha      | 90                |
| beta       | 105.843(8)        |
| gamma      | 90                |
| volume     | 1191.34(8)        |
| Z          | 4                 |
| size       | 0.200x0.300x0.650 |
| density    | 1.289             |
| resol      | 0.73              |
| nreflot    | 6914              |
| nrefls     | 2469              |
| Rint       | 0.028             |
| sigaloverl | 0.0422            |
| npar       | 325               |
| R1         | 0.0396            |
| wR2        | 0.0456            |
| GOF        | 1.1117            |

**(S)-5-amino-N-(1-phenylethyl)-1H-1,2,4-triazole-1-carboxamide : (Mass spectrometry, ES M<sup>+</sup>=232.1)**

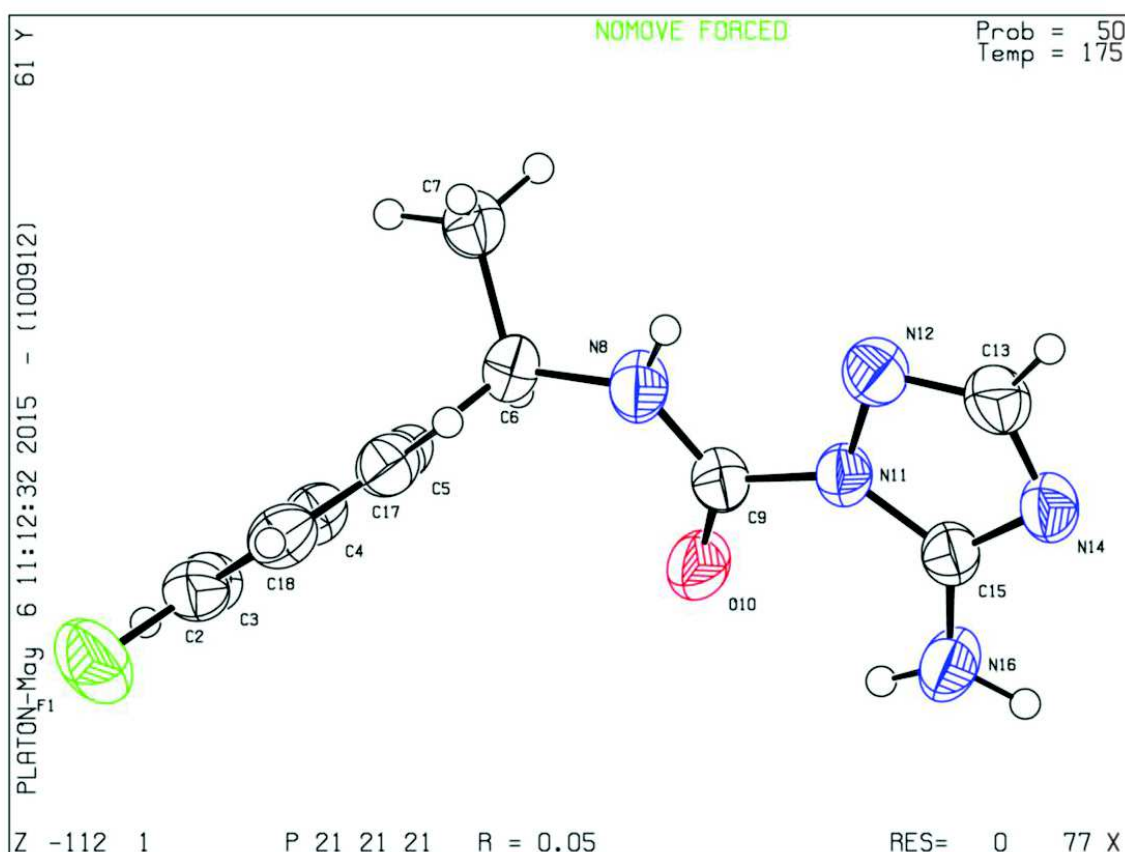
**RMN<sup>1</sup>H (DMSO-d<sub>6</sub>, 300 MHz) δ (ppm) = 1.51 (d, 3H, CH<sub>3</sub>) ; 4.96 (qv, 1H, CH<sub>3</sub>CHNH) ; 7.21-7.26 (m, 1H, CHCHCH phenyl) ; 7.30-7.35 (m, 2H, CHCHCH phenyl) ; 7.40-7.42 (dm, 2H, CHCCH phenyl) 7.57 (s, 1H, N CHN triazole), 8.52-8.58 (d, 1H, CH-NH-C)**

## Compound 7

**(R)-5-amino-N-(1-(4-fluorophenyl)ethyl)-1H-1,2,4-triazole-1-carboxamide : (Mass spectrometry, ES M<sup>+</sup>=250.1)**

**RMN<sup>1</sup>H (DMSO-d<sub>6</sub>, 300 MHz)**  $\delta$  (ppm) = 1.48 (d, 3H, CH<sub>3</sub>) ; 4.98 (qv, 1H, CH<sub>3</sub>CHNH); 7.11-7.16 (m, 2H, CHCCH phenyl) ; 7.45-7.50 (m, 2H, CHCFCH phenyl) ; 7,57 (s, 1H, N CHN triazole), 8.61-8.64 (d, 1H, CH-NH-C)

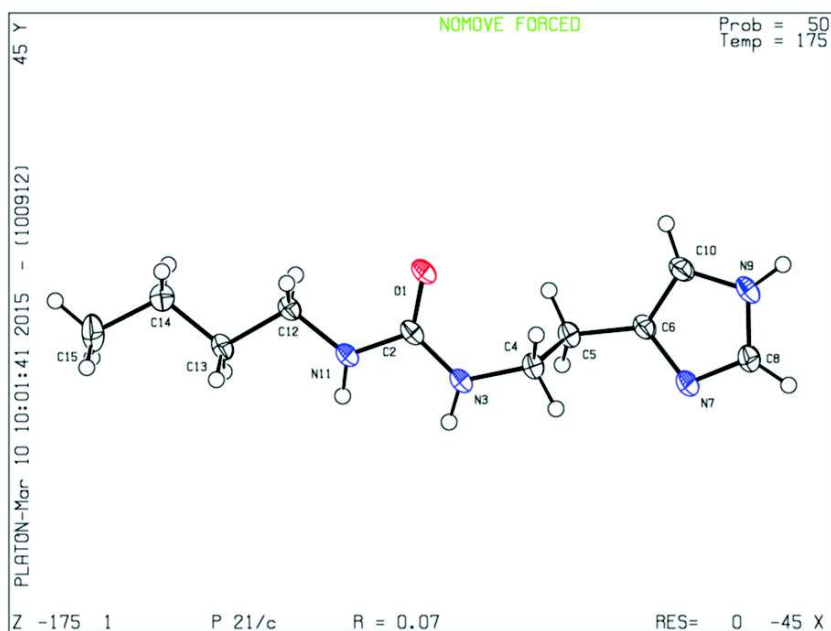
Compound 8



**(S)-5-amino-N-(1-(4-fluorophenyl)ethyl)-1H-1,2,4-triazole-1-carboxamide: (Mass spectrometry, ES M<sup>+</sup>=250.1)**

**RMN<sup>1</sup>H (DMSO-d<sub>6</sub>, 300 MHz)**  $\delta$  (ppm) = 1.50 (d, 3H, CH<sub>3</sub>) ; 4.96 (qv, 1H, CH<sub>3</sub>CHNH); 7.12-7.18 (m, 2H, CHCCH phenyl) ; 7.43-7.48 (m, 2H, CHCFCH phenyl) ; 7,58 (s, 1H, N CHN triazole), 8.60-8.62 (d, 1H, CH-NH-C)

## Compound 9



Crystallographic table

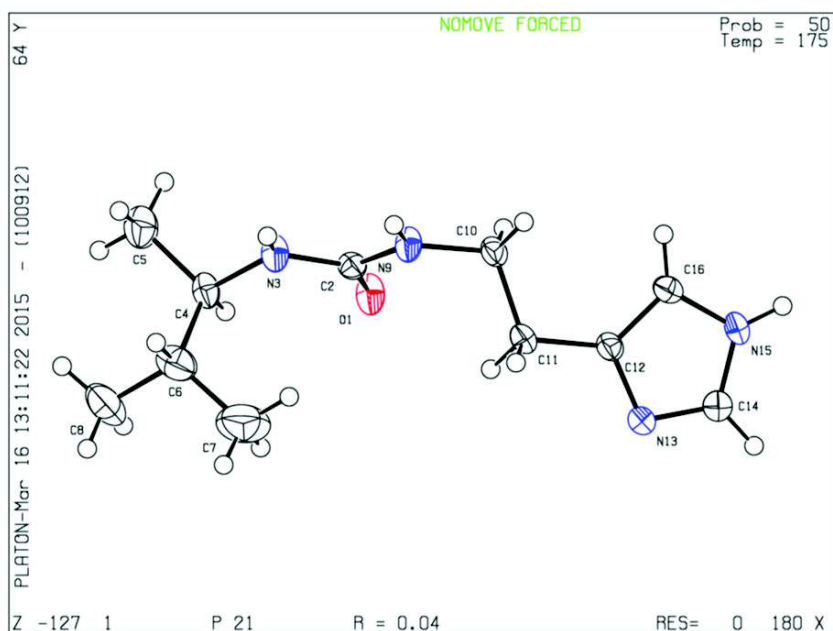
|            |                   |
|------------|-------------------|
| compound   | 9                 |
| chemsum    | C10H18N4O         |
| moiety     | C10H18N4O         |
| SG         | P21/c             |
| a          | 11.2054(8)        |
| b          | 5.6226(7)         |
| c          | 17.6834(14)       |
| alpha      | 90                |
| beta       | 93.730(6)         |
| gamma      | 90                |
| volume     | 1111.76(9)        |
| Z          | 4                 |
| size       | 0.120x0.350x0.400 |
| density    | 1.256             |
| resol      | 0.73              |
| nreflot    | 4784              |
| nrefls     | 2154              |
| Rint       | 0.030             |
| sigmaoverl | 0.0445            |
| npar       | 145               |
| R1         | 0.0687            |
| wR2        | 0.0702            |
| GOF        | 0.8775            |

**1-(2-(1H-imidazol-4-yl)ethyl)-3-butylurea : (Mass spectrometry, ES M<sup>+</sup>=211.1)**

**RMN<sup>1</sup>H (DMSO-d<sub>6</sub>, 300 MHz) δ (ppm) = 0,86 (t, 3H, CH<sub>3</sub>CH<sub>2</sub>) ; 1,30 (m, 4H, CH<sub>3</sub>CH<sub>2</sub>CH<sub>2</sub>CH<sub>2</sub>) ; 2,58 (t, 2H, NHCH<sub>2</sub>CH<sub>2</sub>) ; 2,96 (q, 2H, CH<sub>2</sub>CH<sub>2</sub>NH) ; 3,21 (q, 2H, CH<sub>2</sub>CH<sub>2</sub>NH) 5,75 (s mod, 1H, NHCH<sub>2</sub>) ; 5.83 (s mod, 1H, NHCH<sub>2</sub>) ; 6,78 (s, 1H, C CHNH imidazole) ; 7,55 (s, 1H, N CHNH imidazole)**



## Compound 10

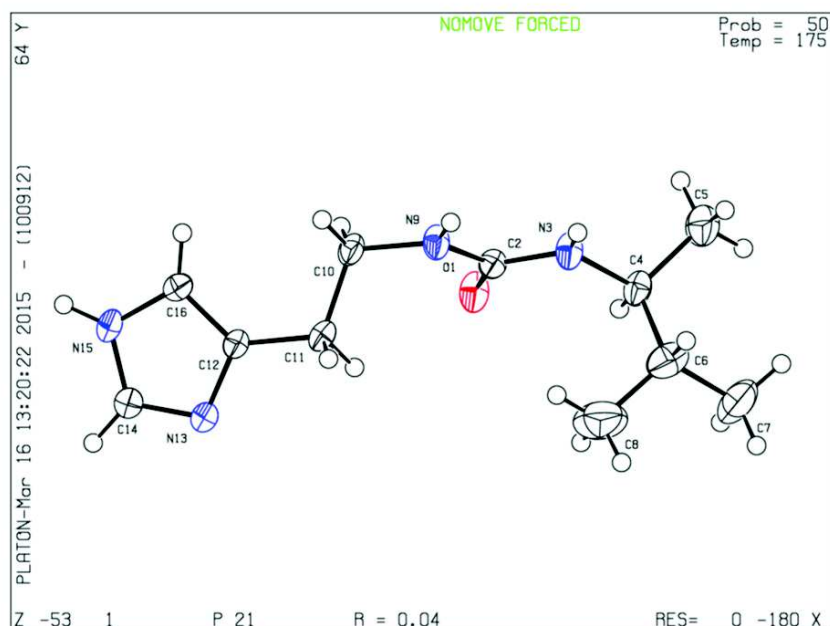


| Crystallographic table |                   |
|------------------------|-------------------|
| compound               | 10                |
| chemsum                | C11H20N4O1        |
| moiety                 | C11H20N4O1        |
| SG                     | P21               |
| a                      | 4.62268(15)       |
| b                      | 10.0266(4)        |
| c                      | 13.7382(7)        |
| alpha                  | 90                |
| beta                   | 94.676(4)         |
| gamma                  | 90                |
| volume                 | 634.64(3)         |
| Z                      | 2                 |
| size                   | 0.050x0.200x0.200 |
| density                | 1.174             |
| resol                  | 0.73              |
| nrefot                 | 4578              |
| nrefls                 | 1388              |
| Rint                   | 0.000             |
| sigmaoverl             | 0.0474            |
| npar                   | 154               |
| R1                     | 0.0419            |
| wR2                    | 0.0427            |
| GOF                    | 1.0796            |

**(R)-1-(2-(1H-imidazol-4-yl)ethyl)-3-(3-methylbutan-2-yl)urea : (Mass spectrometry, ES M<sup>+</sup>=225.2)**

**RMN<sup>1</sup>H (DMSO-d<sub>6</sub>, 300 MHz)**  $\delta$  (ppm) = 0,81 (q, 6H, CH<sub>3</sub>CHCH<sub>3</sub>) ; 0,92 (d, 3H, CH<sub>3</sub>CHHC<sub>2</sub>) ; 1,57 (h, 1H, CH<sub>3</sub>CHCH<sub>3</sub>) ; 2,60 (t, 2H, NHCH<sub>2</sub>CH<sub>2</sub>) ; 3,21 (q, 2H, CH<sub>2</sub>CH<sub>2</sub>NH); 3,45 (m, 1H, CH<sub>2</sub>CH<sub>3</sub>CHNH); 5,68 (s mod, 1H, NHCH<sub>2</sub>) ;5,71 (s mod, 1H, NHCH<sub>2</sub>) ; 6,82 (s,1H,C CHNH imidazole) ; 7,51 (s,1H,N CHNH imidazole)

## Compound 11



Crystallographic table

|             |                   |
|-------------|-------------------|
| compound    | 11                |
| chemsum     | C11H20N4O         |
| moiety      | C11H20N4O         |
| SG          | P21               |
| a           | 4.6208(2)         |
| b           | 10.0307(4)        |
| c           | 13.7383(8)        |
| alpha       | 90                |
| beta        | 94.654(5)         |
| gamma       | 90                |
| volume      | 634.67(4)         |
| Z           | 2                 |
| size        | 0.100x0.200x0.500 |
| density     | 1.174             |
| resol       | 0.73              |
| nreflot     | 5215              |
| nrefls      | 1458              |
| Rint        | 0.028             |
| sigmaloverl | 0.0408            |
| npar        | 154               |
| R1          | 0.0390            |
| wR2         | 0.0417            |
| GOF         | 1.0714            |

### (S)-1-(2-(1H-imidazol-4-yl)ethyl)-3-(3-methylbutan-2-yl)urea : (Mass spectrometry, ES M<sup>+</sup>=225.2)

**RMN<sup>1</sup>H (DMSO-d<sub>6</sub>, 300 MHz)** δ (ppm) = 0,81 (q, 6H, CH<sub>3</sub>CHCH<sub>3</sub>) ; 0,92 (d, 3H, CH<sub>3</sub>CHHC<sub>2</sub>) ; 1,56 (h, 1H, CH<sub>3</sub>CHCH<sub>3</sub>) ; 2,57 (t, 2H, NHCH<sub>2</sub>CH<sub>2</sub>) ; 3,20 (q, 2H, CH<sub>2</sub>CH<sub>2</sub>NH); 3,45 (m, 1H, CH<sub>2</sub>CH<sub>3</sub>CHNH); 5,68 (s mod, 1H, NHCH<sub>2</sub>) ;5.70 (s mod, 1H, NHCH<sub>2</sub>) ; 6,76 (s,1H,C CHNH imidazole) ; 7,51 (s,1H,N CHNH imidazole)

## Compound 12

### 1-(2-(1H-imidazol-4-yl)ethyl)-3-hexylurea : (Mass spectrometry, ES M<sup>+</sup>=239.1)

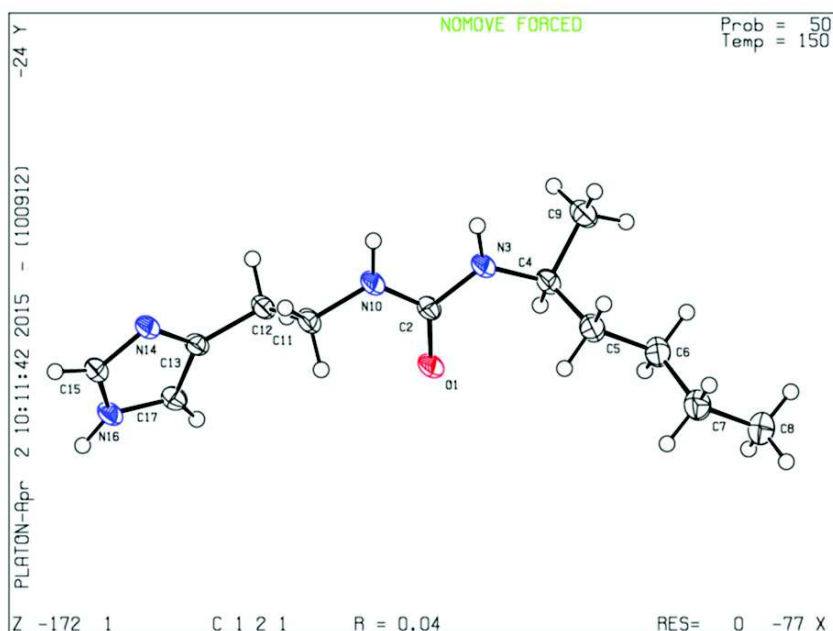
**RMN<sup>1</sup>H (DMSO-d<sub>6</sub>, 300 MHz)** δ (ppm) = 0,86 (t, 3H, CH<sub>3</sub>CH<sub>2</sub>) ; 1,24-1.34 (m, 8H, CH<sub>3</sub>(CH<sub>2</sub>)<sub>4</sub>CH<sub>2</sub>) ; 2,57 (t, 2H, NHCH<sub>2</sub>CH<sub>2</sub>) ; 2,96 (q, 2H, CH<sub>2</sub>CH<sub>2</sub>NH) ; 3,21 (q, 2H, CH<sub>2</sub>CH<sub>2</sub>NH) 5,75 (s mod, 1H, NHCH<sub>2</sub>) ;5.84 (s mod, 1H, NHCH<sub>2</sub>) ; 6,75 (s,1H,C CHNH imidazole) ; 7,54 (s,1H,N CHNH imidazole)

### Compound 13

**(R)-1-(2-(1H-imidazol-4-yl)ethyl)-3-(hexan-2-yl)urea** : (Mass spectrometry, ES  $M^{*+}=239.3$ )

**RMN<sup>1</sup>H (DMSO-d<sub>6</sub>, 300 MHz)**  $\delta$  (ppm) = 0,86 (t, 3H, CH<sub>3</sub>CH<sub>2</sub>) ; 0,97 (d, 3H, CH<sub>3</sub>CHHC<sub>2</sub>)  
1,24 (m, 6H, CH<sub>3</sub>(CH<sub>2</sub>)<sub>3</sub>CH<sub>2</sub>) ; 2,57 (t, 2H, NHCH<sub>2</sub>CH<sub>2</sub>) ; 3,21 (q, 2H, CH<sub>2</sub>CH<sub>2</sub>NH);  
3,54 (m, 1H, CH<sub>2</sub>CH<sub>3</sub>CHNH); 5,64 (s mod, 1H, NHCH<sub>2</sub>) ;5.69 (s mod, 1H, NHCH<sub>2</sub>) ;  
6,81 (s,1H,C CHNH imidazole) ; 7,51 (s,1H,N CHNH imidazole)

### Compound 14



Crystallographic table

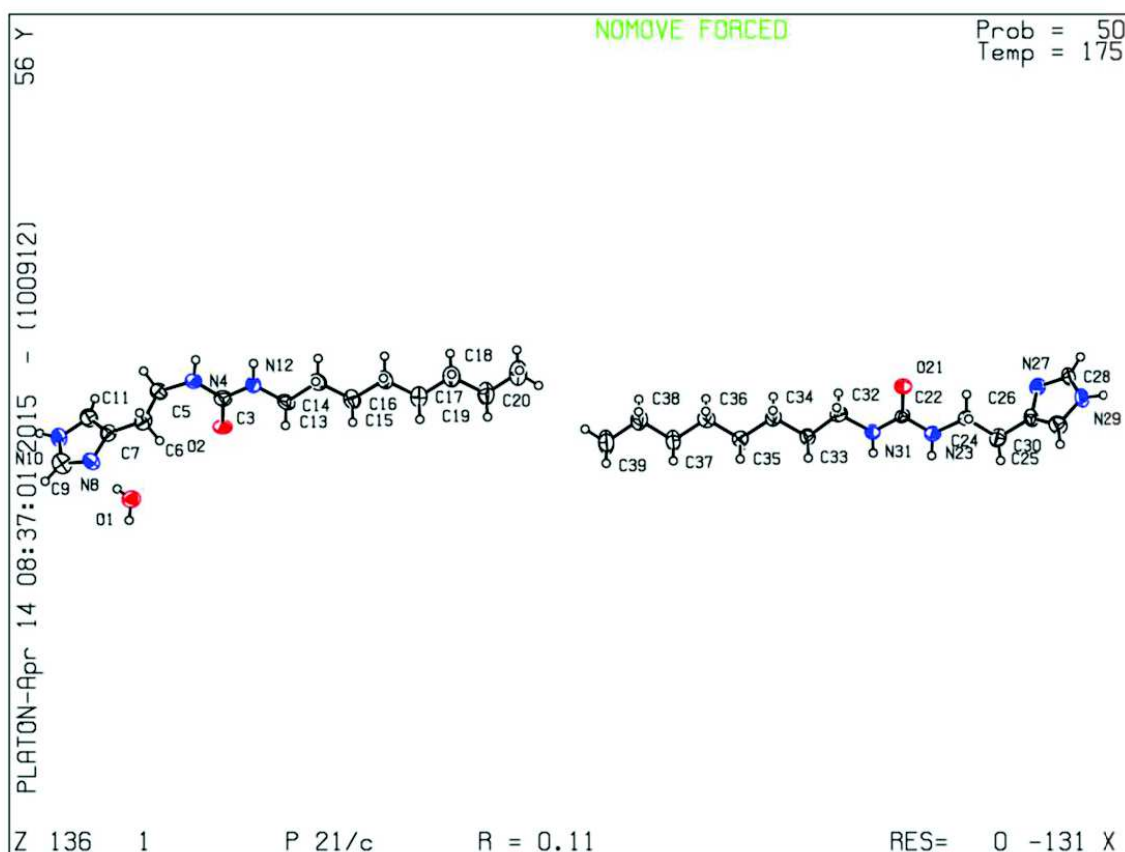
|             |                   |
|-------------|-------------------|
| compound    | 14                |
| chemsum     | C12H22N4O1        |
| moiety      | C12H22N4O1        |
| SG          | C121              |
| a           | 29.6347(8)        |
| b           | 5.17090(10)       |
| c           | 9.2471(3)         |
| alpha       | 90                |
| beta        | 106.304(2)        |
| gamma       | 90                |
| volume      | 1360.02(4)        |
| Z           | 4                 |
| size        | 0.050x0.075x0.100 |
| density     | 1.164             |
| resol       |                   |
| nreflot     | 5138              |
| nrefls      | 2909              |
| Rint        | 0.012             |
| sigmaloverl |                   |
| npar        | 220               |
| R1          | 0.0364            |
| wR2         | 0.0412            |
| GOF         | 1.0750            |

**(S)-1-(2-(1H-imidazol-4-yl)ethyl)-3-(hexan-2-yl)urea** : (Mass spectrometry, ES  $M^{*+}=239.2$ )

**RMN<sup>1</sup>H (DMSO-d<sub>6</sub>, 300 MHz)**  $\delta$  (ppm) = 0,84 (t, 3H, CH<sub>3</sub>CH<sub>2</sub>) ; 0,97 (d, 3H, CH<sub>3</sub>CHHC<sub>2</sub>)  
1,23 (m, 6H, CH<sub>3</sub>(CH<sub>2</sub>)<sub>3</sub>CH<sub>2</sub>) ; 2,56 (t, 2H, NHCH<sub>2</sub>CH<sub>2</sub>) ; 3,20 (q, 2H, CH<sub>2</sub>CH<sub>2</sub>NH);

3,54 (m, 1H, CH<sub>2</sub>CH<sub>3</sub>CHNH); 5,63 (s mod, 1H, NHCH<sub>2</sub>) ;5.70 (s mod, 1H, NHCH<sub>2</sub>) ;  
 6,80 (s,1H,C CHNH imidazole) ; 7,50 (s,1H,N CHNH imidazole)

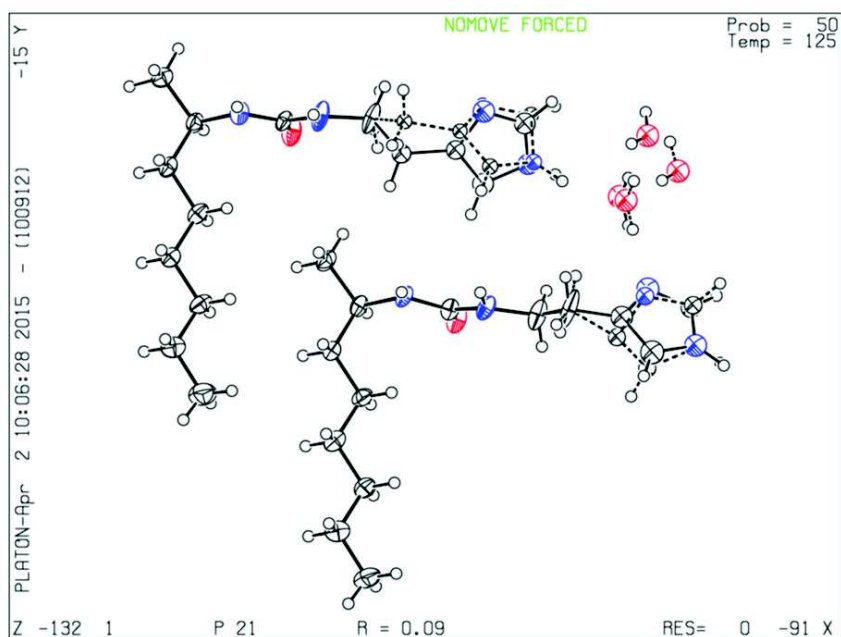
Compound 15



**1-(2-(1H-imidazol-4-yl)ethyl)-3-octylurea : (Mass spectrometry, ES M<sup>+</sup>=267.1)**

**RMN<sup>1</sup>H (DMSO-d<sub>6</sub>, 300 MHz)** δ (ppm) = 0,86 (t, 3H, CH<sub>3</sub>CH<sub>2</sub>) ; 1,25-1.34 (m, 12H, CH<sub>3</sub>(CH<sub>2</sub>)<sub>6</sub>CH<sub>2</sub>) ; 2,58 (t, 2H, NHCH<sub>2</sub>CH<sub>2</sub>) ; 2,95 (q, 2H, CH<sub>2</sub>CH<sub>2</sub>NH) ; 3,21 (q, 2H, CH<sub>2</sub>CH<sub>2</sub>NH) 5,74 (s mod, 1H, NHCH<sub>2</sub>) ;5.82 (s mod, 1H, NHCH<sub>2</sub>) ; 6,76 (s,1H,C CHNH imidazole) ; 7,52 (s,1H,N CHNH imidazole)

## Compound 16

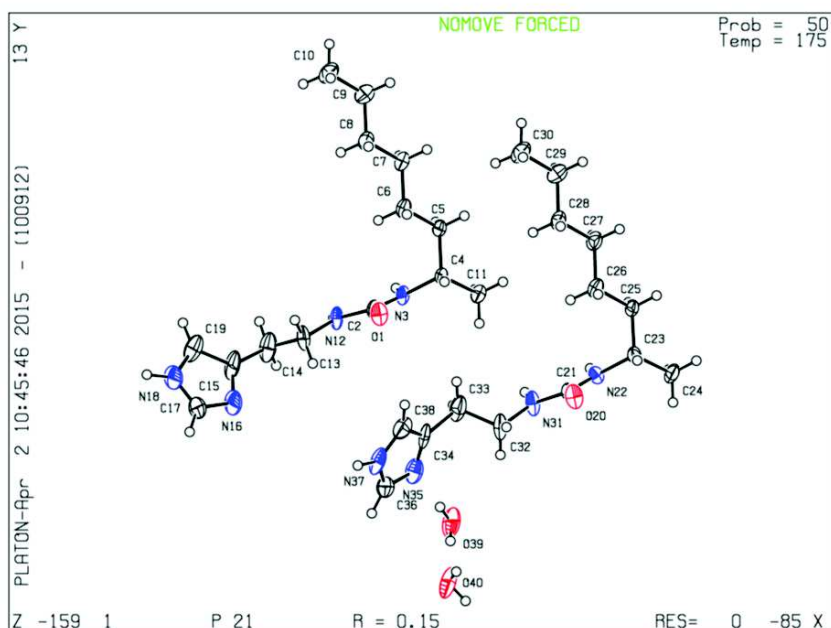


| Crystallographic table |                |
|------------------------|----------------|
| compound               | 16             |
| chemsum                | C14H28N4O2     |
| moiety                 | C14H26N4O, H2O |
| SG                     | P21            |
| a                      | 12.766(4)      |
| b                      | 4.5679(11)     |
| c                      | 28.756(7)      |
| alpha                  | 90             |
| beta                   | 96.47(2)       |
| gamma                  | 90             |
| volume                 | 1666.3(4)      |
| Z                      | 4              |
| size                   | 0.02x0.05x0.10 |
| density                | 1.134          |
| resol                  |                |
| nreflot                | 19206          |
| nrefls                 | 2999           |
| Rint                   | 0.070          |
| sigaloverl             |                |
| npair                  | 349            |
| R1                     | 0.0922         |
| wR2                    | 0.1094         |
| GOF                    | 1.0948         |

### (R)-1-(2-(1H-imidazol-4-yl)ethyl)-3-(octan-2-yl)urea : (Mass spectrometry, ES M<sup>+</sup>=267.2)

**RMN<sup>1</sup>H (DMSO-d<sub>6</sub>, 300 MHz)**  $\delta$  (ppm) = 0,85 (t, 3H, CH<sub>3</sub>CH<sub>2</sub>) ; 0,97 (d, 3H, CH<sub>3</sub>CHHC<sub>2</sub>) ; 1,24 (m, 10H, CH<sub>3</sub>(CH<sub>2</sub>)<sub>5</sub>CH<sub>2</sub>) ; 2,57 (t, 2H, NHCH<sub>2</sub>CH<sub>2</sub>) ; 3,20 (q, 2H, CH<sub>2</sub>CH<sub>2</sub>NH) ; 3,53 (m, 1H, CH<sub>2</sub>CH<sub>3</sub>CHNH) ; 5,67 (s mod, 1H, NHCH<sub>2</sub>) ; 5,69 (s mod, 1H, NHCH<sub>2</sub>) ; 6,82 (s, 1H, C CHNH imidazole) ; 7,51 (s, 1H, N CHNH imidazole)

## Compound 17



| Crystallographic table |                   |
|------------------------|-------------------|
| compound               | 17                |
| chemsum                | C14H28N4O2        |
| moiety                 | C14H26N4O,H2O     |
| SG                     | P21               |
| a                      | 12.8000(3)        |
| b                      | 4.5826(2)         |
| c                      | 28.8266(11)       |
| alpha                  | 90                |
| beta                   | 96.488(3)         |
| gamma                  | 90                |
| volume                 | 1680.05(6)        |
| Z                      | 4                 |
| size                   | 0.020x0.035x0.050 |
| density                | 1.124             |
| resol                  |                   |
| nreflot                | 23942             |
| nrefls                 | 3300              |
| Rint                   | 0.058             |
| sigmaloverl            |                   |
| npar                   | 361               |
| R1                     | 0.1540            |
| wR2                    | 0.1687            |
| GOF                    | 1.0674            |

### (S)-1-(2-(1H-imidazol-4-yl)ethyl)-3-(octan-2-yl)urea : (Mass spectrometry, ES $M^{*+}=267.2$ )

**RMN<sup>1</sup>H (DMSO-d<sub>6</sub>, 300 MHz)**  $\delta$  (ppm) = 0,85 (t, 3H, CH<sub>3</sub>CH<sub>2</sub>) ; 0,97 (d, 3H, CH<sub>3</sub>CHHC<sub>2</sub>)  
1,23 (m, 10H, CH<sub>3</sub>(CH<sub>2</sub>)<sub>5</sub>CH<sub>2</sub>) ; 2,57 (t, 2H, NHCH<sub>2</sub>CH<sub>2</sub>) ; 3,20 (q, 2H, CH<sub>2</sub>CH<sub>2</sub>NH);  
3,49 (m, 1H, CH<sub>2</sub>CH<sub>3</sub>CHNH); 5,66 (s mod, 1H, NHCH<sub>2</sub>) ;5.69 (s mod, 1H, NHCH<sub>2</sub>) ;  
6,75 (s,1H,C CHNH imidazole) ; 7,51 (s,1H,N CHNH imidazole)

## **Protocols for transport experiments**

### **Cation and proton transport using ratiometric fluorescence techniques**

All fluorescence experiments were performed on a PerkinElmer LS 55 fluorimeter.

### **Vesicle preparation for fluorescence experiments**

Egg yolk L- $\alpha$ -phosphatidylcholine (EYPC chloroform solution, 20 mg, 26 mmol) was dissolved in a 1:1 CHCl<sub>3</sub>/MeOH mixture (2 ml total volume), the solution was evaporated under reduced pressure and the resulting thin film was dried under high vacuum for 2 h. The lipid film was hydrated in 0.4 mL of phosphate buffer (10 mM sodium phosphate, pH = 6.4, 100 mM NaCl) containing 10  $\mu$ M HPTS (pyranine, 8-hydroxypyrene-1,3,6-trisulfonic acid trisodium salt) for 40 min. After hydration, the suspension was submitted to 5 freeze-thaw cycles (liquid nitrogen, water at room temperature). The large multilamellar liposome suspension (0.4mL) was submitted to high-pressure extrusion at room temperature (21 extrusions through a 0.1  $\mu$ m polycarbonate membrane afforded a suspension of LUVs with an average diameter of 100 nm). The LUV suspension was separated from extravesicular dye by size exclusion chromatography (SEC) (stationary phase: Sephadex G-50, mobile phase: phosphate buffer) and diluted to 2.8 ml with the same phosphate buffer to give a stock solution with a lipid concentration of 3.66 mM (assuming 100% of lipid was incorporated into liposomes).

### **Sodium transport experiments**

The preparation of the vesicles is described beforehand. 100  $\mu$ L of HPTS-loaded vesicles (stock solution) was suspended in 1.9 mL of the buffer (PBS 10mM pH=6.4 containing 100mM of NaCl) and placed into a fluorimetric cell. The emission of HPTS at 510 nm was monitored with excitation wavelengths at 403 and 460 nm simultaneously. During the experiment, 20  $\mu$ L of a 0-30 mM DMSO solution of the compound of interest was added at t = 50s, followed by injection of 21  $\mu$ L of 0.5 M aqueous NaOH at t = 100s. The addition of the NaOH resulted in a pH increase of approximately 1 pH unit in the extra vesicular buffer. Maximal possible changes in dye emission were obtained at t = 500s by lysis of the liposomes with detergent (40  $\mu$ L of 5% aqueous Triton X100). The experiment

is ended at  $t = 800$ s. This offers a window of 500 seconds of transport. The final transport trace was obtained as a ratio of the emission intensities monitored at 460 and 403 nm and normalized to 100% of transport.

In the case of other ions the protocol is adapted by changing the 100 mM NaCl in the PBS buffer with a solution of the respective ion.

### **Proton transport experiments**

The preparation of the vesicles is described previously. 100  $\mu$ L of HPTS-loaded vesicles (stock solution) was suspended in 1.9 mL of the buffer (PBS 10mM pH=6.4 containing 100mM of KCl) and placed into a fluorimetric cell. The emission of HPTS at 510 nm was monitored with excitation wavelengths at 403 and 460 nm simultaneously. During the experiment, 20  $\mu$ L of a 0-maximum allowed concentration mM DMSO solution of the compound of interest was added at  $t = 50$ s, followed by injection of 20  $\mu$ L of 1 nM solution of valinomycin in DMSO at  $t = 100$ s. at time =150s an injection of 21  $\mu$ L of 0.5 M aqueous NaOH. The addition of the NaOH resulted in a pH increase of approximately 1 pH unit in the extra vesicular buffer. Maximal possible changes in dye emission were obtained at  $t = 500$ s by lysis of the liposomes with detergent (40  $\mu$ L of 5% aqueous Triton X100). The experiment is ended at  $t = 800$ s. This offers a window of 500 seconds of transport. The final transport trace was obtained as a ratio of the emission intensities monitored at 460 and 403 nm and normalized to 100% of transport. This offers a window of 500 seconds of transport. The final transport trace was obtained as a ratio of the emission intensities monitored at 460 and 403 nm and normalized to 100% of transport.

### **Proton transport using stopped flow techniques (performed by Yuexiao Shen at Penn State University)**

6 mg/ml PC, and 400 mmol/ml fluorescently labeled dextran (D-3305, Life Technologies) were first dissolved in buffer containing 10 mM HEPES, 100 mM KCl and pH=6.4 and the detergent *n*-octyl- $\beta$ -D-glucoside (OG, 4% w/v). The liposomes formed after being dialyzed for 36 hours and were subsequently extruded through the 0.2  $\mu$ m track-etched filters. The resulting monodisperse unilamellar vesicles were further subject to size exclusion in order to remove residual free dye. Because of the dilution of the size



exclusion process, the purified liposomes, with 400 mM/mL fluorescent dextran only encapsulated inside the vesicles, contained approximately 3 mg/ml PC. 1  $\mu$ l valinomycin (0.5 mg/ml in DMSO) and 10  $\mu$ l imidazole compounds (various concentrations in DMSO) were then added to 400  $\mu$ l fluorescent vesicles. After 5 min, the mixture was mixed with same buffer at pH of 8.4 in stopped flow experiments, which caused a pH gradient across the lipid bilayers (pH 6.4 inside the vesicles and pH 7.4 outside the vesicles). The fluorescent signals ( $\lambda_{\text{ex}}=494$  nm,  $\lambda_{\text{em}}=521$ nm) were recorded on the stopped-flow instrument at a fixed photomultiplier tube value of 571 V. The fluorescent vesicles at different pH without the additions of valinomycin and imidazole compounds were prepared and tested on the stopped-flow for fluorescence vs. pH calibration.

### **Vesicle preparation for Stopped flow experiments**

A mixture of PC (Egg yolk L- $\alpha$ -phosphatidylcholine, EYPC chloroform solution, 18.6 mg, 24.2 mmol), PS (L- $\alpha$ -phosphatidylserine, Brain, Porcine, sodium salt chloroform solution, 5 mg, 6.04 mmol) and cholesterol (3 $\beta$ -Hydroxy-5-cholestene, 5-Cholesten-3 $\beta$ -ol, powder, 11.7 mg, 30.3 mmol), corresponding to a 4:1:5 molar ratio, was dissolved in a 1:1 CHCl<sub>3</sub>/MeOH mixture (5 ml total volume). The solution was evaporated under reduced pressure and the resulting thin film was dried under high vacuum for 2 h. The lipid film was hydrated in 1 mL of phosphate buffer (10 mM sodium phosphate, pH = 6.4, 100 or 200 mM sucrose) for 40 min. After hydration, the suspension was submitted to 5 freeze-thaw cycles (liquid nitrogen, water at room temperature). The large multilamellar liposome suspension (1mL) was submitted to high-pressure extrusion at room temperature (21 extrusions through a 0.1  $\mu$ m polycarbonate membrane afforded a suspension of LUVs with an average diameter of 100 nm). The LUV suspension was then diluted to 7 ml with the same phosphate buffer to give a stock solution with a concentration of 8.61 mM (assuming 100% of lipid was incorporated into liposomes).

### **Water transport using stopped flow techniques**

Phosphatidylcholine (chicken egg, PC) and phosphatidylserine (porcine brain, PS) were purchased from Avanti Polar Lipids. Cholesterol (Chl) was obtained from Sigma. They were used without further purification.

Two incorporation methods were employed to introduce the imidazole derivatives within the lipidic phase.

**METHOD 1 (performed at Penn State University):** Liposomes were prepared using the film rehydration method (1). The imidazole compounds, in chloroform/methanol mixture ( $\text{CHCl}_3/\text{MeOH}$ , v/v: 1/1) were added to the 1 mg PC/PS/Chl mixture with a molar ratio of 4/1/5. The solution was dried on a rotary evaporator and subsequently under high vacuum to remove residual solvent. After rehydration with 1 ml buffer containing 10 mM Hepes (pH=7), 100 mM NaCl and 0.01%  $\text{NaN}_3$ , the suspension was incubated with stirring at 4 °C for 24 h and extruded through 0.2  $\mu\text{m}$  track-etched filters for 10 times (Whatman, UK) to obtain monodisperse unilamellar vesicles, the size of which was characterized by dynamic light scattering (Zetasizer Nano, Malvern Instruments Ltd., UK). The water permeability tests were conducted on a stopped-flow instrument (SF-300X, KinTek Corp., USA). Exposure of vesicles to hypertonic osmolyte (10 mM Hepes, 300 mM NaCl, 0.01%  $\text{NaN}_3$  and pH=7) resulted in the shrinkage of the vesicles due to an outwardly directed osmotic gradient. The abrupt decrease of the vesicle size led to the increase in the light scattering at 90° according to the Rayleigh-Gans theory applied to this system (2). The changes of light scattering caused by vesicle shrinkage were recorded at a wavelength of 600 nm

**METHOD 2 (Performed at IEM Montpellier):** Liposomes were prepared using the same film rehydration method as above. A PC/PS/Chl mixture with a molar ratio of 4/1/5 was dissolved in chloroform/methanol mixture ( $\text{CHCl}_3/\text{MeOH}$ , v/v: 1/1). The solution was dried on a rotary evaporator and subsequently under high vacuum to remove residual solvent. After rehydration with 1 ml buffer containing 200 mM sucrose / 10 mM PBS buffer solution (pH=6.4), the suspension was extruded through 0.1  $\mu\text{m}$  track-etched filters for 21 times (Whatman, UK) to obtain monodisperse unilamellar vesicles, the size of which was characterized by dynamic light scattering (Zetasizer Nano, Malvern Instruments Ltd., UK). The water permeability tests were conducted on a stopped-flow instrument (SFM3000 + MOS450, Bio-Logic SAS, Claix, France). Exposure of vesicles to hypertonic & hypotonic osmolyte (400 & 0 mM sucrose / 10 mM PBS buffer solution, pH=6.4) resulted in the

shrinkage and swelling of the vesicles due to an outwardly and inwardly directed osmotic gradient. The changes of light scattering were recorded at a wavelength of 345 nm.

### **Stopped flow experiments**

100  $\mu$ l of the vesicles prepared according to the described protocol are suspended in 1.880  $\mu$ l of an isotonic solution of buffer, PBS, 10mM, pH=6.4, containing a known concentration of sucrose (100mM or 200mM). An aliquot (20 $\mu$ l) of active compound in different concentrations, or blank (DMSO) is injected. The sample is then let to rest for 30 minutes so that the channels are formed. The sample containing the SUVs and the pre-formed channels is loaded in one of the reservoirs of the instrument. A solution containing the same buffer with a different osmolality (+ or – 100 mOsm) is loaded in another reservoir of the instrument. The measurements are made by quickly mixing the two solutions in equal volumes thus resulting the osmotic shock. The analysis is carried out for 4 seconds, enough time so that the system reaches equilibrium and the signal becomes a flat line.

### **Formation of liposomes for DLS experiments**

Egg yolk L- $\alpha$ -phosphatidylcholine (EYPC chloroform solution, 20 mg, 26 mmol) was dissolved in a 1:1 CHCl<sub>3</sub>/MeOH mixture (2 ml total volume), the solution was evaporated under reduced pressure and the resulting thin film was dried under high vacuum for 2 h. The lipid film was hydrated in 0.4 mL of phosphate buffer (10 mM sodium phosphate, pH = 6.4, 100 mM NaCl) for 40 min. After hydration, the suspension was submitted to 5 freeze-thaw cycles (liquid nitrogen, water at room temperature). The large multilamellar liposome suspension (0.4mL) was submitted to high-pressure extrusion at room temperature (21 extrusions through a 0.1  $\mu$ m polycarbonate membrane afforded a suspension of LUVs with an average diameter of 100 nm). The LUV suspension was diluted to 2.8 ml with the same phosphate buffer to give a stock solution with a lipid concentration of 3.66 mM (assuming 100% of lipid was incorporated into liposomes).

## **Chapter 3**

### **Electrode cleaning**

The gold on glass plates were thoroughly washed with ethanol and MilliQ water. The electrochemical cleaning was done in a 3 electrode cell (Ag/AgCl ref, steel counter electrode) using a 0.1M HCl solution. The potential was varied between 0.6 and -0.8V with a speed of 100mV/s. this cycle was repeated 8 times. The electrode was then rinsed with MilliQ water and dried.

### **Electrodeposition of mesoporous silica layer**

The silica matrix was made through electrodeposition methods with a procedure adapted from Walcarius et al. [125, 143-145] A mixture of tetraethylsiloxane (TEOS) and (3-mercaptopropyl)trimethoxysilane (MPTMS) in ethanol was mixed with CTAB (hexadecyltrimethylammonium bromide) as template agent dissolved in a 0.1 M solution of NaNO<sub>3</sub>. The solution was aged under stirring for 2.5h at pH 3 prior to electrodeposition. The mesoporous silica films were deposited by applying a negative potential of -1.4 V for 10 s on the gold electrode immersed in the pre-hydrolysed precursor solution. The electrode was removed from the solution and the electrodeposited surfactant-templated film was cured overnight at 60 °C and washed in ethanol.

### **Alkylation of mesoporous silica layer and subsequent in-pores self-assembly of TAA nanowires.**

The resulting electrode was modified with hexyltrichlorosilane (C6) in a toluene solution at 60 °C for 6 h in order to obtain a hydrophobic surface coating, covalently linked to the inner silica mesopores. Triarylamines were non-covalently confined in the hydrophobic mesopores by immersing the functionalized electrodes in a 1.5 mM chloroform solution of TAA that was irradiated for one hour with a halogen lamp of 20 W.

### **Bioelectrode preparation**

15 mg of commercial carbon powder Super P (TIMCAL) were sonicated for 5 min in PBS (phosphate buffer solution) pH=5 and stirred for 30 min. 333 µL of this mixture were pipetted over 5 mg of Laccase enzyme from *Trametes Versicolor* (20 U/mg\*solid), and mixed for 2 min. Separately, a solution of ABTS (2,2'-azino-bis(3-ethylbenzothiazoline-6-sulphonic acid)) was made out of 2.7 mg of ABTS in 500 µL of

PBS at pH=5 and homogenized. 100  $\mu\text{L}$  of the enzyme solution were mixed with 90  $\mu\text{L}$  of the ABTS solution, and stirred for another 30 min. 10  $\mu\text{L}$  of Nafion resin (5 wt%) solution were added and the solution was homogenized for another 3 min. The electrode surfaces were pre-treated with a solution of PAA. 15  $\mu\text{L}$  of the enzyme solution was drop-cast on a surface of 20  $\text{mm}^2$  (estimated laccase loading of 560  $\mu\text{g}/\text{cm}^2$ ). The electrodes were then left to dry at room temperature and then stored in the fridge.

### **X-ray photoelectron spectrometry-XPS**

XPS analyses were performed on a KRATOS Axis Nova (Kratos Analytical, Manchester, United Kingdom), using  $\text{AlK}\alpha$  radiation, with 20 mA current and 15 kV voltage (300 W), under a base pressure of  $10^{-8}$  to  $10^{-9}$  Torr in the sample chamber. The incident monochromatic X-ray beam was focused on a 0.7 mm x 0.3 mm area of the samples bearing surface. XPS survey spectra were collected in the range of  $-10 \div 1200$  eV, with a resolution of 1 eV, at a pass energy of 160 eV. The high resolution spectra for all the elements identified in the survey spectra were collected using a pass energy of 20 eV and a step size of 0.1 eV. XPS data fitting were performed making use of the Vision Processing software (Vision2 software, Version 2.2.10), and mixed Gaussian-Lorentzian curves. The linear background was subtracted before the peak areas were corrected. The binding energy of the C 1s peak was normalized to 285 eV. Elemental analyses were performed using a scanning electron microscope (Quanta 200-FEI) equipped with an energy-dispersive X-ray spectroscopy system (EDX). Elemental nitrogen analysis was performed on a Perkin Elmer 2410 Series II CHNS/O ANALYZER 2400. We thank I. A. Dascalu ("Petru Poni" Institute of Macromolecular Chemistry of Romanian Academy, Iasi, Romania) for XPS Measurements.

### **Other experimental data**

#### **Influence of Electrolyte Solutions**

The electrochemical characterization of the electrodes was made in several electrolyte solutions ( $\text{NaNO}_3$ ,  $\text{KClO}_4$ , PBS pH=7) using the redox probe  $\text{Ru}(\text{NH}_3)_3\text{Cl}_3$ . This variation was used to describe the type of the system created. Classical electrodes have a well-defined, integer surfaces which behave in a predictable manner. In the case of our

designed systems, there is a question of the behavior of the array of nanoscale contacts, namely would they function as a whole or as individual contacts. An accurate description of the fashion in which these nanofibers conduct electricity is imperative. One of the premises of designing the modified electrode was the metal-like conductive properties of the TAA1; therefore the contact's response is key to the devices' functioning. These two aspects were characterized by doing scan speed variation tests on the electrodes in three different electrolyte solutions:  $\text{NaNO}_3$ ,  $\text{KClO}_4$ , and PBS (in Figure 109, Figure 110 and Figure 111) represent these experiments.

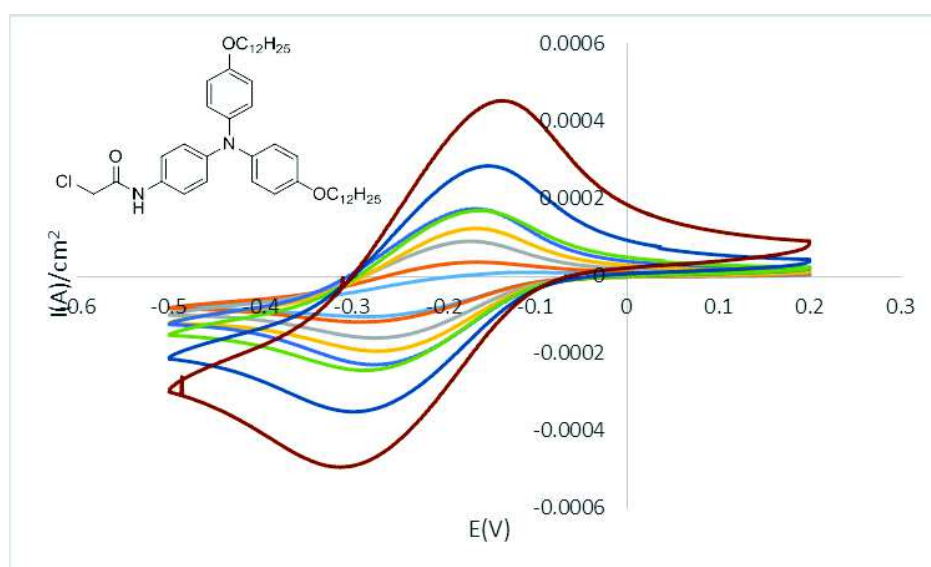


**Figure 109:** Scan speed experiments in  $\text{NaNO}_3$  (0.1M) redox couple  $\text{Ru}^{3+}/\text{Ru}^{2+}$ , TAA1 system ref.  $\text{Ag}/\text{AgCl}$ . Speed varied between 5 and 200 mV/s. The electrochemical signal increases with the increase of the scan speed. Light blue- 5 mV/s; Orange- 10 mV/s; Gray- 20 mV/s; Yellow- 30 mV/s; Blue- 40 ; Green- 50 mV/s; Dark Blue- 100 mV/s; Dark red- 200 mV/s.

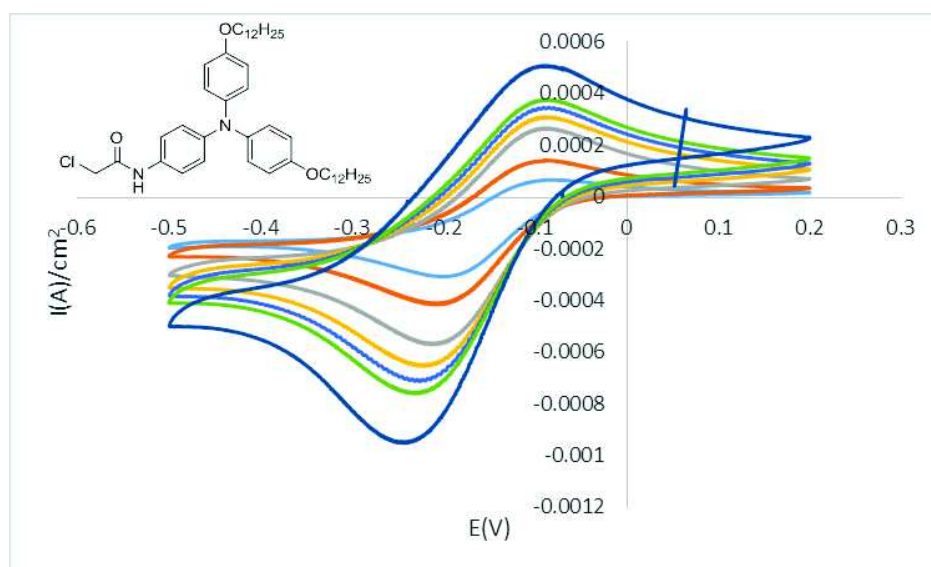


Figure 110: Scan speed experiments in KClO<sub>4</sub> (0.1M) redox couple Ru<sup>3+</sup>/Ru<sup>2+</sup> TAA1 system ref. Ag/AgCl. Speed varied between 5 and 100 mV/s. The electrochemical signal increases with the increase of the scan speed. Light blue- 5 mV/s; Orange- 10 mV/s; Gray- 20 mV/s; Yellow- 30 mV/s; Blue- 40 ; Green- 50 mV/s; Dark Blue- 100 mV/s.

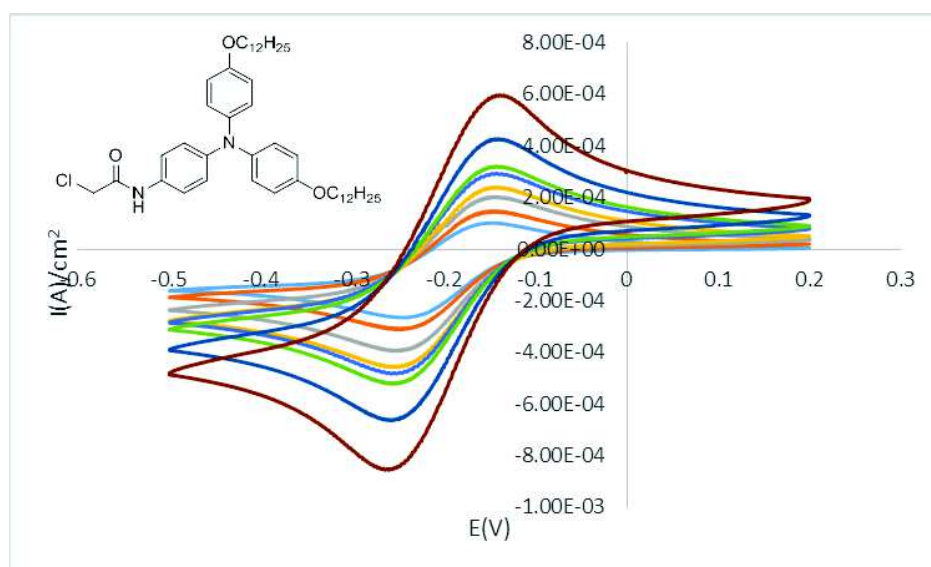


Figure 111: Scan speed experiments in PBS, pH=7 (0.1M) redox couple Ru<sup>3+</sup>/Ru<sup>2+</sup> TAA1 system ref. Ag/AgCl. Speed varied between 5 and 200 mV/s. The electrochemical signal increases with the increase of the scan speed. Light blue- 5 mV/s; Orange- 10 mV/s; Gray- 20 mV/s; Yellow- 30 mV/s; Blue- 40 ; Green- 50 mV/s; Dark Blue- 100 mV/s; Dark red- 200 mV/s.

The fact that the systems react to the variation of the scan speed indicates that they are indeed electrochemically active and electron transfer is coupled to the diffusion of species. From the intensity value of the electrode it was concluded that the size of the anion does affect the functioning of the system and there are small variations that could be found as seen from Figure 112. The peak-to-peak separation  $\Delta E$ , have very similar values (100 mV for  $\text{NaNO}_3$ , 84 mV for PBS and 81 mV for  $\text{KClO}_4$ ), making  $\text{KClO}_4$  the most efficient electrolyte.

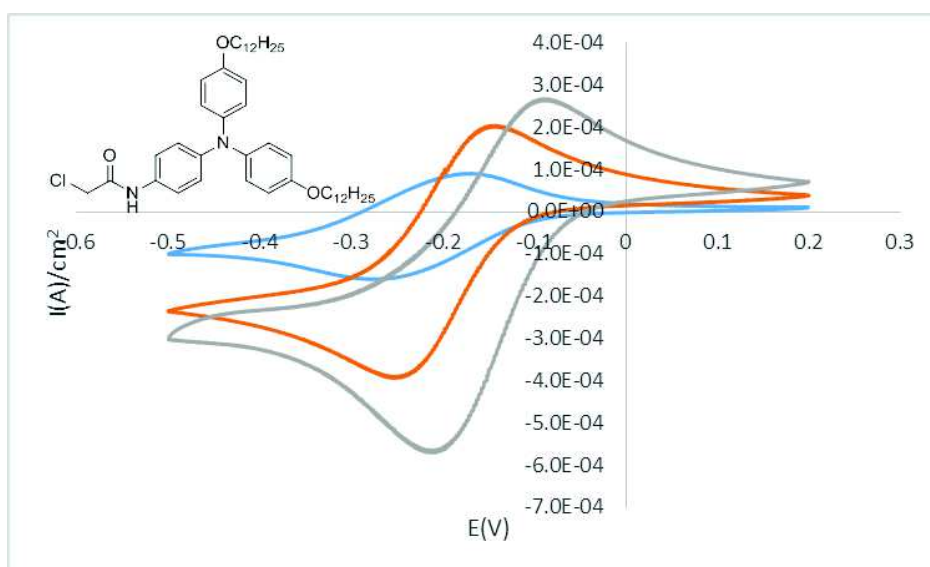
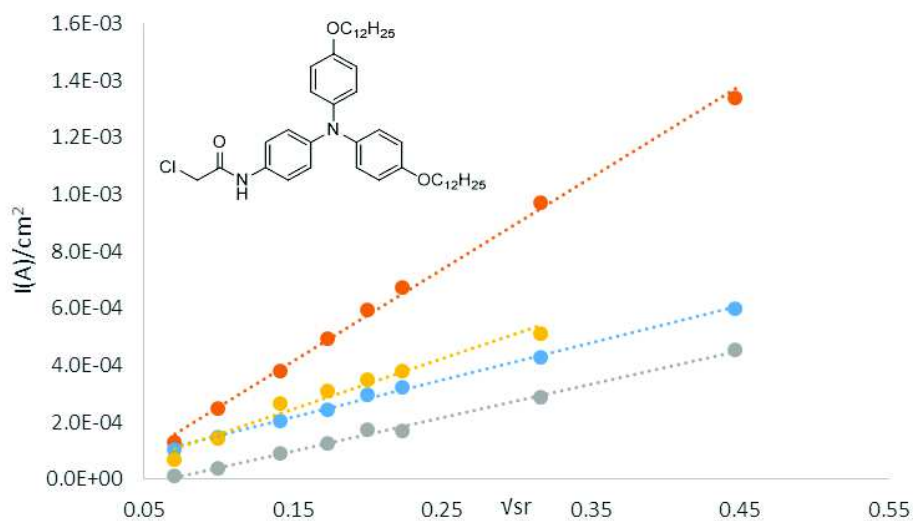


Figure 112: Influence of electrolyte on a TAA1 electrode redox couple  $\text{Ru}^{3+}/\text{Ru}^{2+}$ , scan speed 20mV/s ref.  $\text{Ag}/\text{AgCl}$ . Electrolyte solutions  $\text{NaNO}_3$  (light blue), PBS (orange),  $\text{KClO}_4$  (gray) having the same concentration (0.1M). Differences in current intensity observable.





**Figure 113: Linear dependencies of the oxidation peak current intensity vs. the square root of scan speed. Up- Orange - porous electrode in NaNO<sub>3</sub>; Gray - TAA1 electrode in NaNO<sub>3</sub>; Blue - TAA1 electrode in PBS; Yellow - TAA1 electrode in KClO<sub>4</sub>. In all cases an electrolyte concentration of 0.1M was used together with the redox couple redox couple Ru<sup>3+</sup>/Ru<sup>2+</sup> ref. Ag/AgCl**

By using the peak intensities a correlation between them and the square root of the scan speed can be made as predicted by the Randles-Sevcik equation. These representations are presented in Figure 113. All of them present a linear dependency with very good R<sup>2</sup> values, over 0.95. This implies that the diffusion of the ruthenium ions is the limiting factor of the charge passing through the electrodes and not the intrinsic conduction displayed by the TAA1 wires. If another type of dependency would have been found, the system's electrical properties would be in question. Thus, the doped electrodes behave as a gold electrode would, implying the metal like conductivity of the TAA1. A scan speed variation on a porous electrode was also performed and the same linear dependency is also presented in Figure 113. The experiments were also used to characterize the TAA2 system in NaNO<sub>3</sub> with very similar results. These results are presented in Figure 114.

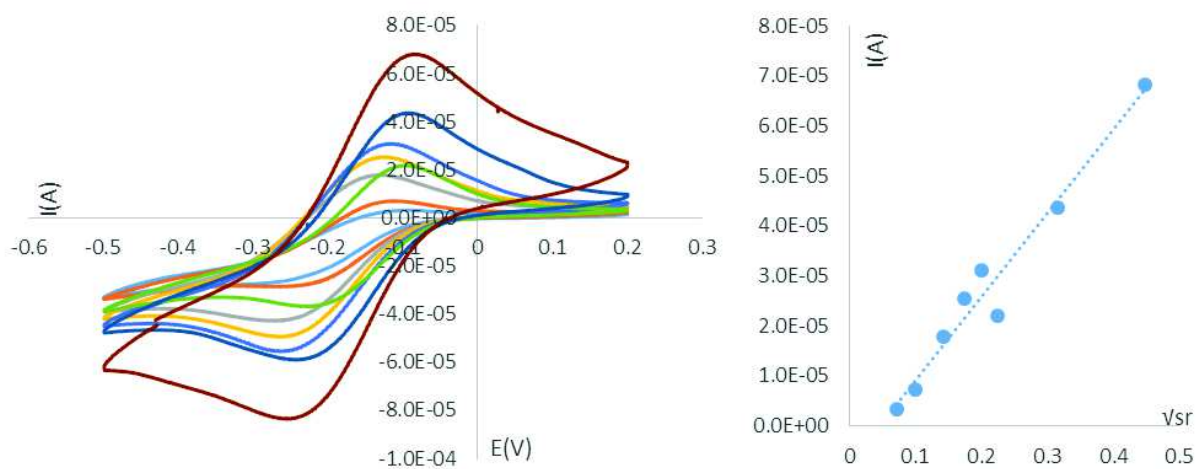


Figure 114: Scan speed tests on a TAA2 electrode in 0.1 M NaNO<sub>3</sub>, redox couple Ru<sup>3+</sup>/Ru<sup>2+</sup>, ref. Ag/AgCl, (left) and linear dependency of I<sub>ox</sub> vs. the square root of the scan speed (right). Curve colors: Light blue- 5 mV/s; Orange- 10 mV/s; Gray- 20 mV/s; Yellow- 30 mV/s; Blue- 40 ; Green- 50 mV/s; Dark Blue- 100 mV/s; Dark red- 200 mV/s.

Performance of the biocathodes over 4 weeks

The data is presented in Table 22.

Table 22: Normalized and numerical values for the evolution of current intensity for the four types of biocathodes tested.

| Porous electrode |           |            | Modified C6 electrode |           |            | TAA1 electrode |           |            |
|------------------|-----------|------------|-----------------------|-----------|------------|----------------|-----------|------------|
| days             | I (A)     | % activity | days                  | I (A)     | % activity | days           | I (A)     | % activity |
| 1                | -1,25E-04 | 100,00%    | 1                     | -1,44E-04 | 100,00%    | 1              | -2,43E-04 | 100,00%    |
| 4                | -9,76E-05 | 78,14%     | 5                     | -6,69E-05 | 46,59%     | 5              | -1,96E-04 | 80,62%     |
| 8                | -3,96E-05 | 31,66%     | 13                    | -2,37E-05 | 16,52%     | 13             | -9,29E-05 | 38,30%     |
| 15               | -4,52E-05 | 36,20%     | 21                    | -1,74E-05 | 12,14%     | 21             | -5,28E-05 | 21,75%     |
| 25               | -2,71E-05 | 21,67%     | 26                    | -2,23E-05 | 15,53%     | 26             | -5,36E-05 | 22,12%     |

## Bibliography

- [1] A. Lehninger, D. L. Nelson, and M. M. Cox, *Lehninger principles of biochemistry*. New York: W.H. Freeman, 2005.
- [2] S. P. Hansen and T. M. Fyles, "Carrier-mediated electro dialysis.," *Chem. Commun. (Camb)*., vol. 47, no. 22, pp. 6428–6430, 2011.
- [3] S. Varma, D. Sabo, and S. B. Rempe, "K<sup>+</sup>/Na<sup>+</sup> Selectivity in K Channels and Valinomycin: Over-coordination Versus Cavity-size constraints," *J. Mol. Biol.*, vol. 376, no. 1, pp. 13–22, 2008.
- [4] D. A. Doyle, "The Structure of the Potassium Channel: Molecular Basis of K<sup>+</sup> Conduction and Selectivity," *Science (80-. )*., vol. 280, no. 5360, pp. 69–77, Apr. 1998.
- [5] Y. Zhou, J. H. Morais-Cabral, A. Kaufman, and R. MacKinnon, "Chemistry of ion coordination and hydration revealed by a K<sup>+</sup> channel-Fab complex at 2.0 Å resolution.," *Nature*, vol. 414, no. 6859, pp. 43–8, Nov. 2001.
- [6] E. Gouaux and R. Mackinnon, "Principles of selective ion transport in channels and pumps.," *Science*, vol. 310, no. 5753, pp. 1461–5, Dec. 2005.
- [7] J.-M. Lehn and J. Sanders, "Supramolecular Chemistry. Concepts and Perspectives," *Angew. Chemie.*, vol. 34, no. 22, 1995.
- [8] J.-M. Lehn, "Supramolecular Chemistry—Scope and Perspectives Molecules, Supermolecules, and Molecular Devices(Nobel Lecture)," *Angew. Chemie Int. Ed. English*, vol. 27, no. 1, pp. 89–112, Jan. 1988.
- [9] M. Barboiu, "Dynamic interactive systems: dynamic selection in hybrid organic-inorganic constitutional networks.," *Chem. Commun. (Camb)*., vol. 46, no. 40, pp. 7466–7476, 2010.
- [10] P. Blondeau, Y. M. Legrand, A. Van Der Lee, G. Nasr, and M. Barboiu, "Multiple processing of metal-ion coordination, anion-binding, hydrogen-bonding-self-assembly and  $\pi$ - $\pi$  stacking subprograms in silver (I) coordination polymers," *Rev. Chim.*, vol. 59, no. 3, pp. 260–265, 2008.
- [11] G. Nasr, T. Macron, A. Gilles, E. Petit, and M. Barboiu, "Systems membranes – combining the supramolecular and dynamic covalent polymers for gas-selective dynameric membranes," *Chem. Commun.*, vol. 48, no. 59, p. 7398, 2012.

- [12] M. Michau, M. Barboiu, R. Caraballo, C. Arnal-Hérault, P. Perriat, A. Der Van Lee, and a. Pasc, "Ion-conduction pathways in self-organised ureidoarene-heteropolysiloxane hybrid membranes," *Chem. - A Eur. J.*, vol. 14, no. 6, pp. 1776–1783, 2008.
- [13] M. Michau, R. Caraballo, C. Arnal-Hérault, and M. Barboiu, "Alkali cation- $\pi$  aromatic conduction pathways in self-organized hybrid membranes," *J. Memb. Sci.*, vol. 321, no. 1, pp. 22–30, 2008.
- [14] A. Cazacu, A. Pasc-Banu, and M. Barboiu, "Molecular and supramolecular dynamics - A versatile tool for self-organization of polymeric membranes systems," *Macromol. Symp.*, vol. 245–246, pp. 435–438, 2006.
- [15] C. Arnal-Hérault, M. Michau, and M. Barboiu, "Mixed supramolecular cation-carrier and anion-carrier facilitated transport for the selective alkali cations transport," *J. Memb. Sci.*, vol. 321, no. 1, pp. 94–99, 2008.
- [16] A. Cazacu, C. Tong, A. Van Der Lee, T. M. Fyles, and M. Barboiu, "Columnar self-assembled ureido crown ethers: An example of ion-channel organization in lipid bilayers," *J. Am. Chem. Soc.*, vol. 128, no. 29, pp. 9541–9548, 2006.
- [17] C. Arnal-Hérault, M. Barboiu, E. Petit, M. Michau, and A. van der Lee, "Cation- $\pi$  interaction: a case for macrocycle-cation  $\pi$ -interaction by its ureidoarene counteranion," *New J. Chem.*, vol. 29, no. 12, p. 1535, 2005.
- [18] M. Barboiu, a. Meffre, Y.-M. Legrand, E. Petit, L. Marin, M. Pinteala, and a. V. D. Lee, "Frustrated ion-pair binding by heteroditopic macrocyclic receptors," *Supramolecular Chemistry*, vol. 26, no. 3–4. Taylor & Francis, pp. 223–228, 2013.
- [19] M. Barboiu, Y. Le Duc, A. Gilles, P.-A. Cazade, M. Michau, Y. Marie Legrand, A. van der Lee, B. Coasne, P. Parvizi, J. Post, and T. Fyles, "An artificial primitive mimic of the Gramicidin-A channel.," *Nat. Commun.*, vol. 5, no. May, p. 4142, 2014.
- [20] M. Barboiu, A. Cazacu, S. Mihai, Y.-M. M. Legrand, G. Nasr, Y. Le Duc, E. Petit, and A. van der Lee, "Dynamic constitutional hybrid materials-toward adaptive self-organized devices Mihail Barboiu,\* Adinela Cazacu, Simona Mihai, Yves-Marie Legrand, Arie van der Lee," *Microporous Mesoporous Mater.*, vol. 1189, no. 1–3, pp. 51–57, Apr. 2009.
- [21] Y.-M. Legrand, M. Michau, A. van der Lee, and M. Barboiu, "Homomeric and heteromeric self-assembly of hybrid ureido-imidazole compounds," *CrystEngComm*, vol. 10, no. 5, p. 490, Apr. 2008.

- [22] Y. LeDuc, M. Michau, A. Gilles, V. Gence, Y. M. Legrand, A. Vanderlee, S. Tingry, and M. Barboiu, "Imidazole-quartet water and proton dipolar channels," *Angew. Chemie - Int. Ed.*, vol. 50, no. 48, pp. 11366–11372, 2011.
- [23] S. Mihai, A. Cazacu, C. Arnal-Herault, G. Nasr, A. Meffre, A. van der Lee, and M. Barboiu, "Supramolecular self-organization in constitutional hybrid materials," *New J. Chem.*, vol. 33, no. 11, p. 2335, Nov. 2009.
- [24] A. Cazacu, Y.-M. Legrand, A. Pasc, G. Nasr, A. Van der Lee, E. Mahon, and M. Barboiu, "Dynamic hybrid materials for constitutional self-instructed membranes," *Proc. Natl. Acad. Sci.*, vol. 106, no. 20, pp. 8117–8122, Apr. 2009.
- [25] E. Sabadini, K. R. Francisco, and L. Bouteiller, "Bis-urea-based supramolecular polymer: The first self-assembled drag reducer for hydrocarbon solvents," *Langmuir*, vol. 26, no. 3, pp. 1482–1486, 2010.
- [26] J. Fremaux, L. Fischer, T. Arbogast, B. Kauffmann, and G. Guichard, "Condensation approach to aliphatic oligourea foldamers: Helices with N-(Pyrrolidin-2-ylmethyl)ureido junctions," *Angew. Chemie - Int. Ed.*, vol. 50, no. 48, pp. 11382–11385, 2011.
- [27] J. J. Van Gorp, J. a J. M. Vekemans, and E. W. Meijer, "C3-symmetrical supramolecular architectures: Fibers and organic gels from discotic trisamides and trisureas," *J. Am. Chem. Soc.*, vol. 124, no. 49, pp. 14759–14769, 2002.
- [28] N. Roy, E. Buhler, and J. M. Lehn, "The tris-urea motif and its incorporation into polydimethylsiloxane-based supramolecular materials presenting self-healing features," *Chem. - A Eur. J.*, vol. 19, no. 27, pp. 8814–8820, 2013.
- [29] S. Matile, A. Som, and N. Sordé, "Recent synthetic ion channels and pores," *Tetrahedron*, vol. 60, no. 31, pp. 6405–6435, Jul. 2004.
- [30] A. L. Sisson, M. R. Shah, S. Bhosale, and S. Matile, "Synthetic ion channels and pores (2004-2005).," *Chem. Soc. Rev.*, vol. 35, no. 12, pp. 1269–86, Dec. 2006.
- [31] S. Matile, A. Vargas Jentsch, J. Montenegro, and A. Fin, "Recent synthetic transport systems.," *Chem. Soc. Rev.*, vol. 40, no. 5, pp. 2453–74, May 2011.
- [32] S. Futaki, M. Fukuda, M. Omote, K. Yamauchi, T. Yagami, M. Niwa, and Y. Sugiura, "Alamethicin–Leucine Zipper Hybrid Peptide: A Prototype for the Design of Artificial Receptors and Ion Channels," *J. Am. Chem. Soc.*, vol. 123, no. 49, pp. 12127–12134, Dec. 2001.
- [33] S. Terrettaz, W.-P. Ulrich, R. Guerrini, A. Verdini, and H. Vogel, "Immunosensing by a Synthetic Ligand-Gated Ion Channel Financial support from the board of the Swiss Federal Institutes of Technology (SPP Minast, 7.06) is acknowledged. We

- thank G. Corradin for numerous discussions and J. Lakey for critical reading of the,” *Angew. Chem. Int. Ed. Engl.*, vol. 40, no. 9, pp. 1740–1743, May 2001.
- [34] P. Läuger, “Mechanisms of Biological Ion Transport— Carriers, Channels, and Pumps in Artificial Lipid Membranes,” *Angew. Chemie Int. Ed. English*, vol. 24, no. 11, pp. 905–923, Nov. 1985.
- [35] S. Oiki, R. E. Koeppe, and O. S. Andersen, “Voltage-dependent gating of an asymmetric gramicidin channel.,” *Proc. Natl. Acad. Sci. U. S. A.*, vol. 92, no. 6, pp. 2121–5, Mar. 1995.
- [36] S. B. HLADKY and D. A. HAYDON, “Discreteness of Conductance Change in Bimolecular Lipid Membranes in the Presence of Certain Antibiotics,” *Nature*, vol. 225, no. 5231, pp. 451–453, Jan. 1970.
- [37] T. E. Andreoli, “On the anatomy of amphotericin B-cholesterol pores in lipid bilayer membranes,” *Kidney Int.*, vol. 4, no. 5, pp. 337–345, Nov. 1973.
- [38] B. de Kruijff and R. A. Demel, “Polyene antibiotic-sterol interactions in membranes of *Acholeplasma laidlawii* cells and lecithin liposomes. 3. Molecular structure of the polyene antibiotic-cholesterol complexes.,” *Biochim. Biophys. Acta*, vol. 339, no. 1, pp. 57–70, Feb. 1974.
- [39] M. A. Ghannoum and L. B. Rice, “Antifungal agents: mode of action, mechanisms of resistance, and correlation of these mechanisms with bacterial resistance.,” *Clin. Microbiol. Rev.*, vol. 12, no. 4, pp. 501–17, Oct. 1999.
- [40] A. Chaudhuri, S. Haldar, H. Sun, R. E. Koeppe, and A. Chattopadhyay, “Importance of indole NH hydrogen bonding in the organization and dynamics of gramicidin channels,” *Biochim. Biophys. Acta - Biomembr.*, vol. 1838, no. 1 PARTB, pp. 419–428, 2014.
- [41] I. Basu, A. Chattopadhyay, and C. Mukhopadhyay, “Ion channel stability of Gramicidin A in lipid bilayers: Effect of hydrophobic mismatch,” *Biochim. Biophys. Acta - Biomembr.*, vol. 1838, no. 1 PARTB, pp. 328–338, 2014.
- [42] S. S. Rawat, D. a Kelkar, and A. Chattopadhyay, “Monitoring gramicidin conformations in membranes: a fluorescence approach.,” *Biophys. J.*, vol. 87, no. 2, pp. 831–843, 2004.
- [43] S. Kubota, S. Ozaki, J. Onishi, K. Kano, and O. Shirai, “Selectivity on ion transport across bilayer lipid membranes in the presence of gramicidin A.,” *Anal. Sci.*, vol. 25, no. 2, pp. 189–193, 2009.

- [44] D. a Kelkar and A. Chattopadhyay, "The gramicidin ion channel: a model membrane protein.," *Biochim. Biophys. Acta*, vol. 1768, no. 9, pp. 2011–2025, 2007.
- [45] P. Greisen, K. Lum, M. Ashrafuzzaman, D. V Greathouse, O. S. Andersen, and J. A. Lundbæk, "Linear rate-equilibrium relations arising from ion channel-bilayer energetic coupling.," *Proc. Natl. Acad. Sci. U. S. A.*, vol. 108, no. 31, pp. 12717–22, Aug. 2011.
- [46] A. Nakano, Q. Xie, J. V. Mallen, L. Echegoyen, and G. W. Gokel, "Synthesis of a membrane-insertable, sodium cation conducting channel: kinetic analysis by dynamic sodium-23 NMR," *J. Am. Chem. Soc.*, vol. 112, no. 3, pp. 1287–1289, Jan. 1990.
- [47] G. W. Gokel, R. Ferdani, J. Liu, R. Pajewski, H. Shabany, and P. Uetrecht, "Hydraphile channels: models for transmembrane, cation-conducting transporters.," *Chemistry*, vol. 7, no. 1, pp. 33–9, Jan. 2001.
- [48] H. Shabany and G. W. Gokel, "Enhancement of cation transport in synthetic hydraphile channels having covalently-linked headgroups," *Chem. Commun.*, no. 23, pp. 2373–2374, Jan. 2000.
- [49] W. M. Leevy, S. T. Gammon, T. Levchenko, D. D. Daranciang, O. Murillo, V. Torchilin, D. Piwnica-Worms, J. E. Huettner, and G. W. Gokel, "Structure-activity relationships, kinetics, selectivity, and mechanistic studies of synthetic hydraphile channels in bacterial and mammalian cells.," *Org. Biomol. Chem.*, vol. 3, no. 19, pp. 3544–50, Oct. 2005.
- [50] W. M. Leevy, M. E. Weber, P. H. Schlesinger, and G. W. Gokel, "NMR and ion selective electrode studies of hydraphile channels correlate with biological activity in *E. coli* and *B. subtilis*.," *Chem. Commun. (Camb)*, no. 1, pp. 89–91, Jan. 2005.
- [51] T. M. Fyles, T. D. James, and K. C. Kaye, "Activities and Modes of Action of Artificial Ion-Channel Mimics," *J. Am. Chem. Soc.*, vol. 115, no. 26, pp. 12315–12321, 1993.
- [52] T. M. Fyles, "Synthetic ion channels in bilayer membranes.," *Chem. Soc. Rev.*, vol. 36, no. 2, pp. 335–347, 2007.
- [53] J. K. W. Chui and T. M. Fyles, "Ionic conductance of synthetic channels: analysis, lessons, and recommendations," *Chem. Soc. Rev.*, vol. 41, no. 1, p. 148, 2012.
- [54] T. M. Fyles, "How Do Amphiphiles Form Ion-Conducting," pp. 2847–2855, 2013.
- [55] J. L. Atkins, M. B. Patel, M. M. Daschbach, J. W. Meisel, and G. W. Gokel, "Anion complexation and transport by isophthalamide and dipicolinamide derivatives:

- DNA plasmid transformation in *E. coli*,” *J. Am. Chem. Soc.*, vol. 134, no. 33, pp. 13546–13549, 2012.
- [56] C. R. Yamnitz, S. Negin, I. A. Carasel, R. K. Winter, and G. W. Gokel, “Dianilides of dipicolinic acid function as synthetic chloride channels.,” *Chem. Commun. (Camb)*, vol. 46, no. 16, pp. 2838–2840, 2010.
- [57] Z. Yin, Z. Li, W.-Z. Yang, J. He, and J.-P. Cheng, “Pseudo-Polymorphs of N,N'-Bis(4-nitrophenyl)-2,6-Pyridinedicarboxamide,” *Struct. Chem.*, vol. 16, no. 6, pp. 641–647, Nov. 2005.
- [58] S. J. Coles, J. G. Frey, P. A. Gale, M. B. Hursthouse, M. E. Light, K. Navakhun, and G. L. Thomas, “Anion-directed assembly: the first fluoride-directed double helix,” *Chem. Commun.*, no. 5, pp. 568–569, Feb. 2003.
- [59] N. Sakai, K. C. Brennan, L. A. Weiss, and S. Matile, “Toward Biomimetic Ion Channels Formed by Rigid-Rod Molecules: Length-Dependent Ion-Transport Activity of Substituted Oligo( p -Phenylene)s,” *J. Am. Chem. Soc.*, vol. 119, no. 37, pp. 8726–8727, Sep. 1997.
- [60] L. A. Weiss, N. Sakai, B. Ghebremariam, C. Ni, and S. Matile, “Rigid Rod-Shaped Polyols: Functional Nonpeptide Models for Transmembrane Proton Channels †,” *J. Am. Chem. Soc.*, vol. 119, no. 50, pp. 12142–12149, Dec. 1997.
- [61] M. M. Tedesco, B. Ghebremariam, N. Sakai, and S. Matile, “Modeling the Selectivity of Potassium Channels with Synthetic, Ligand-Assembled  $\pi$  Slides,” *Angew. Chemie Int. Ed.*, vol. 38, no. 4, pp. 540–543, Feb. 1999.
- [62] V. Sidorov, F. W. Kotch, G. Abdrakhmanova, R. Mizani, J. C. Fettinger, and J. T. Davis, “Ion Channel Formation from a Calix[4]arene Amide That Binds HCl,” *J. Am. Chem. Soc.*, vol. 124, no. 10, pp. 2267–2278, Mar. 2002.
- [63] S. K. Berezin and J. T. Davis, “Catechols as Membrane Anion Transporters,” *J. Am. Chem. Soc.*, vol. 131, no. 7, pp. 2458–2459, Feb. 2009.
- [64] S. K. Berezin, “Synthetic anionophores for basic anions as ‘Presumably, OH<sup>-</sup>/Cl<sup>-</sup>-antiporters’: From the synthetic ion channels to multi-ion hopping, anti-Hofmeister selectivity, and strong positive AMFE,” *J. Membr. Biol.*, vol. 247, no. 8, pp. 651–665, 2014.
- [65] C. Schalley, Ed., *Analytical Methods in Supramolecular Chemistry*. Weinheim, Germany: Wiley-VCH Verlag GmbH & Co. KGaA, 2006.
- [66] G. Benga, “The first discovered water channel protein, later called aquaporin 1: Molecular characteristics, functions and medical implications,” *Mol. Aspects Med.*, vol. 33, no. 5–6, pp. 518–534, 2012.



- [67] G. M. Preston, T. P. Carroll, W. B. Guggino, and P. Agre, "Appearance of water channels in *Xenopus* oocytes expressing red cell CHIP28 protein.," *Science*, vol. 256, no. 5055, pp. 385–7, Apr. 1992.
- [68] B. L. de Groot, T. Frigato, V. Helms, and H. Grubmüller, "The mechanism of proton exclusion in the aquaporin-1 water channel.," *J. Mol. Biol.*, vol. 333, no. 2, pp. 279–93, Oct. 2003.
- [69] P. Agre, L. S. King, M. Yasui, W. B. Guggino, O. P. Ottersen, Y. Fujiyoshi, A. Engel, and S. Nielsen, "Aquaporin water channels—from atomic structure to clinical medicine.," *J. Physiol.*, vol. 542, no. Pt 1, pp. 3–16, Jul. 2002.
- [70] P. Agre, "Aquaporin water channels (nobel lecture)," *Angew. Chemie - Int. Ed.*, vol. 43, no. 33, pp. 4278–4290, Aug. 2004.
- [71] G. Benga, "Foreword to the special issue on water channel proteins (aquaporins and relatives) in health and disease: 25 Years after the discovery of the first water channel protein, later called aquaporin 1," *Mol. Aspects Med.*, vol. 33, no. 5–6, pp. 511–513, 2012.
- [72] C. X. Zhao, H. B. Shao, and L. Y. Chu, "Aquaporin structure-function relationships: Water flow through plant living cells," *Colloids Surfaces B Biointerfaces*, vol. 62, no. 2, pp. 163–172, 2008.
- [73] E. M. Campbell, A. Ball, S. Hoppler, and A. S. Bowman, "Invertebrate aquaporins: A review," *J. Comp. Physiol. B Biochem. Syst. Environ. Physiol.*, vol. 178, no. 8, pp. 935–955, 2008.
- [74] A. Frick, M. Järvå, and S. Törnroth-Horsefield, "Structural basis for pH gating of plant aquaporins," *FEBS Lett.*, vol. 587, no. 7, pp. 989–993, 2013.
- [75] B. Wu and E. Beitz, "Aquaporins with selectivity for unconventional permeants.," *Cell. Mol. Life Sci.*, vol. 64, no. 18, pp. 2413–21, Sep. 2007.
- [76] C. a. Wraight, "Chance and design-Proton transfer in water, channels and bioenergetic proteins," *Biochim. Biophys. Acta - Bioenerg.*, vol. 1757, no. 8, pp. 886–912, 2006.
- [77] V. Percec, A. E. Dulcey, V. S. K. Balagurusamy, Y. Miura, J. Smidrkal, M. Peterca, S. Nummelin, U. Edlund, S. D. Hudson, P. A. Heiney, H. Duan, S. N. Magonov, and S. A. Vinogradov, "Self-assembly of amphiphilic dendritic dipeptides into helical pores.," *Nature*, vol. 430, no. 7001, pp. 764–8, Aug. 2004.
- [78] V. Percec, A. E. Dulcey, M. Peterca, M. Ilies, M. J. Sienkowska, and P. A. Heiney, "Programming the internal structure and stability of helical pores self-assembled

- from dendritic dipeptides via the protective groups of the peptide.," *J. Am. Chem. Soc.*, vol. 127, no. 50, pp. 17902–9, Dec. 2005.
- [79] M. Peterca, V. Percec, A. E. Dulcey, S. Nummelin, S. Korey, M. Ilies, and P. A. Heiney, "Self-assembly, structural, and retrostructural analysis of dendritic dipeptide pores undergoing reversible circular to elliptical shape change.," *J. Am. Chem. Soc.*, vol. 128, no. 20, pp. 6713–20, May 2006.
- [80] M. S. Kaucher, M. Peterca, A. E. Dulcey, A. J. Kim, S. a. Vinogradov, D. a. Hammer, P. a. Heiney, and V. Percec, "Selective transport of water mediated by porous dendritic dipeptides," *J. Am. Chem. Soc.*, vol. 129, no. 38, pp. 11698–11699, Sep. 2007.
- [81] J. G. Rudick and V. Percec, "Induced helical backbone conformations of self-organizable dendronized polymers.," *Acc. Chem. Res.*, vol. 41, no. 12, pp. 1641–52, Dec. 2008.
- [82] B. M. Rosen, D. A. Wilson, C. J. Wilson, M. Peterca, B. C. Won, C. Huang, L. R. Lipski, X. Zeng, G. Ungar, P. A. Heiney, and V. Percec, "Predicting the structure of supramolecular dendrimers via the analysis of libraries of AB<sub>3</sub> and constitutional isomeric AB<sub>2</sub> biphenylpropyl ether self-assembling dendrons.," *J. Am. Chem. Soc.*, vol. 131, no. 47, pp. 17500–21, Dec. 2009.
- [83] K. Koga, G. T. Gao, H. Tanaka, and X. C. Zeng, "Formation of ordered ice nanotubes inside carbon nanotubes.," *Nature*, vol. 412, no. 6849, pp. 802–5, Aug. 2001.
- [84] B. J. Hinds, N. Chopra, T. Rantell, R. Andrews, V. Gavalas, and L. G. Bachas, "Aligned multiwalled carbon nanotube membranes.," *Science*, vol. 303, no. 5654, pp. 62–5, Jan. 2004.
- [85] L. E. Cheruzel, M. S. Pometun, M. R. Cecil, M. S. Mashuta, R. J. Wittebort, and R. M. Buchanan, "Structures and solid-state dynamics of one-dimensional water chains stabilized by imidazole channels.," *Angew. Chem. Int. Ed. Engl.*, vol. 42, no. 44, pp. 5452–5, Nov. 2003.
- [86] Z. Fei, D. Zhao, T. J. Geldbach, R. Scopelliti, P. J. Dyson, S. Antonijevic, and G. Bodenhausen, "A Synthetic Zwitterionic Water Channel: Characterization in the Solid State by X-ray Crystallography and NMR Spectroscopy," *Angew. Chemie*, vol. 117, no. 35, pp. 5866–5871, Sep. 2005.
- [87] H.-T. Zhang, Y.-Z. Li, T.-W. Wang, E. N. Nfor, H.-Q. Wang, and X.-Z. You, "A ZnII-Based Chiral Crystalline Nanotube," *Eur. J. Inorg. Chem.*, vol. 2006, no. 17, pp. 3532–3536, Sep. 2006.

- [88] S. Guha, M. G. B. Drew, and A. Banerjee, "Formation of a one-dimensional helical alignment of water molecules within a water-mediated supramolecular helix using molecular self-assembly of a water-soluble short pseudopeptide," *Tetrahedron Lett.*, vol. 47, no. 45, pp. 7951–7955, Nov. 2006.
- [89] M. R. Ghadiri, J. R. Granja, and L. K. Buehler, "Artificial transmembrane ion channels from self-assembling peptide nanotubes.," *Nature*, vol. 369, no. 6478, pp. 301–4, May 1994.
- [90] C. H. Görbitz, "Microporous organic materials from hydrophobic dipeptides.," *Chemistry*, vol. 13, no. 4, pp. 1022–31, Jan. 2007.
- [91] U. S. Raghavender, S. Aravinda, N. Shamala, Kantharaju, R. Rai, and P. Balaram, "Characterization of water wires inside hydrophobic tubular peptide structures.," *J. Am. Chem. Soc.*, vol. 131, no. 42, pp. 15130–2, Oct. 2009.
- [92] P. K. Thallapally, G. O. Lloyd, J. L. Atwood, and L. J. Barbour, "Diffusion of Water in a Nonporous Hydrophobic Crystal," *Angew. Chemie*, vol. 117, no. 25, pp. 3916–3919, Jun. 2005.
- [93] C. Y. Tang, Y. Zhao, R. Wang, C. Hélix-Nielsen, and a. G. Fane, "Desalination by biomimetic aquaporin membranes: Review of status and prospects," *Desalination*, vol. 308, pp. 34–40, 2013.
- [94] M. Kumar, J. E. O. Habel, Y. X. Shen, W. P. Meier, and T. Walz, "High-density reconstitution of functional water channels into vesicular and planar block copolymer membranes," *J. Am. Chem. Soc.*, vol. 134, no. 45, pp. 18631–18637, 2012.
- [95] M. Kumar, M. Grzelakowski, J. Zilles, M. Clark, and W. Meier, "Highly permeable polymeric membranes based on the incorporation of the functional water channel protein Aquaporin Z.," *Proc. Natl. Acad. Sci. U. S. A.*, vol. 104, no. 52, pp. 20719–24, Dec. 2007.
- [96] X.-B. Hu, Z. Chen, G. Tang, J.-L. Hou, and Z.-T. Li, "Single-molecular artificial transmembrane water channels.," *J. Am. Chem. Soc.*, vol. 134, no. 20, pp. 8384–7, May 2012.
- [97] C. Cheng, L. L. C. Olijve, R. Kausik, S. Han, C. Cheng, L. L. C. Olijve, R. Kausik, and S. Han, "Cholesterol enhances surface water diffusion of phospholipid bilayers Cholesterol enhances surface water diffusion of phospholipid bilayers," *J. Chem. Phys.*, vol. 513, 2014.
- [98] H. Zhao, S. Sheng, Y. Hong, and H. Zeng, "Proton Gradient-Induced Water Transport Mediated by Water Wires Inside Narrow Aquapores of Aquafoldamer Molecules," pp. 1–7, 2014.

- [99] K. Kuwajima, H. Yamaya, and S. Sugai, "The burst-phase intermediate in the refolding of beta-lactoglobulin studied by stopped-flow circular dichroism and absorption spectroscopy.," *J. Mol. Biol.*, vol. 264, no. 4, pp. 806–22, Dec. 1996.
- [100] M. J. Pandya, P. B. Williams, C. E. Dempsey, P. R. Shewry, and A. R. Clarke, "Direct Kinetic Evidence for Folding via a Highly Compact, Misfolded State," *J. Biol. Chem.*, vol. 274, no. 38, pp. 26828–26837, Sep. 1999.
- [101] M. Kumar, M. M. Payne, S. K. Poust, and J. L. Zilles, "Biomimetic Membranes for Sensor and Separation Applications," pp. 43–62, 2012.
- [102] J. Tong, J. T. Canty, M. M. Briggs, and T. J. McIntosh, "The water permeability of lens aquaporin-0 depends on its lipid bilayer environment.," *Exp. Eye Res.*, vol. 113, pp. 32–40, Aug. 2013.
- [103] K. Kano and J. H. Fendler, "Pyranine as a sensitive pH probe for liposome interiors and surfaces. pH gradients across phospholipid vesicles," *Biochim. Biophys. Acta - Biomembr.*, vol. 509, no. 2, pp. 289–299, May 1978.
- [104] A. Burykin and A. Warshel, "What really prevents proton transport through aquaporin? Charge self-energy versus proton wire proposals.," *Biophys. J.*, vol. 85, no. 6, pp. 3696–706, Dec. 2003.
- [105] M. Ø. Jensen, U. Röthlisberger, and C. Rovira, "Hydroxide and proton migration in aquaporins.," *Biophys. J.*, vol. 89, no. 3, pp. 1744–59, Sep. 2005.
- [106] H. Nakagawa, Y. Kobori, M. Yoshida, and K. Yamada, "Chiral recognition by single bilayered phosphatidylcholine vesicles using [5]thiaheterohelicene as a probe," *Chem. Commun.*, no. 24, pp. 2692–2693, 2001.
- [107] M. Juba, D. Porter, S. Dean, S. Gillmor, and B. Bishop, "Characterization and performance of short cationic antimicrobial peptide isomers.," *Biopolymers*, vol. 100, no. 4, pp. 387–401, 2013.
- [108] S. C. D. N. Lopes, A. Fedorov, and M. a R. B. Castanho, "Chiral recognition of D-kyotorphin by lipidic membranes: Relevance toward improved analgesic efficiency," *ChemMedChem*, vol. 1, no. 7, pp. 723–728, 2006.
- [109] P. Behaviors, H. Umakoshi, C. Engineering, E. Science, R. December, and A. January, "The partitioning behaviors of L - / D -Trp in a solvent-water system modified with a phospholipid and a liposome membrane system were compared . Trp was partitioned to the interface of chloroform-water system supplemented with phospholipid . As the methan," vol. 20, pp. 213–217, 2013.

- [110] H. Umakoshi and K. Suga, "Use Liposome as a Designable Platform for Molecular Recognition from 'Statistical Separation' to 'Recognitive Separation,'" *Solvent Extr. Res. Dev.*, vol. 20, pp. 1–13, 2013.
- [111] C. T. Kresge, M. E. Leonowicz, W. J. Roth, J. C. Vartuli, and J. S. Beck, "Ordered mesoporous molecular sieves synthesized by a liquid-crystal template mechanism," *Nature*, vol. 359, no. 6397, pp. 710–712, Oct. 1992.
- [112] S.-H. Wu, C.-Y. Mou, and H.-P. Lin, "Synthesis of mesoporous silica nanoparticles.," *Chem. Soc. Rev.*, vol. 42, no. 9, pp. 3862–75, May 2013.
- [113] K.-S. Jang, H.-J. Kim, J. R. Johnson, W. Kim, W. J. Koros, C. W. Jones, and S. Nair, "Modified Mesoporous Silica Gas Separation Membranes on Polymeric Hollow Fibers," *Chem. Mater.*, vol. 23, no. 12, pp. 3025–3028, Jun. 2011.
- [114] X. Fang, X. Zhao, W. Fang, C. Chen, and N. Zheng, "Self-templating synthesis of hollow mesoporous silica and their applications in catalysis and drug delivery.," *Nanoscale*, vol. 5, no. 6, pp. 2205–18, Mar. 2013.
- [115] C. Lei, Y. Shin, J. Liu, and E. J. Ackerman, "Entrapping Enzyme in a Functionalized Nanoporous Support," *J. Am. Chem. Soc.*, vol. 124, no. 38, pp. 11242–11243, Sep. 2002.
- [116] I. I. Slowing, B. G. Trewyn, S. Giri, and V. S.-Y. Lin, "Mesoporous Silica Nanoparticles for Drug Delivery and Biosensing Applications," *Adv. Funct. Mater.*, vol. 17, no. 8, pp. 1225–1236, May 2007.
- [117] T. Nakamura, F. Sugihara, H. Matsushita, Y. Yoshioka, S. Mizukami, and K. Kikuchi, "Mesoporous silica nanoparticles for  $^{19}\text{F}$  magnetic resonance imaging, fluorescence imaging, and drug delivery," *Chem. Sci.*, vol. 6, no. 3, pp. 1986–1990, Feb. 2015.
- [118] Z. Li, J. C. Barnes, A. Bosoy, J. F. Stoddart, and J. I. Zink, "Mesoporous silica nanoparticles in biomedical applications.," *Chem. Soc. Rev.*, vol. 41, no. 7, pp. 2590–605, Apr. 2012.
- [119] F. Tang, L. Li, and D. Chen, "Mesoporous silica nanoparticles: synthesis, biocompatibility and drug delivery.," *Adv. Mater.*, vol. 24, no. 12, pp. 1504–34, Mar. 2012.
- [120] A. Walcarius, E. Sibottier, M. Etienne, and J. Ghanbaja, "Electrochemically assisted self-assembly of mesoporous silica thin films.," *Nat. Mater.*, vol. 6, no. 8, pp. 602–8, Aug. 2007.
- [121] M. Barboiu, A. Cazacu, S. Mihai, Y.-M. Legrand, G. Nasr, Y. Le Duc, E. Petit, and A. van der Lee, "Dynamic constitutional hybrid materials-toward adaptive self-

- organized devices,” *Microporous Mesoporous Mater.*, vol. 140, no. 1–3, pp. 51–57, Apr. 2011.
- [122] S. Mihai, Y. Le Duc, D. Cot, and M. Barboiu, “Sol–gel selection of hybrid G-quadruplex architectures from dynamic supramolecular guanosine libraries,” *J. Mater. Chem.*, vol. 20, no. 42, p. 9443, Oct. 2010.
- [123] A. Cazacu, S. Mihai, G. Nasr, E. Mahon, A. van der Lee, A. Meffre, and M. Barboiu, “Lipophilic polyoxomolybdate nanocapsules in constitutional dynamic hybrid materials,” *Inorganica Chim. Acta*, vol. 363, no. 15, pp. 4214–4219, Dec. 2010.
- [124] Y. Le Duc, A. Gilles, S. Mihai, V. Rouessac, S. Tingry, and M. Barboiu, “Dynamic constitutional electrodes toward functional fullerene wires,” *Chem. Commun. (Camb.)*, vol. 49, no. 35, pp. 3667–9, May 2013.
- [125] D. Mann, A. Javey, J. Kong, Q. Wang, and H. Dai, “Ballistic Transport in Metallic Nanotubes with Reliable Pd Ohmic Contacts,” *Nano Lett.*, vol. 3, no. 11, pp. 1541–1544, Nov. 2003.
- [126] A. R. Harutyunyan, G. Chen, T. M. Paronyan, E. M. Pigos, O. A. Kuznetsov, K. Hewaparakrama, S. M. Kim, D. Zakharov, E. A. Stach, and G. U. Sumanasekera, “Preferential growth of single-walled carbon nanotubes with metallic conductivity,” *Science*, vol. 326, no. 5949, pp. 116–20, Oct. 2009.
- [127] A. A. Green and M. C. Hersam, “Processing and properties of highly enriched double-wall carbon nanotubes,” *Nat. Nanotechnol.*, vol. 4, no. 1, pp. 64–70, Jan. 2009.
- [128] K. Lee, S. Cho, S. H. Park, A. J. Heeger, C.-W. Lee, and S.-H. Lee, “Metallic transport in polyaniline,” *Nature*, vol. 441, no. 7089, pp. 65–8, May 2006.
- [129] F. J. M. Hoeben, P. Jonkheijm, E. W. Meijer, and A. P. H. J. Schenning, “About supramolecular assemblies of pi-conjugated systems,” *Chem. Rev.*, vol. 105, no. 4, pp. 1491–546, Apr. 2005.
- [130] A. P. H. J. Schenning and E. W. Meijer, “Supramolecular electronics; nanowires from self-assembled pi-conjugated systems,” *Chem. Commun. (Camb.)*, no. 26, pp. 3245–58, Jul. 2005.
- [131] V. Percec, M. Glodde, T. K. Bera, Y. Miura, I. Shiyanovskaya, K. D. Singer, V. S. K. Balagurusamy, P. A. Heiney, I. Schnell, A. Rapp, H. W. Spiess, S. D. Hudson, and H. Duan, “Self-organization of supramolecular helical dendrimers into complex electronic materials,” *Nature*, vol. 419, no. 6905, pp. 384–387, Sep. 2002.

- [132] H. Nishihara, T. Kwon, Y. Fukura, W. Nakayama, Y. Hoshikawa, S. Iwamura, N. Nishiyama, T. Itoh, and T. Kyotani, "Fabrication of a Highly Conductive Ordered Porous Electrode by Carbon-Coating of a Continuous Mesoporous Silica Film," *Chem. Mater.*, vol. 23, no. 13, pp. 3144–3151, Jul. 2011.
- [133] L. Welte, A. Calzolari, R. Di Felice, F. Zamora, and J. Gómez-Herrero, "Highly conductive self-assembled nanoribbons of coordination polymers.," *Nat. Nanotechnol.*, vol. 5, no. 2, pp. 110–5, Mar. 2010.
- [134] P. Samorì, X. Yin, N. Tchebotareva, Z. Wang, T. Pakula, F. Jäckel, M. D. Watson, A. Venturini, K. Müllen, and J. P. Rabe, "Self-assembly of electron donor-acceptor dyads into ordered architectures in two and three dimensions: surface patterning and columnar 'double cables'.," *J. Am. Chem. Soc.*, vol. 126, no. 11, pp. 3567–75, Mar. 2004.
- [135] J. P. Hill, W. Jin, A. Kosaka, T. Fukushima, H. Ichihara, T. Shimomura, K. Ito, T. Hashizume, N. Ishii, and T. Aida, "Self-assembled hexa-peri-hexabenzocoronene graphitic nanotube.," *Science*, vol. 304, no. 5676, pp. 1481–3, Jun. 2004.
- [136] R. Bhosale, A. Perez-Velasco, V. Ravikumar, R. S. K. Kishore, O. Kel, A. Gomez-Casado, P. Jonkheijm, J. Huskens, P. Maroni, M. Borkovec, T. Sawada, E. Vauthey, N. Sakai, and S. Matile, "Topologically matching supramolecular n/p-heterojunction architectures.," *Angew. Chem. Int. Ed. Engl.*, vol. 48, no. 35, pp. 6461–4, Jan. 2009.
- [137] V. Faramarzi, F. Niess, E. Moulin, M. Maaloum, J.-F. Dayen, J.-B. Beaufrand, S. Zanettini, B. Doudin, and N. Giuseppone, "Light-triggered self-construction of supramolecular organic nanowires as metallic interconnects," *Nat. Chem.*, vol. 4, no. 6, pp. 485–490, 2012.
- [138] S. Sayen and A. Walcarius, "Electro-assisted generation of functionalized silica films on gold," *Electrochem. commun.*, vol. 5, no. 4, pp. 341–348, 2003.
- [139] M. Etienne, J. Cortot, and A. Walcarius, "Preconcentration electroanalysis at surfactant-templated thiol-functionalized silica thin films," *Electroanalysis*, vol. 19, no. 2–3, pp. 129–138, 2007.
- [140] A. Walcarius and E. Sibottier, "Electrochemically-induced deposition of amine-functionalized silica films on gold electrodes and application to Cu(II) detection in (hydro)alcoholic medium," *Electroanalysis*, vol. 17, no. 19, pp. 1716–1726, 2005.
- [141] E. Moulin, F. Niess, M. Maaloum, E. Buhler, I. Nyrkova, and N. Giuseppone, "The hierarchical self-assembly of charge nanocarriers: A highly cooperative process promoted by visible light," *Angew. Chemie - Int. Ed.*, vol. 49, no. 39, pp. 6974–6978, Sep. 2010.

- [142] E. Moulin, J.-J. Cid, and N. Giuseppone, "Advances in supramolecular electronics - from randomly self-assembled nanostructures to addressable self-organized interconnects.," *Adv. Mater.*, vol. 25, no. 3, pp. 477–87, Jan. 2013.
- [143] E. Moulin, F. Niess, G. Fuks, N. Jouault, E. Buhler, and N. Giuseppone, "Light-triggered self-assembly of triarylamine-based nanospheres.," *Nanoscale*, vol. 4, no. 21, pp. 6748–51, Nov. 2012.
- [144] Y. Domoto, E. Busseron, M. Maaloum, E. Moulin, and N. Giuseppone, "Inside Back Cover: Control over Nanostructures and Associated Mesomorphic Properties of Doped Self-Assembled Triarylamine Liquid Crystals (Chem. Eur. J. 5/2015)," *Chem. - A Eur. J.*, vol. 21, no. 5, pp. 2271–2271, Jan. 2015.
- [145] A. Wolf, E. Moulin, J. J. Cid Martín, A. Goujon, G. Du, E. Busseron, G. Fuks, and N. GIUSEPPONE, "pH and light-controlled self-assembly of bistable [c2] daisy chain rotaxanes," *Chem. Commun.*, vol. 51, no. 20, pp. 4212–4215, Jan. 2015.
- [146] I. Nyrkova, E. Moulin, J. J. Armao, M. Maaloum, B. Heinrich, M. Rawiso, F. Niess, J.-J. Cid, N. Jouault, E. Buhler, A. N. Semenov, and N. Giuseppone, "Supramolecular self-assembly and radical kinetics in conducting self-replicating nanowires.," *ACS Nano*, vol. 8, no. 10, pp. 10111–24, Oct. 2014.
- [147] I. Ivanov, T. Vidaković-Koch, and K. Sundmacher, "Recent advances in enzymatic fuel cells: Experiments and modeling," *Energies*, vol. 3, no. 4, pp. 803–846, Apr. 2010.
- [148] F. Davis and S. P. J. Higson, "Biofuel cells-Recent advances and applications," *Biosens. Bioelectron.*, vol. 22, no. 7, pp. 1224–1235, 2007.
- [149] E. H. Yu and K. Scott, "Enzymatic biofuel cells-fabrication of enzyme electrodes," *Energies*, vol. 3, no. 1, pp. 23–42, 2010.
- [150] N. Mano and L. Edembe, "Bilirubin oxidases in bioelectrochemistry: Features and recent findings," *Biosens. Bioelectron.*, vol. 50, pp. 478–485, 2013.
- [151] N. Mano, V. Soukharev, and A. Heller, "A laccase-wiring redox hydrogel for efficient catalysis of O<sub>2</sub> electroreduction," *J. Phys. Chem. B*, vol. 110, no. 23, pp. 11180–11187, 2006.
- [152] D. Selloum, a. A. Chaaya, M. Bechelany, V. Rouessac, P. Miele, and S. Tingry, "A highly efficient gold/electrospun PAN fiber material for improved laccase biocathodes for biofuel cell applications," *J. Mater. Chem. A*, vol. 2, no. 8, p. 2794, Jan. 2014.



- [153] A.-F. Che, V. Germain, M. Cretin, D. Cornu, C. Innocent, and S. Tingry, "Fabrication of free-standing electrospun carbon nanofibers as efficient electrode materials for bioelectrocatalysis," *New J. Chem.*, vol. 35, no. 12, p. 2848, 2011.
- [154] W. E. Farneth, B. A. Diner, T. D. Gierke, and M. B. D'Amore, "Current densities from electrocatalytic oxygen reduction in laccase/ABTS solutions," *J. Electroanal. Chem.*, vol. 581, no. 2, pp. 190–196, Aug. 2005.
- [155] W. Nogala, E. Rozniecka, I. Zawisza, J. Rogalski, and M. Opallo, "Immobilization of ABTS – laccase system in silicate based electrode for bioelectrocatalytic reduction of dioxygen," *Electrochem. commun.*, vol. 8, no. 12, pp. 1850–1854, Dec. 2006.
- [156] K. Karnicka, K. Miecznikowski, B. Kowalewska, M. Skunik, M. Opallo, J. Rogalski, W. Schuhmann, and P. J. Kulesza, "ABTS-modified multiwalled carbon nanotubes as an effective mediating system for bioelectrocatalytic reduction of oxygen.," *Anal. Chem.*, vol. 80, no. 19, pp. 7643–8, Oct. 2008.
- [157] K. Servat, S. Tingry, L. Brunel, S. Querelle, M. Cretin, C. Innocent, C. Jolival, and M. Rolland, "Modification of porous carbon tubes with enzymes: application for biofuel cells," *J. Appl. Electrochem.*, vol. 37, no. 1, pp. 121–127, Nov. 2006.